Network computing for ab initio modeling the chemical storage of alternative energy

Carles Martí Aliod

Université Fédérale
Toulouse Midi-Pyrénées

THÈSE

En vue de l'obtention du

DOCTORAT DE L'UNIVERSITÉ DE TOULOUSE

Délivré par l'Université Toulouse 3 - Paul Sabatier

Cotutelle internationale : Università degli Studi di Perugia - Dipartimento di Chimica Biologia e Biotecnologie

---

Présentée et soutenue par

Carles MARTI ALIOD

Le 14 décembre 2018

Simulation de processus de stockage chimique pour l'énergie renouvelable

---

Ecole doctorale : **SDM - SCIENCES DE LA MATIERE - Toulouse**

Spécialité : **Physico-Chimie Théorique**

Unité de recherche :
LCPQ-IRSAMC - Laboratoire de Chimie et Physique Quantiques

Thèse dirigée par
Fernand SPIEGELMAN et Noelia Faginas Lago

Jury

M. Antonio Aguilar Navarro, Rapporteur
M. György Lendvay, Rapporteur
M. Leonardo Belpassi, Examinateur
Mme Paola Belanzoni, Examinateur
M. Ramón Sayós, Examinateur
M. Stefano Evangelisti, Examinateur
Mme Karine Costuas, Examinateur
Tzonka Mineva, Examinateur
M. Fernand SPIEGELMAN, Directeur de thèse
Mme Noelia Faginas Lago, Co-directeur de thèse

UNIVERSITÀ DEGLI STUDI DI PERUGIA
Dipartimento di Chimica, Biologia e Biotecnologie

UNIVERSITÉ DE TOULOUSE - PAUL SABATIER
Laboratoire de Chimie et Physique Quantiques

Doctorate in Chemical Sciences (XXXI cycle)
Curriculum: Theoretical Chemistry and Computational Modeling
Scientific Area CHIM/03

Networked computing for ab initio modeling the chemical storage of alternative energy

Doctoral Thesis
Carles Martí Aliod

Supervisors:

Prof. Fernand Spiegelman

Dr. Noelia Faginas Lago

Dr. Jérôme Cuny

Prof. Marzio Rosi

Prof. Antonio Laganà

Coordinator:

Prof. Piergiorgio Casavecchia

Academic year 2017-2018
October 2018

"*Choose a job you love, and you will never have to work a day in your life...*"

Confucius

"*...Because that field isn't hiring*"

Acknowledgments

My first and most important acknowledgments are for my Thesis Supervisors, Prof. Fernand Spiegelman, Prof. Antonio Laganà, Prof. Marzio Rosi, Dr. Jerôme Cuny, Dr. Noelia Faginas Lago and also in the first period to Dr. Leonardo Pacifici for all what I learned from you. A lot of science but also a lot of the science solvation shell (The How-To Science). These three years of PhD wouldn't have been the ones I have learned the most in my life without your contribution. I would like to thank you also for the nice ambiance you have given to each one of the periods I have spent with you and the patience you got.

A similar acknowledgement is deserved by Prof. Cecilia Coletti and Prof. Mathias Rapacioli. My work with the quantum-classical method, and all the programming with the qcmet code would have been just not possible without your knowledge, Cecilia. I would like to thank you as well for all the nice ambiance I had each time I visited Chieti, and extend that thanks to all the people working there. I would like to thank you Mathias for all the support I received from you both for the programming part of deMon and the scientific discussion of the topics for which you had always very good ideas to solve my problems. Make yours as well the thanks for the ambiance I had in Toulouse, I could not think of a better work relation than the one that I had with you all. To Prof. Pirani and Prof. Garcia, I would like to thank you as well for the good collaboration we had.

My project was one among 15 of MSCA-ITN-EJD-TCCM all coordinated by the Supervisory board with the lead of Prof. Manuel Yañez. I would like to thank the whole consortium for this opportunity and encourage you to repeat the experience with the feedback from us obtained. I would like to give an extra thank to Manuel and Wilson for all the hidden work necessary to make all this happen. I would like to thank the European Comission through the MSCA for the Financial Support. I also would like to thank Prof. Casavecchia and Dr. Jérôme Cuny for their work done regarding coordination of Doctoral Schools.

Als meus pares un agraïment especial. Fa falta molta paciència per suportar-me durant 30 anys i pico. He après molt de vosaltres, en tots els sentits. I si sóc qui sóc avui en dia és tant pel que he heredat genèticament com per totes experiències que he viscut amb vosaltres.

El gràcies més sentit és pels amics incondicionals: Per ordre alfabètic, l'Alonso, el Gadea, el Jan i el Serri. Diuen que els amics són la família que s'escull, en el meu cas no pot ser més veritat. Gràcies, perquè sou a qui dec més ser la persona que sóc. Dels milers d'experiències que hem viscut junts, vull donar-vos les gràcies sobretot per les discussions de física i ciència bevent birres, van ser sens dubte la llavor d'on ha sortit aquesta tesi doctoral. Segur que us heu adonat que hem cambiat molt en els últims anys. L'estima que us tinc però, no canviarà.

A te, Ester, un grazie molto speciale. Sei la persona più diversa di me che

conosco e nonostante questo andiamo d'accordo in un modo troppo bello. Abbiamo condiviso tanto nonostante la distanza, ma quello che voglio ringraziarti di più è il farmi vedere il mondo con altri occhi. Per non smetterla di sorprendermi mai, per ricordarmi ogni giorno che la vita è per godersela. E per farmi rendere conto che che anch'io sbaglio.

La meva curiositat científica s'hagués quedat com això, mer interès científic si no fós pel Fermín. A part de ser un referent tant personal com científic vull dedicar-te un gràcies per obrir-me la porta del món de la investigació científica. Crec que si no fós per tu hagués pres una altra via. Espero poder, en un futur, treballar junts un cop la meva formació estigui a l'alçada de la teva.

Patri, quizás no lo sabes pero eres la persona que he conocido en el doctorado con quien me he llevado mejor. Gracias por todos los momentos que hemos vivido, por las risas que nos hemos hechao. Agradecer también a todos los otro españoles que he conocido a Toulouse, sobretodo Rubén, por los momentos que hemos vivido.

I would like to extend the thanks for all the good moments spent in Toulouse to François and Evgeny. Guys I really had lots of fun with you, it's really nice to see theoretical chemists/physicist/mathematicians as fun as you are!

La meva experiència immediatament anterior al doctorat va ser amb la gent de Can Cocobongo, el Guille, el Jordi, l'Alonso, i el Molas agraïr-vos que la convivència anés tant bé de mantenir la relació durant el doctorat.

Marc (Laporte), gràcies per escriure'm i no deixar que la relació mori, m'has demostrat ser un molt bon amic, gràcies per venir-me a veure a Roma, gràcies de veritat, et valoro més del que et penses, i perdó per no respondre o escriure més sovint, et prometo que anirem a fer birres quan tingui temps.

La mia esperienza di dottorato cominciò fin dall'inizio in modo inmigliorabile nel collegio innamorati. A tutti i ragazzi che ho conosciuto là, grazie per farmi sentire uno di voi. Il grazie più speciale è senza dubbio per Milu, Simo, Perla e Marco, è stata una fortuna ritrovarvi dopo il mio periodo a Toulouse. Una menzione voglio farla anche a Piccinno, Masano e Roberto, tre persone con cui mi sono sentito tanto a mio agio e che mi dispiace non aver potuto condividere di più.

During this three years, the 15 PhD students composing the EJD-TCCM we met on different cities all around europe to improve our knowledge on computational chemistry. In that time I had the luck to meet and now count as friends, 5 of them, Stefano, Jelle, Andi, Martina and Max. Thanks for making this experience go beyond the pure scientific meetings. I'm looking forward to meeting you soon.

Durante il mio periodo a Perugia, ho avuto la fortuna di trovare anche dentro del dipartimento gente con cui ho condiviso tanti bei momenti, grazie a tutti, con una menzione speciale a Jimmy, per confermare ancora che si può fare scienza e avere vita sociale.

Je voudrais remercier tous les gens de l'IRSAMC avec lesquels j'ai eu le plaisir de partager des repàs, des bières après le travail et des conversations scientifiques très interessantes. Parmi eux, une mention speciale à Bastien avec qui j'ai partagé beaucoup de très bons moments, merci beaucoup!

Finalment, un gràcies una mica particular al Barça, concretament al 1r equip de futbol. M'heu donat moltes alegries, i m'heu ajudat molt a desconnectar de tot. Extendre l'agraïment a Kevin Roldán. Contigo empezó todo!

Contents

List of Figures

List of Tables

Acronyms

BO	Born-Oppenheimer
ca.	*circa*
CAS	Complete Active Space
CASPT2	Complete Active Space second-order Perturbation Theory
CM	Center of Mass
DFT	Density Functional Theory
DFTB	Density Functional based Tight Binding
DFT	Discrete Variable Representation
EAM	Embedded Atomic Potentials
e.g.	*exempli gratia*
EPOC	Electrochemical Promotion Of Catalysis
fcc	Face Centered Cubic
FFT	Fast Fourier Transform
FQ	Full-Quantum
hcp	Hexagonal Close Packed
i.e.	*id est*
HPC	High Performance Computing
ILJ	Improved Lennard-Jones
KMC	Kinetic Monte Carlo
MEP	Minimum Energy Path
MRCI	Multi-Reference Configuration Interaction
NN	Neural Network
NP	NanoParticle
PES	Potential Energy Surface
QC	Quantum-Classical
QCT	Quasi-Classical Trajectory
SOP	Split-OPerator
TDWP	Time-Dependent Wave Packet
TS	Transition State
TST	Transition State Theory

Chapter 1

Introduction

Global warming and fossil fuel depletion are two of the biggest concerns humanity faces these days. Indeed for the former one, there is a huge consensus on the anthropogenic source of global warming causes [1–4] being the emission of greenhouse gases like carbon dioxide, methane and nitrous oxide the main responsibles in the increase of the greenhouse effect leading to the global warming according to the Intergovernmental Panel on Climate Change,[5] the UNO depending experts group. The same working group published a second report on the plausible impacts of the mentioned global warming including rising sea levels, changing precipitation, expansion of deserts, ocean acidification and retreat of glaciers, permafrost and sea ice[6] and proposing as a possible response to this thread the emission reduction of greenhouse gases, specially carbon dioxide involved in combustion processes.

Fossil fuel sources arriving to depletion, is yet another reason pushing for a change in the energy production landscape. In 1956 it was first proposed by M. King Hubbert [7] that oil production rate was following a bell-shaped curve based on discovery rates, production rates and cumulative production, classifying time periods into which phase was the predominant, in early stages discovery rates push production rate upwards, in a subsequent phase equilibrium among discovery and finite amount of resources makes the curve reach its maximum leading in the near the bell-top region. From that point on, extraction rates outstrip discovery ones leading to an irreversible decline up to depletion of sources. This theory, known as "peak oil" theory or "Hubbert peak" theory has had a considerable criticism having both followers and detractors [8–10], however, the discrepancy is in the details of the curve shape more than on the fact of depletion of fossil fuels.

With the aforementioned considerations it is also a consensus, not only for the scientific community but for policy makers and global society in general that a new energetic model is needed. Many strategies have been proposed, one of the more promising ones was the emergence of biofuels [11–13] however, its advent caused in 2007 the popularly know "Tortilla Crisis"[14–16] when agricultural goods like sunflower seed and specially corn, greatly grew in prise due to the new demand of the biofuel industry leading to a dramatic impact on the poorest classes of Mexico and other latin American countries whose food base was the corn made tortillas. Hence the need of seeking an alternative source of energy able to satisfy the needed criteria, namely producing it from renewable energy sources, being non contaminant, not interfering with the food production, and if possible able to be used with current facilities thus decreasing the cost of its implementation.

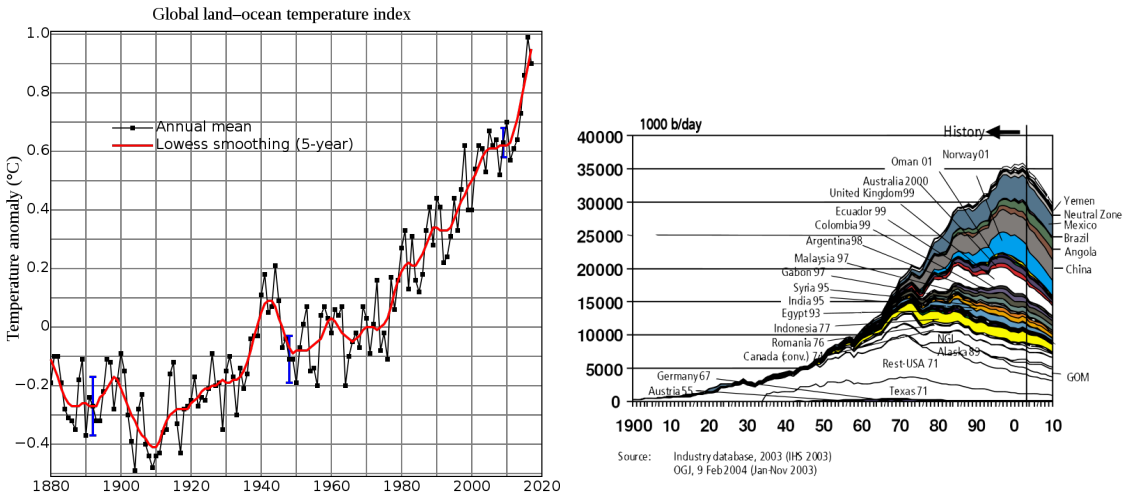

Figure 1.1: Left panel: Global mean surface-temperature change from 1880 to 2017, relative to the 1951–1980 mean. The 1951-1980 mean is 14.18 °C. Author: NASA Goddard Institute for Space Studies. Right panel: 2004 U.S. government predictions for oil production other than in OPEC and the former Soviet Union. Author: Department of Energy of the United States of America

Renewable energy sources of electricity like wind, solar, geothermal, hydropower, biomass, etc. can indeed play the role of main static energy sources substituting thermal power plants and, in a longer term, nuclear energy sources. Nevertheless, they have an irregular production on time, solar energy depends on the amount of light reaching the panels, changing on the cloudiness, and on a night-day basis, wind energy also depends on whether the wind blows and hydropower on the season-depending rains. Therefore the need of storing the excess energy when production overtakes demand and taking advantage of the stored energy when the demand outstrips production. Furthermore, for moving energy sources like the ones needed by means of transportation, where the fossil fuels have a large implementation, there is still a need for finding an energy vector able to efficiently substitute them by at least having similar properties in terms of energy density per mass and volume, reasonable recharging times, in addition to the already mentioned requirement of being non contaminating, not interfering with the food production and able to be produced in a renewable way.

An energy vector that meets most of the mentioned requirements is molecular hydrogen obtained by taking the electricity, produced from renewable energy sources (be it excess energy or produced ad hoc.), and perform the electrolysis of water. The storage of this hydrogen, however, is difficult due to its light weight leading to extreme storing conditions with exceptionally high pressures and/or very low temperatures. Furthermore, its low viscosity and high diffusivity causes huge difficulties in its transport as a result of the unavoidable leaks happening not only through joints but also with diffusion in materials bulk. An alternative to storing directly molecular hydrogen is offered by the Sabatier process (Equation (1.1)), consisting in making the hydrogen react with waste carbon dioxide CO_2 in a catalyzed reaction to give methane and water. Common State-of-the-art catalysts consists on different kinds of dispersion of Nickel over some kind of support (*e.g.* alumina or silica) with usual doping of ruthenium, both as solid solution alloys and surface

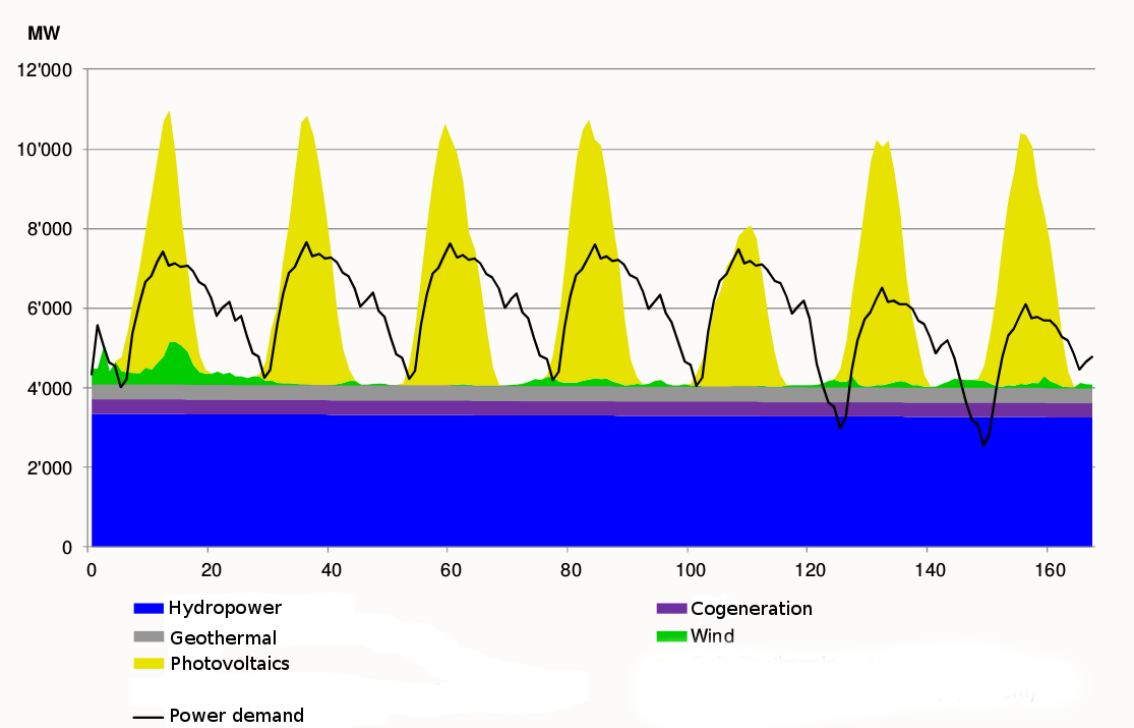

Figure 1.2: Scenario of power production including different energy sources and consumption for a model week in Switzerland 2050 expressed in hours. The available electricity generation exceeds the electricity demand. In the night hours, however, despite lower electricity demand, situations with supply shortages occur in several hours. Source: Swiss Federal Office of Energy SFOE. Author: Prognos

nanoparticles.

$$CO_2 + 4H_2 \rightarrow CH_4 + 2H_2O \tag{1.1}$$

Methane is a more manageable gas than hydrogen and there are already facilities for its distribution via pipelines. Furthermore, it can be easily converted back to electrical power in the existing thermal plants with no generation of additional CO_2. This global and circular approach to the technologies proposed for CO_2 conversion does not only improve manageability, raise resource efficiency and minimize environmental impact (due to its carbon neutral nature) but it also fosters social and market acceptance (as a valid alternative to the past heavily carbon dominated energy technologies). In addition, the proposed technology offers a natural way of exploiting fluctuating or even discontinuous (as is often the case of the renewable) energy sources thanks to its ability to accumulate for deferred usage any provided amount of energy (this will help to eliminate the problem of stopping electricity generation from large plants during periods of low consumption). This is important, for example, in the case of nuclear and large scale thermoelectric plants. Finally, the economic impact and the social benefits obtained from the proposed technology are evident when considering the flexibility of modulating the use of accumulated methane to generate electricity, feed pipelines, bottle it and even to form clathrate hydrates for safe and cheap distribution for deferred and delocalized consumption. The process can, in fact, be used both as an energy "accumulator" and as a "subsidiary carbon neutral fuel production plant".

This process places itself at the seam between the present large demand of fuels and the need for recycling the large amount of CO_2 generated by natural and human activities. The valorisation of that waste CO_2 is matched by its utilization for storing energy from renewable sources (or low cost energy) to produce methane. Present scientific research and technologies will allow, in fact, its easy storage, safe transport, and efficient use as fuel.

Apart from the already mentioned methanation of carbon dioxide via heterogeneous catalysis, also known as the Sabatier process, has yet other uses than energy storage or vector for transports. Carbon dioxide is from the chemical point of view an attractive C_1 building block for organic synthesis[17–19] including urea, salycilic acid, polycarbonates, and fuels [20]. Its use includes purification of syngas[21], and recent developments investigated by NASA make its use to recycle carbon dioxide astronauts generate when breathing in spatial missions.[22–24]

The priorities of the European commission are indeed moving towards the objective of establishing a global transition to a climate neutral economy and the relevant directives for investment into low-carbon innovation. In particular, recently (November 2016), the EU Commission has also launched a package of measures called "Clean Energy for all Europeans" aiming at making Europe a leader in renewable energies by devoting its Research, Innovation and Competitiveness component to the acceleration of Clean Energy Innovation (COM(2016)763)[25]. The related work programme supports research, demonstration, innovation and market-uptake actions across different low-carbon energy sectors (with priorities in renewable energy, smart energy systems energy efficiency for carbon capture, utilization and storage) aimed at strengthening EU leadership in affordable and integrated energy storage solutions.

One of the positive aspects of the Sabatier reaction is its exothermic nature ($\Delta G_{298K} = -130.8 kJ/mol$) making the reaction self-sustainable with no need of external energy provision other than the activation one at the beginning of the reaction process, negligible if working in continuous operation, and thus sparing on energy consumption with its related increased in energetic efficiency. Its drawback is the complicated and slow kinetics of an eight-electron exchange process that make it non-productive at room temperature without the presence of any catalyst.

The choice of the heterogeneous catalyst is indeed an important step when carrying out the reaction, which in literature, studies have been conducted using different metal elements including Ni, Ru, Pt, Rh and Pd. [26–30] Even if the best catalytic properties in terms of activity and selectivity are those of ruthenium-based catalysts [31], nickel is the most used for commercial uses due to its lower cost. Commercially, large support surfaces made of oxides are used due to their influence on the dispersion of the metal catalyst through anchoring metal particles [32] and their active role in the catalytic process.[26] Indeed, many supports with same active phase have been investigated and have been reported to have different activities [26, 31, 33]

A key element affecting the rate of methane production for the Sabatier process (the purely heterogenously catalyzed process), is a good reactor design. This is of paramount importance for the reaction to occur in a controlled (both in terms of energy and in terms of mass and heat flow) fashion i.e. in a good pressure and temperature condition. Good reactor design can even lead to a decrease of the catalyst poisoning playing with the above mentioned parameters. An alternative to the traditional heterogeneous catalysis is the electrochemically promoted one

(EPOC), which has been applied to a variety of catalytic reaction with incremented energy efficiency results.[34] For the Sabatier the EPOC catalysis was indeed studied by means of Rh catalyst.[35, 36]

Carbon dioxide methanation plants are still in an embryonic stage, being Germany the only country decisevely investing on the subject as a result of the political strategies enforcing a carbon-neutral economy. Most of the projects existing nowadays are prototype ones with a finite lifetime.[37] There exist, however, few commercial ones, to the best of the author knowledge, three of them. The first one to carry out the full power-to-methane process was the ZSW 250-kW_{el} going to operation at the end of 2012 [38]. Later on Audi, built a second one in Werlte, Germany[39] using the electricity produced ad hoc in the north sea, in order to produce the methane for their cars. Closing the list of the more important ones there is the HELMETH project [40] which saw the light on 2017. It is clear that carbon dioxide methanation is still not completely stablished process for commercial purposes, but recent improvements on the composing technologies [41] suggests a promising forecast.

Some of the above mentioned developments were taken into actual implementation by PLC System while assembling the PROGEO apparatus, (the PLC System facilitiy on which the secondment of the present PhD Thesis has been carried out) a composite machine performing the whole power-to-gas process as follows in Section 2.1:

a) taking electricity from the net to electrolyse water and produce molecular hydrogen,

b) reducing carbon dioxide to methane through the Sabatier process tailored for small users in a circular economy scheme,

c) storing methane using a safe and energetically convenient (like for example that of clathrate hydrates) technology facilitating deferred utilization.

As to improve the efficiency of the current technology, an understanding of the kinetics ruling the catalytic process is of capital importance. In spite of being a well established textbook example, the mechanism of the Ni-catalyzed CO_2 methanation is still not fully understood [42] as we shall discuss later in Section 2.3. State-of-the-art mechanisms to describe the process fall into two main schemes:

> Schema (A): the reaction is considered to happen through the adsorption of CO as an intermediate [43, 44],
>
> Schema (B): the reaction is considered to happen through a direct hydrogenation of adsorbed CO_2[45–47].

Furthermore, even for schema (A) no consensus has been achieved on the further steps. One hypothesis maintains that reaction evolves towards a CO dissociation to C + O,[48, 49] another considers the CO to be directly hydrogenated[50] while a third one (proposed by Martin et al. [51]) considers the mechanisms mainly as occurring through the disproportionation of CO, being, in all three cases, the proposed reaction the rate limiting one.

Steady-state transient measurements on the reaction using a TiO_2-supported ruthenium catalyst performed by Marwood et al.[52] suggested a mechanism based

on the formation of formate as the active species for the methane production through carbon monoxide intermediate. More specific experimental studies carried out to get the energy barriers of the process in a mono-facet approach (Ni(100)) by looking at the importance of surface modifiers [53], confirmed the formation of CO as and intermediate.

In the line of detailed studies, theoretical works have been also conducted to try to give even a more in detail information on the kinetics of the process by calculating energy barriers using typically Density Functional Theory (DFT). Results have been published for different molecule-surface interactions, including the Ni (111) surface.[54–58] A theoretical approach based on semiempirical methods was also used for achieving a deep insight into the mechanism implying the total dissociation of reactant species up to adsorbed atoms and the subsequent recombination back to methane and water products.[59]

The computational study of the catalytic process using electronic structure methods is of invaluable importance especially to the end of obtaining values for the energy barriers in the heterogeneously catalyzed process. However, the investigation should be pushed ahead to detailed kinetic analysis based on the resolution of the master equations of the reaction mechanism which can give a quantitative prediction and benchmark for the proposed mechanisms and associated energy barrier values, and offer the possibility of a direct check of the validity of the approach by means of a comparison of computed and measured quantities. All this will provide valid suggestions on how the efficency of the Sabatier reaction can be improved.

For that a kinetic study of the reaction over Ni (111) using the Kinetic Monte Carlo (KMC) method has been, indeed, performed and the secondment work was devoted to the comparison of computed and measured outcomes. Further results of the computational simulations mimicking the catalytic methane producing processes based on the KMC method are reported in Section 2.3 of Chapter 2 in order to provide both key information and theoretically based rationalizations on the shape of the measured yield curves when plotted as a function of the temperature T. In this respect, the thesis provides indications on which developments of the catalytic scheme could be adopted.

Being ruthenium the most active metal to catalyze the Sabatier reaction,[50, 60, 61] the existing literature examining its properties as catalyst is quite abundant.[27, 62–64] Due to its high cost, an optimization of the surface-area relation is essential for a commercial competitivity leading to the formation of nanoparticle-based catalysts. It's higher activity, partially makes up costs, by enabling lower temperature working conditions. Beyond their use in the Sabatier reaction, the purely *per se* study of ruthenium, or more generally, metal clusters and nanoparticles have attracted a wide and continuous interest in chemistry, Molecular Physics and Condensed Matter, both experimentally[65–78] and theoretically (see for instance the review by Fernando et al.[79]). This interest relies both on the fundamental interest of understanding how the metallic properties build up to the bulk through a continuous growth and on a manifold of applications in various fields. Among the other metallic systems, ruthenium materials have been widely investigated due to their very rich chemistry[65] and their large palette of applications such as catalysis[66–69], theranostics and medical applications[70–72], photovoltaics and molecular electronics[73–76] or magnetic properties[77, 78]. Ruthenium clusters and nanoparticles offer convenient reactive environments to understand at the atomic scale the role of

electronic structure, size and and shape in the chemistry of ruthenium compounds, namely nano-catalysis.

Although not as abundant as for other metals and as for the use of bulk ruthenium as a catalyst, a significant theoretical literature is available for ruthenium clusters and nanoparticles. A few investigations with high level wavefunction type methods such as CAS/CASPT2 or MRCI were published for very small clusters, essentially dimers[80–82]. Even in the case of neutral dimers, the elucidation of the nature of ground state does not seem to be fully elucidated. The ability of the various DFT functionals to obtain the correct ground state of Ru_2 was discussed by Pramathan and collaborators[83], larger clusters in the range $n = 4 - 20$ atoms were essentially investigated via DFT. Note that even in the case of Ru_4 they pointed the discrepancies between various functionals about the ground state structures, evidencing a close competition between a square conformation and a high spin tetrahedral structure [84].

Almost all investigations done for the medium size clusters (n=5-20) [84–90] found evidence for the predominance of cubic-like structures, quite different from the usual tetrahedral-based packing (icosahedral, decahedral or face centered cubic (fcc)) encountered for a number of other noble or transition metal clusters. The calculations for anions also found occurrence of cubic motifs for the small clusters (n=4-9,11-12), double-layered hexagonal structure (n=13-16) and finally the onset octahedral structures (n=18-20), also predominant in medium-size clusters with sizes n=28,38 and 44. Investigations concerning larger systems, namely nanoparticles[91–94] were more abundant in literature. Gavnholt and Schiøtz[91] derived DFT estimates to discuss the interplay between structure and reactivity of ruthenium nanoparticles up to 10^4 atoms extrapolating data from DFT calculations of nanoparticles (NP) up to 323 atoms. Soini et al.[95] discussed the scaling properties of hexagonal close packed (hcp) and fcc type ruthenium nanoparticles. Recently, Nanba and coworkers [94] determined the cohesive energy of the decahedral fcc, icosahedral fcc, truncated octahedral fcc, and hcp Ru-NPs with sizes between 55 and 1557 atoms and found that the icosahedral fcc Ru-NPs became closer to that of the hcp ones with decreasing nanoparticle size.

DFT is certainly a method of choice to address the electronic structure of nanoparticles in a size range up to a few thousands or even possibly now 10 thousands atoms in single point calculations. Nevertheless in the size range larger than a few tenths of thousand atoms, DFT is still too consuming in terms computer resources to be straightforwardly combined in extensive dynamical calculations, such as global optimization algorithms and/or Monte Carlo of Molecular dynamical simulations with sufficient statistical sampling. Although many simulations in the field of nanoparticles are conducted with classical potentials, such as for instance the Embedded Atom Potentials (EAM), those are not necessarily likely to describe the structural patterns on the whole size range from the small clusters to the bulk. Moreover they obviously cannot describe the electronic properties such as ionization, electronic spectra or magnetization, all directly related to the explicit description of electronic structure.

In between first principle calculations and simple interatomic potentials, intermediate schemes such as the semi-empirical methods or approximate methods derived from DFT are characterized by an improved speed-up enabling to address larger scale simulations in a size domain still difficult for DFT, despite all the progresses

accomplished in the quest for speed-up and linear scaling, especially for metal systems were the electronic properties are not easy to converge via space localization schemes used in a number of linear scaling algorithms. The Density Functional based Tight Binding (DFTB) [96, 97] has emerged as one of the efficient computational schemes, still retaining explicit description of the electrons.

Parameters are always an essential issue in approximate methods. DFTB simulations have been carried out for RuPt clusters[92]. Electronic parameters (namely the Slater Koster files) for the whole periodic table and in particular Ru-Ru interactions, files were recently published by Wazidunaan and Heine[98], but the repulsive interactions were not determined in the latter study. The details of the DFTB study of ruthenium-based compounds is presented in Chapter 4.

Despite the fact that the technologies considered for the implementation of the Sabatier reaction are based on a heterogeneous catalytic process, new technologies making this reaction happen in a partial gas phase environment are under development by giving rise to a plasma-assisted process.[99–102]

The development of plasma-assisted catalysis is a promising tool for enhancing energy efficiency, lowering by-product formation and increasing activities of catalyzed processes specially for the treatment of all kind of waste gas.[103] Of special interest is the development of non-thermal plasma, typically consisting of electron beams accelerated until reaching temperatures of the order of few thousands to tenths of thousands Kelvin in the beam, while keeping temperatures in the gas at few hundreds of °C thus enabling the catalyst not to decompose. The collision of the electron beam with gas-phase molecules results into the formation of both ionic species and excited ones, leading to the formation of radicals and, among the most common ones, there is the formation of OH from water dissociation[104, 105], which later on, reacts to produce other radicalary species.[106]

Several papers have reported the synergistic effects, of the plasma-assisted catalysis, leading to efficiencies and selectivities, better than the sum of its separate processes. [107–109]

The efficiency on the methanation of both CO and CO_2 was highly improved as reported by Jwa et al [99] when using dielectric barrier discharge non-thermal plasma process in combination with Ni/zeolite heterogeneous catalysis with a decrease of 120 K in the temperature threshold at different Ni loads of the catalyst. Nizio et al. [100] reported conversions of 97% with 90% CH_4 efficiency in a ceria-zirconia supported nickel catalyst with almost 80% conversion at 80 °C, where the plasma-less reaction had no activity at all.

In spite of the promising future of the plasma-assisted processes, few theoretical studies have been performed the in detail analysis of the occurring reactions up to date[110–112] mainly due to the high complexity of the gas-phase soup and possible interactions between all elements of the plasma and the catalyst surface. However, molecular scattering methods, can indeed shed light to the gas-phase processes occurring among activated species, by calculating the needed rate coefficients for understanding the kinetic behaviour.

The field of molecular scattering computer simulations has a large history of developments being one of the milestones of computational chemistry and becoming the prototypic field of method benchmark for high level of theory dynamical simulations. Different approaches have been developed along the years using different approximations and levels of theory.

The first attempt to simulate a molecular collision was done by Mazur and Rubin[113] for a generic approach:

$$A + BC \rightarrow AB + C \tag{1.2}$$

but it wasn't until 1976 that Schatz and Kuppermann did a complete full-quantum (FQ) treatment including all the degrees of freedom for the $H + H_2 \rightarrow H_2 + H$ [114] although earlier works studied the same system with reduced dimensionality. Subsequent studies of, first, isotopic variants, and afterwards including other atoms were done in the following 10 years, it wasn't until 1993, that Manthe et al. reported the study of the first FQ study of four-body scattering process.[115] It was for the reaction $OH + H_2$, the initial treatment, however, only included cumulative reaction probabilities, but not the state-to-state ones, due to the fact that, only interaction region was treated. This latter collisional process became the prototypic one for the four-body scattering processes with many studies have being published along the years with different and each time better Potential Energy Surfaces (PES).[116–120] Furthermore this reaction is of high importance in plasma-assisted Sabatier processes due to the inclusion of both a reactant (H_2) and one of the most active species generated in the plasma (OH).

Besides the FQ treatment, and its highly demanding computational cost, limiting its implementation, other approaches were developed by taking more approximations. Classical methods, have been widely applied to molecular collision simulations often giving surprisingly good results. This is specially valid where the desired observables can be obtained through averaging over more detailed quantities. These methods however pay the price of neglecting quantum effects, (ie. tunneling, resonance and interference) generally leading to bad results when they are present. A way to deal with the problem is the inclusion of certain degree of quantization in the so-called semiclassical methods. Among them, of particular interest is the quantum-classical (QC) method developed by Billing et al.[121, 122] In polyatomic systems, in fact, the QC method partially decouples the degrees of freedom for their quantum treatment while the remaining ones are treated classically in a fully coupled fashion using expectation values of the quantally treated quantities for its inclusion in the semiclassical Hamiltonian. In the present thesis, the study of the $OH + H_2$ by means of the quantum-classical method is carried out with special interest on the role of long-range effects on both reactive and inelastic collisional processes.

Indeed, the main aim of this PhD project is the investigation of renewable energy storage process by attacking it from different points of view and different scales so as to provide a solid ground for a converging comparison of experiment and computation on the methane formation from CO_2 using solid state catalyzed processes. For that, a collaborative research, has been build composed by the research group of the University of Perugia (UPG), the University Paul Sabatier of Toulouse (UPS-LCPQ), and PLC System. In particular, the project leverages the different expertise of the University departments and of the private companies and research centers for the experimental and theoretical treatments of elementary reactive and non reactive molecular processes. In particular, the project relies on the engineering capabilities of designing, building and experimenting innovative apparatuses of the PLC System srl, specialized in designing, installing and monitoring energy supplying apparatuses with the support of auxiliary SMEs.

At the University of Perugia, the gas phase processes of the plasma-assisted reac-

tion has been investigated using the quantum-classical (QC) method, in the University Paul Sabatier of Toulouse (UPS-LCPQ) the research was focused on the study of the structure of ruthenium clusters and nanoparticles and their role as catalysts of the Sabatier reaction. Research at the PLC System secondment company was concerned both with the experimental implementation of the traditional Sabatier reaction as pure heterogeneous catalysis of the PROGEO apparatus and, in parallel and in order to aid the experimental development, with the computer simulations of the kinetics on Ni(111) catalyzed Sabatier reaction. The prototypal experimental implementations were carried out at the Italian National Research Agency for new technologies, energy and sustainable economic growth (ENEA). Additional tests and developments were carried out at RPC srl, RDpower srl and Master-UP srl. The aim of this collaborative endeavour is the development of new knowledge and validated laboratory technology to build a novel apparatus for producing carbon neutral methane through chemical catalytic conversion of CO_2 waste flue gases using renewable energies. The streamline of such project is the carrying out of basic and applied research and its application to the design, testing and development for building.

The present thesis is structured in the following way. In Chapter 2 the implementation of the Sabatier process, namely the purely heterogeneous catalysis one and the simulation of its kinetics with the necessary theoretical methods description are presented comprising all the work done regarding the secondment at PLC System. In Chapter 3 the OH + H_2 reactive and inelastic scattering processes simulating an important gas-phase reaction occurring on the plasma are dealt with by first introducing the considered methods and subsequently, the results are presented. Lastly, in Chapter 4 the study of ruthenium clusters and nanoparticles is done using the DFTB method. First an outlook on the physical foundation of the methods used is given to subsequently present the results. Validating the ability of the DFTB method to predict the structural, energetical, electronic and spin-related properties of ruthenium in both cluster and nanoparticle scale has been the principal focus of the work in this thesis.

Chapter 2

The Sabatier process

In this chapter the heterogeneously catalyzed methanation of carbon dioxide (i.e. the Sabatier process) is treated by describing the work done in relation to the Secondment at PLC System. The actual implementation of the Sabatier reaction in the PROGEO machine, with a description of its constituting components and its technical setup is dealt with in Section 2.1. The theoretical basis needed for the understanding of the kinetics simulation of the Sabatier process is given in Section 2.2. Finally the results obtained when using the kinetic Monte Carlo method for simulating the kinetics of the Sabatier reaction on Ni(111) are presented in Section 2.3.

2.1 The Implementation of Sabatier's reaction: The PROGEO apparatus

As already mentioned in the Introduction (Chapter 1), the Sabatier reaction,

$$CO_2 + 4H_2 \rightarrow CH_4 + 2H_2O \tag{2.1}$$

converts carbon dioxide into methane by means of an heterogeneous catalyst, typically, commercial ones are based on nickel. The reaction, has been extensively studied both theoretically and experimentally, and its implementation goes from prototype apparatuses, to commercially productive ones in bigger facilities.

This thesis work has been based on the use of the prototype apparatus called PROGEO[123] and on the collaboration among researchers of the laboratories of the University of Perugia and of ENEA [124]. In particular, the project leverages the combination of the different fields of expertise of the Departments of Chemistry, Biology and Biotechnology [125–132] and of Civil and Environmental Engineering of the University of Perugia and on the engineering capabilities of designing, building and experimenting innovative apparatuses of ENEA researchers.

The PROGEO apparatus (PROGEO 20 kW)[123], has been assembled at the PLC System s.r.l. company[133]. PROGEO 20 kW targets low level users who wish to combine the usage of cheap energy (saving on costs) with the recycling of CO_2 (saving on carbon tax and environment pollution) for their business. However, the next planned PROGEO apparatus ESODIS 0.5 MW, will target industrial applications (though still of a prototype type more suited for small power plants.[134]). Accordingly, the Power-to-Gas technology of PROGEO 20 kW aims at entering the

market of innovative electricity storage apparatus via waste CO_2 valorization. More in detail PROGEO converts low cost electricity into methane through:

- an electrolyzation stage in which electricity is converted into high purity hydrogen (H_2).
- a methanation stage in which hydrogen reacts with carbon dioxide (CO_2) to produce methane (CH_4) and steam water.

Due to the exothermic nature of the reaction, the setup requires no additional energetic cost for self-sustainability. Furthermore, due to the possibility of coupling the reactor to plants generating CO_2 as a by-product the relevant technology has an added value for enhancing carbon neutral economy.

The PROGEO apparatus has also the following positive additional characteristics:

- a fast start-up thanks to a highly flexible solution;
- the possibility of being used for feeding both electrical and methane distribution nets;
- a great safety level thanks to an intrinsically passive control system;
- an extremely large number of charge/discharge cycles;
- a modular integrability in stacks.

Experimental measurements of methane yields of PROGEO have been carried out in a first step using CO_2 bottles enabling to work at more stable and standardized conditions to, in a second step using CO_2 produced from grapes fermentation provided by IRVO [135]. The measurements show a complete compatibility with the catalyst used for the methanation process in PROGEO. The used catalyst is KATALCO$_{JM}$ 11-4MR [136] a commercial product of the Johnson Matthey company (made of silicate hydrous, silicon oxide, nickel, nickel oxide, magnesium oxide, graphite porous small cylinders of average diameter 3.1 mm and height 3.6 mm containing metallic nickel) whose 2500X micrography is shown in Figure 2.1

The PROGEO reactor is designed for a maximum flux of CH_4 out of 1 m^3/h at standard temperature and pressure. As shown in Figure 2.2, it is articulated in twin columns (twin flow channels) externally cooled thanks to shared laminar elements in order to dissipate the heat produced by the exothermicity of the reaction (ΔH_{298K} = -164.9 kJ mol^{-1}). Design parameters of the reactor are: GHSV (Gas Hourly Space Velocity) (ml h^{-1} g^{-1}) and SV (Space Velocity) (h^{-1}). Another useful parameter is the ratio between the total flux of gas and the exposed surface of the catalyst indicated as GHCS (Gas Hourly Catalyst Surface) (cm h^{-1}). The value of the reactor parameters of the present version of the PROGEO apparatus are: GHSV = 3200 ml h^{-1} g^{-1} and SV = 2100 h^{-1} leading to a GHCS parameter of 155 cm h^{-1} . The resulting features of the present PROGEO apparatus shown in Figure 2.2 are:

- External diameter of the single channel 60 mm.
- Catalyzed total length 660 mm.

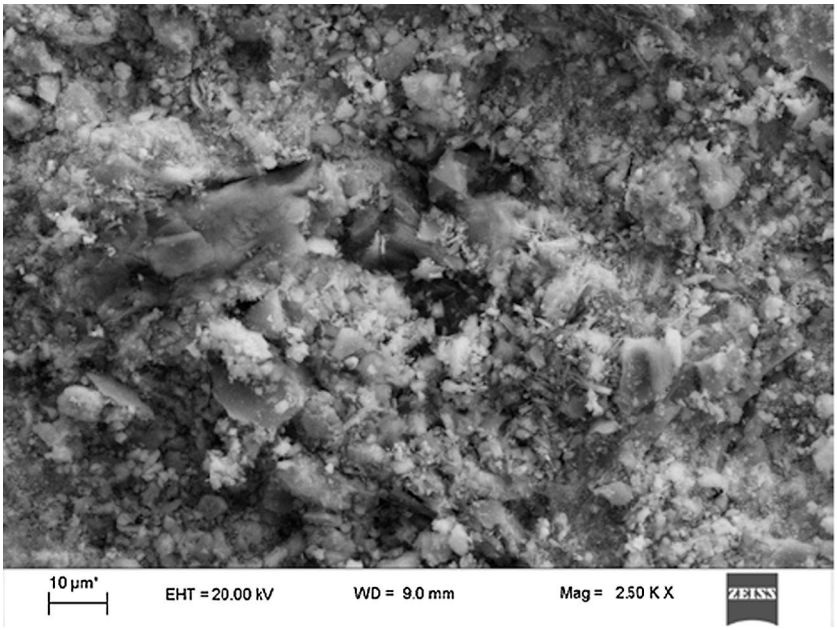

Figure 2.1: 2500X micrography of the commercial catalyst KATALCO$_{JM}$ 11-4MR [137]

Figure 2.2: A picture of the twin columns of the PROGEO reactor.[137]

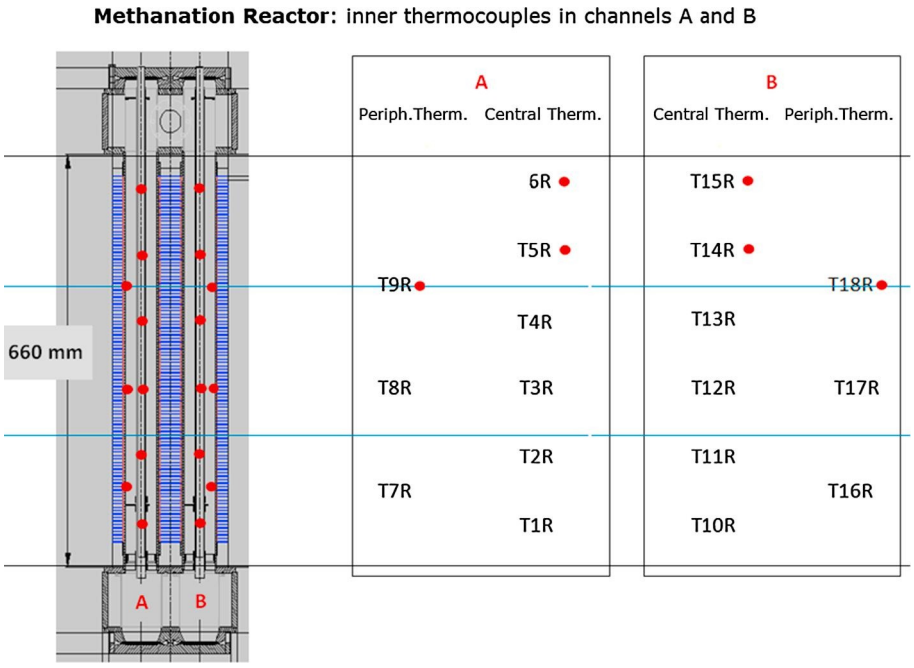

Figure 2.3: Cross section of the reactor twin columns and locations of the related thermocouples (red dots). On the right hand side the labels of the thermocouples.[137]

- Maximum inlet flux (H_2 + CO_2) 6 m^3/h at standard temperature and pressure.
- Reference Molar ratio (CO_2/H_2) 1/5;
- Maximum outlet flux (CH_4) 1 m^3/h at standard temperature and pressure.

Experimental measurements have been carried out by varying:

- the CO_2/H_2 molar ratio from a minimum of 1/4 to a maximum of 1/5.5;
- the reactor temperature from a minimum of 220 °C to a maximum of 450 °C;
- the H_2 flux from a minimum of 0.8 m^3/h at standard temperature and pressure to a maximum of 2.5 m^3/h at standard temperature and pressure;
- the pressure from a minimum of 1 bar to a maximum of 2 bar.

A key element for a quantitative measurement of the reaction yield is the regular monitoring of the temperature both along the central axis of each channel (maximum temperature) and along the peripheral axis (minimum temperature). In Figure 2.3 the location and labels of the channel thermocouples (6 axial and 3 peripheral) are shown as dots together with the cross section of the twin columns.

The methanation reactions occur mainly on the top segment of the reactor close to the inlet (90% in the first 200 mm). Accordingly, most of the produced heat is detected by the central thermocouples (T5, T6 and T14, T15). The average of the measured percentage of produced methane is plotted as a function of the molar ratio and temperature in Figure 2.4 As is apparent from the figure, the threshold temperature is 240 °C and the range of temperature of optimal yield (> 80%) is

T [°C] \ MR	4	4.5	5	5.5
240	47	56	65	68
245	49	58	66	70
250	51	60	68	72
255	52	62	69	74
260	54	63	70	75
265	56	65	71	77
270	57	67	73	78
275	58	68	74	79
280	60	69	75	81
285	61	70	77	82
290	62	71	78	82
295	63	72	79	83
300	64	73	80	84
305	64	73	81	84
310	65	74	82	84
315	65	74	82	84
320	66	74	83	84
325	66	74	83	84
330	66	74	83	84
335	66	73	83	83
340	66	73	82	82
345	65	72	81	82
350	65	71	80	80
355	64	70	79	79
360	64	69	77	78
365	63	67	75	76
370	62	66	72	74
375	60	64	69	72
380	59	62	66	70

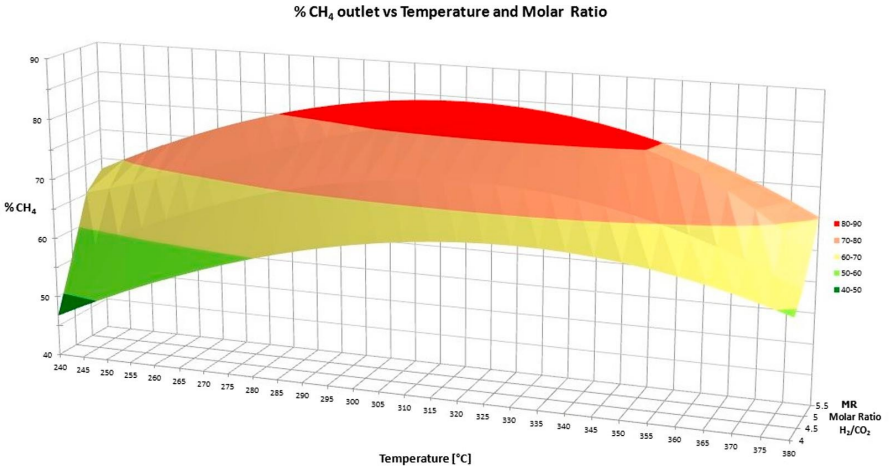

Figure 2.4: Results of CH_4 yield at different conditions of temperature and molar ratio

280–350 °C. The molar ratio has a significant impact on the percentage of produced methane with the optimum value of the CO_2/H_2 ratio being 1/5.

The Secondment activities at PLC System facilities during the months June-August 2016 have been devoted to identifying the problems spotted after the transfer of the PROGEO apparatus from Acerra to Perugia with the operators of the PLC SYSTEM, the members of the Departments of Chemistry Biology and Biotechnology and of Civil and Environmental engineering, the personnel of the RD Power and the RPC. The three sections of the apparatus have been examined in detail. Namely they are:

1. The appropriate handling of renewable energy sources to generate hydrogen.

2. The optimal management of the carbon dioxide reduction to methane.

3. The storage of the produced methane as methane hydrate.

A problem common to all sections was found to be the lack of documentation of the disconnection phase (and the consequent difficulty of a correct reassembling of the several components like the heat exchanger, automated control circuitry, the temperature monitoring at the various points of the reactor, etc.). This has created difficulties to the restoring of the original functionalities. As to the first section the major problem has been the impossibility of using the electrolyzer due to the high demand of electricity especially at restarting phase. For carrying out the experiments the electrolyzer has been replaced by a hydrogen bottle. As to the second section the major problem was the reintegration of the heat exchanger (with the consequent reduction of yield) and the difficulty of operating with the gas chromatography in the present installation. As to the third section no attempt has been already made to establish a physical connection. Despite all that the apparatus is presently used for refinement of its working parameters and for comparison with the new apparatus ESODIS (0.5 MW), with the newly designed electrolyzer and with the new developments of the simulation software.

2.2 Theoretical Methods

In order to assist the technical development of PROGEO, and in parallel to the experimental setup of the apparatus, simulations of the kinetics of reactions taking place inside the PROGEO apparatus have been carried out. In this section a review of the main kinetic concepts, an overview of the methods used nowadays to simulate the kinetics of heterogeneous catalysis processes, and the description of the kinetic Monte Carlo (KMC) method as the one chosen to simulate the kinetics of our system are given.

2.2.1 Kinetics concepts

The majority of reactions occurring in real life, including the Sabatier reaction, do not take place in a single step. As a matter of fact, the overall process can be split into more elementary steps, whose combination leads to a sequence (mechanism) connecting the reactants to the products of the overall reaction. For illustrative purposes let us consider the following simple reversible general reaction as an example:

$$A_2 + 2B \rightleftharpoons 2AB \tag{2.2}$$

One can assume that it results from the combination of the two following simpler steps

$$\begin{aligned} A_2 + B &\rightleftharpoons A_2B \\ A_2B + B &\rightleftharpoons 2AB \end{aligned} \tag{2.3}$$

However, as it is common with real-life mechanisms, new experimental evidences might reveal the insufficiency of this mechanism, to rationalize the overall process and hence the second step could be further decomposed leading to the following set of steps:

$$\begin{aligned} A_2 + B &\rightleftharpoons A_2B \\ A_2B + B &\rightleftharpoons A_2B_2 \\ A_2B_2 &\rightleftharpoons 2AB \end{aligned} \tag{2.4}$$

A mechanism with a finer agreement to experimental findings better suits the assumption that elementary steps are the most detailed sensible description of no further decomposable (at molecular level) steps of the process. Accordingly, the mechanism of a reaction is the set of elementary steps which compose a general reaction. In this example, then, the steps composing Equation (2.4) are to be considered the mechanism of reaction given in Equation (2.2)

In heterogeneous catalysis (or surface chemistry), species adsorb on the surface either chemically with strong bonds, or physically with long range interactions. A useful cartoon to give a rationale for adsorbed kinetical processes is achieved by treating the adsorption site as an additional species identified by the symbol *. Accordingly, the following equation represents the reversible dissociative adsorption process of A_2 molecule:

$$A_2 + 2^* \rightleftharpoons 2A^* \tag{2.5}$$

Another differential concept between reactions on surfaces and the pure gas-phase or dissolution ones is that on surface, the concept of concentrations makes no sense, and concentrations are replaced by coverages defined as the rate of adsorption sites occupied by a given species:

$$\theta_A = \frac{n_{A^*}}{\sum_{I=1}^{N^*} n_{I^*}} \tag{2.6}$$

being θ_A the coverage of A, n_{A^*} the number of adsorbed A species, and $\sum n_{I^*}$ all the species adsorbed on the surface, including free adsorption sites. In the same way, rates are expressed in turnover frequencies corresponding to the number of molecules reacted per site and per unit time. The formalism developed with coverages is completely parallel to the one based on concentrations. For this reason we adopt here the concentration formalism whose usage is more widespread in lecture books.

Switching back to concentration formalism, a fundamental concept in kinetics is the rate of formation of a given species, this is how fast the concentration of considered species changes on time. It can be formulated, taking B as an example, the following way:

$$r_B \equiv \frac{d[B]}{dt} \tag{2.7}$$

where r_B is the rate of formation of B and $[B]$ its concentration. The rate of formation of reactants, like in the case of B in the forward Equations (2.2) and (2.3), will be negative ($r_B \equiv d[B]/dt < 0$) as it will be consumed and thus its concentration will decrease on time. However, this definition is not sufficiently general. As a matter of fact, in Equation (2.2) we have that for every A_2 molecule consumed, two molecules of B are consumed as well ($r_B = 2r_A$). For a more global description we can define the rate of the reaction in Equation (2.2) as:

$$r = \frac{1}{a_2}\frac{d[A_2]}{dt} = \frac{1}{b}\frac{d[B]}{dt} = \frac{1}{ab}\frac{d[AB]}{dt} \tag{2.8}$$

where a_2, b, and ab are the stoichiometric coefficients of the respective species in capitals including the sign (negative for reactants and positive for products), for that particular reaction. For some reactions (all elementary ones and in certain cases some that are not) the reaction rate can be expressed as a product of concentrations to the power of an exponent times a coefficient k. Given a generic reaction i, its rate r_i can be expressed as:

$$r_i = k_i[A]^{\alpha}[B]^{\beta} \tag{2.9}$$

where k_i, α and β are independent of concentration. k_i is the so called rate coefficient (or improperly called rate constant due to its dependence on the temperature T) and represents the ease of a reaction to happen when the involved species meet in space. α and β are the partial order of reaction of their Latin-written-equivalent species (A and B respectively), leading to a global order of reaction of $\alpha + \beta$.

For the first step in Equation (2.4) the forward and reverse reaction rates are given by:

$$\begin{aligned} r_1 &= k_1[A_2][B] \\ r_{-1} &= k_{-1}[A_2B] \end{aligned} \tag{2.10}$$

being k_1 and k_{-1} the rate coefficients for the forward and reverse processes respectively. It can also be seen that the forward reaction is global second order, while the reverse one is first order.

Many species are involved in more than one step with the global change of its concentration on time being composed of more than one term. If one takes as an example the case of the B species, it is involved in the first and second steps, both forward and backwards, being thus the rate of its consumption/production:

$$\frac{d[B]}{dt} \equiv r_B = -k_1[A_2][B] + k_{-1}[A_2B] - k_2[A_2B][B] + k_{-2}[A_2B] \tag{2.11}$$

where the sign of each term in the right-hand side of the equation is the b_i stoichiometric coefficient of B for each i elementary step, being in this case, its absolute value in all elementary steps equal to 1. We can write a similar expression for each species present in the mechanism. If the mechanism is more complex than a three steps one, as it usually is (it can consist of hundreds of elementary steps), Equation (2.9) can be extended to other steps by writing a more generic expression:

$$\frac{d[L]}{dt} \equiv r_L = \sum_{i=1}^{m} \left(l_i k_i \prod_{R=1}^{N} [R]^{\rho_{iR}} \right) \tag{2.12}$$

where r_L is the rate of formation of the L species, $[L]$ its concentration, m the number of steps composing the system, l_i the stoichiometric coefficient of L in the step i, k_i the rate coefficient of the step i, N the total number of reactants participating in the step i, $[R]$ the concentration of the reactant R (interchangeable for partial pressure or coverage of the R species in the analogous gas-phase and adsorbed process developments) and ρ_{iR} the order of R in the i step. The set of all r_L equations of the mechanism constitutes a system of interdependent differential equations (the rate of consumption of each species depends on the concentration of other species). The goal of microkinetic modelling is precisely the (not trivial at all) solution of the aforementioned system of equations composed by all r_j steps, which allows to verify if a proposed mechanism describes the overall process or not. Main existing methods to solve the system of equations composed by equations like Equation (2.12) (except kinetic Monte-Carlo which will be treated in more detail in Section 2.2.2) use one of the following approximations here summarized:

Steady State approximation consists on assuming that the net rate of formation for intermediates is zero. This does not imply that the coverage by the intermediates is small.

Quasi-equilibrium approximation If all steps are orders of magnitude faster than the slowest one, we can use the quasi-equilibrium approximation. For the fast steps we use the corresponding equilibrium equations instead of the kinetic equations.

2.2.2 The kinetic Monte-Carlo method

Kinetic Monte Carlo Method (KMC)[138, 139] accomplishes its goal of solving the system of differential equations, without any a priori approximation (in opposition to

steady state approximation and quasi-equilibrium approximation) and deals as well with the stochastic nature of real life processes by making use of a pseudo-random number generator and, in our case, the use of a rejection-free algorithm[138].

The algorithm is applicable to simulate the evolution of, not only kinetics of chemical reactions, but also all processes which can be modelled by considering the system in a certain state and a number of multiple transitions that state can evolve to, and on which an a priori knowledge of the rate of transitions is known beforehand. Other fields of application of this algorithm are: surface diffusion, dislocation mobility[140], surface growth[141], vacancy diffusion in alloys (this was the original use [142]), coarsening of domain evolution, defect mobility and clustering and viscoelasticity of physically crosslinked networks[143].

When using KMC to solve the system of differential equations and thus simulate the kinetics of chemical processes, the goal will typically be to know if a proposed mechanism, with its associated rate coefficients for each step, is consistent with the experimental findings, or to compare which is the fastest mechanism among different possibilities.

This is achieved by solving the set of differential equations arising from the proposed mechanism (or ensemble of potential mechanisms) in a stochastic manner, being each elementary step like the one in Equation (2.12). The first input to the algorithm will thus be the mechanism of all the considered steps, and their associated rate coefficients. The initial state of the system, must also be given as an input.

The basic algorithm works by splitting time in timesteps, and at each timestep evaluate which state the system is at and which are the possible states the system can evolve to. For simulating kinetics, the system's initial state will be a given set of reactants expressed in concentrations/pressures/coverages and the possible transitions would be the reaction the system can evolve through, towards a new set of species (intermediates/products) different than the initial one. The probability (W) that the system reacts towards a given state is calculated by considering the rate coefficient of that reaction and of all other possible reactions:

$$W_{r_a} = \frac{k_a}{\sum_{i=1}^{N} k_i} \tag{2.13}$$

where W_{r_a} is the probability of the process r_a to occur, k_a its rate coefficient, N the number of total available processes and k_i their respective rate coefficients. This way each transition is assigned a probability, being the sum of all possible transitions/reactions to happen equal to one (that is why the algorithm is rejection-free).

Once calculated the probabilities of each transition to occur, each transition is assigned a range between 0-1, equal to the probability, that transition has to happen, as exemplified in Figure 2.5. A pseudo-random number is generated and the transition that number fall in, the system is made evolve towards it.

In surface catalyzed processes, the graph-theoretical KMC is used [144]: The catalyst is represented by a symbolic grid of sites where reactions happen, and the set of possible transitions (reactions) is evaluated site by site by considering which species is adsorbed at a given site, and which are their neighbours with whom the molecule at the given site can react with. This way the set of possible reactions to occur is limited by the neighborhood of the site considered. The evaluation is repeated site by site, until all sites are made evolve.

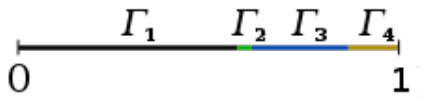

Figure 2.5: Probability range distribution for the choice of transition

Graph theory[145] is used to calculate the neighborhood of each site, determining this way, all the possible reactions to happen. The lattice grid must be chosen so as to replicate the characteristic neighboring relations of the real surface lattice to be simulated. Accordingly, periodic boundary conditions are typically applied. The grid is, thus, going to give information on which adsorbate is present on each site, and which are its neighbors.

One of the characteristics of the rejection free algorithm is the variable timestep. This is calculated by considering the fact that rate coefficients are turnover frequencies (in time^{-1} units). The timestep Δt is then formulated by taking the inverse of the sum of rate coefficients for all possible processes at all possible sites:

$$\Delta t = \frac{1}{\sum_{j=1}^{N_{site}} \sum_{i=1}^{N_{proc}} k_i} \tag{2.14}$$

To sum up, the algorithms does:

- calculate the probability for each process as mentioned in Equation (2.13)
- associate each process to a range according to the calculated probabilities like represented in Figure 2.5
- generate a number between 0 and 1 with a pseudorandom number generator, and choose the process associated to the range the number falls.
- increase the time by Δt as calculated in Equation (2.14)

To clarify the concept, the following example can be considered. The simulation starts with an empty grid, no species are present at any site. The values for the partial pressures of the gas interacting with the surface are needed in order to enable the adsorption processes to occur. The algorithm, at this point, is going to consider adsorption processes as the only available ones because the grid is empty. Starting with the first site, the probability of adsorbing species A becomes:

$$W_{A^*} = \frac{r_{A^*}}{\sum_{I=1}^{G} r_{I^*}} \tag{2.15}$$

where, W_{A^*} is the probability of adsorbing A, r_{A^*} is the adsorption reaction rate of A, $\sum_{I=1}^{G} r_{I^*}$ is the sum of rates of all the possible adsorption processes. The same way, the probability of adsorbing all other gas species is calculated.

The process of choosing which species is going to adsorb is carried out as described before: from the rate coefficients of all adsorption process the respective probabilities are calculated and one of them is chosen by means of the pseudorandom generator. The process is repeated for every site, and when the last site is assigned, the time is increased accordingly.

Once the surface has some species adsorbed on it, different processes can happen (e.g. desorption processes to empty the site again, reaction processes among species in neighboring sites and diffusion processes from one occupied site to an empty one). Then probabilities are calculated again and the process is repeated site by site.

2.2.3 The evaluation of rate coefficients

As already mentioned, the goal of all methods in microkinetic modelling is the time evolution of species in reaction mechanisms which normally consists of tenths, if not hundreds of elementary steps. Because of the large number of processes to be considered, an approximate method to calculate the rate coefficients of the intervening elementary steps is needed. The ones concerning reactants adsorbed onto the surface are calculated using the Arrhenius equation (i.e. as the product of a constant pre-exponential factor A by an exponential term) as:

$$k = Ae^{\frac{-E_a}{k_B T}} \tag{2.16}$$

where k_B is the Boltzmann constant, E_a the activation energy ant T the temperature. This expression can be derived as a simplification of collision theory, on which it is assumed that the collision of two partners leads to reaction if they have the correct spatial orientation and a minimum amount of energy (E_a). From the Maxwell-Boltzmann distribution it can be derived that the amount of molecules at temperature T to have an energy equal or higher than E_A is equal to $e^{\frac{-E_a}{k_B T}}$. Furthermore from kinetic theory it is known that a molecule at temperature T has an average velocity of $\sqrt{\frac{8k_B T}{\pi m}}$, where m is the system's mass. This terms are included in the full temperature-dependent rate coefficient as:

$$k(T) = \rho\sigma\sqrt{\frac{8k_B T}{\pi\mu}}e^{\frac{-E_a}{k_B T}} \tag{2.17}$$

where σ is the reactive cross section and ρ an steric factor, two terms corresponding to the spatial efficiency of the collision, which a simple expression cannot be drawn easily. Without entering in the details of these two last mentioned terms in Equation (2.17), the preexponential factor simplifies the value of $\rho\sigma\sqrt{\frac{8k_B T}{\pi\mu}}$ which has a complex dependence with temperature as being just simply a constant.

The two terms conceptually refer to an intermediate molecular geometry of the system associated with the Transition State (TS) that is assumed to separate reactants and products along a properly chosen coordinate (the reaction coordinate). Moreover, once crossed the TS, they are assumed not to recross back thus neglecting orientation effects.

The Arrhenius equation expressed incorporates the information related to the elementary process for which E_a is the difference between the energy associated with the stationary point of the potential Minimum Energy Path (MEP) at the TS and that associated with the original asymptote of the process (the reactants). In low level approximations, the pre-exponential factor can be given by the simplified expression $k_B T/h$ (where k_B is the usual Boltzmann constant, T is the temperature and h the Planck constant). A more accurate formulation of the rate coefficients makes use of the partition function of the intermediate state (incorporating so far the information about the remaining degrees of freedom):

$$A = \frac{k_B T}{h} \frac{Q^{TS}}{Q^r} \tag{2.18}$$

where Q^{TS} is the transition state partition function and Q^r the partition function of adsorbed reactants. Each partition function is calculated assuming that rotations and translations are frustrated or hindered and therefore can be assimilated to vibrational degrees of freedom. In such case, the harmonic approximation of the vibrational partition function is used and the expression:

$$Q_{vib,x} = \prod_k \frac{exp(\frac{-h\nu}{2k_B T})}{1 - exp(\frac{-h\nu}{k_B T})} \tag{2.19}$$

is usually adopted. In Equation (2.19) $Q_{vib,x}$ is the total vibrational partition function of the X species, k refers to the vibrational normal modes and ν its vibrational frequency.

In the adsorption of gaseous species the most frequently used expression for the rate of reaction is the well known Hertz-Knudsen equation[146]:

$$r_i^{ad} = S_{0,i} A_{site} \frac{p_i}{\sqrt{2\pi m_i k_B T}} \tag{2.20}$$

where $S_{0,i}$ is the sticking coefficient (for which we take the value 1 in this work), A_{site} is the area of the adsorption site, p_i is the partial pressure of species i and m_i its mass.

2.3 Sabatier kinetics Results

Thus, the initial rationalization of the processes involved in the production of methane via the Sabatier reaction (i.e. by making H_2 + CO_2 react on a catalytic surface[147]) has been performed by following the Kinetic Monte Carlo (KMC) method and concretely using the Graph-Theoretical KMC methodology.[144, 148].

The Sabatier reaction, in spite of being a well established reaction, the mechanism of the Ni-catalyzed CO_2 methanation is still not fully understood as we shall discuss later in this section. The already mentioned measurements presented in Section 2.1 performed on PROGEO suggest that the production of CH_4 with a H_2/CO_2 ratio of 5:1 (hydrogen excess) is effective in producing CH_4 with a good yield. This way reaction conditions at the KMC calculations have been set to recreate the experimentally optimized ratio as to try to reproduce experimental results. Furthermore, simulations were also intended to shed light upon the elucidation of the Sabatier process kinetic mechanism by giving a theoretical point of view on the state-of-the-art mechanisms proposed so far. As mentioned before, they fall into two main schemes:

- scheme(A) considers the reaction happening through adsorbed CO as intermediate[43, 44],
- schema (B) considers a direct hydrogenation of adsorbed CO_2[45–47].

Furthermore, even for the subsequent steps of the schema (A) no consensus has been achieved on the further steps. One hypothesis maintains that reaction evolves towards a CO dissociation to C + O,[48, 49] another considers the CO to be directly hydrogenated[50] while a third one (proposed by Martin et al. [51]) considers the mechanisms mainly as occurring through the disproportionation of CO, being, in all three cases, the proposed reaction the rate limiting one.

The KMC simulations performed by us include the four mentioned possibilities as illustrated in Table 2.1 on which we included the most important diffusion steps.

Step	$\mathbf{E}_a$ forward (kJ/mol)	$\mathbf{E}_a$ reverse (kJ/mol)
$CO_2 + * \leftrightarrow CO_2*$	0.0 [56]	8.3 [57]
$H_2 + 2* \leftrightarrow 2H*$	4.0 [56]	77.1 [57]
$CO + * \leftrightarrow CO*$	0.0 [56]	127.7 [57]
$H_2O + * \leftrightarrow H_2O*$	0.0 [56]	49.0 [57]
$CO_2* + H* \leftrightarrow COOH* + *$	113.1 [57]	155.6 [57]
$CO_2* + 2H* \leftrightarrow C(OH)_2* + 2*$	292.3 [57]	217.8 [57]
$CO_2* + * \leftrightarrow CO* + O*$	93.7 [57]	169.3 [57]
$COOH* + * \leftrightarrow CO* + OH*$	306.8 [57]	308.7 [57]
$C(OH)_2* + H* \leftrightarrow CH_2O* + OH*$	98.7 [57]	125.7 [57]
$CH_2O* + H* \leftrightarrow CH_2* + OH*$	163.7 [57]	154.1 [57]
$CO* + * \leftrightarrow C* + O*$	237.4 [57]	111.8 [57]
$CO* + 2H* \leftrightarrow CH* + OH* + *$	221.4 [57]	146.1 [57]
$2CO* \leftrightarrow CO_2* + C*$	339.6 [58]	109.0 [58]
$C* + H* \leftrightarrow CH* + *$	69.2 [57]	154.1 [57]
$CH* + H* \leftrightarrow CH_2* + *$	68.2 [57]	61.9 [57]
$CH_2* + H* \leftrightarrow CH_3* + *$	71.4 [57]	105.6 [57]
$CH_3* + H* \rightarrow CH_4 + 2*$	137.4 [57]	178.7 [57]
$O* + H* \leftrightarrow OH* + *$	137.9 [57]	116.0 [57]
$OH* + H* \leftrightarrow H_2O* + *$	137.9 [57]	99.9 [57]
$H* + * \leftrightarrow * + H*$	13.0 [56]	13.0 [56]
$CO* + * \leftrightarrow * + CO*$	10.0 [56]	10.0 [56]
$O* + * \leftrightarrow * + O*$	48.0 [56]	48.0 [56]
$OH* + * \leftrightarrow * + OH*$	21.0 [56]	21.0 [56]

Table 2.1: Elementary processes intervening in the H_2 + CO_2 and related activation energies (with the source reference in square brackets at their right hand side) for the forward and reverse process. Species with an asterisk (*) aside refer to adsorbed ones, meanwhile asterisk by their own refer to free adsorption sites.

Using the activation energy values given in the table and the appropriate preexponential factor, the time evolution of the system components was computed at the desired conditions of temperature, pressure and initial gas phase molar fractions.

As a first step, an optimization of the most important parameters of the KMC simulation has been performed. When taking original reaction rates, simulation times are really small. This happens because the kinetic Monte Carlo timestep (Δt) is taken as

$$\Delta t = \frac{1}{\sum_{i=1}^{n} \sum_{j=1}^{k} r_{ij}},$$

where r_{ij} is the ith reaction on the jth site, n is the total number of considered steps and k the number of sites.

Since diffusion rates are far larger than reactive ones, the program spends most of the time simulating the former ones. In order to accelerate the convergence of

the calculations, pre-exponential factors for diffusive processes were multiplied by a scaling factor ($\alpha \in (0,1]$). When this scaling factor is applied a huge increase in timestep is obtained, enabling to simulate longer times. It is always important to take care that no change on the final results would occur when applying this scaling factor. The final adopted values of α, which led to six orders of magnitude increase in the simulated time, are given in Table 2.2 .

Process	**original preexponential factor**	**α coefficient applied**
H* + * ↔ * + H*	$2.027{\cdot}10^{13}$	10^{-4}
CO* + * ↔ * + CO*	$2.027{\cdot}10^{13}$	10^{-5}
O* + * ↔ * + O*	$2.027{\cdot}10^{13}$	10^{-2}
OH* + * ↔ * + OH*	$2.027{\cdot}10^{13}$	10^{-3}

Table 2.2: Elementary processes with optimized scaling factor α was applied. Species with an asterisk (*) aside refer to adsorbed ones, meanwhile asterisk by their own refer to free adsorption sites.

Another parameter that was also optimized in the simulation is the size of the grid (given as the number of copies of the unit cell in two dimensions). We point out here that in our case the used unit cell contains two sites (and not one as in the primitive). In this case too, a compromise between the length of the simulation time and the convergence of the results had to be achieved. A value of 25×25 unit cells was found to still reproduce the results of larger lattices while significantly reducing computation time.

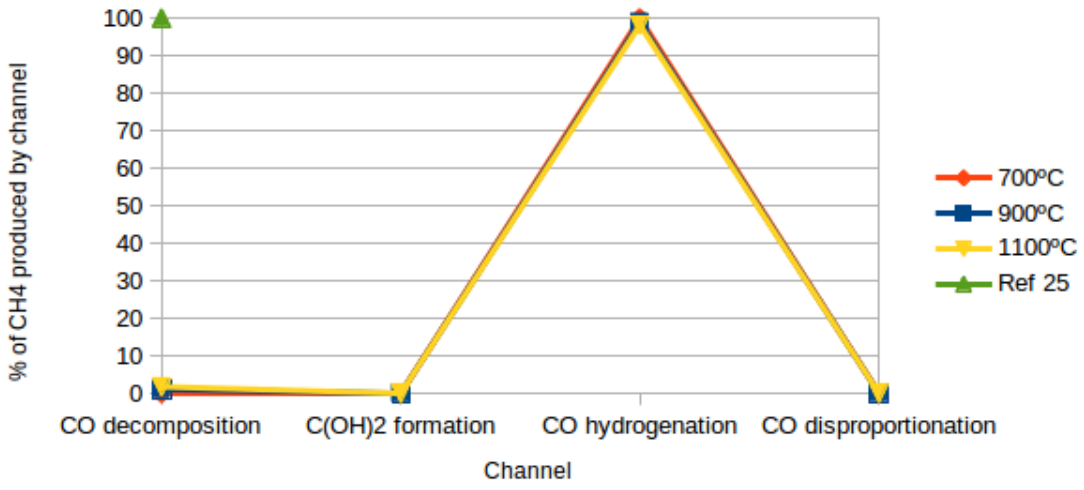

Figure 2.6: Percent of formation of CH_4 from the different candidate rate determining steps (reaction mechanism). Green value is not quantitative but only to indicate which is the rate limiting step proposed.

Using the optimized parameters several runs were performed by varying the temperature (T=300, 500, 600, 700, 800, 900, 1000 and 1100°C) so as to find out which mechanism was the one occurring the most. The rate limiting steps of each

one were the CO decomposition (CO* + * ↔ C* + O*), the $C(OH)_2$ formation (CO_2* + 2H* ↔ $C(OH)_2$* + 2*), the CO hydrogenation (CO* + 2H* ↔ CH* + OH* + *) and the CO disproportionation (2CO* ↔ CO_2* + C*) with species with an asterisk (*) aside refer to adsorbed ones (asterisks by their own refer to free adsorption sites). Computed results show that while at 300 and 500 °C, no CH_4 is formed, from 600 to 1100 °C methane is indeed produced and, as shown in Figure 2.6 the largest fraction of produced CH_4 (well above 90%) is obtained from mechanism A (the hydrogenation of the adsorbed CO concretely through the process CO* + 2H* ↔ CH* + OH* + *).

The mechanism producing methane in the most optimal way can thus be summarized as the following steps:

$$CO_2(g) + * \leftrightarrow CO_2*$$
$$H_2(g) + 2* \leftrightarrow 2H*$$
$$CO_2* + * \leftrightarrow CO* + O*$$
$$CO* + 2H* \leftrightarrow CH* + OH* + *$$
$$CH* + H* \leftrightarrow CH_2* + *$$
$$CH_2* + H* \leftrightarrow CH_3* + *$$
$$CH_3* + H* \rightarrow CH_4 + 2*$$
$$O* + H* \leftrightarrow OH* + *$$
$$OH* + H* \leftrightarrow H_2O* + *$$
$$H_2O* \leftrightarrow H_2O(g) + *$$

However other steps may contribute as well to the methane formation or formation of intermediates promoting reaction.

At the same time, the CO decomposition as such plays always a residual (even more marginal at low temperatures) role. This finding is in contrast with the dominance of mechanism B proposed by the authors of ref [57] that postulates a CO decomposition into C + O on the ground of some ab initio electronic structure considerations (see the green triangle shown in Figure 2.6 upper left corner) without resorting into a true kinetic study.

The analysis of the computed CH_4 yield at a pressure of 10 atm and a H_2/CO_2 ratio of 5:1 as a function of temperature (T) (see Fig. 2.7) exhibits a threshold at about 700°C. The yield grows to about 70% at 900°C and reaches almost 100% at 1100°C. As it is apparent from the figure there is a clear difference between the measured and the computed threshold temperature, possibly due to the fact that we were simulating only Ni(111) surface instead of the whole catalyst, which is far more complex [136]. As a matter of fact, the computed threshold temperature is 600°C higher than the experimental one and the computed rate of increase of the yield as a function of T is one half of that of the experiment. However, it is highly satisfactory that our first attempt to simulate computationally the yield of the Ni catalyzed process of PROGEO, reaction happens at some extent.

The result suggests that the Kinetic Monte Carlo (KMC) method used for our calculations is probably the best way to simulate the kinetics of this type of catalytic chemical reactions. This is not surprising because the method makes use of no approximations, and only a pseudo-random number generator to stochastically solve the Master equations of the kinetic system. One of the main drawbacks of the methodology, however, is the impossibility to simulate processes involving gas species whose concentrations vary on time. In order to take into account this feature of the

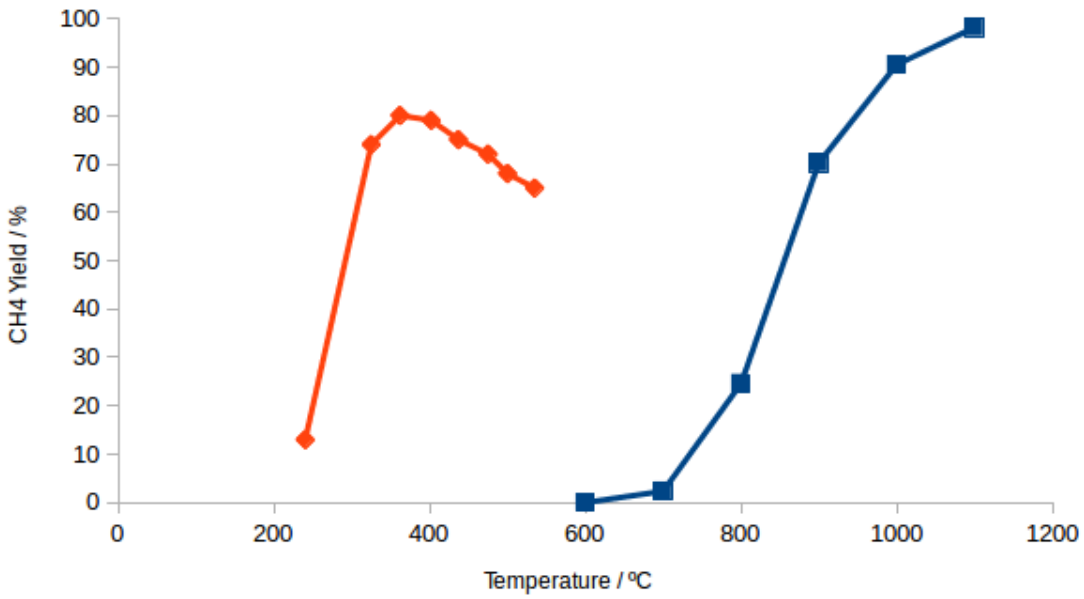

Figure 2.7: Comparison of the yield of CH_4 as a percent of the CO_2 reacted at different temperatures for the experimental apparatus PROGEO (orange) and calculated with KMC method (blue) with all mechanisms

system we have modified the model by splitting the simulation in time intervals. The simulation starts at the input-given conditions, and runs a KMC simulation at these conditions. Once the first interval ends, partial and total pressures are recalculated taking into account the number of reacted species. The next simulation starts at these new conditions of total and partial pressures. This procedure is repeated until the initial ending criterion is achieved. With this finite-volume-reactor model we can obtain more accurate results of how a reaction occurs. Gaseous intermediates can be desorbed and re-adsorbed during the simulation to give a more complete view of the kinetic process. One of the most interesting outcomes from this implementation is the possibility of products (CH_4 and H_2O) and intermediates to desorb and re-adsorb making a much more plausible scenario of the real life processes. Another important aspect is and a highest accurate calculation of yields by implicitely

2.4 Conclusion and outlook

In this Chapter we have discussed the problems met when implementing a simulation of the PROGEO methanator. The fact that the reaction took place by resulting into CH_4 formation results in a general qualitative agreement of the simulation with the experimental results shows that not only the problem is a suitable problem to investigate and improve but it already confirms that mechanisms suggested on the pure ground of ab initio electronic structure calculations can be completely wrong. On the contrary even simplified (assuming Arrhenius like formulations of the rate coefficients) calculations lead to results qualitatively in agreement with measurements performed on an experimental apparatus. Furthermore, the kinetic study pointed the CO hydrogenation as the rate limiting step for the reaction to occur. This fact may instigate the research for new catalyst to promote this reaction.

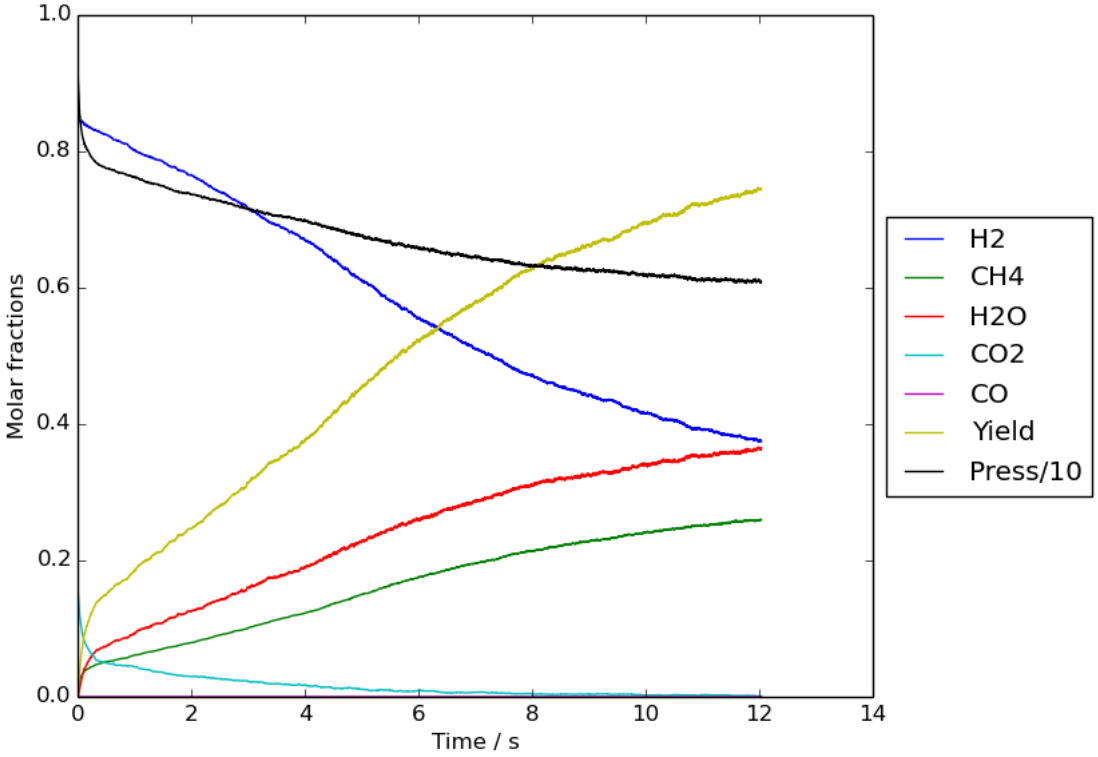

Figure 2.8: Change on the gas phase species molar fractions for the Sabatier reaction with all mechanisms as a function of time.

On the computational side, however, the quantitative differences between computed and measured quantities confirm that there is need for improvement obtainable for a more complex approach. In a approach, in fact, the expected improvements are provided not only from the possibility of getting accurate ab initio data (thanks to the better availability of High Performance Computing (HPC) resources), of combining complementary expertise, of picking up more appropriate codes. Moreover, the discussion of the results obtained clearly indicates the need for further improvements in the

- evaluation of the performance of the simulation under different conditions like different pressure or gas phase reactive molar fractions;
- improvement of the chemical mechanisms with the incorporation into the formulation of the rate coefficients corrective terms associated with the partition functions of reactants and transition states, tunneling effects, sticking coefficients, etc.;
- better accuracy in the calculated energy barriers thus substantially improving the rate coefficients (due to its exponential dependence)
- investigation of the possibility of obtaining the evaluation of the rate coefficients from accurate dynamical calculations;
- performing a sensitivity analysis to evaluate the effect of different catalysts;

- better integration of conditions with output statistical analysis and further graphical tools supporting a better understanding

Furthermore the development of the new methodology combining successive calculations to enable changes in the gas-phase partial pressures allowed a more realistic description of the conditions inside the reactor. With this implementation, new magnitudes like yield of reaction could be calculated for a better comparison with experimental results.

Regarding the experimental implementation of the Sabatier process via the PROGEO apparatus allowed to identify some problems that often are quite far to the theoretician scope in the daily routine like:

- Documentation issues of the set-up of the apparatus.
- Logistical problems with the work-flow of set-up.
- The necessary certifications for the correct usage of the apparatus.
- Limitations in the present facilities for a high intensity electricity input.
- The difficulties in the coupling of clathrate apparatus.
- The complexity of the real catalyst preventing a proper modeling fom a theoretical point of view.

All in all the combination of the experimental apparatus allowed first-hand experimental measurements to be compared with theoretical predictions. This fact revealed the need for a comparison with experimental results produced in a more detailed way, like single facet experiments.

Chapter 3

Study of the scattering of OH + H_2

The simulation of reactive scattering processes using molecular dynamics allows the calculation of reactive and inelastic cross sections and out of them of the rate coefficients of the intervening elementary reactions useful for the description of gas-phase processes occurring in the plasma-assisted Sabatier reaction. Among the many reactions occurring on the plasma, the OH + H_2 has its importance as it considers one of the most important activated species present in the plasma, the OH, with one of the reactants, the H_2. Furthermore, the reaction has been considered as the prototype reaction for the four-body collisional processes for which plenty of studies and Potential Energy Surfaces (PES) have been published. This fact has made the validation of the method used, and the analysis of obtained results an easier task by being able to compare the present results with the ones already available in literature. In order to perform the simulations of reactive scattering processes, we have decided to use the quantum-classical (QC) method developed by Billing et al.[121, 149]. The main feature of this method is the different treatment of the degrees of freedom, some of them are treated quantally, and some of them classically. This makes the method to account for some of the most common quantum effects in reactive scattering simulations, like considering zero point energy, whether vibrational degrees of freedom are quantally treated, or tunneling effects for light atoms which can lead to fractional one-trajectory reactivities among others. The treatment of the quantum degrees of freedom consists on the representation of the wavefunction using a grid method and propagate it using the split operator method. Classical degrees of freedom instead are integrated using the predictor-corrector method. The advantages of the OH + H_2 has been extensively studied in many works [116, 117, 120, 150], which makes it perfect to test the method and analyze its inelastic behaviour by choosing to treat quantally the vibrational degrees of freedom. Furthermore a new PES was developed recently, which allowed a more accurate description of the reaction.[120]

In this chapter we will first introduce the theoretical foundations of the molecular scattering process in Section 3.1, the parallelization of the quantum-classical code, using the shared memory paradigm an its OpenMP implementation to speedup the program will be discussed in Section 3.2. In the same section the use of the bond-order variables as the ones to represent and sample the PES are discussed. Finally obtained results with the quantum-classical program for both reactive and inelastic

scattering processes are presented in Section 3.3.

3.1 Theoretical Methods

Due to the quantal nature of atoms and molecules, methods to simulate reactive scattering processes should be based on the solution of the relevant Schrödinger equation on the system's Potential Energy Surface (PES). In our case the PES, also used in Chapter 4, is introduced in Section 3.1.1. The special treatment of the long-range region in terms of the Improved Lennard Jones model to express the van der Waals interaction, and the Coulomb law for expressing the electrostatic potential due to the interaction of the OH dipole with the H_2 quadrupole caused by its inhomogeneous charge distribution, is given in Section 3.1.2. Details on the used time dependent method to integrate scattering equations are given in Section 3.1.3 while details on the use of the quantum-classical technique for dealing with reactive scattering is introduced in Section 3.1.5. Finally the generation of estimates for experimental observables, like reaction probabilities, cross sections and rate coefficients, are shown in Section 3.1.6

3.1.1 The potential energy surface

The running of dynamical calculations of molecular scattering properties of a chemical system requires knowledge of the interaction of the involved molecules. The calculation of molecular interactions requires the use of quantum mechanics and the integration of the many-body Schrödinger equation:

$$i\hbar\frac{\partial\Psi(t,\mathbf{R},\mathbf{r})}{\partial t} = \hat{H}\Psi(t,\mathbf{R},\mathbf{r}), \tag{3.1}$$

where $\mathbf{R}$ are the coordinates of nuclei and $\mathbf{r}$ the coordinates of electrons. Being this a many-body problem, its analytic solution is, in general, impossible. If taken wisely, approximations can lead to the solution of the desired problem with a satisfactory level of accuracy. The first level of approximation to be adopted is the Born-Oppenheimer (BO) one. The BO approximation states that, due to the difference in mass between nuclei and electrons ($m_p \approx 1836 m_e$, with m_p being the mass of the proton and m_e that of the electron), the description of their motion can be decoupled and solved separately.

When simulating molecular scattering processes, this approximation is indeed introduced. Accordingly, the "electronic structure problem" (the solution of the Schrödinger equation for a system of electrons interacting under the field generated by a fixed nuclei geometry) is solved separately to the actual motion of the nuclei, the "nuclei dynamics". We do not deal here with solution of the electronic structure problem (that is left to Section 4.1). This allows us to use in this section the coordinates r and R only for the nuclei, with r being typically used for the relative coordinates of the atoms within a molecule, and R being used for representing intermolecular distances.

In order to combine together the potential energy obtained from solving the electronic structure at a given nuclei configuration with the actual nuclei dynamics one can use the so-called "direct methods". In direct methods the electronic energies are calculated on-the-fly at each geometry associated with the nuclei dynamics [151–

153]. In this approach, however, convergence problems can occur for the electronic structure calculations [154].

An alternative strategy consists in taking first the step of solving the electronic structure problem at different nuclei configurations sampling the different possible configurations of nuclei. The sampling has to be sufficiently large to cover, in a representative way, the configurations of nuclei that the dynamics is going to explore. This pointwise representation of the potential energy configuration-space is called "Electronically adiabatic potential energy Surface" sometimes referred as simply the potential energy surface or PES. Not many but different strategies have been proposed as how the sampling should be done.[155–157]

In order to get a continuous and derivable potential energy function of the nuclei coordinates able to run the dynamics upon, an interpolation of the electronic structure energy data is needed with a smooth, accurate and computationally efficient function.

Different fitting strategies have been proposed during the years including the use of polynomials on both, physical coordinates [158] and bond order coordinates [159], making use of simplified ab initio methods [160], using rotating atomic potentials [117], splines [118], with permutationally invariant fits [161], or constructing a modified Shepard interpolation scheme [162]. The dawn of neural networks (NN) has completely changed the landscape, almost all PES nowadays are fitted with this method due to its high computational efficiency.[120, 163] Their use, however, needs to be taken with caution, as they may lead to unphysical behavior as illustrated in Section 3.3.

3.1.2 Long-Range interactions: The Improved Lennard-Jones

The importance of considering long-range interactions is often neglected in the PES building process. For example, in general, when producing a highly accurate PES for reactive processes, most of the calculations of ab initio energies are performed for configurations relevant to strong interaction geometries (i.e. distances up to ~ 8 Å). On the contrary, the sampling of long-range configurations is poor, despite the fact that it plays a major role in the low temperature range dynamics (of interest in various fields like astrochemical studies) and inelastic scattering processes.

The Perugia group, instead, has devoted since long great attention to an appropriate formulation of the long-range components of the interaction. As a matter of fact, using ad hoc scattering experiments and high level ab initio calculations, the Perugia group has recently proposed a formulation of the potential for diatom-diatom systems [164] based on the separation of intra and intermolecular contributions, $V = V_{intra} + V_{inter}$. V_{intra} is then usually expressed as the sum of the Morse potentials, V_{Morse}, of the two diatoms as defined in Equation (3.2).

$$V_{Morse}(r) = D_e(e^{-2a(r-r_e)} - 2e^{-a(r-r_e)}) \tag{3.2}$$

The intermolecular component V_{inter} is described, instead, as the sum of an electrostatic and a van der Waals contribution:

$$V_{inter} = V_{elect} + V_{vdW}. \tag{3.3}$$

The electrostatic term takes into account the interaction between the permanent multipole moments of the diatoms and, in the $OH + H_2$ case considered here, it

consists of a dipole-quadrupole contribution [165]

$$V_{elect}(R,\gamma) = \frac{p_{OH}Q_{H2}}{R^4}\,\mathcal{Y}(\gamma) \tag{3.4}$$

with p_{OH} being the dipole moment of the OH molecule, Q_{H_2} the quadrupole moment of H_2 due to the non-homogeneous charge distribution along the bond, and $\mathcal{Y}(\gamma)$ a bipolar spherical harmonics giving the dependence of the interaction upon the mutual orientation of the diatoms.

The van der Waals term is dealt with by the Improved Lennard-Jones (ILJ)[164] model, according to which the dispersion is considered as a bond-bond interaction rather than an atom-atom contribution:

$$V_{vdW}(R,\gamma) = \varepsilon\left[\frac{6}{n-6}\left(\frac{R_m}{R}\right)^n - \frac{n}{n-6}\left(\frac{R_m}{R}\right)^6\right] \tag{3.5}$$

where γ collectively represents the set of Jacobi angles for the diatoms and R_m and ε are the distance at the minimum of the interaction potential and its potential well depth, respectively.

The additional exponential parameter n, depending on the orientation γ and the R distance, is a key feature of the ILJ model. Its radial dependence is given by:

$$n(R) = \beta + 4.0(\frac{R}{R_m})^2 \tag{3.6}$$

where β is a parameter depending on the nature and the hardness of the interacting particles leading to a more realistic representation of both repulsion (first term in square brackets of Equation (3.5)) and attraction (second term in square brackets of Equation (3.5)). β is here taken equal to 9, a value typical of van der Waals interactions in neutral-neutral systems [164].

3.1.3 Nuclear Dynamics: Time-dependent wavepacket approach

Once a suitable PES is built to describe in a realistic way the interaction of atoms, the dynamics can be run to obtain the desired observable, namely the rate coefficients.

In this thesis we consider the following time dependent techniques:

- Time-Dependent Wave Packet (TDWP),
- Quasi-Classical Trajectory (QCT),
- quantum-classical (QC) method as a mix of the first two.

Time-independent methods are also a common choice in the simulation of molecular scattering processes, however, there is a feature of the quantum time-dependent wavepacket approach (TDWP) that makes it preferable over the time-independent one, and that made the former one the approach chosen for the calculations of this thesis. In TDWP, in fact, one does not need to evaluate the full quantum S matrix of the scattering problem. This means that the numerical effort can be focused on the initial molecular quantum states of interest. In addition, the TDWP method

provides a more intuitive (mostly graphical) description of the underlying dynamics still within the quantal framework. All in all one can easily appreciate the simplicity of the formalism, the easy implementability of the numerical technique, the interpretability of the dynamics and the intuitiveness of the results. Furthermore, formally, the TDWP technique relies on the same three steps as the trajectory calculations: the initialization of the system in its reactants' configuration, the time evolution of the system, and the analysis of the system's final state.

The TDWP method derives from the time-dependent Schrödinger equation as formulated in Equation (3.1). After the application of the Born-Oppenheimer approximation (and the relaxation over electronic coordinates) one can write:

$$i\hbar\frac{\partial\Psi(t,\mathbf{R})}{\partial t} = \hat{\mathcal{H}}\Psi(t,\mathbf{R}), \tag{3.7}$$

with the nuclear coordinates $\mathbf{R}$ being the only spatial coordinates of the system. Equation (3.7) is first-order in time and its solution may be written as:

$$\Psi(t,\mathbf{R}) = \hat{U}(t,t_0)\Psi(t,\mathbf{R}) \tag{3.8}$$

with $\hat{U}(t,t_0)$ being the time-evolution operator. If the Hamiltonian is explicitly time-independent, as is most often the case of molecular scattering processes, the time-evolution operator takes the form:

$$\hat{U}(t,t_0) = e^{-i\hat{H}(t-t_0)/\hbar} \tag{3.9}$$

where the "exponential of an operator" is defined via the Taylor series expansion around $x_0 = 0$:

$$e^A = \sum_{n=0}^{\infty}\frac{A^n}{n!} \tag{3.10}$$

When using the TDWP approach the first step consists in the preparation of the initial wave packet. To this end, for molecular scattering processes, the two colliding partners need to be placed far enough to make the diatom-diatom interaction negligible. A usual choice for representing the system are the Jacobi coordinates of reactants [166] (as seen in Figure 3.2).

A common choice for the nuclear wavefunction building procedure is expressing the total nuclear wavefunction as a product of Gaussian wavepacket for the translational (unbound) degrees of freedom, Morse wavefunction for vibrational ones and rigid rotor (see for example ref [167]) for the rotational ones.

A usual way to deal with the wavefunction is to discretize it using a grid method [168]. Care should be taken when choosing the grid spacing and size to include all possible channels and avoid the wavefunction to overlap the grid boundary while still accounting for a representative cut of the momentum space.

3.1.3.1 Evaluation of $\hat{H}\Psi$

Once the initial wavefunction is suitably prepared, time-evolution is carried out by iterating the application of the time-evolution operator for sufficiently small timesteps. For each timestep, this implies the repeated application of the Hamiltonian as specified in Equations (3.8) to (3.10).

The Hamiltonian consists of a kinetic energy operator $\hat{T}$ and a potential energy one $\hat{V}$, which can be applied separately to the system's wavefunction:

$$\hat{H}\Psi = \hat{T}\Psi + \hat{V}\Psi \equiv -\frac{\hbar^2}{2m}\nabla^2\Psi + \hat{V}\Psi. \tag{3.11}$$

The potential energy operator $\hat{V}$ is diagonal with respect to coordinate space (i.e. it can be applied by multiplying V times the wavepacket at each point of the coordinate grid). The kinetic energy operator $\hat{T}$, instead, is non-local because it implies the caculation of the second derivative. This is a true bottleneck of the TDWP procedure. Different strategies exist in order to handle the evaluation of the kinetic energy operator:

The finite difference approach[169, 170] is one of the most simple strategies to solve the problem, it is based in the numerical solution of the wavefunction second derivative (∇^2). In a three-point implementation of the method, the gradient is calculated numerically by adopting the following equation:

$$\frac{\partial^2\Psi(x_i)}{\partial x} = \frac{\Psi(x_{i-1}) + \Psi(x_{i+1}) - 2\Psi(x_i)}{(\Delta x)^2} \tag{3.12}$$

This method, however, results in a substantial error accumulation if a not fine enough grid is applied.

The Fast Fourier Transform (FFT) Method, introduced by Feit et al. [171] and Kosloff and Kosloff [172], fostered a significant advance in time-dependent quantum mechanics. This method to calculate the second derivative involves a Fourier transforming of the wavefunction from the coordinate to the momentum space, followed by its multiplication by $-k^2$ and a back-transforming into the coordinate space again. The FFT transform is:

$$\Psi(k) = \frac{1}{\sqrt{2\pi}}\int_{-\infty}^{\infty}\Psi(x)e^{-ikx}dx \equiv FT[\Psi(x)] \tag{3.13}$$

with the back transform $FT^{-1}[\Psi(x)]$ corresponding to the application of the inverse of FT (that is FT^{-1}). The main advantage of the method is that the kinetic energy operator is local in the momentum space and this is why in the momentum space its application consists only of the multiplication of the wavefunction by the value of ik in the grid.

The method however, requires the grid to have periodic boundary conditions. This implies band limiting the wavefunction for the non periodic cases (like in reactive scattering). A highly attractive feature of the FFT method is that its computational cost increases as $Nlog(n)$ with respect to the number N of the grid points, making the method even more suitable for large systems.

The discrete variable representation method (DVR) introduced by Light et al. [173, 174] is based in the expansion of the wavefunction into an orthonormal basis set. As a result, the wavefunction can be formulated in terms of products of time-dependent coefficients times time-independent basis functions:

$$\Psi(x,t) = \sum_{i}^{N} a_i(t)\phi_i(x)dx \tag{3.14}$$

where the coefficients are calculated by projecting the system wavefunction onto the basis functions.

$$a_i(t) = \int \phi_i^*(x)\Psi(x,t)dx \tag{3.15}$$

and use a quadrature rule, typically the Gaussian quadrature, to express the basis function ϕ_i as product of its value at the jth point by its weight w_j taking the time-dependent coefficients the following form:

$$a_i(t) = \sum_{j}^{N} w_j\phi_i^*(x_j)\Psi(x_j,t)dx \tag{3.16}$$

where w_j is the weight in the selected quadrature scheme associated to the grid point x_j. Substituting Equation (3.16) into Equation (3.14) we get:

$$\begin{aligned}\Psi(x,t) &= \sum_{i,j}^{N} w_j\phi_i^*(x_j)\Psi(x_j,t)\phi_i(x)dx \\ &= \sum_{j}^{N} \Psi_j\psi_j(x)\end{aligned} \tag{3.17}$$

where we have compact notation by defining:

$$\begin{aligned}\Psi_j &= \sqrt{w_j}\Psi(x_j,t) \\ \psi_j(x) &= \sqrt{w_j}\sum_{i}^{N} \phi_i^*(x_j)\phi_i(x)\end{aligned} \tag{3.18}$$

The inclusion of w_j in ψ_j ensures normality in the definition. This approach allows us to express the derivative of the wavefunction as:

$$\frac{\partial^n\Psi(x,t)}{\partial x^n} = \sum_{j}^{N} \Psi_j\frac{\partial^n\psi_j(x)}{\partial x^n} \tag{3.19}$$

where,

$$\frac{\partial^n\psi_j(x)}{\partial x^n} = \sqrt{w_j}\sum_{i}^{N} \phi_i^*(x_j)\frac{\partial^n\phi_i(x)}{\partial x^n} \tag{3.20}$$

with the advantage that these derivatives are time independent, and its calculation can be done once at the beginning of the simulation to make available their value at time propagation.

3.1.3.2 Time propagation

With a method to evaluate the Hamiltonian (the kinetic energy operator) chosen, the next step is choosing its application, i.e. choosing the time propagation method.

The split-operator method (SOP), introduced by Feit and Fleck [171, 175], consists on the separate application of the kinetic energy operator, $\hat{T}$ and the potential one $\hat{V}$ into two different exponentials, with a given Δt it could be approximated as:

$$exp\left(\frac{-i\Delta t\hat{H}}{\hbar}\right) = exp\left(\frac{-i\Delta t\hat{T}}{2\hbar}\right) exp\left(\frac{-i\Delta t\hat{V}}{\hbar}\right) exp\left(\frac{-i\Delta t\hat{T}}{2\hbar}\right) + O(\Delta t^3) \quad (3.21)$$

where $O(\Delta t^3)$ is the error associated with this approximation because of the noncommutability of potential energy and kinetic energy operators. The method was originally developed for use with FFT by first Fourier transforming the wavefunction to the momentum space, multiply it by the free kinetic energy propagator, $exp\left(\frac{-ip^2\Delta t}{4m\hbar}\right)$, transform it back to coordinate space, multiply by $exp\left(\frac{-i\Delta t\hat{V}}{\hbar}\right)$, to finally Fourier transforming it again to momentum space and apply again the free kinetic energy propagator. Except for the initial and the final timesteps of the simulation, the last evaluation of the kinetic energy operator of a given integration step and the first one of the next step can be combined together by propagating Δt instead of $\Delta t/2$ and thus reduce the number of Fourier Transforms. The formalism presented in Equation (3.21), is called the potential referenced SOP. An alternative formalism can be adopted by sandwiching the kinetic energy operator in between the potential energy one in the so called kinetic referenced SOP. Thanks to the resulting merge of the half timesteps, both formalism differ only on the application of the first and the last half timesteps of the simulation. The approach here presented and used in our implementation is called the second-order split-operator method. Another approach developed by Bandrauk and Shen [176–178] takes higher splitting schemes to approximate the commutator between potential energy and kinetic energy operators. This reduces the error to $O(\Delta t^4)$. The method implies the evaluation of more exponentials per step, but makes the computation more efficient by permitting to use a larger timestep in the propagation.

The Chebyshev polynomial expansion method developed by Tal-Ezer and Kosloff [179] is especially useful for long time propagations necessary for collisions involving complex formations or long-lived resonance states because it reduces the number of Hamiltonian evaluations to a minimum. In order to exploit the advantage of using this approach, one needs to confine the spectrum of the Hamiltonian in the interval (-1,1), where the Chebyshev polynomials are bound, by renormalising the Hamiltonian. To achieve this, an a priori knowledge of the spectrum of the Hamiltonian is needed. Assuming a Fourier method is used, the following values are a suitable choice:

$$\begin{aligned} E_{max} &= \frac{\hbar^2\pi^2}{2m(\Delta x)^2} + V_{max} \\ E_{min} &= V_{min} \\ \bar{E} &= \frac{1}{2}(E_{max} + E_{min}) \\ \Delta E &= \frac{1}{2}(E_{max} - E_{min}) \end{aligned} \quad (3.22)$$

where V_{min} is the minimum value of the Potential energy at the given PES and V_{max} a value high enough to never reach during simulations but not as high as to

work within a range of the Hamiltonian much smaller than (-1,1) thus losing computational efficiency and accuracy. At this point the Hamiltonian is renormalized by shifting its eigenvalues to the range (-1,1):

$$\hat{H}_{norm} = \frac{(\hat{H} - \hat{1}\bar{E})}{\Delta E}. \tag{3.23}$$

In this way the time evolution operator $\hat{U}$ can be expressed as mentioned above and further expanded in a Chebyshev polynomials as:

$$\begin{aligned} exp\left(\frac{-i\hat{H}t}{\hbar}\right) &= exp\left(\frac{-it\bar{E}}{\hbar}\right) exp\left(\frac{-i\Delta E t\hat{H}_{norm}}{\hbar}\right) \\ &= exp\left(\frac{-it\bar{E}}{\hbar}\right) \sum_{n=0}^{\infty} C_n J_n\left(\frac{\Delta E t}{\hbar}\right) T_n(-i\hat{H}_{norm}) \end{aligned} \tag{3.24}$$

where $C_n = 1$ for $n = 0$ and $C_n = 2$ for $n \geq 1$, J_n are Bessel functions of the first kind of order n and $T_n(-i\hat{H}_{norm})$ are complex Chebyshev polynomials satisfying the recurrence relationship:

$$\phi_{n+1} = -2i\hat{H}_{norm}\phi_n + \phi_{n-1} \tag{3.25}$$

where $\phi_n = T_n(-i\hat{H}_{norm})\Psi(0)$, setting $\phi_1 = \Psi(0)$ and $\phi_2 = -i\hat{H}_{norm}\Psi(0)$. The most attractive part of the method is the exponential decay of Bessel functions $J_n(\alpha)$ with $\alpha = \Delta E t/\hbar$ for $\alpha > n$, needing only few higher order terms in the polynomial expansion for numerical convergence. Accordingly, the propagation can be performed using larger steps (or even only one step if no information of the intermediate steps is needed), allowing so far larger propagation times to be simulated.

The Lanczos recursion scheme [180] applied to wavefunction propagation is an adaptation of the general method to iteratively solve eigenvalue problems on which the given matrix is reduced to its tridiagonal form spanning only a subspace of the original one. This allows to solve the eigenvalue problem through its diagonalization. The adaptation was first brought by Park and Light [181]. The conversion is implemented via the following scheme:

$$\begin{aligned} &\hat{H}\phi_0 = \alpha_0\phi_0 + \beta_0\phi_1 \\ &\hat{H}\phi_j = \beta_{j-1}\phi_{j-1} + \alpha_j\phi_j + \beta_j\phi_{j+1}, \quad j = 1, N_L - 1 \end{aligned} \tag{3.26}$$

where N_L is the number of Lanczos recursions and ϕ_0 is taken to be $\Psi(0)$. Orthonormality is required for the ϕ_j's and the coefficients are obtained through the projection following Hilbert space inner product $\alpha_j = (\phi_j, \hat{H}\phi_j)$ and $\beta_{j-1} = (\phi_{j-1}, \hat{H}\phi_j)$. For β_0 the value is set to 0 while performing the recursions.

The Hamiltonian formulated in this way has the form:

$$\hat{H}_{N_L} = \begin{pmatrix} \alpha_0 & \beta_0 & 0 & \dots & \dots & 0 \\ \beta_0 & \alpha_1 & \beta_1 & 0 & \dots & 0 \\ 0 & \beta_1 & \alpha_2 & \beta_2 & \dots & 0 \\ \vdots & \vdots & \vdots & \ddots & \vdots & \vdots \\ 0 & 0 & 0 & \dots & \alpha_{N_L-2} & \beta_{N_L-2} \\ 0 & 0 & 0 & \dots & \beta_{N_L-2} & \alpha_{N_L-1} \end{pmatrix} \tag{3.27}$$

where we reduced the size of the matrix from NxN to N_LxN_L. We can now rewrite the propagation operator in the usual exponential form by adopting the following Hamiltonian:

$$\hat{U}(t_0 + \Delta t, t_0) = exp\left(\frac{-i\Delta t\hat{H}_{N_L}}{\hbar}\right) \tag{3.28}$$

The number of recursion steps depends on the chosen timestep, with more recursions being needed for larger timesteps.

3.1.4 Nuclear Dynamics: Quasiclassical approach

There are cases in which a full quantum-mechanical (FQ) treatment of the dynamics of molecular system cannot be implemented mainly because the associated computational effort is too large. The most popular alternative is, then, to run the dynamics of the nuclei using classical mechanics means on a PES derived from quantum mechanical electronic structure calculations. These approaches are called Quasi-Classical Trajectory (QCT) techniques. QCT techniques greatly simplify dynamical calculations by neglecting the quantum nature of atoms and molecules. An a priori evaluation of the capacity of QCT to accurately reproduce full-quantum (FQ) results can be done by taking the considerations on relevant effects listed below:

- The larger the masses of the system are, the better QCT techniques are going to perform. This is due to the fact that the de Broglie wavelength decreases with linear momentum, being the QCT approach more accurate for heavy atoms. In the limit of de Broglie wavelengths smaller than grid spacing, FQ calculations tend to the same results as QCT.

- Similarly, higher kinetic energy leads to smaller de Broglie wavelength and makes the outcomes of the QCT treatment more similar to those of the quantum one.

- Averaging the dynamical outcomes over a large number of trajectories leads to more accurate results according to the fact that Monte Carlo approximates to the numerical evaluation of integrals converge slowly with the number of trials.[182]

- Total energy of colliding species smaller than (or approximately equal to) energy barriers leads to typically inaccurate QCT results due to the neglect of the zero point energy.

- Classically forbidden transitions, as other small state-to-state transition probabilities, are not well described by QCT

- QCT is not accurate when resonance features or other interference phenomena occur.

By keeping in mind the above mentioned warnings, the use of QCT techniques can end up by calculating a large variety of molecular processes properties by simply following the laws of classical mechanics under the effect of the gradients associated with the pre-calculated electronic structure embodied into the PES. In QCT approaches the prefix *quasi* arises from the fact that initial energetic conditions in which the system is initially prepared are chosen equal to the discrete values of the reactants quantum internal energy states. Such "quasi" classical discretization is also enforced on the product molecule internal energy states.

3.1.4.1 Equations of motion

For consistency with quantum mechanics treatments, the classical ones are often based on the Hamilton formalism (this allows also to avoid the calculation of second derivatives). In this formalism the Hamiltonian of the system is defined as:

$$H(\mathbf{r}, \mathbf{p}) = T(\mathbf{p}) + V(\mathbf{r}) \tag{3.29}$$

with $\mathbf{r} \equiv \{r_i; i = 1, ...3N - 6\}$ being the set of position coordinates and $\mathbf{p}$ being the associate linear momenta. The relevant Hamilton equations of motion are then:

$$\begin{aligned} \dot{r}_i &\equiv \frac{dr_i}{dt} = \frac{\partial H}{\partial p_{r_i}} = \frac{\partial T}{\partial p_{r_i}} \qquad (i = 1, ..., 3N - 6) \\ \dot{p}_{r_i} &\equiv \frac{dp_{r_i}}{dt} = -\frac{\partial H}{\partial r_i} = \frac{\partial T}{\partial r_i} \qquad (i = 1, ..., 3N - 6) \end{aligned} \tag{3.30}$$

3.1.4.2 Initial conditions

Initial parameters related to the motion of atoms are defined through the internal rotational energy, internal vibrational energy and collisional energy of the reacting molecules. The first two are selected according to quantum mechanics, thus a discrete set of values are only available for selection.

Under the constraint of these initial quantum-like discretizations (and when required also of a given total energy and angular momentum) and of an initial distance among the centers of mass large enough to make negligible the interaction among different molecules, the initial values of coordinates and momenta (called the "collision parameters") are allowed to vary to make each trajectory different from the others (for example, by changing the angular ones in order to have different relative orientations of molecules on space). A correct and sufficiently extended sampling of the collision parameters is of paramount importance in order to get a representative set of trajectories and as to give enough sampling due to QCT usually uses Monte-Carlo integration and its convergence requires a large sampling.[182, 183] For example, the impact parameter b (graphically exemplified on Figure 3.1) is calculated as:

$$b = r_{CM} \sin(\theta) \tag{3.31}$$

where r_{CM} the radius among centers of mass (CM) of colliding partners and θ the angle between r_{CM} and its associated momentum. The impact parameter is related

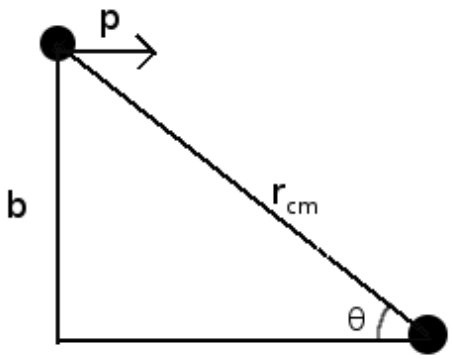

Figure 3.1: Collisional Impact parameter b for standard collision between centers of mass

to the orbital angular momentum, and to the collisional momentum being aligned to intermolecular vector. This parameter has a particular importance since it is related to the opacity functions, a non-observable quantity very useful to rationalize collisional properties. The sampling is done by generating trajectories among 0 and b_{max}, a parameter optimized by ensuring that its value is large enough to cover all the trajectories leading to reactive conditions, and small enough to make the majority of the sampled values belong to the domain where reactions may happen.

3.1.4.3 Calculation of Trajectory

The next problem is to calculate a trajectory. This is accomplished by numerically integrating the equations of motion starting from the chosen set of collision parameters. Several algorithms have been proposed in the literature for inegrating the set differential equations given in Equation (3.30) in order to describe the time evolution of a collisional process.[184]

The most popular algorithms for collisional studies of chemical reactions are the fourth-order Runge-Kutta-Gill and the Adams-Moulton method. The latter is a predictor-corrector method [185] and is most often used with fourth-order predictor and fifth-order corrector (sometimes higher order formulations are used as well). For both approaches either a fixed-size timestep or a variable one can be used. The best choice includes the evaluation of the overhead due to the dynamic adoption of variable step that reduces the number of interaction evaluations and of equations to integrate.

For each trajectory, time is integrated until the final species produced by the collision are reached (either reactants or products). The evaluation of the system being in one of its final states needs to be done by carefully analyzing the appropriate quantities (eg. distances and/or momenta) ensuring the system has arrived to a desired final state. As soon as one of them is produced, the integration is stopped and a check of the nature of the products is carried out.

3.1.4.4 Product Analysis

Once trajectory integration is completed, results are analyzed to acquire the information relevant to the kinetic studies (reaction probabilities, cross sections, rate

coefficients and opacity functions). A more in detail analysis of how observables are evaluated is given in Section 3.1.6. However it has to be pointed out here that in the QCT method, as opposite to the FQ one, probabilities are obtained in a binary way (a given trajectory is either reactive or or not). For such an analysis interatomic distances are typically the quantities to be considered. Accordingly, the accuracy of QCT results is bound to the number of integrated trajectories.

Typically different sets of trajectories are run at fixed collisional energies or even at fixed vibrational/rotational energies of reactants if state-to-state studies are aimed to be performed, while all other initial conditions are set randomly to cover as much as possible the configuration space. Next, averaged cross sections are calculated as described in Section 3.1.6. For vibrational and rotational energy transfers analysis the first step is the change of coordinates to a set better describing final product arrangements (no change in non reactive events). Expressions for quantities associated with collision products in terms of the generalized coordinates of position r' and momenta p' for internal coordinates and R' and P' for intermolecular position and momenta are given below. Bold typography is used to refer to the whole set of coordinates. For each atomic arrangement, its associate coordinate transformation has to be considered as extensively explained at ref. [186].

Total Energy:

$$H' = \sum_i \frac{1}{2\mu_i} {p'_i}^2 + {P'_i}^2 + V(\mathbf{r}', \mathbf{R}') \tag{3.32}$$

Internal Energy:

$$\tilde{\epsilon}_{int} = \sum_i \frac{1}{2\mu_i} {p'_{vib,i}}^2 + {p'_{rot,i}}^2 + V_{vib,i} + V_{rot,i} \tag{3.33}$$

Internal angular momentum:

$$\tilde{J'}_{int} = \mathbf{r'_i} \times \mathbf{p'_{rot,i}} \tag{3.34}$$

Relative Angular momentum:

$$\tilde{J'}_{rel} = \mathbf{R}' \times \mathbf{P}' \tag{3.35}$$

Total Angular momentum:

$$\tilde{J'}_{tot} = \tilde{J'}_{rel} + \tilde{J}_{int} \tag{3.36}$$

Also some pseudo quantum numbers for both the vibrational and rotational degrees of freedom can be calculated for diatoms as follows:

$$\begin{aligned} \tilde{j'} &= -\frac{1}{2} + \frac{1}{2}\left[1 + 4\frac{\tilde{J'}_{int}\tilde{J'}_{int}}{\hbar^2}\right]^{1/2} \\ \tilde{v} &= -\frac{1}{2} + \frac{1}{\pi\hbar}\int_{r-}^{r+}\left\{2m\left[\tilde{\epsilon}_{int} - V(r) - \frac{\tilde{J}_{int}\tilde{J}_{int}}{2mr^2}\right]\right\}dr \end{aligned} \tag{3.37}$$

where $r\pm$ are the diatomic turning points of the effective potential at the energy $\epsilon'_i nt$ and are determined using the Newton-Raphson iteration technique.

It has to be pointed out, here, that, since classical mechanics gives a continuous range of values for all its observables, its associated pseudoquantum numbers belong to the continuous range as well, making these quantum numbers useful only for qualitative comparison with FQ results.

3.1.5 Nuclear Dynamics: The quantum-classical approach

For systems consisting on a moderate size ($N \geq 4$) with both, light atoms, where quantum effects are important, and heavier ones, the quasi-classical description may not be convenient and full-quantum (FQ) treatment may be computationally to expensive. Different ways have been proposed in order to include quantum effects in a classical frame in the so-called semiclassical methods[187]. Among them the quantum-classical method developed by Billing[121, 122] is a specially interesting alternative. The method consists in spliting the treatment of different degrees of freedom into classically and quantally treated and coupling them via an effective Hamiltonian using the mean field of the given observables formulated as their expectation value.

A full and detailed derivation of the method is out of the scope of the present thesis and a more pedagogical introduction to the method is given. It is intended to present the formalism by exemplifying the method into putting the focus on the treatment of four-body collisions leading to both reactive and inelastic processes, specially the vibrational exchange. For a more detailed derivation of the quantum-classical formalism, details are given in the following studies: refs.[188–192]

The choice of which degrees of freedom are treated quantally and which classically depends greatly on the system chosen to study and their examined quantities. In the present case the aim was to study the reactive processes and vibrational energy exchange of the OH + H_2 collision, being thus the natural choice for quantally treated degrees of freedom, the vibrational ones, since it allows an accurate treatment for both the vibrational exchange and the H_2 bond breaking, treating all the remaining degrees of freedom classically. Reactive probability is calculated by analyzing the amount of wavefunction flux evaluated along a dividing line located on the grid in the product region (in correspondence with the breaking bond (H_2 in the present case)).

The splitting of the different degrees of freedom into quantally and classically treated is done via the Hamiltonian of the system (inside the Born-Oppenheimer approximation and considering the nuclear degrees of freedom). Starting with its usual expression in the body fixed reference frame where total translation and rotation is included in the reference system and only relative positions and momenta are considered thus using reduced masses μ:

$$\hat{H} = -\sum \frac{\hbar^2}{2\mu_i}\nabla_i^2 + V(\mathbf{r}) \tag{3.38}$$

The time-independent Schrödinger equation can be written as:

$$\hat{H}\Psi = E\Psi \tag{3.39}$$

For the case of the four-body problem it is convenient to express the Hamiltonian with spherical coordinates of the Jacobi vectors (Figure 3.2), having each vector a radial r_i, a polar angle θ_i and an azimuth angle ϕ_i components. This choice, however, leads to a redundant description of angular degrees of freedom (6 instead of 3):

$$\hat{H} = -\sum_{i=1}^{3} \frac{\hbar^2}{2\mu_i}\left[\frac{\partial^2}{\partial {r_i}^2} + \frac{2}{r_i}\frac{\partial}{\partial r_i} + \frac{1}{r_i^2}\left(\frac{\partial^2}{\partial\theta_i} + \cot\theta_i\frac{\partial}{\partial\theta_i} + \frac{1}{\sin^2\theta_i}\frac{\partial^2}{\partial\phi_i^2}\right)\right] + V(r;t) \tag{3.40}$$

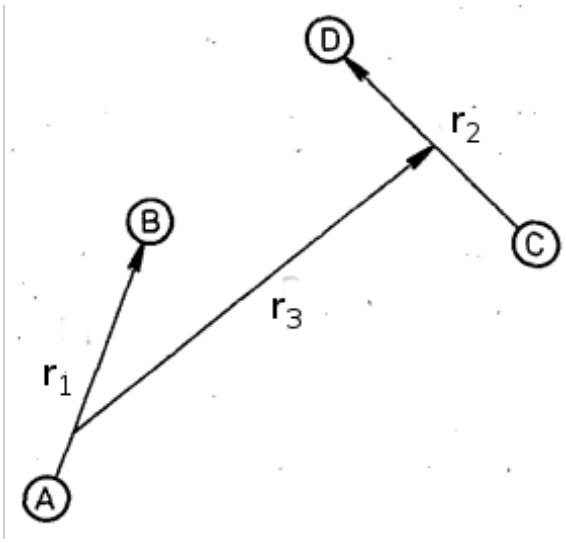

Figure 3.2: The Jacobi coordinates for reactants in four body systems

The choice of spherical coordinates allows to eliminate first derivatives in r_i by operating the wavefunction the following way:

$$\Psi = \frac{\psi}{\prod r_i} \tag{3.41}$$

This way the new Schrödinger equation takes the form:

$$\hat{H}'\psi = E\psi \tag{3.42}$$

and the new Hamiltonian does not have first derivatives anymore:

$$\hat{H}' = -\sum_{i=1}^{3} \frac{\hbar^2}{2\mu_i} \left[\frac{\partial^2}{\partial {r_i}^2} + \frac{1}{r_i^2} \left(\frac{\partial^2}{\partial \theta_i} + \cot\theta_i \frac{\partial}{\partial \theta_i} + \frac{1}{\sin^2\theta_i} \frac{\partial^2}{\partial \phi_i^2} \right) \right] + V(\mathbf{r}) \tag{3.43}$$

At this point the splitting of the different degrees of freedom is performed by formulating a semiclassical Hamiltonian where in the classical degrees of freedom (all angular ones with their associated momenta and the intermolecular one with its associated momentum) the classical momentum p substitutes the quantum momentum operator.

$$\hat{H}'_{SC} = -\sum_{i=1}^{2} \frac{\hbar^2}{2\mu_i} \frac{\partial^2}{\partial {r_i}^2} + \sum_{i=1}^{3} \frac{1}{2\mu_i r_i^2} \left(p_{\theta_i}^2 + \frac{1}{\sin^2\theta_i} p_{\phi_i}^2 \right) + \frac{p_{r_3}}{2\mu_3} + V(\mathbf{r})\psi \tag{3.44}$$

In order to merge the quantal and classical degrees of freedom, the observables in the quantally treated ones are parsed into the classical Hamiltonian using a mean field approximation, namely by taking the expectation values of the quantal counterparts and formulating an effective semiclassical Hamiltonian as:

$$H_{sc}^{eff} = \frac{\langle \psi \mid \hat{H}'_{SC} \mid \psi \rangle}{\langle \psi \mid \psi \rangle} \tag{3.45}$$

where the Dirac notation is taken, meaning integration over the quantum degrees of freedom:

$$\begin{aligned} H_{sc}^{eff} = &\sum_{i=1}^{2} \langle T_i \rangle + \frac{p_{r_3}}{2\mu_3} + \frac{1}{2\mu_3 r_3^2}\left(p_{\theta_3}^2 + \frac{1}{\sin^2\theta_3} p_{\phi_3}^2\right) \\ &+ \sum_{i=1}^{2} \frac{1}{2\mu_i}\left(p_{\theta_i}^2 + \frac{1}{\sin^2\theta_i} p_{\phi_i}^2\right)\left\langle \frac{1}{r_i^2} \right\rangle + V^{eff}(\langle \mathbf{r} \rangle) \end{aligned} \tag{3.46}$$

where $\langle X \rangle$ denotes the expectation value of observable X and V_{eff} is approximated as the potential energy at the coordinates given by classical coordinates and the expectation value of the quantal ones. The time evolution of the system is carried out by simultaneously integrating the classical equations of motion and solving the time-dependent Schrödinger equation. This is given by:

$$i\hbar \frac{\partial \psi}{\partial t} = \left\{ \sum_{i=1}^{2} \left[-\frac{\hbar^2}{2\mu_i} \frac{\partial^2}{\partial {r_i}^2} + \frac{1}{2\mu_i r_i}\left(p_{\theta_i}^2 + \frac{1}{\sin^2\theta_i} p_{\phi_i}^2\right)\right] + V(\mathbf{r}) \right\} \psi \tag{3.47}$$

which makes use of classically rotational degrees of freedom for its solution. For both problems strategies explained in Sections 3.1.3 and 3.1.4 can be applied. The initial wavefunction is given as a product of the two Morse oscillator functions of the reactant diatoms,

$$V_{Morse} = D_e(1 - e^{-\alpha(r - r_e)})^2 \tag{3.48}$$

$$\psi(r_1, r_2, t = 0) = \varphi_{v_1}(r_1)\varphi_{v_2}(r_2). \tag{3.49}$$

The solution of Equation (3.47) is carried out by a standard two dimensional grid method using the FFT method for the evaluation of the kinetic energy operator and the SOP method for time propagation. The integration of Equation (3.46) is done with a predictor-corrector method.

3.1.6 Calculation of probabilities, cross sections and rate coefficients

Due to the fact that both quantum and classical equations of motions are integrated at the same time, it is possible to compute the initial state-selected reaction probabilities at the initial vibrational quantum numbers of diatoms v_{1i} and v_{2i} and the rotational pseudoquantum numbers $\tilde{j}_{1i}$ and $\tilde{j}_{2i}$ and at the given dihedral rotational pseudoquantum number $\tilde{l}$. The reaction probability, $P^R_{v_{1i}, v_{2i}, \tilde{j}_{1i}, \tilde{j}_{2i}}$ is evaluated from the flux $J(r_1, t; r_2^*)$, along a dividing line located on the grid in the product region in correspondence with the breaking bond (H_2 in the present case) from the expression:

$$J(r_1, t; r_2^*) = \frac{\hbar}{\mu_2} \mathrm{Im}\left(\psi(r_1, r_2, t)^* \frac{\partial \psi(r_1, r_2, t)}{\partial r_2} \right)\Big|_{r_2 = r_2^*} \tag{3.50}$$

and integrating it over both time and the remaining quantum variable. Indeed the flux method is used, due to the fact that final products of reaction are composed

of degrees of freedom arising from a mixture of quantally and classically treated degrees of freedom making impossible to project the final wavefunction to the product states.

Once the flux has been analyzed the reactive components of the wavefunction are eliminated by means of an absorbing potential placed at the last points of the grid in r_2.

Vibrational state specific thermally averaged cross sections, $\sigma_{v_{1i},v_{2i}}(E_{cl},T_0)$, which include contributions from higher rotational states populated at the considered initial values of the classical energy E_{cl} (i.e. the sum of the kinetic energy coming from the contribution of translational and orbital motions plus the rotational energies of the diatoms) can then be computed from the expression:

$$\langle\sigma_{v_{1i},v_{2i}}(E_{cl},T_0)\rangle = \frac{\pi\hbar^6}{8\mu_3(k_BT_0)^3I_1I_2}\times$$
$$\int_0^{l_{max}} \mathrm{d}l(2l+1)\int_0^{\tilde{j}_{1max}} \mathrm{d}\tilde{j}_1(2\tilde{j}_1+1)\int_0^{\tilde{j}_{2max}} \mathrm{d}\tilde{j}_2(2\tilde{j}_2+1)P^R_{v_{1i},v_{2i},\tilde{j}_{1i},\tilde{j}_{2i}}$$

where k_B is the Boltzmann constant, T_0 is an arbitrary reference temperature; $l_{max}, \tilde{j}_{1_{max}}$ and $\tilde{j}_{1_{max}}$ are the maximum values for $l, \tilde{j}_1$ and $\tilde{j}_2$ considered for a given total classical energy E_{cl}; I_1 and I_2 are the moments of inertia of the two reactants.

From the the value of the cross section (evaluated as defined in Equation (3.51)) one can estimate the vibrational state specific rate coefficients as:

$$k_{v_{1i},v_{2i}}(T) = \left(\frac{8k_BT}{\pi\mu_3}\right)\left(\frac{T_0}{T}\right)^3\int_0^{\infty}\mathrm{d}(\beta E_{cl})e^{-\beta E_{cl}}\langle\sigma_{v_{1i},v_{2i}}(E_{cl},T_0)\rangle \tag{3.51}$$

where $\beta = 1/(k_BT)$.

From the wavefunction remaining on the grid after roiving the reactive part of the wavepacket, one can also obtain information about inelastic scattering and, in particular, about the exchange of vibrational quanta. This is carried out by projecting the final wavefunction on the asymptotic vibrational states:

$$P^{NR}_{v_{1i},v_{2i}\to v_{1f},v_{2f}} = \left|\int \mathrm{d}r_1\int \mathrm{d}r_2\psi(r_1,r_2,t)\phi_{v_{1f}}(r_1)\phi_{v_{2f}}(r_2)\right|^2 \tag{3.52}$$

where the superscript NR stands for nonreactive.

The non reactive probability can then be used to calculate average cross sections for vibrational energy transfer within the following equation, similar to Equation (3.51),

$$\langle\sigma_{v1i,v2i\to v1f,v2f}(E_{cl},T_0)\rangle = \tfrac{\pi\hbar^6}{8\mu_3(k_BT_0)^3I_1I_2}\times \tag{3.53}$$
$$\textstyle\int_0^{l_{max}}\mathrm{d}l(2l+1)\int_0^{\tilde{j}_{1max}}\mathrm{d}\tilde{j}_1(2\tilde{j}_1+1)\int_0^{\tilde{j}_{2max}}\mathrm{d}\tilde{j}_2(2\tilde{j}_2+1)P^{NR}_{v1i,v2i\to v1f,v2f}$$

and the corresponding rate coefficients:

$$k_{v1i,v2i\to v1f,v2f}(T) = \tag{3.54}$$
$$= \left(\tfrac{8k_BT}{\pi\mu_3}\right)\left(\tfrac{T_0}{T}\right)^3\textstyle\int_0^{\infty}\mathrm{d}(\beta U_{cl})e^{-\beta U_{cl}}\langle\sigma_{v1i,v2i\to v1f,v2f}(E_{cl},T_0)\rangle$$

where E_{cl} has been replaced by the symmetrized semiclassical energy, U_{cl}:

$$U_{cl} = \frac{\Delta E}{2} + E_{cl} + \left(\frac{\Delta E^2}{16 E_{cl}}\right) \tag{3.55}$$

with ΔE being the energy gap between the transitions of interest. This symmetrization is needed to approximately restore the quantum mechanical detailed balance principle.

3.2 Computational implementation and details

In this section the work regarding the parallelization of the quantum-classical code using the Shared memory paradigm and its OpenMP implementation, the representation of the PES using the Bond Order coordinates, and the computational details of the Quantum Classical Simulations are discussed. A combined approach is used, where the subject and the theory are introduced and the details and results are presented altogether.

3.2.1 Code Parallelization

On 1965 Moore gave birth to the Moore's law, he stated that the number of transistors in a dense integrated circuit doubles about every year[193]. 10 years later, he revised his statement updating the frequency of doubling the number of transistors to a biannual basis[194], in the more known version of it. It has to be pointed out that Moore's law is an observation and projection of a historical trend and not a physical or natural law. However, the trend stayed true until 2012, when size of transistors reached the nanometric scale. At this size, the heat dissipation, the manipulation and quantum effects, play a non-negligible role limiting the evolution of computer power.

In the need of increasing computational power, the developing computer companies started to think on joining computing machines and processors to give solution to the computational demand. The idea was to spread the work into different processors taking each a part of the total workload, each processor was to be in charge of different tasks, this way the computational power of new machines is still able to increase year by year.

However, this solution has a drawback, computer programs are made of different subroutines, which combined accomplish the desired goal. Each subroutine implements an algorithm and not all algorithms have the same potential to be parallelized. Many tasks in a computer program need information from other tasks to be able to run. Iterative algorithms need the information of $n-1th$ step to carry the nth step. In many cases a computer program has different types of tasks or algorithms, some of them are completely independent and thus able to be executed independently by separate processors (they can be run in parallel) and some of them are not. Algorithms which are parallelized constitute the parallel region inside the computer code.

The instruction to tell each processor which tasks should carry out, when should it do them, how tasks depend among themselves, the communication between processors and other constraints to take into account should be built into the program

code. The procedure of giving all these instruction to processors is called the parallelization of the code.

The distribution of tasks to the processors at the beginning of the parallel region, and the collection of data at the end of it generates an extra workload called the overhead. Both the parallelizability of an algorithm and the overhead due to its parallelization need to be taken into consideration when deciding how the parallelization of a computer program is actually carried out. The amount of work each task consist of, is expressed as the "granularity". Since the overhead is typically the same for coarse-grain tasks than for fine-grain ones, parallelization consisting on coarse grain tasks tend to have smaller relation between the overhead and the actual task workload being more optimal. Coarse grain tasks are big pieces of workload passed to the processor all together while for fine grain, the opposite happens.

Tasks can have different workloads, many times the associated workload of a task is only known at the run time, when the task ends. This can lead to some processors finishing their work before other ones, diminishing the efficiency of the parallelization. A dynamic scheduling can help rearranging tasks at the runtime, however extra overheads are generated for dynamic scheduling due to the more intervening nature. Anticipating how the tasks are going to be, to choose the appropriate scheduling scheme is important when carrying out the parallelization.

For setting up all the mentioned aspects on a program parallelization, many parallelizing languages exist which encompass all the mentioned features. Among all of them they could be classified, according to which kind of Parallelization they do, into three categories:

Distributed Memory Paradigm Each processor works in a completely independent way to the other ones with its own memory. It has only access to the information he needs at every moment, this is, all variables are different from processor to processor and communication among processors is done via point-to-point communications. There is a main processor in charge to distribute and collect the work, while the other ones only execute the tasks. Due to the slow communication among processors, this kind of parallelization is good for algorithms with a high balance of independent work.

Shared Memory Paradigm aims to distribute work between processors connected to the same memory chip. Communication between processors is done actually by accessing zones of the memory on which all processors can have access to. This kind of parallelization requires a good knowledge of the memory structure and requires a specific declaration on which kind of variable is each, basically if all processors share the same information on that variable, or if each processor has its own copy of the variable independent from the other ones. Clauses to schedule the work also exist like in Distribute memory paradigm. This paradigm is good when information needs to be shared among processors.

GPU parallelization Graphical Processing units (GPU) consist on lots of very small processors able to execute small tasks, they traditionally were used to rapidly manipulate and alter memory to accelerate the creation of images in a frame buffer intended for output to a display device. The architecture of a single GPU computer unit has a completely different structure, which is called a 'stream processor' in

supercomputing. Multiple-stream processors obtain their input from other stream processors via dedicated pipes Every stream processor has an individual memory interface. Memory-access latency can be further hidden by calculations. The same program can thus execute on many data elements in parallel, unhindered by a single memory interface. The GPU is especially suited for problems that can be expressed as data-parallel computations, in which the same program is executed on many data elements in parallel with a high ratio of arithmetic operations to global memory operations.

The code used to run simulations of the OH + H_2 scattering process implements the quantum-classical method for the 4-body cases. It uses, then, a trajectory approach: many replicas of the system are prepared in different initial conditions (translational energy, vibrational and rotational states, space configurations, angular momentum, etc.) to make them evolve on time and finally analyze the obtained collision trajectories. From the parallel programming point of view, each trajectory is a task able to be treated completely independently with respect to the other ones. These kind of algorithms where almost the whole workload is independent and no communications exist except from the initial preparation of the system, and final collection of data are called embarrassingly parallel algorithms, and they are the ones which have better parallel behavior.

Considering the computational resources available, the shared memory paradigm was the most suitable approach being its most spread implementation is OpenMP[195]. Since the code we were using was written in Fortran, the Fortran implementation of OpenMP was used.[196] However, the code used was build in the F77 version of Fortran, while OpenMP was only available for F95 versions and later. The first step in order to parallelize the code was then, an update of the given code to F95 version of Fortran.

With the F95 version of the code the parallelization was possible. The distribution for the workload was performed by assigning different trajectories to the various threads. Taking this way the coarsest grain possible approach, minimizing this way the initial and final ovehead due to load task. The scheduling used was the guided one. In this approach, each task consist of a given number of trajectories. At the beginning of the execution, the number of trajectories per task is big, this way reducing the overhead due to task distribution, when processors finish their initial work, smaller tasks are given, to ensure an equal repartition of tasks leading to no idle processors.

The piece of most relevant relevant code (the one defining the parallel region on the do loop) used for the parallelization is the following:

⋮

```
EK=0.00011962659192089D0*EDEF
AIN1=AM12*RAV10*RAV10
AIN2=AM34*RAV20*RAV20

!$omp parallel do default(private) &
!$omp shared(AM1, AM2, AM3, AM4, AM12, AM34, AMY, &
!$omp RE1, DE1, BETA1, RE2, DE2, BETA2, DR1, &
```

```
!$omp DR2, R1MIN, R1MAX, R2MIN, R2MAX, VIMA, HBAR, &
!$omp PHIRE, PHIIM, PRMT, NTRA, &
!$omp WV, WAVEX, NV1, NV2, NJ1, NJ2, IIN, IOUT, NL, &
!$omp RMAX, BIMPMAX, NIP, VABS, EDEF, &
!$omp AKB, PI, TO, VOLEM, ANORMO, RAV10, RAV20, EK, &
!$omp IX, IY, IZ, AIN1, AIN2) &
!$omp firstprivate(DT, PSINRE, PSINIM, PROB, SUM) &
!$omp reduction(+:FLUXTOT, SIGMA_TOT, CROSSR, &
!$omp CROSSNR, PROBT) &
!$omp copyin(/CSE/,/AVER/,/POTEN/,/FLUX1/,init2),
!$omp num_threads(threads)

DO ITAL=1,NTRA
    IF (IOUT.EQ.1) THEN

                    ⋮
```

where all variables have been declared according to their usage (shared, firstprivate, reduction(+). Default behaviour is set to private. Variables declared as shared are available to all processors thus sharing the same value. Private variables are declared independently in the piece of memory inherent to each processor, the initial value of the variable when entering the parallel region is not defined. Firstprivate variables are same as private variables, but the initial value inside the parallel region is set equal to the value before the parallel region. Reduction variables are same as private variables except that at the end of the parallel region its value is combined according to the sign specified, in the present case the + value is used thus the final value after the parallel region is the sum of the values of each of the cores.

The speedup, $S(p)$, test is a standardized measure, of the parallelization efficiency with the number of processors. The speedup is calculated as follows:

$$S(p) = \frac{t_{seq}}{t_{par}(p)} \tag{3.56}$$

where p is the number of processors, t_{seq} is the time needed for the sequential (not parallel) code to run a simulation, and $t_{par}(p)$ is the time needed for the parallel code to run the simulation on the given number of processors. Figure 3.3 shows the speedup test for the parallelization of our quantum-classical code. The combination of the embarrasingly parallel nature of the trajectory program and the selected coarse grain scheme leads to performances close to ideal (Figure 3.3 solid line). However, the efficiency, formulated as S/p, gets reduced when the number of processors increases. This behaviour is a common trend due to the fact that, at a given workload to be distributed among an increasing number of processors the workload per processor is smaller, while the overhead stays constant. The resulting ratio of overhead/workload becomes also bigger, thus decreasing the efficiency of the parallelization.

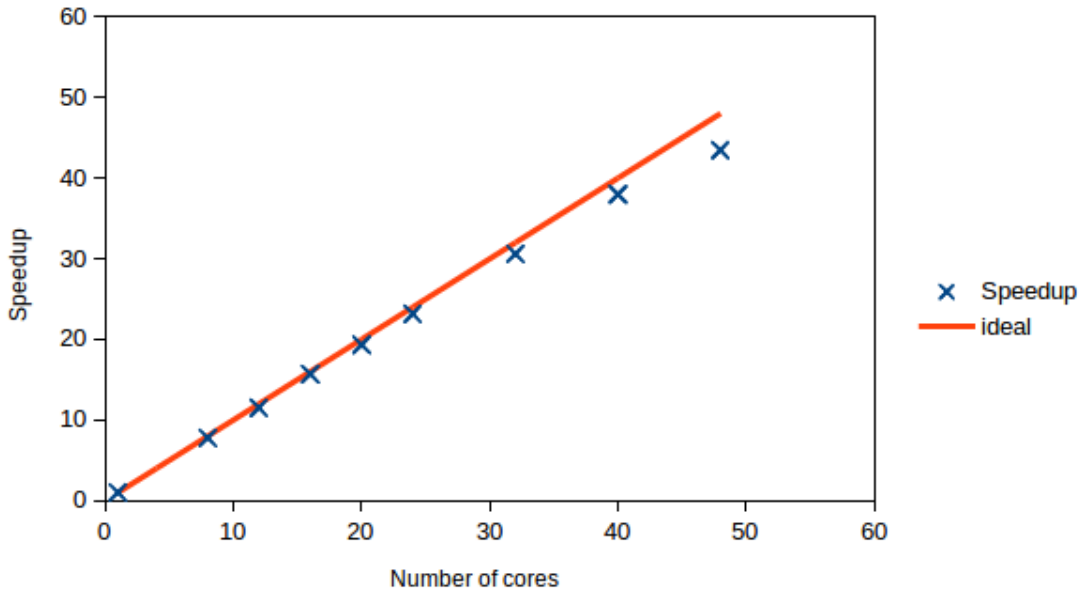

Figure 3.3: Measured Speedup (crosses) of the QC code using up to 48 cores. The solid line shows the ideal behaviour.

3.2.2 The Rotating Bond-Order approach to the representation of the PES for long-range interactions

In this section we trace back the evolution of our approach to progress variables for molecular processes with special attention on the intermolecular van der Waals, V_{vdw}, and electrostatic, V_{elect}, potentials evolution. In reactive and non-reactive processes approaching sufficiently in depth the close interaction region of the PES, not only the initial configurations of the molecular system are involved but also the highly excited and/or strongly deformed ones.

Let us consider first the case of a diatomic molecule slightly distorted with respect to the equilibrium position (say molecule b) and another diatomic one strongly distorted (say molecule a). When molecule a is sufficiently stretched, it becomes more convenient to express intermolecular potential adopting a two-particle-in-a-molecule (or a two pseudoatom (pa)-bond pairs) formulation rather than the bond-bond one as descibed in Section 3.1.2. This means that, at intermediate values of the intermolecular distance R of the molecular partners, both V_{vdW} and V_{elect} must gradually evolve from a bond to a separated-atoms formulation of the interaction. Accordingly, the V_{vdW} and V_{elect} interactions are partitioned into two pa_1-bond and pa_2-bond terms at all values of r (including $r = r_e$) to ensure a smooth transition of the system from diatom–diatom to excited diatom–diatom and then to dissociated diatom–diatom (or, correspondingly, from a relaxed "bond" to a stretched bond and then to a "near dissociated" molecular representation). This implies that the diatomic electric dipole $p(r)$ and quadrupole $Q(r)$ smoothly evolve, as r increases into the corresponding asymptotic separated atoms arrangements, following the electronic configuration associated to the ground state.

It has also to be pointed out here that, as the value of intramolecular distance, r, becomes comparable with that of intermolecular one, R, the formulation of V_{elect} must be turned into a sum of Coulomb contributions defined in terms of partial

charges derived from a charge distribution on the molecular frame and that the value of $Q(r)$ is crucial for the definition of the dependence of the charge distribution on r. Accordingly, the potential energy V can be formulated as:

$$V = \sum_{i=1}^{2} V_{intra}^{(i)}(r_i) + \sum_{k=1}^{2} V_{inter}^{(k)}(R_{k-bond}, \theta_{k-bond}) + V_{inter}^{elect} \tag{3.57}$$

in which R_{k-bond} is the distance between the pseudoatom pa_k and the bond center of mass of the less deformed diatom and θ_{k-bond} is the related angle in the plane. In Equation (3.57), the sum over k involves the two pseudoatom-bond pairs and represents the van der Waals component of the interaction that in our approach is usually formulated as an ILJ potential.

Transitions between different channels can be associated with strongly deformed molecular configurations. In these cases, to the end of enforcing a proper behavior on both short and long-range shapes, $V_{intra}^{(i)}(r_i)$ has been formulated as:

$$V_{intra}^{(i)}(r_i) = V_{BO}^{(i)}(r_i)s(r_i) + V_{ILJ}^{(i)}(r_i)1 - s(r_i) \tag{3.58}$$

where $V_{BO}^{(i)}(r_i)$ is a bond order polynomial([159] as

$$V_{BO}^{(i)}(r_i) = \sum_{i=1}^{\infty} c_i n^i \tag{3.59}$$

(usually truncated in our approach to the second order, having thus the Morse potential shape) optimized to reproduce the close interaction regions, and $s(r_i)$ is some kind of sigmoid function acting as continuous switching function satisfying thus continuity on the whole function domain.

However, neither the intermolecular distance R nor any of the involved intramolecular ones r can be taken as a single appropriate progress variable to pivot the switching between different channel oriented formulations of the interaction (not only between two different arrangements but also between long-range and strong interaction regions). For this purpose, one has to resort to a smooth and continuous adaptable combination of coordinates (such as the polar formulation of the BO coordinates [197, 198]).

To exemplify the concept, a cut of the MF1 PES [199] corresponding to the collinear $[N_2]$ + O_2 → $[N_2]O$ + O with frozen N_2 has been ploted in traditional coordinates r_{O-N} and r_{O-O} in Figure 3.4. $[N_2]$ frozen at the value of 0.71 Å.

As can be seen from Figure 3.4, where the full reactive channel is represented, the shape of the potential energy channel for a nonreactive collision with frozen N_2 and fixed $\phi_{NNO} = \pi$ can be fairly simply described as a one-dimensional diatomic potential function (say a Morse-like function) smoothly evolving as a function of the internuclear distance r_{O-N} up to a certain extent into the close interaction region (and then evolving back). However, when the system approaches the region of closer distances (or one wants to explicitly describe a closer interaction of one oxygen atom with the frozen N_2, individual diatomic internuclear distances are not a continuity variable suited to describe the evolution of the process even if reaction is excluded. For this reason, one has to work out a more suitable progress variable smoothly switching between the two internuclear distances involved in the representation even if limited to a short interval.

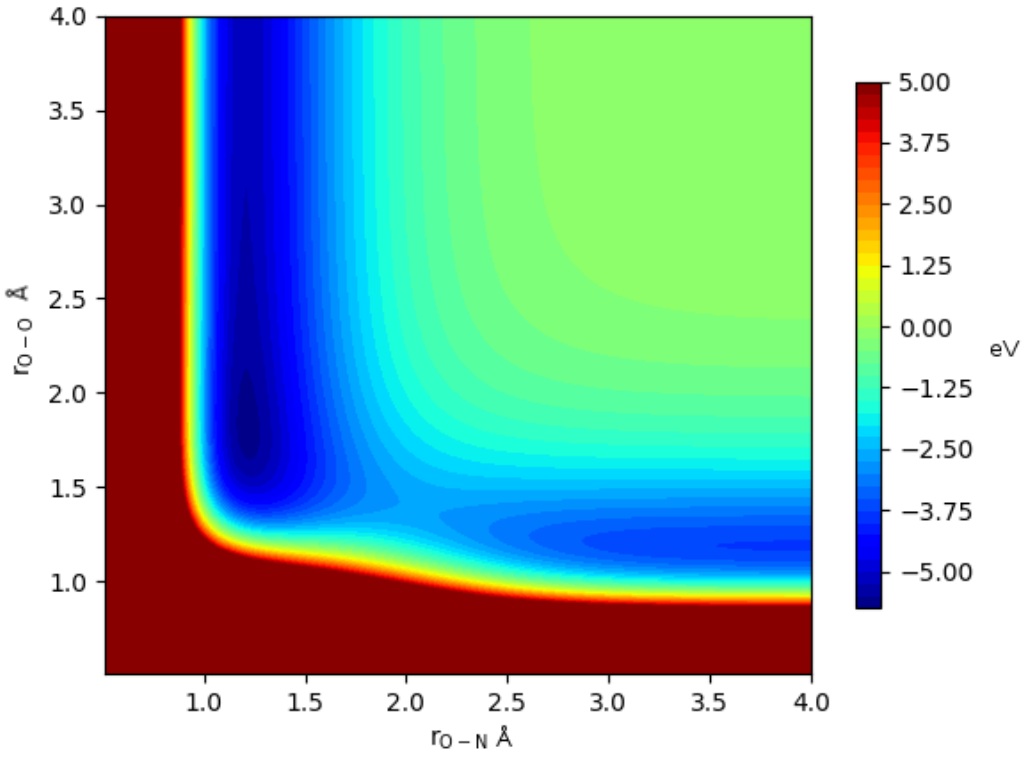

Figure 3.4: cut of the MF1 PES [199] corresponding to the collinear $[N_2]$ + O_2 → N_2O + O with frozen N_2in the traditional inter-atomic radial coordinates in Å

Before starting with the development of the rotating bond order formalism, it is necessary to point out that the considered system is treated as a pseudotriatomic one, considering the non interacting N a mere spectator when focusing on the reaction coordinates. We will hereinafter use the notation AB + C → A + BC. B will the reaction center appearing as subindex in all formalism.

When adopting the just-mentioned internuclear distance representation, a popular way of approaching the problem is to adopt the so-called "rotating Morse oscillator model" in which at fixed A-B-C angle ϕ_B a one-dimensional model potential (usually a Morse-like one), initially coinciding with the entrance channel diatom AB (O–O) and after a proper rotation coinciding with that of the exit channel pseudodiatom BC ($[N_2]$O), is used. The internuclear distance of such diatom is $\sigma_B(r)$ defined as:

$$\sigma_B(r) = [(r^*_{AB} - r_{AB})^2 + (r^*_{BC} - r_{BC})^2]^{1/2} \tag{3.60}$$

and centered on r^*_{AB},r^*_{BC}. The rotation angle μ_B is defined as:

$$\mu_B = \tan^{-1}\left[\frac{r^*_{AB} - r_{AB}}{r^*_{BC} - r_{BC}}\right] \tag{3.61}$$

In Equations (3.60) and (3.61), r_{AB} and r_{BC} are the two internuclear coordinates, and r^*_{AB} and r^*_{BC} are the coordinates of the fixed ϕ_B plane rotation center (set to have values larger (say a multiple) than the corresponding diatomic equilibrium distances. The formalism applies to all the possible processes of the diatom–pseudodiatom. The piecewise nature of the above-defined progress variable μ_B and the associated possible artificial loss of flux between the entrance and exit

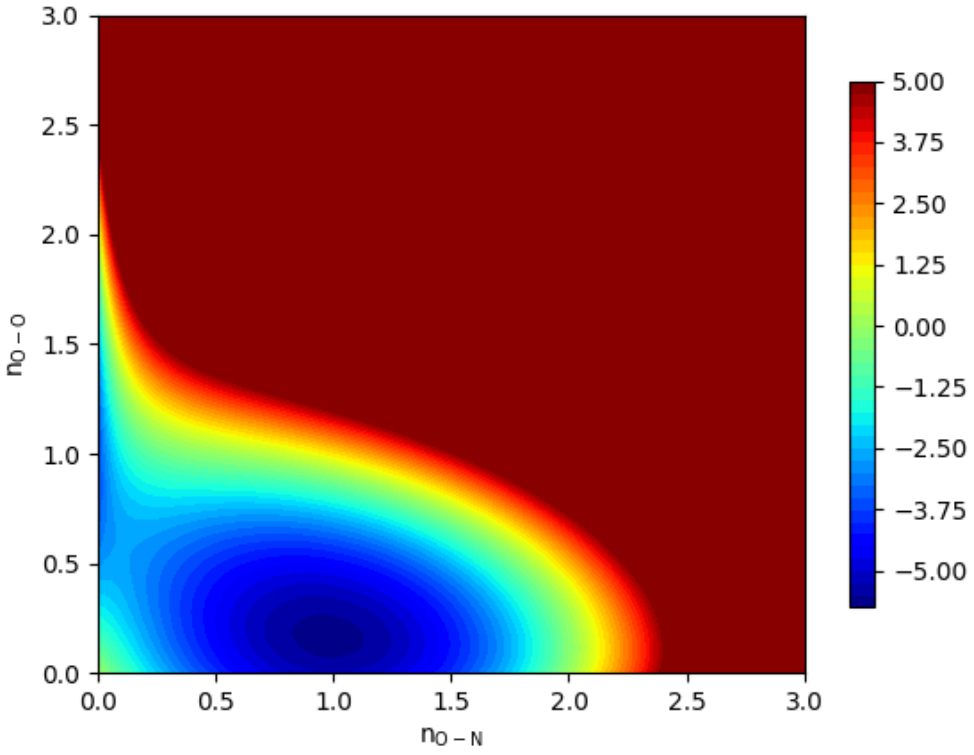

Figure 3.5: Cut of the MF1 PES in the bond-order coordinates

channels prompted the formulation of a better progress variable. A suitable alternative is represented by the already mentioned BO coordinates n_i defined as $n_i = exp[-\beta_{diat}(r_i - r_{ie})]$ for two, three, and four-body systems. [159, 200–204] In BO representations, the physical unlimited space of the internuclear distances is mapped into the finite one of the related bond order coordinates in which the infinity of the internuclear distance corresponds to the zero of the corresponding BO coordinate, while the zero of the internuclear distance corresponds to a positive finite value of the corresponding BO coordinate. The related BO contour maps specific of the O_2 + N_2 diatom–pseudodiatom analysis at fixed collinear collision angle ϕ_O are plotted in Figure 3.5. As apparent from the figure, a natural progress variable taken at different fixed values of the angle ϕ_B formed by the bond of the reactant diatom AB of channel B and that of the chosen product BC, respectively (O-O and O-N), is smoothly and continuously connecting the entrance and the exit channel polar angle ϕ_B defined as

$$\phi_B = \tan^{-1}\left[\frac{n_{AB}}{n_{BC}}\right] \tag{3.62}$$

instead of the previously defined angle $\mu_B(r)$ (defined in terms of the related internuclear distances). The coordinate associated with ϕ_B is the radius ρ_B (the related overall stretching of the system) defined as

$$\rho_B = (n_{AB}^2 + n_{BC}^2)^{1/2} \tag{3.63}$$

An obvious outcome of the BO representation is the formulation of the so-called rotating bond order (ROBO) model potential.[197] In the simplest cases, the ROBO potential has been formulated as a low-order polynomial in ρ_B and ϕ_B as follows:

$$V_B^{BO}(\Phi_B;\phi_b;\rho_B) = D(\Phi_B;\phi_b)P(\Phi_B;\phi_b;\rho_B) \tag{3.64}$$

in which $D(\Phi_B;\phi_b)$ describes the evolution along ϕ_B of the fixed Φ_B minimum energy path (MEP) of the potential energy channel from reactants (at $\phi_B = 0$) to products (at $\phi_B = \pi$). At the same time, $P(\Phi_B;\phi_b;\rho_B)$ describes the radial width of the potential channel at fixed values of Φ_B and ϕ_b that can be given simple polynomial formulations (such as the harmonic or proper anharmonic ones) respectful of the symmetry of the molecular system and easily switchable from a channel to a different one.[205–207] An advantage of adopting the polar BO coordinates formalism (and in particular of the related progress variable ϕ_b consists in the possibility of describing in a continuous way the evolution of the system interaction from the entrance to the exit channel through the deformation of the colliding molecules into transients.

3.2.3 Computational details of scattering process OH + H_2

In this section necessary numeric details of computational simulation of the scattering process OH + H_2 are given by fixing the parameters introduced in Section 3.1.

For the calculations carried out, a grid method was used to represent and integrate the two-dimensional wavefunction (only the two vibrational degrees of freedom are treated quantally), the FFT method was used to evaluate the kinetic energy operator on the wavefunction and the Split-Operator method was used as to carry out wavefunction propagation. Regarding the classical degrees of freedom, the predictor-corrector method was used to integrate the classical equations of motion.

For the calculations to be reliable, convergency tests aimed at optimizing the simulation parameters have been performed. The parameters obtained from the optimization procedure are summarized in Table 3.1. As to the extension of the internuclear distance grid, simulations at different upper and lower grid limits for both r_{OH_c} and $r_{H_aH_b}$ (r_1 and r_2 in the notation of the equations of Section 3.1) have been performed. Tests have been carried out at 0.3, 0.4, 0.5 and 0.6 Å as the minimum value of r_{OH_c} (r_{OH_cmin}) and at 1.5, 2.0, 2.5, 3.0, 4.0 Å as its maximum value (r_{OH_cmax}). Similarly for $r_{H_aH_bmin}$ and $r_{H_aH_bmax}$ tests have been performed at $r_{H_aH_b}$ equal to 0.15, 0.20, 0.3, 0.4 and 0.5 Å and at 3.0, 4.0 and 5.0 Å, respectively. The initial value of the diatoms centers of mass distance, r_3, was also tested. However, it seems that the potential energy surface is accurate up to r_3= 8 Å ca., as also suggested by the fact that fitting points in ref. [120] extend up to ca. 15 bohr. Thus, the value of r_3= 7 Å was chosen as initial parameter for all simulations.

Different Δt values have also been used (0.01, 0.02, 0.04, 0.08, and 0.1 fs) to the end of evaluating the convergence of the treatment within the integration time step. The number of trajectories has also been optimized at the lowest energy of 0.1 eV by checking the convergence of the results. Table 3.1 shows the adopted values of the various parameters.

3.3 Results and discussion

In this section the results of simulations of $OH + H_2$ collisional processes using the quantum-classical (QC) method will be presented. First a benchmark of the method

Parameter	Value
$N_{r_{OH_c}}$	42
$N_{r_{H_aH_b}}$	81
$r_{OH_{cmin}}$, $r_{OH_{cmax}}$, Δr_{OH_c} (Å)	0.40 2.5 0.05
$r_{H_aH_{bmin}}$, $r_{H_aH_{bmax}}$, $\Delta r_{H_aH_b}$ (Å)	0.15 4.0 0.05
r_3 (Å)	7.0
Δt (fs)	0.04
Number of trajectories at each energy value	30,000

Table 3.1: Optimized parameters used for the simulations. $N_{r_{OH_c}}$ and $N_{r_{H_aH_b}}$ represent the number of grid points along r_{OH_c} and $r_{H_aH_b}$ coordinates, respectively; r_3 is the distance between the centers of mass of the diatoms.

by comparing our results with the QC code with the ones obtained by Zhang et al. [120] using a full-quantum (FQ) method, is presented in Section 3.3.1, subsequently, a description of the building process of the improved PES is given in Section 3.3.2, the state-selected reactive probabilities obtained with the Improved PES are presented in Section 3.3.3 and their associated rate coefficients in Section 3.3.4.

3.3.1 Method benchmark

State specific reactive probabilities were calculated for total angular momentum $J = 0$, vibrational quantum numbers $v_{OH} = 0$ and $v_{H_2} = 0$, and rotational angular momentum $j_{OH} = 0$ and $j_{H_2} = 0$. Results were compared with the FQ ones of Chen et al. [120] done at same conditions and changing only initial translational energies (Figure 3.6). The Figure shows the good agreement of the two results which differ for less than 10%, with the quantum-classical (QC) probabilities slightly overestimating the FQ ones in the vibrational ground state for the two diatoms.

A further qualitative analysis can be made by comparing QC results with the experimental ones. The latter show a marked increase of the reaction probability when H_2 is vibrationally excited [208] (specially for $v_{H_2} = 1$ with respect to $v_{H_2} = 0$), whereas no significant change in the reaction rate is observed upon vibrational excitation of OH [209] (for $v_{OH} = 1$ with respect to $v_{OH} = 0$). Indeed, our results confirm the higher efficiency of the initial vibrational excitation of the reactant H_2 in promoting the reaction (see Figure 3.7). The plots of the QC reactive probability (compare crosses ($v_{OH} = 0, v_{H_2} = 0$) with green points ($v_{OH} = 0, v_{H_2} = 1$) and red solid circles ($v_{OH} = 0, v_{H_2} = 2$)) of Figure 3.7) show a significant increase of the reactive probability of the system with v_{H_2}, that is from 0.1 to 0.2 larger than that of the neighbour lower vibrational state in the whole investigated collisional energy range. In contrast, the vibrational excitation of OH from $v_{OH} = 0$ to $v_{OH} = 1$ and $v_{OH} = 2$ has no appreciable effect on the value of the reactive probability of the system: as shown in Figure 3.7, the reaction probability computed for different values of the vibrational quantum numbers of OH are in this case hardly distinguishable from that of $v_{OH} = 0$, in agreement with the experimental results of ref. [209] and the theoretical ones of refs. [210, 211]. In particular, our results also show a very small increase in the reaction probabilities for $v_{OH} = 1$, with respect to $v_{OH} = 0$, at small energies (not appreciable in Figure 3.7). This difference in the reaction probabilities tends to vanish as the energy increases.

The good agreement between QC and FQ approaches for $v_{OH} = v_{H_2} = 0$ and,

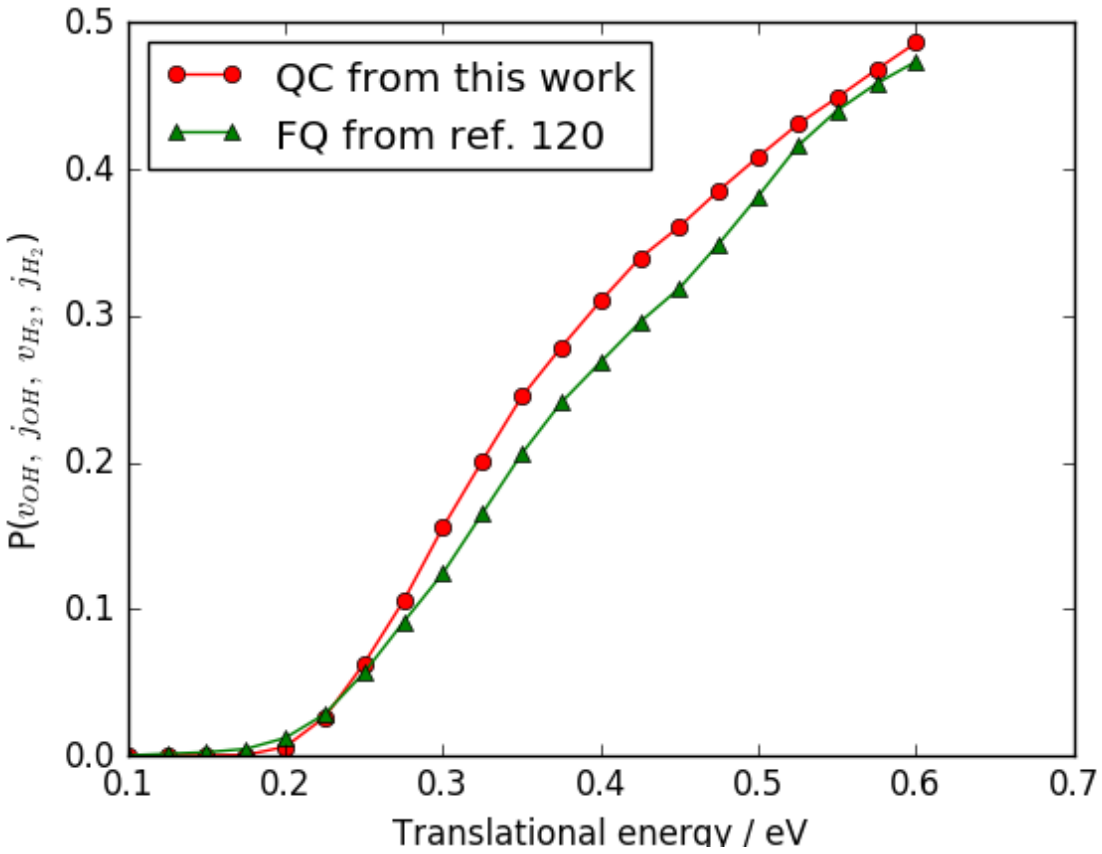

Figure 3.6: State specific ($J = L = 0$, $v_{OH} = v_{H_2} = 0$, $j_{OH} = j_{H_2} = 0$) OH + H_2 → H_2O + H reactive probability plotted as a function of the translational energy (QC results in red, FQ results in green)

qualitatively, between QC results and experiments is a significant test for the present approach, taking into account that the computational effort of these calculations is only slightly larger than quasi-classical trajectory (QCT) methods and that relevant quantum effects (like the zero point energy of the diatoms) are included in the treatment.

Once proven that QC calculations can provide reliable results, we focused our investigation on the understanding of the reaction mechanism. For this reason, we have analyzed the trajectories associated with the QC calculations performed using the same initial conditions of the quantum study. The product H_2O molecule is formed by the binding to OH of one of the hydrogens in which H_2 breaks. This is in agreement with the fact that, as shown in Figure 3.7, an increase of the vibrational excitation of the hydrogen molecule (and, therefore, the stretching of the related bond) is indeed the key factor in promoting reactivity as also observed by other studies [208].

Typically, the trajectories associated with the initial conditions of the reactants mimicking those of quantum calculations follow two qualitatively different paths to reactions. The first one (see Figure 3.8, upper panel) is consistent with a direct mechanisms in which H_2 dissociates and one of the dissociated H sticks on the OH molecule while the remaining hydrogen atom flies away. The second one (see Figure 3.8, lower panel) is typical of a long lived intermediate complex forming mechanism that leads to more effective energy redistributions among the various

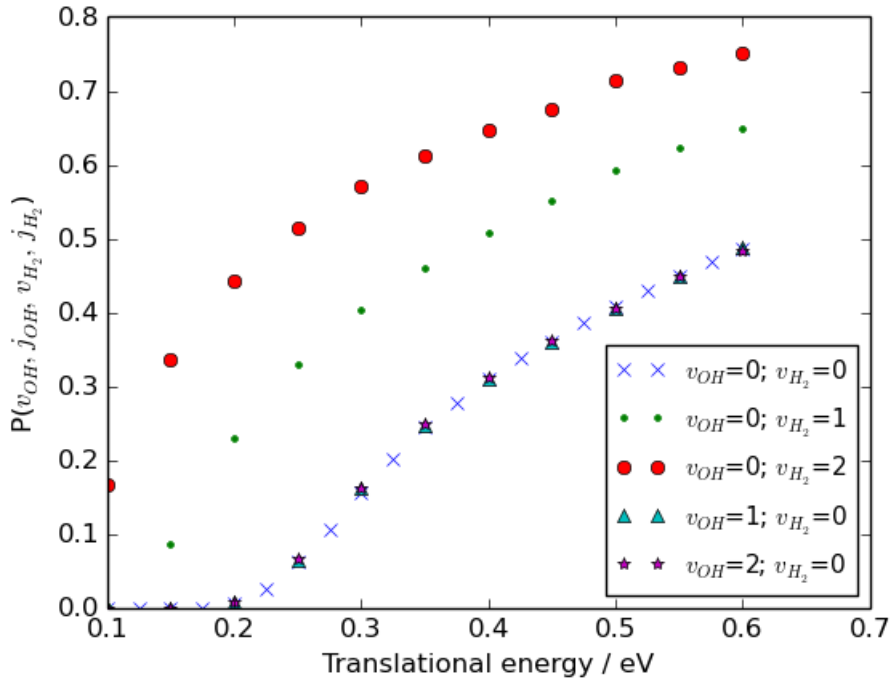

Figure 3.7: State specific ($L = 0$, $j_{OH} = j_{H_2} = 0$) OH + H_2 → H_2O + H QC reactive probability plotted as a function of the translational energy at different initial vibrational levels of the reactants.

degrees of freedom.

Our calculations also allowed to single out an effect that only FQ and QC calculations can spot, while it might go undetected in pure quasi-classical trajectory calculations due to their poor discretization method. This effect is the vibrational excitation of the non reacted OH molecule as a result of the already commented formation of an intermediate long-lived complex. This is clearly shown in Figure 3.8, lower panel, where the quantum expectation value of r_{OH} after collision becomes sensibly larger.

The possibility of producing vibrationally excited OH after collision is confirmed by the calculations of the probabilities for vibrational energy exchange process. An accurate quantitative evaluation of vibration-to-vibration and vibration-to-translation energy transfer cross sections and rate constants would require an initial distance of the centers of mass of the diatoms much larger than 8 Å, which, as already mentioned, seems to be the largest distance at which the PES is still reliable. Indeed the long-range part of the potential is known to play a crucial role in these non reactive events, particularly when resonant or near resonant processes are concerned. Because of this, in the present section only qualitative considerations about the diatoms vibrational population distribution after non reactive collisions are going to be considered.

Figure 3.9 shows the QC state-to-state non-reactive probabilities corresponding to initially state-selected vibrational states as a function of the final vibrational level at fixed reactant collisional energies. In every case vibrationally elastic collisions are largely predominant, and they have been removed from the graphs to better focus on vibrational energy redistribution. Panels referring to the initial ($v_{H_2} = 0$,

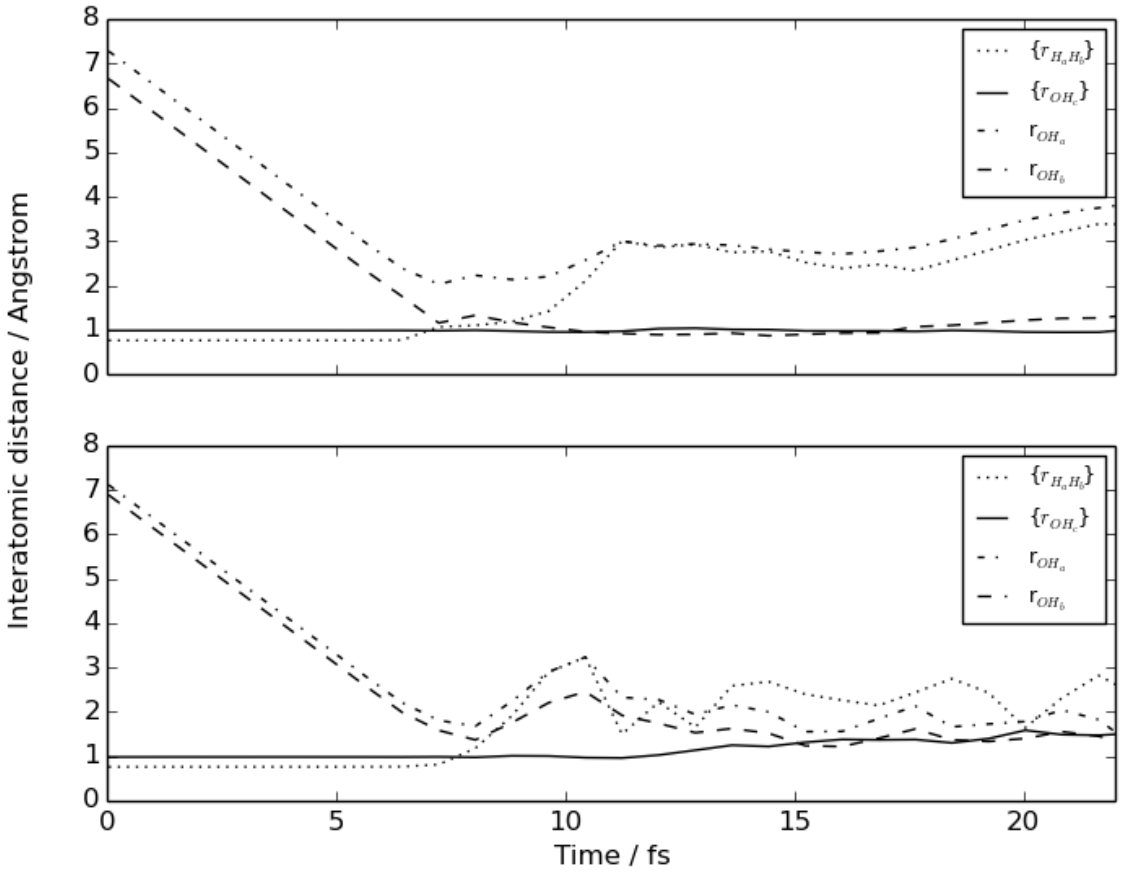

Figure 3.8: Plot of a direct (upper panel) and intermediate forming (lower panel) trajectories, for J=0, v_{OH}=0, v_{H_2}=0 at a collisonal energy of 0.3 eV. Classical values of r_{OH_a} (dashed-dotted line), r_{OH_b} (double dashed-dotted line) and quantum expectation values of $\{r_{H_aH_b}\} = \frac{\langle\psi|r_{H_aH_b}|\psi\rangle}{\langle\psi|\psi\rangle}$ (dotted line) and $\{r_{OH_c}\} = \frac{\langle\psi|r_{OH_c}|\psi\rangle}{\langle\psi|\psi\rangle}$ (solid line) are reported as a function of propagation time.

$v_{OH} = 0$) state show that population of the first excited vibrational states only occurs, with very small probability, when the initial translational energy is larger than $\Delta E = E_{v=1} - E_{v=0}$, being $\Delta E = 0.516$ eV for H_2 and $\Delta E = 0.442$ eV for OH.

State-to-state probabilities for initially excited states show that the exchange of one quantum of vibrational energy between the collision partners is more likely for $(v_{H_2} = 1, v_{OH} = 0) \rightarrow (v_{H_2} = 0, v_{OH} = 1)$ than for $(v_{H_2} = 0, v_{OH} = 1) \rightarrow (v_{H_2} = 1, v_{OH} = 0)$ process, and even more so for $(v_{H_2} = 2, v_{OH} = 0) \rightarrow (v_{H_2} = 1, v_{OH} = 1)$ with respect to $(v_{H_2} = 0, v_{OH} = 2) \rightarrow (v_{H_2} = 1, v_{OH} = 1)$ process. This might be an indication of a tendency to the depletion of excited H_2 and an increase of excited OH in the final states. Furthermore, at higher translational energies vibrationally excited H_2 is more prone to react and, thus, is much less efficient in populating higher vibrational levels.

In Figure 3.9 it also can be seen some strange results. Namely, being $v_{OH,0}$ the initially state-selected OH vibrational level, the higher population of the $v_{OH,0} + 2$ than $v_{OH,0} + 1$ for initial states $v_{OH,0} = 0, 1, 2$ or the higher population of vibrational excited states at lower translational energy (at 0.1 eV higher than 0.3 and 0.6 eV) like in the case $(v_{H_2} = 2, v_{OH} = 0) \rightarrow (v_{H_2} > 2, v_{OH} = 0)$. This suggests some unphysical behaviour of the PES.

3.3.2 The long-range potential-improved PES

In Section 3.3.1 we successfully tested the ability of the QC method to simultaneously calculate probabilities for reactive OH ($^2\Pi$) + H_2 ($^1\Sigma_g^+$) $\rightarrow$ H_2O (X^1A_1) + H(^2S) and vibrational energy transfer events in OH ($^2\Pi$) + H_2 ($^1\Sigma_g^+$) collisions using the Potential Energy Surface (PES) developed by Zhang and coworkers (CXZ) [120]. The CXZ PES is based upon more than 17000 accurate ab initio points interpolated using a neural network procedure ensuring a good description of all reaction channels and a computationally fast evaluation of the interaction for the relevant molecular geometries. Indeed the CXZ PES allowed us to run a large number of QC calculations using much less computer time compared with previous reported PES's for the same system.

The production of reliable probabilities and cross sections for vibration-to-vibration (VV) or vibration-to-translation (VT) processes requires large enough initial distances between the colliding partners. By using the CXZ PES fitted to a set of ab initio points not extending beyond an initial separation of the colliding partners larger than 15 a_0 some of the transition probabilities computed for inelastic scattering of vibrationally selected reactants showed either unconverged or unusual properties (this is the case of probabilities of populating vibrational excited states at small translational energies (even smaller than the required vibrational quantum of energy) or for two OH vibrational quanta excitations (see Figure 3.9)

In order to find a rationale for the mentioned anomalies, we analyzed in detail the shape of the CXZ PES at different selected configurations (collinear (I), perpendicular (L), parallel (Z or H), etc.) of the colliding diatoms, as reported in Figure 3.10 (and in Appendix A for additional configurations) in black line. The particularly evident anomaly of the CXZ PES is the fact that it shows unphysical features at large R values: some configurations (like H and X, or the collinear one when the H atom of OH is oriented towards H_2) show an unphysically attractive and others (the perpendicular L configuration, the collinear one when the O atom of

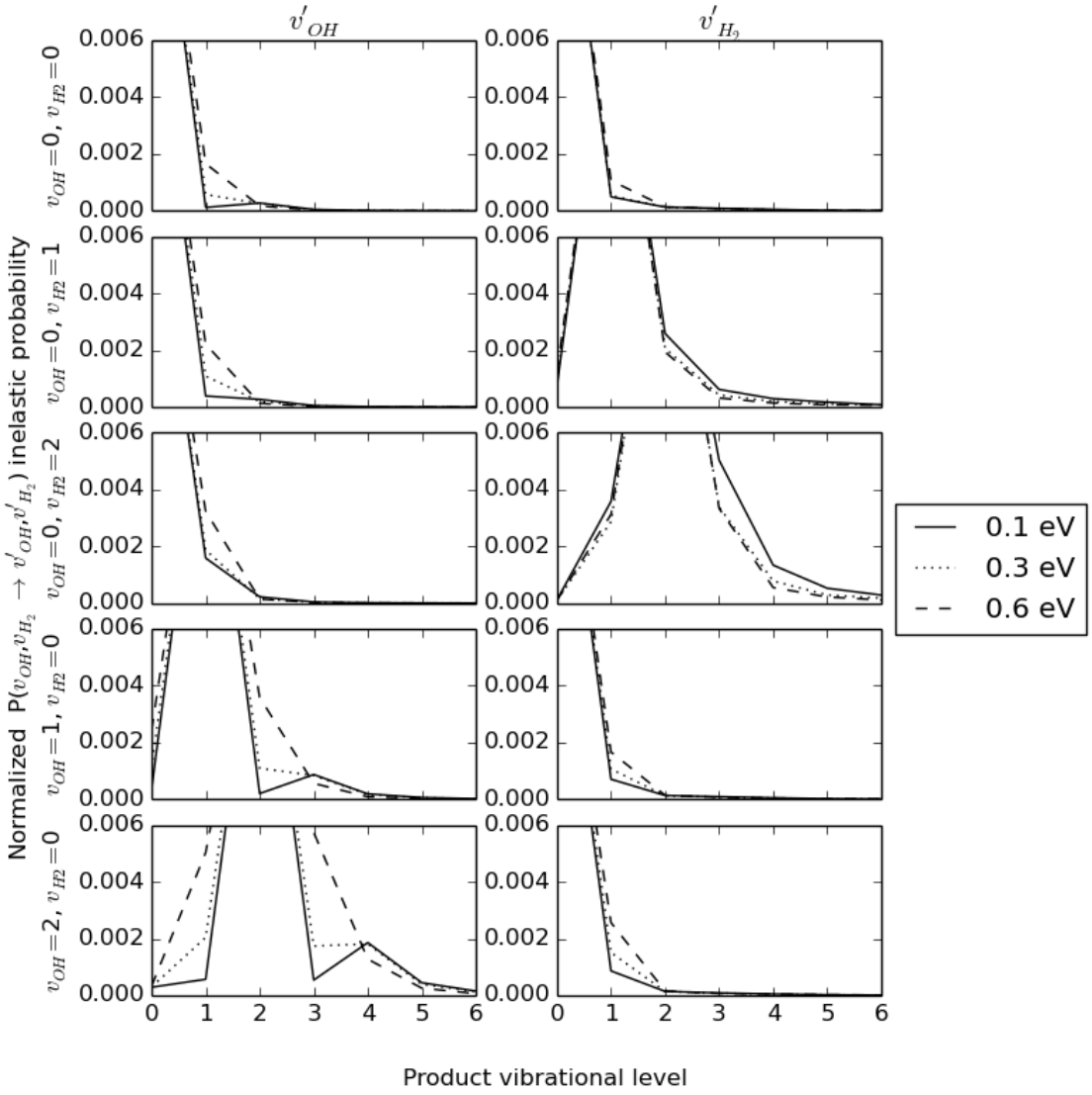

Figure 3.9: Non reactive state (v_{OH}, v_{H_2}) to state (v'_{OH}, v'_{H_2}) probabilities plotted as a function of one of the product vibrational level at E_{tr}=0.1 eV, solid line, E_{tr}=0.3 eV, dotted line, and E_{tr}=0.6 eV, dashed line.

OH is oriented towards H_2, etc.) an unphysical repulsive behaviour at the beginning of the long-range to subsequently steadily grow again, which might be the result of extending the neural network procedure for fitting points in regions were ab-initio points are scarce or even absent.

Such misbehavior is striking at values of R larger than 7 Å, but is non negligible starting from values of R of 6 Å ca. and that, rather than the fact that calculations for inelastic probabilities were initiated at a value of 8 Å, probably too small to obtain accurate enough results, is likely to be a reason for some of the strange results obtained in the analysis of inelastic scattering probabilities.

Although the CXZ PES is proven to give unphysical outcome for long-range potential thus preventing from running simulating events at initial conditions further than $\sim$ 8 Å, the results obtained considering the $J = L = 0$, $v_{OH} = v_{H_2} = 0$, $j_{OH} = j_{H_2} = 0$) OH + H_2 → H_2O + H are not only in very good agreement with

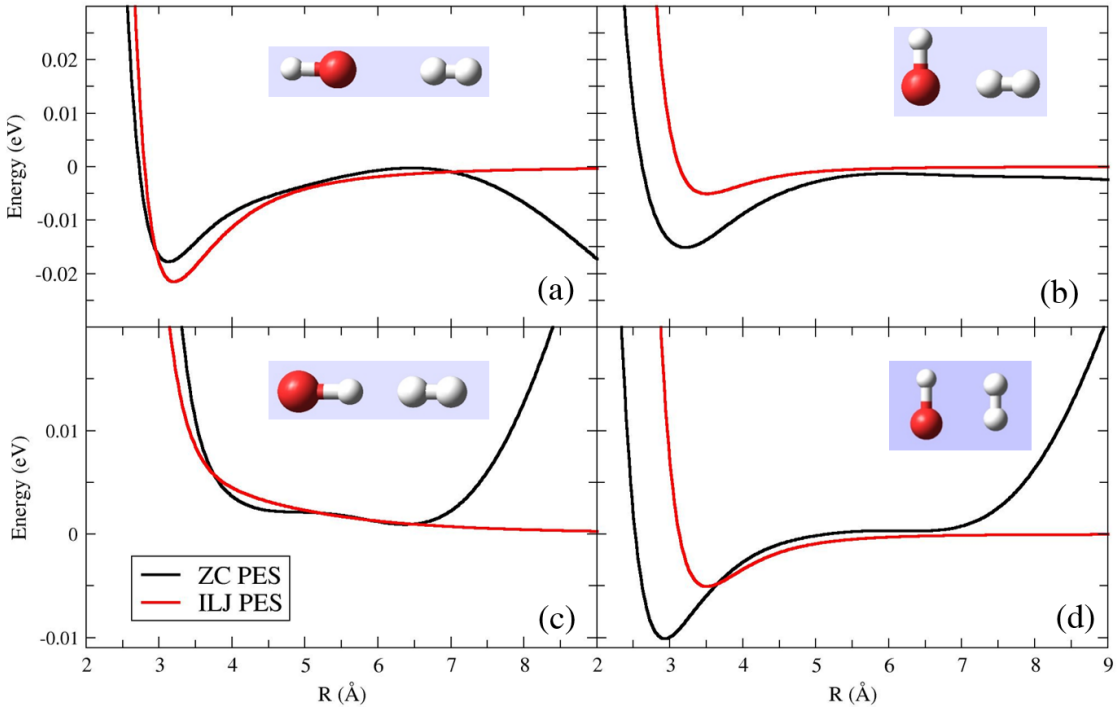

Figure 3.10: Plot of the CXZ potential (black line) and the non-reactive ILJ potential (red line) for collinear configurations (panels a and c), L configuration (panel b) and parallel H geometry (panel d) as a function of the intermolecular distance.

Parameter	**Value OH**	**Value H_2**
D_e (eV)	4.6261	4.74787
a (1/Å)	0.970	0.742
r_e (Å)	2.177	1.946

Table 3.2: Morse parameters for OH and H_2

the ones obtained previously by other potential energy surfaces, but also resulting in a very computationally efficient PES.

We did overcome this problem, while keeping the advantage of relying on the accuracy and ease of calculation of the CXZ PES at short distances, by assuming independent diatoms at long-range and switching to the formulation of the potential shown in Section 3.1.2 where potential is split in sum of $V_{intra} + V_{inter}$, formulating typically the first term as a Morse potential Equation (3.2) and the second one as sum of electrostatic interaction Equation (3.4) plus van der Waals interaction through the ILJ potential Equations (3.5) and (3.6). Actual parameters for both are given in Tables 3.2 and 3.3

The behaviour of this non reactive potential is also shown in Figure 3.10 and Appendix A for the same selected configurations and it generally shows a less attractive well than the reactive PES. The mixed CXZ at short range and ILJ at long-range (CXZILJ) PES is formulated according to the following scheme:

- at $R \leq 5$ Å the original reactive CXZ PES is used (V_{CXZ})
- at $R \geq 7$ Å the non reactive ILJ PES is used (V_{ILJ})

Parameter	Value
p_{OH}	0.3446
Q_{H_2}	0.1355
R_m (Å)	3.506
ε (eV)	0.00505

Table 3.3: long-range potential parameters for H_2+OH

- for 5 Å $< R <$ 7 Å the following smoothly switching sigmoid function is used to combine the CXZ and ILJ formulations of the potential:

$$V_{CXZ-ILJ} = V_{CXZ}\frac{1}{1+e^{-4(R-6)}} + V_{ILJ}\left(\frac{1}{1+e^{4(R-6)}}\right) \tag{3.65}$$

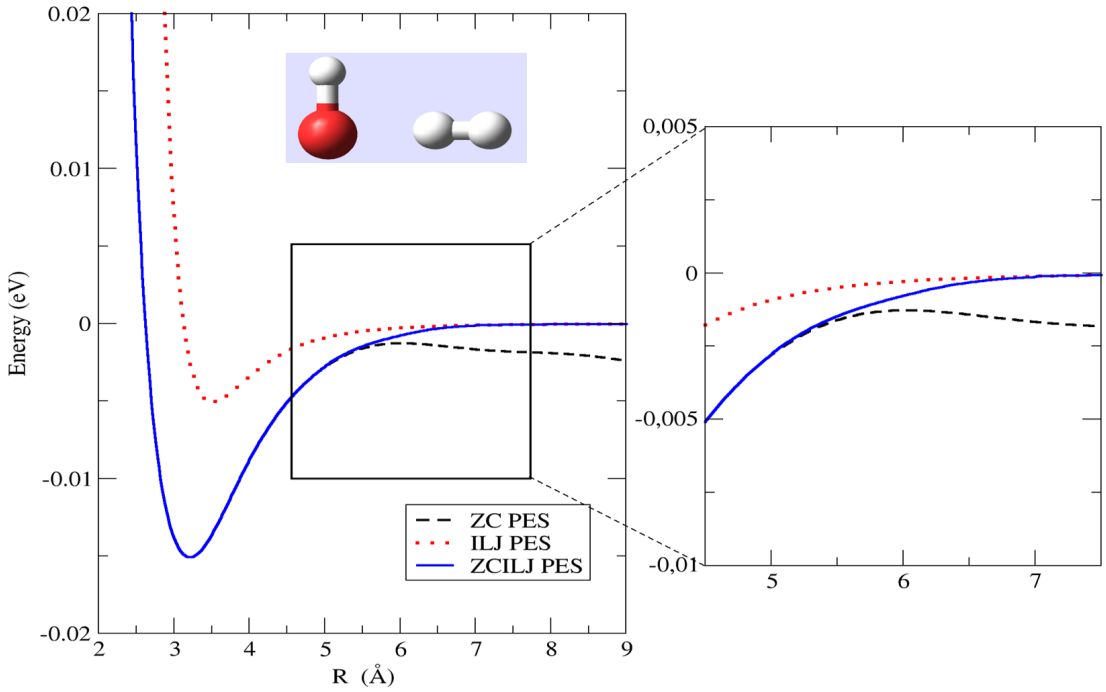

Figure 3.11: long-range corrected potential (Blue solid line) for the X configuration of the approaching diatoms, compared with the CXZ PES (Black dashed line) and the ILJ PES (Red dotted line). The intermediate range region where switching takes place between the two schemes is zoomed in the figure.

Figure 3.11 shows the behavior of the three PES's (CXZ, ILJ and the combined CXZILJ) for the L configuration (all other geometries are reported in Appendix A). It is worth noting that in the intermediate switching region the potential values of the two original PES's are quite close, which is likely to guarantee that both provide a reliable description in that region, which starts to be dominated by non covalent interactions, and a smooth behavior for the CXZILJ PES.

We have then calculated several QC reactive and inelastic scattering probabilities and rate coefficients using the CXZILJ PES starting with an initial separation distance between the colliding diatoms of 15 Å. The results are compared with experimental data and with the outcomes of the calculations performed on the CXZ

PES to highlight and rationalize the inclusion of a corrected long-range tail in the potential.

3.3.3 Initially state selected probabilities

3.3.3.1 Initially state selected reactive probabilities

Reactivity is thought to be mainly driven by short range interactions, so that the vast majority of the potential energy surfaces aim to describe reactive events seldom extend up to initial distances of the colliding partners larger than 8-10 Å and so do nuclear dynamics treatments. Indeed, when we compare probabilities for the reaction OH(v=0)+H_2(v=0) → H_2O+H (Figure 3.12) at null rotational and angular momentum for the diatoms, $j_1 = j_2 = l = 0$, the long-range tail on the potential seems to produce a negligible effect on reactivity, as differences are well within numerical accuracy.

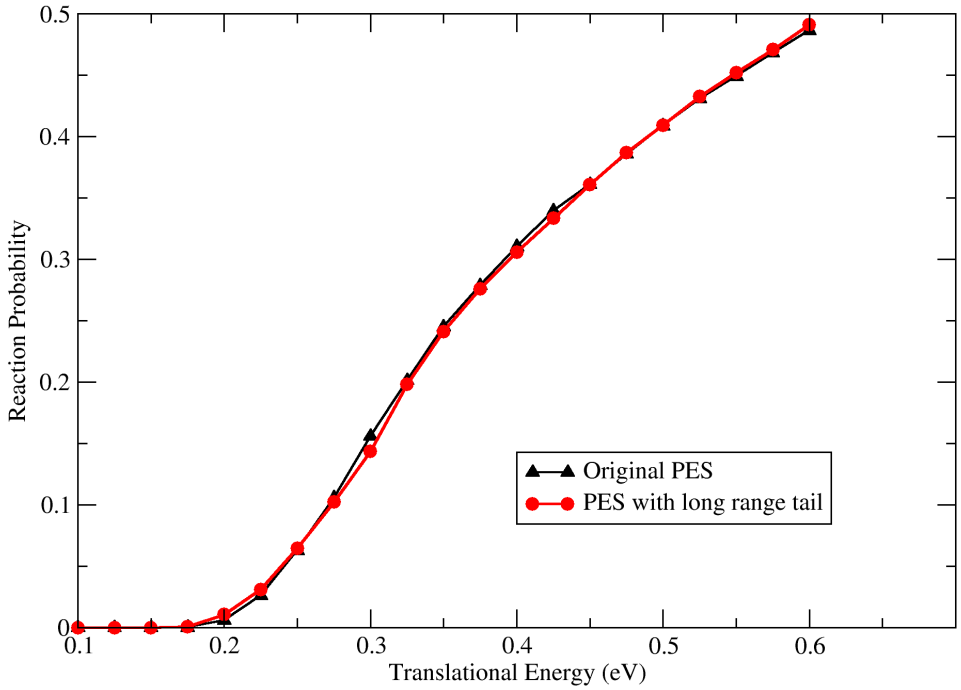

Figure 3.12: Reaction probabilities at $j_1 = j_2 = l = 0$ for the reaction OH(v=0)+H_2(v=0) → H_2O+H calculated with the uncorrected potential energy surface of ref. [120] (black triangles) and with that corrected for the long-range contribution (red circles).

Things change when we examine probabilities for vibrationally excited states of OH and H_2. Figure 3.13 shows that upon increasing vibrational excitation of the OH bond the long-range corrected PES provides smaller reaction probabilities for all values of initial translational energy.

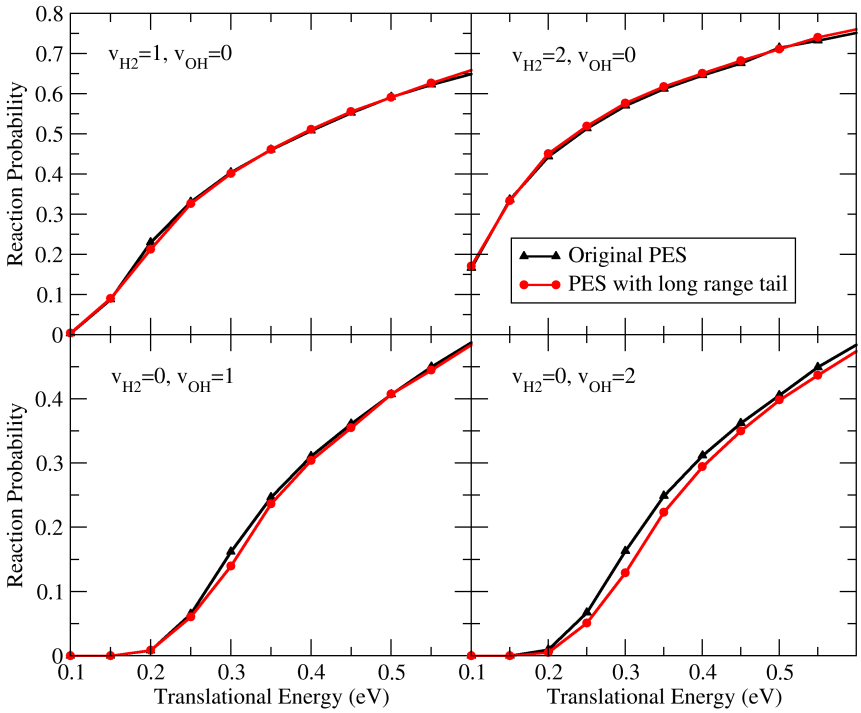

Figure 3.13: Reaction probabilities at $j_1 = j_2 = l = 0$ for the reaction OH+H_2 $\rightarrow$ H_2O+H with the reactants in different excited vibrational states calculated with the uncorrected potential energy surface of ref. [120] (black triangles) and with that corrected for the long-range contribution (red circles).

The difference between the values obtained with the two surfaces on the other hand is hardly noticeable when $v_{H_2} \leq 2$. However, for $v_{H_2} = 3$ (Figure 3.14) the discrepancy is clearly visible at small values of the translational energy. It is worth noting that in this case the trend is opposite to that of vibrationally excited OH, i.e. the long-range corrected surface gives larger reaction probabilities.

Reaction probabilities for vibrationally excited states of both diatoms, $v_{OH} = v_{H_2} = 1$, were also compared (Figure 3.15) to find that there is a clearly visible trend of larger reaction probabilities for the long-range corrected potential. In this case the difference grows with the translational energy.

In order to investigate whether this difference is solely due to the introduction of the long-range correction or also to the use of a larger initial distance R between the centers of mass of the reactants, we repeated the calculation with the LR-corrected PES with a starting value of $R = 8$ Å for the cases OH($v = 0$)+H_2($v = 2$) and OH($v = 2$)+H_2($v = 0$). In the first case (Figure 3.16 upper panel) there is no sensible difference in the results between the original PES and the LR-PES, so no information can be drawn. In the OH($v = 2$)+H_2($v = 0$) case, however, (Figure 3.16 lower panel) shows that at small translational energy values ($E \leq 0.5$ eV), where differences in the reaction probabilities are more marked, their lowering is solely to be ascribed to the introduction of long-range effects in the potential description, whereas small differences at large values of the classical translational energy depend on the use of a larger (15 Å instead of 8 Å) initial separation distance.

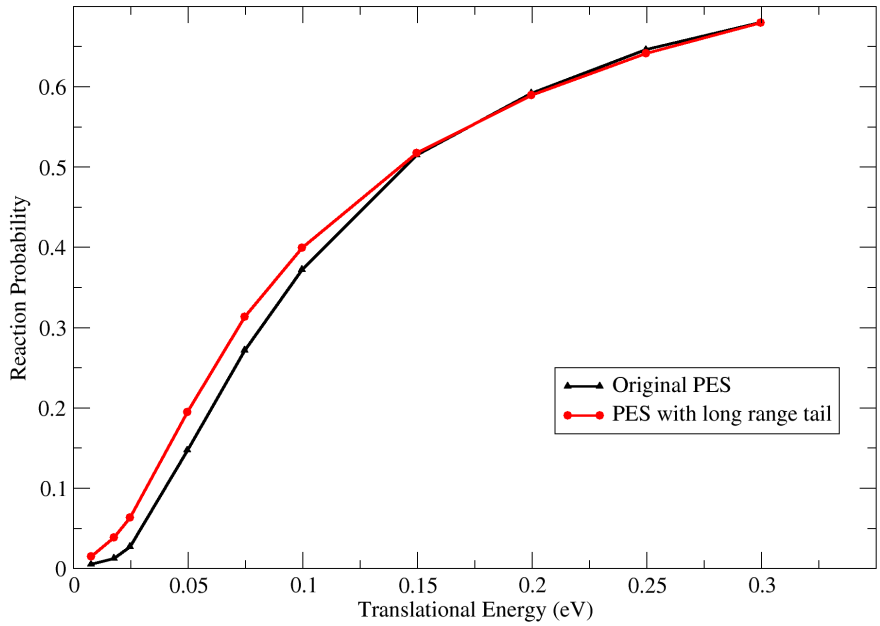

Figure 3.14: Reaction probabilities at $j_1 = j_2 = l = 0$ for the reaction OH($v = 0$)+H_2($v = 3$) $\rightarrow$ H_2O+H calculated with the original potential energy surface of ref. [120] (black triangles) and with that corrected for the long-range contribution (red circles).

It can be noted that comparison of reaction probabilities for null total angular momentum calculated within the present approach and a FQ mechanical method [120] gave larger values for the mixed QC treatment. Though this could simple inferring, one could thus expect that a FQ dynamics method together with the long-range corrected PES might lead to an excellent agreement also from the quantitative viewpoint.

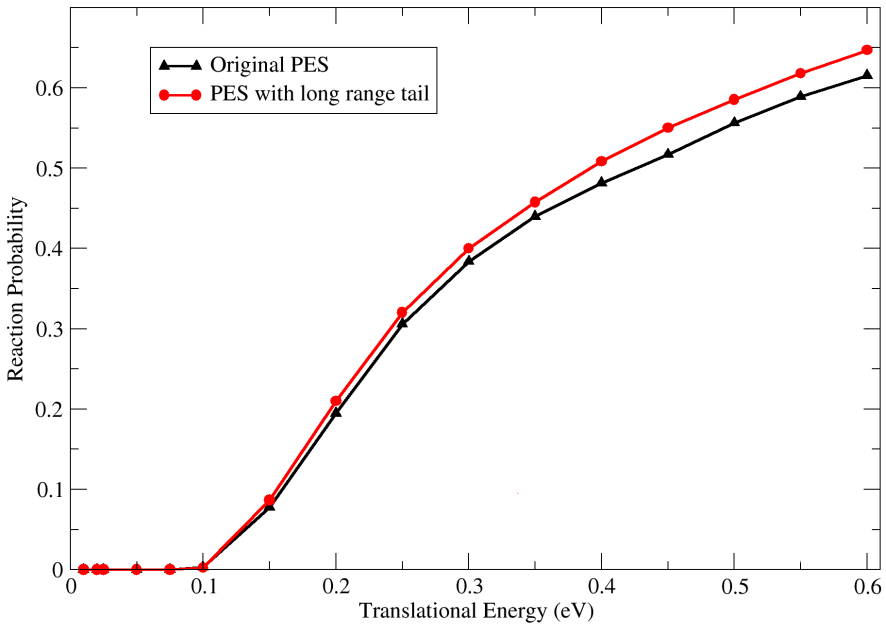

Figure 3.15: Reaction probabilities at $j_1 = j_2 = l = 0$ for the reaction OH($v = 1$)+H_2($v = 1$) $\rightarrow$ H_2O+H calculated with the original potential energy surface of ref. [120] (black triangles) and with that corrected for the long-range contribution (red circles).

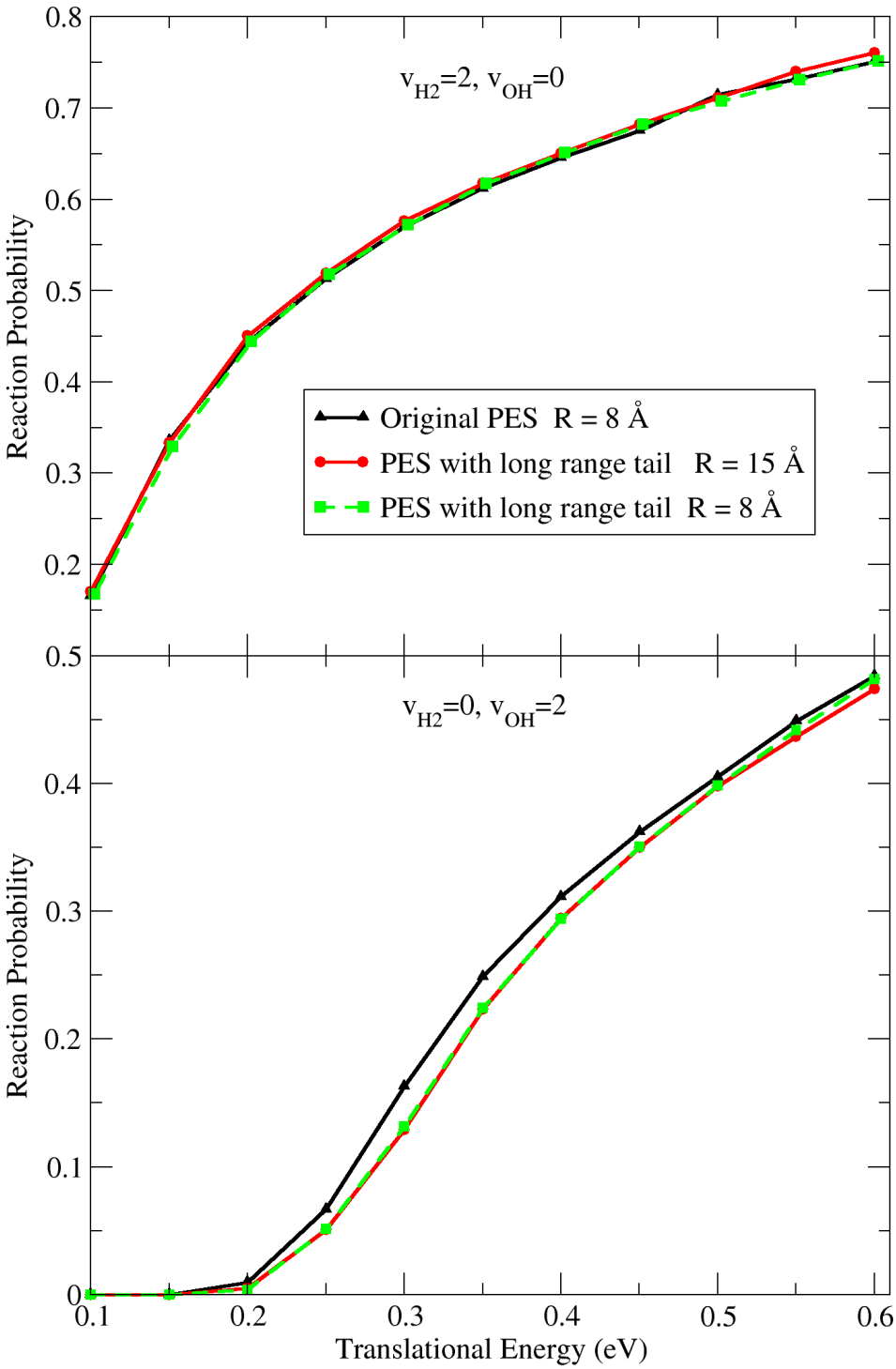

Figure 3.16: Reaction probabilities at $j_1 = j_2 = l = 0$ for the reaction OH($v = 2$)+H_2($v = 0$) $\rightarrow$ H_2O+H calculated with the original potential energy surface of ref. [120] (black triangles) starting at R= 8 Å, with that corrected for the long range contribution (red circles) starting at R= 15 Å, and for the same long-range corrected PES starting at R= 8 Å.

3.3.3.2 Initially state selected non-reactive probabilities

The CXZ-ILJ PES allowed running calculations with initial conditions suitable for a non-reactive analysis ($R > 15$ Å). Figure 3.17 shows the population of final vibrational levels of non-reactive collisions by comparing the results obtained for the trajectories calculated using of both the old CXZ PES (dotted line) and the improved CXZ-ILJ one (solid line) at a value of the classical energy of 0.1 eV and $j_{OH} = j_{H_2} = 0$. It can be seen that the unphysical behavior first presented on Figure 3.9 is not present anymore. Inelastic probabilities follow a decreasing population trend from the nearest levels to the elastic collision towards the further ones. The trend observed on Figure 3.9 for which the transition $(v_{H_2} = 0, v_{OH} = 2) \rightarrow (v_{H_2} = 0, v_{OH} > 0)$ happend in a major extent for low values of classical energy than for the high values $(P_{(v_{H_2}=2, v_{OH}=0)\rightarrow(v_{H_2}>2)}(E_{cl} = 0.1eV) > P_{(v_{H_2}=2, v_{OH}=0)\rightarrow(v_{H_2}>2)}(E_{cl} = 0.6eV))$.

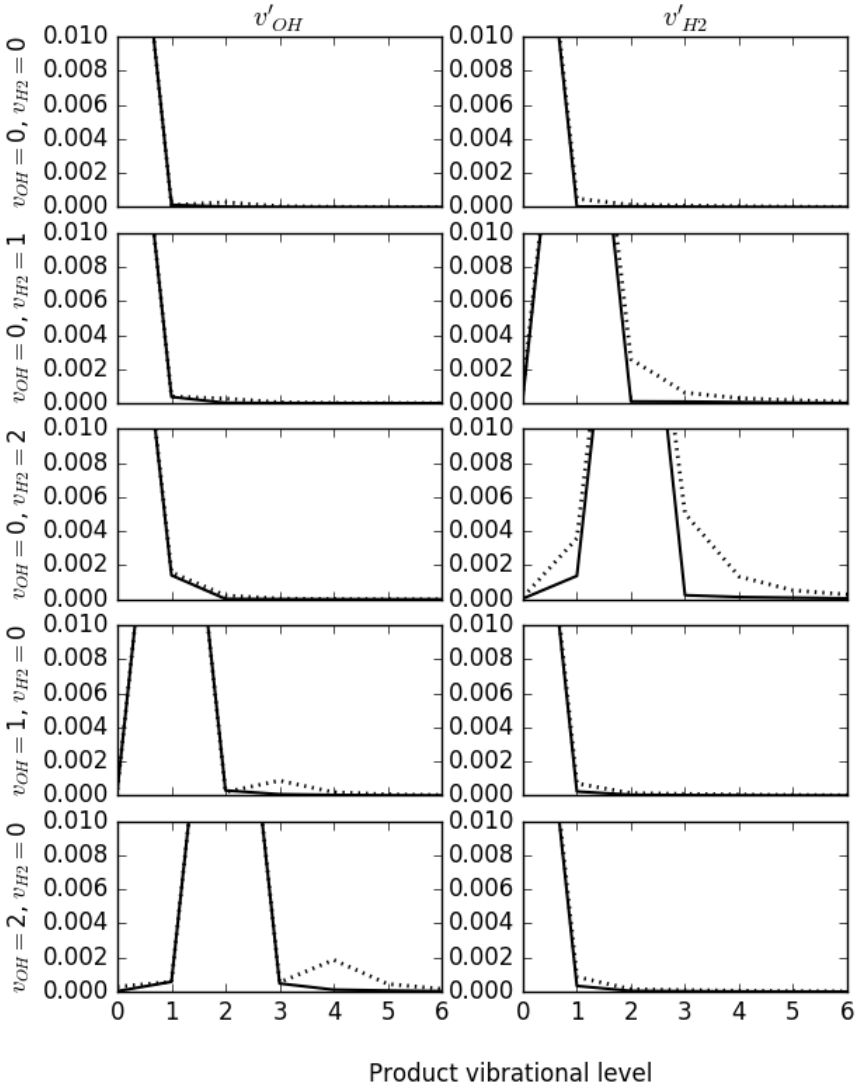

Figure 3.17: Population of final vibrational levels of non-reactive collisions for CXZ PES (dotted line) and the improved CXZ-ILJ one (solid line) at a value of the classical energy of 0.1 eV and $j_{OH} = j_{H_2} = 0$

3.3.4 Computed rate coefficients

The method gives the opportunity to calculate initially state-selected probabilities and rate constants from averaged cross sections as described in Section 3.1.6. In the following, we will examine the effect of introducing the long-range potential correction on all these quantities for both reactive scattering and vibrational energy transfer in inelastic collisions.

In order to perform our investigation 30000 trajectories were propagated for initially state-selected probabilities while 50000 trajectories were needed to reach convergence for averaged cross sections. Cross sections were calculated at 25 different values of initial classical energies ranging from 80 cm^{-1} and 15000 cm^{-1} so to be able to work out the value of the rate coefficient for a wide range of temperatures. For this purpose initial random values for the classical variables were used, with the exception of the initial distance between the diatoms centers of mass, R. In our calculations the value of R was set at $R = 15$ Å that was found to ensure that long-range effects are correctly taken into account for vibrational energy transfer.

When calculating rate coefficients, random values of initial rotational and angular momentum quantum numbers are considered, compatible with the total available classical energy for the classically treated degrees of freedom.

We calculated rate coefficients at different initial values of the diatoms vibrational quantum numbers using the two surfaces. Rate constants for the reactants in their vibrational ground state are reported in Figure 3.18 and compared to experimental data in the temperature ranges 100-400 (panel a) and 400-1100 K (panel b).

As shown by the upper panel of the figure, ZCILJ results exhibit, with respect to the the CXZ ones, a better agreement with the experiment in the 400-1100 K interval of Temperature.

However a proper rationalization of the dynamical behavior of the system and a proper study of the effect of introducing a realistic long-range potential energy can only be performed by analyzing the behavior of state specific probabilities and cross sections.

3.4 Conclusion and outlook

In this chapter we used the quantum-classical technique in order to perform a detailed state-to-state study of the OH + H_2 scattering process and to obviate the heavy computational demand associated with the use of FQ approaches. Furthermore, we exploit the fact that we have been able to gain almost fifty times in speed by running in parallel on a cluster of 48 processors. This has been made possible both by the largely decoupled nature of the classical mechanics component of the QC code and by the compactness of its quantum one that makes the code highly distributable. Our calculations led to an excellent agreement between FQ and QC results. The QC calculations provide a clear evidence for the fact that there exist two different reactive mechanisms for the OH + $H_2 \rightarrow H_2O$ + H reaction: the first one proceeding through a direct attack of the H atom originating from the dissociation of H_2 and a second one forming a long lived complex in which the two H atoms play a longer living interchange of energy among the different degrees of freedom. The two mechanisms also offer a rationale for understanding why the behavior of non reacted H_2 is mostly vibrationally adiabatic (the largest fraction of vibrationally

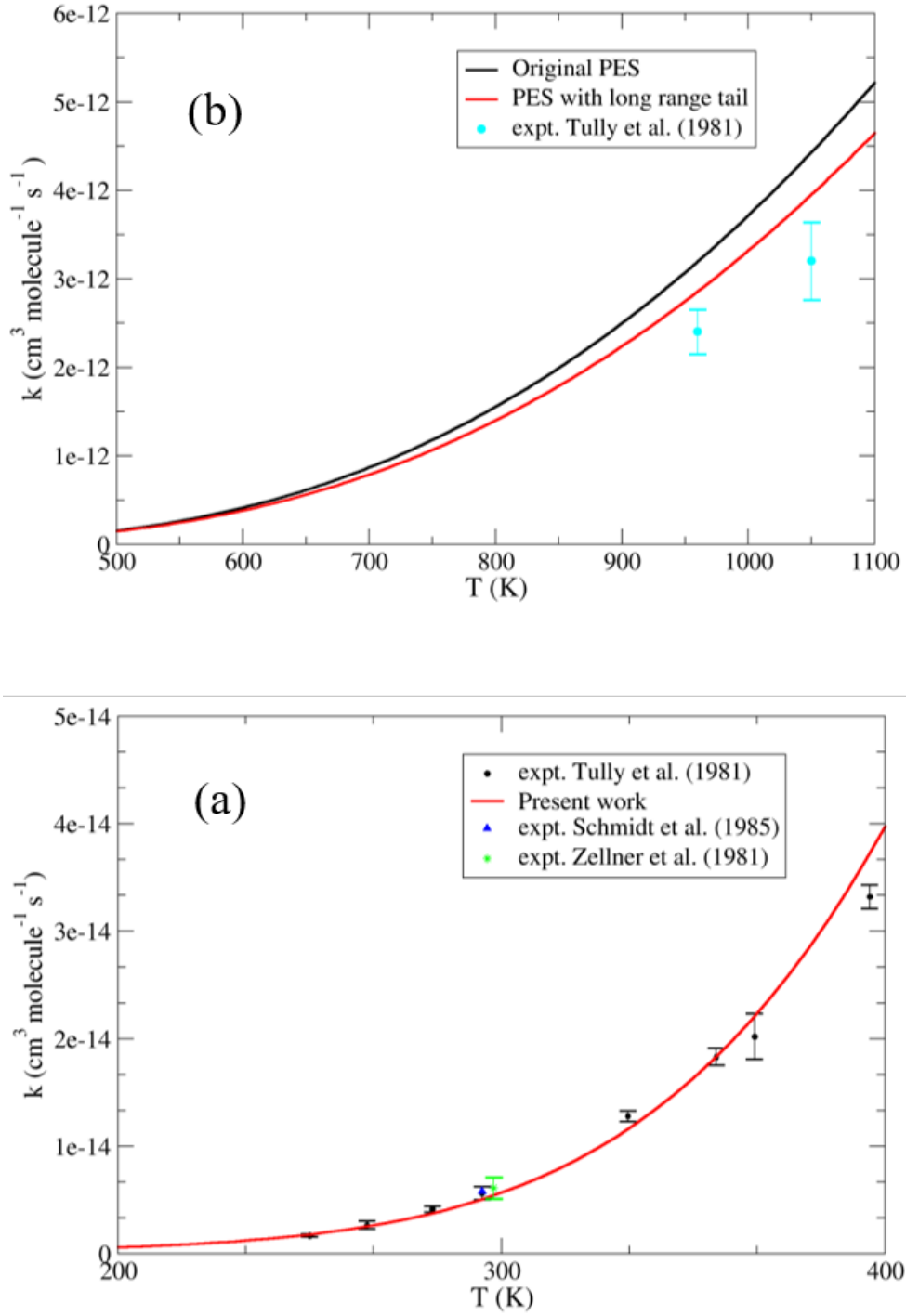

Figure 3.18: Rate coefficients for the reaction OH($v = 0$)+H_2($v = 0$) $\rightarrow$ H_2O+H calculated with the original PES [120] (black line) and Improved PES (red line) in the temperature range 200-400 K (panel a) and 500-1100 K (panel b). Experimental results [208, 212, 213] are also reported for comparison.

excited H_2 ends up by reacting, as shown also by the fact that vibrational excitation of H_2 significantly increases reactivity), while the final vibrational distribution of non reacted OH shows a tendency to give higher vibrational energy distributions. Calculations on internal energy redistribution processes upon non reactive collisions have also demonstrated that the QC code can be effectively used to investigate quantum effects in inelastic scattering. However, in order to get reliable results in this sense, the potential energy surface has to take into account long-range effects, which are essential to accurately evaluate the exchange of vibrational quanta of energy. To this end studies, beside being extended to include larger collision energies and higher vibrational excitations and to calculate averaged quantities so to allow the computation of the relevant rate constants, have been directed on the investigation of how the nature of the potential, and particularly the introduction of a long-range tail to the present PES, affects both the reactive and inelastic energy exchange processes.

Chapter 4

DFTB study of ruthenium clusters

Ruthenium is the metal with the largest activity and selectivity to catalyze the methanation of carbon dioxide. Due to its high cost an optimization of the surface/volume relation is necessary to make a ruthenium-based catalyst be economically competitive against the cheaper nickel-based ones. Nanoparticles indeed possess the largest surface/volume ratio allowing different polymorphs to coexist in a small energy windows offering surface lattices different from the bulk material, and thus leading to new possibilities in their role as catalysts of the carbon dioxide methanation. The study of the catalytic activity of such systems (composed of hundreds if not thousands of atoms) via molecular dynamics, is computationally too demanding for wavefunction methods, and even DFT, to obtain the system's potential energy. Semiempirical methods like Density Functional based Tight Binding (DFTB), hereinafter presented, offer a computaionally cheaper alternative while still acounting for electrons in an explicit way. Indeed it is challenging to see whether a simple model like DFTB, which uses a minimal basis set, and other aproximations in its derivation, is able to catch the peculiarities of ruthenium based materials whose electronic structure is characterized by an equilibrium between electronic delocalization and spin coupling. In the present chapter, indeed the ability of DFTB to accurately reproduce different aspects of ruthenium-based materials in the size range from clusters (n=3-20 atoms) to the bulk, passing though the nanoparticles (n=55-350) is investigated. First the necessary theoretical concepts are introduced in Section 4.1, and the parameters of choice for its implementation are given in Section 4.2. Finally the results coming out from benchmarking the method are presented in Section 4.3.

4.1 Theoretical Methods

Knowing how atoms interact in a system of chemical interest is an essential objective of theoretical chemistry and modeling. Physically this is achieved through resolution of the Schrödinger equation and the obtention of the potential energy of the system and its derivatives respect to the system's chosen coordinates. All current schemes in computational chemistry and modeling need at a certain point the calculation of the potential energy to be able to perform simulations.

There are many methods to calculate the potential energy and its dependence on the system coordinates, these methods can be classified in the following families:

- **Wavefunction methods** model the chemical system of interest by considering a system of electrons under the electrical field generated by a distribution of nuclei. They solve the Schrödinger equation of the electronic system using different levels of approximation to obtain the wavefunction and the energy of the system.

- **Density Functional Theory methods** are based on considering the electronic density of the system, instead of the wavefunction, as the base from which to obtain all the observables of the system. The latter ones formulated as functionals of the electronic density.

- **Semiempirical (Parametrized) methods** make use of certain degree of parametrization (obtained experimentally or computationally with higher level of theory methods) in order to make calculations computationally more efficient while still keeping other quantities calculated from first principles. The Density Functional based Tight Binding (DFTB) method is one of the most accurate methods inside this family. It is derived from DFT, thus preserving the quantum nature of the system and uses parametrization in matrix elements integrals.

- **Force field methods** are based on the expression of the potential energy as analytical sum of different terms. Typically, bond lengths, angles, dihedral angles, improper angles, coulombic interaction and van der Waals interaction, and Embedded Atom Potential (EAM) are often used for metals.

In this section, we will present the first quantum methods.

4.1.1 The Schrödinger Equation and the Born-Oppenheimer approximation

In quantum mechanical systems (e.g. systems formed of atoms) the quantum dynamical behavior is given by the Schrödinger equation:

$$i\hbar\frac{\partial\Psi(t,\mathbf{R},\mathbf{r})}{\partial t} = \hat{\mathcal{H}}\Psi(t,\mathbf{R},\mathbf{r}), \tag{4.1}$$

This equation describes the evolution of the wave function $\Psi(\mathbf{R},\mathbf{r})$ in space and time, where $\mathbf{R}$ represents the coordinates of the nuclei, which are treated as point charges, and $\mathbf{r}$ the coordinates of electrons. $\hat{\mathcal{H}}$ is the Hamilton operator corresponding to the total energy of the system. If the Hamiltonian does not depend on time, it is possible to separate the spatial variables from the temporal ones and the time independent Schrödinger equation is obtained:

$$\hat{\mathcal{H}}\Psi = \mathcal{E}\Psi \tag{4.2}$$

where $\mathcal{E}$ is the total energy of the system. In this equation, the wavefunction $\Psi(\mathbf{R},\mathbf{r})$ depends on the nuclear degrees of freedom $\mathbf{R}$ and electronic ones $\mathbf{r}$.

In a system consisting of K nuclei and N electrons interacting as electrically charged particles, the Hamilton operator has the following form:

$$\hat{\mathcal{H}} = \hat{T}_n + \hat{T}_e + \hat{V}_{nn} + \hat{V}_{ee} + \hat{V}_{en} \tag{4.3}$$

where,

$\hat{T}_n = -\sum_{\alpha=1}^{K} \frac{\hbar^2}{2M_\alpha} \nabla_\alpha^2$ is the kinetic energy operator of the nuclei α where $\hbar$ is the reduced Planck constant, M_α the mass of the α nuclei and ∇^2 the nabla operator evaluating the second derivative with respect to the system's coordinates;

$\hat{T}_e = -\frac{\hbar^2}{2m} \sum_{i=1}^{N} \nabla_i^2$ is the kinetic energy operator of electrons i, with m_i the mass of the i electron;

$\hat{V}_{nn} = \frac{1}{2} \sum_{\alpha \neq \beta}^{K} \frac{Z_\alpha Z_\beta e^2}{|R_{\alpha\beta}|}$ is the potential energy operator of interaction between nuclei α and β having a nuclear charge of Z_α and Z_β times the elementary charge e, respectively and being separated a distance $R_{\alpha\beta}$;

$\hat{V}_{ee} = \frac{1}{2} \sum_{i \neq j}^{N} \frac{e^2}{|r_{ij}|}$ is the potential energy operator of interaction between electrons i and j;

$\hat{V}_{en} = -\sum_{\alpha=1}^{K} \sum_{i=1}^{N} \frac{Z_\alpha e^2}{|R_{\alpha i}|}$ is the potential energy operator of interaction between nuclei α and the electrons i.

By taking the atomic system of units one gets rid of elementary constants in Equation (4.2) and it could be rewritten as:

$$\left\{ -\sum_{\alpha=1}^{K} \frac{1}{2M_\alpha} \nabla_\alpha^2 - \frac{1}{2} \sum_{i=1}^{N} \nabla_i^2 + \frac{1}{2} \sum_{\alpha \neq \beta}^{K} \frac{Z_\alpha Z_\beta}{|R_{\alpha\beta}|} + \frac{1}{2} \sum_{i \neq j}^{N} \frac{1}{|r_{ij}|} - \sum_{\alpha=1}^{K} \sum_{i=1}^{N} \frac{Z_\alpha}{|R_{\alpha i}|} \right\} \Psi = \mathcal{E} \Psi \tag{4.4}$$

Unfortunately, the potential energy terms make the exact analytical solution of this equation impossible. Indeed, in order to obtain the exact analytical solution of the Schrödinger equation, one needs to separate the variables something possible only in the simplest cases of systems with only one nucleus and one electron, that is, the hydrogen-like atoms/ions (H, He^+, Li^{2+}, , Be^{3+}). So, in the general case of polyatomic systems, approximations must be used. One of the most widespread approximation is based on the difference between the masses of nuclei and electrons. Indeed, the mass of the proton is much bigger than the one of the electron ($\frac{m_p}{m_e} \approx 1836$), being the kinetic energy of the two types of particles very different ($T_n << T_e$). This fact allows a decoupling between electronic and nuclear motion, in the so called Born Oppenheimer approximation. When dealing with the electronic structure of a given system and by applying this approximation, it is possible to neglect at first the nuclei kinetic energy operator $\hat{T}_n$ from the total Hamiltonian (see Equation (4.3)) which leads the electronic Hamiltonian H:

$$\hat{H} = \hat{T}_e + \hat{V}_{nn} + \hat{V}_{ee} + \hat{V}_{en} \tag{4.5}$$

In this case, the potential energy operator of interaction between nuclei $\hat{V}_{nn}$ becomes a constant operator with respect to electronic degrees of freedom (it can thus be omitted from Equation (4.5) and the associated potential energy is a constant.

The Born-Oppenheimer approximation thus makes it possible to reduce the total problem by solving a purely electronic for a set of atomic positions (that is, the positions of the nuclei are treated as parameters of the problem):

$$\hat{H}\Phi^{\mathbf{R}}(\mathbf{r}) = E^{\mathbf{R}}\Phi^{\mathbf{R}}(\mathbf{r}) \tag{4.6}$$

where $\Phi^{\mathbf{R}}(\mathbf{r})$ is the electronic wavefunction and $E^{\mathbf{R}}$ the eigenvalue of the Hamiltonian operator (i.e. the total electronic energy) associated to this wavefunction at fixed nuclear coordinates expressed with the superindex $^{\mathbf{R}}$. This equation, which gives the electronic state of the system at the given nuclear coordinates is called the electronic equation.

It should also be emphasized an important feature of the wavefunctions, the normalization condition:

$$\int_{\mathbf{r}}\int_{\mathbf{R}} \Psi^*(\mathbf{R},\mathbf{r})\Psi(\mathbf{R},\mathbf{r})d\mathbf{R}d\mathbf{r} = 1 = \langle\Psi(\mathbf{R},\mathbf{r})|\Psi(\mathbf{R},\mathbf{r})\rangle, \tag{4.7}$$

$$\int_{\mathbf{r}} \Phi^{*\mathbf{R}}(\mathbf{r})\Phi^{\mathbf{R}}(\mathbf{r})d\mathbf{r} = 1 = \langle\Phi^{\mathbf{R}}(\mathbf{r})|\Phi^{\mathbf{R}}(\mathbf{r})\rangle, \tag{4.8}$$

$$\int_{\mathbf{R}} \chi^*(\mathbf{R})\chi(\mathbf{R})d\mathbf{R} = 1 = \langle\chi(\mathbf{R})|\chi(\mathbf{R})\rangle \tag{4.9}$$

This condition shows that the probability of finding the system throughout the space is equal to 1. Here we used the already used Dirac notation $\langle A|B\rangle$. thus simplifying the writing of integrals. From now on, on this chapter, we will refer to the electronic wavefunction $\Phi^{\mathbf{R}}(\mathbf{r})$ as Φ to simplify the notations.

4.1.2 Wavefunction methods

Once derived the electronic equation (see Equation (4.6)), now the problem becomes solving it, and it is analytically impossible, even with the aforementioned approximations, for all molecules except for the singular case of the monoelectronic H_2^+ ion. This is because $\hat{V}_{ee}$ still includes many-body terms namely interacting electrons. A wide variety of methods have been proposed to obtain approximative solutions to the exact electronic function. Each one of these approximations is implemented in one or more calculation packages, however they all have their own advantages and disadvantages. In this section, we will present the methods used in this work which are based on the wavefunction.

4.1.2.1 The Hartree-Fock method

In real atomic systems, electrons interact among them thus being impossible to describe them individually. In simulations, however, the mono-electronic approximation or the approximation of independent electrons is taken as starting point in order to obtain a first approximation from which to add, in subsequent steps, the electron-electron interaction contributions. It comes back to suppose that every electron is in a stationary state in which it does not interact at all with the other electrons. These states are described by mono-electronic wave functions called spinorbitals and written $\phi_i(\mathbf{r_i},\sigma_\mathbf{i})$ (where i is the electron index). If the N electrons of the system

are independent, we can write the total wavefunction of the system as a product of spinorbitals:

$$\Phi = \prod_{i=1}^{N} \phi_i(\mathbf{r}_i, \sigma_i) \tag{4.10}$$

where the $\mathbf{r}_i = \{\mathbf{x}_i, \mathbf{y}_i, \mathbf{z}_i\}$ are the spatial electronic coordinates and the σ_i are the spin coordinates. However, this expression assumes electron i being only in state ϕ_i and thus violates the principle that identical particles are indiscernible. Instead a complete treatment should consider all i electrons being in a superposition of all possible ϕ_i states. Being the electrons fermionic particles, they are represented by antisymmetric states and thus obey the Pauli exclusion principle. In 1929, Slater proposed an expression which respects this principle, and that relies on the work of Heisenberg and Dirac [214, 215], the polyfermionic wavefunction was formulated as an antisymmetric product of N monolectronic wave functions (spinorbitals $\phi_j(\mathbf{r_i}, \sigma_\mathbf{i})$, where the indices i and j correspond to the indexes of the electron and the orbital respectively[216]:

$$\Phi(\mathbf{r}_1, \sigma_1, \mathbf{r}_2, \sigma_2, \ldots, \mathbf{r}_i, \sigma_i, \ldots, \mathbf{r}_N, \sigma_N) = \tag{4.11}$$
$$\frac{1}{\sqrt{N!}} \begin{vmatrix} \phi_1(\mathbf{r}_1, \sigma_1) & \phi_2(\mathbf{r}_1, \sigma_1) & \ldots & \phi_j(\mathbf{r}_1, \sigma_1) & \ldots & \phi_N(\mathbf{r}_1, \sigma_1) \\ \phi_1(\mathbf{r}_2, \sigma_2) & \phi_2(\mathbf{r}_2, \sigma_2) & \ldots & \phi_j(\mathbf{r}_2, \sigma_2) & \ldots & \phi_N(\mathbf{r}_2, \sigma_2) \\ \vdots & \vdots & \ddots & \vdots & & \vdots \\ \phi_1(\mathbf{r}_i, \sigma_i) & \phi_2(\mathbf{r}_i, \sigma_i) & \ldots & \phi_j(\mathbf{r}_i, \sigma_i) & \ldots & \phi_N(\mathbf{r}_i, \sigma_i) \\ \vdots & \vdots & & \vdots & \ddots & \vdots \\ \phi_1(\mathbf{r}_N, \sigma_N) & \phi_2(\mathbf{r}_N, \sigma_N) & \ldots & \phi_j(\mathbf{r}_N, \sigma_N) & \ldots & \phi_N(\mathbf{r}_N, \sigma_N) \end{vmatrix}$$

This representation of the wave function is called a Slater determinant and unlike Equation (4.10), it explicitly contains the indistinguishability of the electrons.

In a first attempt to obtain the spinorbitals and their energies while still accounting for the electron-electron interaction, the Hartree-Fock Method was formulated to subsequently obtain the multielectronic wavefunction through the Slater determinant. The method accounts for the electronic repulsion by means of the mean-field approximation (i.e. each electron feels the interaction of the mean field of all other electrons), the Fock operator is then formulated as follows:

$$\hat{F} = -\frac{\hbar^2}{2m}\nabla^2_{\mathbf{r}_i,\sigma_i} + \hat{V}_{en}(\mathbf{r}_i, \sigma_i) + \sum_{j=1}^{N}(\hat{J}_j - \hat{K}_j) \tag{4.12}$$

The first term corresponds to the kinetic energy of the electron i. The second one describes the electrostatic interaction between this electron and the nuclei. The sum of Coulombian operators $\hat{J}_j$, also called Hartree's term, describes the total average potential created by $N-1$ other electrons onto the spinorbital to the ith electron. Finally, the exchange operator $\hat{K}_j$, also called the exchange term, is the contribution from the antisymmetry of the total wavefunction and it does not have any classical equivalence.

The Fock operator depends on the solution and therefore must be solved self-consistently. In this iterative procedure the first step is choosing an initial guess for each of the N spinorbitals of a system. Given a first trial for the Fock operator, we

can formulate the Fock equation to obtain a better guess for the spinorbitals, which now accounts for the mean field repulsion of all other electrons:

$$\hat{F}\phi_i(\mathbf{r}_i, \sigma_i) = \epsilon_i \phi_j(\mathbf{r}_i, \sigma_i) \tag{4.13}$$

where ϵ_i is the spinorbital energy and, $\hat{F}$ is the Fock operator. The process until convergence is achieved.

If we consider more in detail the meaning of ϵ_i, which is the expectation value of the Fock operator applied to the ith spinorbital, we realize that the total energy could not be calculated as a sum of spinorbital energies because otherwise we would count twice the electronic repulsion interaction for each electron. A $\frac{1}{2}$ term should be incorporated before the sumation in order to account properly for the electronic repulsion. Thus the total energy of the system can be forumlated as:

$$\begin{aligned} E &= \sum_{i=1}^{N} \langle \phi_i | -\frac{\hbar^2}{2m}\nabla^2 + \hat{V}_{en} | \phi_i \rangle + \frac{1}{2}\sum_{i,j=1}^{N}(J_{ij} - K_{ij}) \\ &= \sum_{i=1}^{N} \epsilon_i + \frac{1}{2}\sum_{i,j=1}^{N}(J_{ij} - K_{ij}) \end{aligned} \tag{4.14}$$

where in this case K_{ij} and J_{ij} correspond to the Hartree and exchange terms only among the i and j electrons. The Hartree Fock method gives us an iterative method to optimize spinorbitals. In quantum chemistry, a convenient way to obtain the trial spinorbitals is to express them in a basis set expansion formulated as linear combinations of hydrogenic atomic orbitals:

$$\phi_i = \sum_{s=1}^{b} c_{si}\chi_s \tag{4.15}$$

The set of wavefunctions chosen to represent the spinorbitals is called the basis set. Substitution of the expansion into the Hartree-Fock equation gives:

$$\sum_s c_{si}\hat{F}\chi_s = \epsilon_i \sum_s c_{si}\chi_s \tag{4.16}$$

Being r a new index for the same basis set we can generate b equations multiplying at each equation for a different basis function ${}^*\chi_r$ and integrate through the full space to solve for the ϵ_i. This defines the so called Hartree-Fock-Roothaan equations:

$$\sum_{s=1}^{b} c_{si}(F_{rs} - \epsilon_i S_{rs}) = 0, \quad r = 1, 2, ..., b \tag{4.17}$$

$$F_{rs} \equiv \langle \chi_r \mid \hat{F} \mid \chi_s \rangle, S_{rs} \equiv \langle \chi_r \mid \chi_s \rangle \tag{4.18}$$

where S_{rs} is the overlap of the r basis function with the s one (the projection formulated as the internal product). This set of equations depend parametrically on the coefficients c_{si}. Variational method states that for a system with a given wavefunction and an approximate wavefunction which depends on some parameters, the energy of the real wavefunction is always going to be lower or equal than the

energy of the approximate wavefunction for which the parameters minimize the energy for. In order to obtain the coefficients, the equation can be expressed in the determinantal form:

$$det(F_{rs} - \epsilon_i S_{rs}) = 0 \tag{4.19}$$

which roots provides the value of ϵ_i.

The Hartree-Fock (HF) method has had remarkable success in the development of treatments of the electronic structure in quantum chemistry and condensed matter theory. However, it does not take into account wavefunction fluctuations beyond the mean-field, namely electronic static and dynamic correlation. The correlation energy E_c is defined as the difference between the exact energy of a system, E, and the energy of HF, E_{HF}:

$$E_c = E - E_{\mathrm{HF}} \tag{4.20}$$

The HF energy of a system is therefore always above than the exact energy of that system. The order of correlation energy magnitude can be estimated by considering the exact energy and E_{HF} for the helium atom. The exact energy is -2,86168 a.u. while HF energy is -2.90372 a.u. Thus, in this simple case of 2 electrons, the correlation energy is 26.0 kcal/mol. This value for a simple electron pair is of the order of magnitude than the energy of some chemical bonds. It is, thus, very important to take into account the correlation energy to describe the actual chemical systems.

4.1.2.2 Post Hartree-Fock methods

Many methods exist whose aim is to account for the mentioned correlation energy. Among them the most spread are: Møller-Plesset, Configuration Interaction, Coupled Cluster among others.

Møller-Plesset Perturbation Theory. One of the simplest methods of calculating correlation for the ground state is the Møller-Plesset (MP) theory [217]. This is a particular case of the perturbation theory also known as Rayleigh-Schrödinger pertubation theory (RS) [218].

The perturbation theory is a procedure in which the Hamiltonian is expressed as $\hat{H} = \hat{H}^0 + \lambda\hat{V}$ [219] where, $\hat{H}^0$ is a reference Hamiltonian and a perturbation V multiplied by a dummy variable λ that controls the size of the perturbation. The wavefunction and the energies are expressed in power series in λ:

$$\Phi_n = \Phi_n^0 + \lambda\Phi_n^1 + \lambda^2\Phi_n^2 + ... \tag{4.21}$$
$$E_n = E_n^0 + \lambda E_n^1 + \lambda^2 E_n^2 + ... \tag{4.22}$$

Substituting these expressions in Schrödinger equation and by collecting the terms of the same order in relation to λ, we obtain the sequence of equations next:

$$\begin{aligned} H^0\Phi_n^0 &= E_n^0\Phi_n^0, \\ H^0\Phi_n^1 + V\Phi_n^0 &= E_n^0\Phi_n^1 + E_n^1\Phi_n^0, \\ H^0\Phi_n^2 + V\Phi_n^1 &= E_n^0\Phi_n^2 + E_n^1\Phi_n^1 + E_n^2\Phi_n^0, \end{aligned} \tag{4.23}$$

In the Møller-Plesset perturbation theory the zeroth order wavefunction is the determinant obtained in the Hartree-Fock Method and the zeroth order Hamiltonian is the sum of one-electron Fock operators. Resolving all these equations, one obtains the corrections of order i by the terms of smaller order and thus corrections of the wavefunction and energy can be obtained, in principle, at any order, though its computational cost is toodemanding.

Configuration Interaction. The method, known also as CI, is a linear variational method that expresses the total wavefunction as linear combination of Slater determinants:

$$\Psi = c_0\Phi_0 + \sum_{I>0} c_I\Phi_I \tag{4.24}$$

The Φ_0 determinant is typically the Slater determinant arising from the Hartree-Fock or Multi-Configurational Self-Consistent Field methods and subsequent terms are determinant obtained through excitation of one or more electrons to higher energy spinorbitals. Coefficients of the determinants are optimized by applying the variational method. Full-CI (at the given basis set) considers all possible excitations and gives the exact solution at the given basis set. However, the number of determinants has a factorial dependence on the basis set size, increasing the computational cost of the method also factorially. That's why truncated CI is a common practice in order to save computational time, specially considering the inclusion of Davidson correction which gives an estimate of higher exitation from the single and double ones. However, the truncated CI method is neither additive nor size-consistent.

Coupled Cluster Theory Another method to take into account the effect of correlation is the Coupled Cluster theory [220]. It's based in the same principle than CI that, considering determinants with excited electrons leads to a size consistent description of the correlation energy. The method consists of generating the correlated polyelectronic wavefunction by means of an exponential operator acting on a reference determinant. The wavefunction is expressed like:

$$\Phi = e^{\hat{T}}\Phi_0 \tag{4.25}$$

$\hat{T}$ is an excitation operator operating on Φ_0, the reference Slater determinant, typically build with the Hartree-Fock method. $\hat{T} = \hat{T}_1 + \hat{T}_2 + \hat{T}_3 + ... + \hat{T}_N$ being the sum of simple, double, triple, up to Nple excitations, where at the same time each contains a linear combination of all the possible excitations of their type.

$$\hat{T}_1\Phi_0 = \sum_i^{occ}\sum_a^{virt} t_i^a\Phi_i^a, \quad \hat{T}_2\Phi_0 = \sum_{i>j}^{occ}\sum_{a>b}^{virt} t_{ij}^{ab}\Phi_{ij}^{ab}, \quad etc \tag{4.26}$$

The aim of a CC calculation is to find the coefficients $t_i^a, t_{ij}^{ab}, t_{ijk}^{abc}$ for all $i, j, k, ...$ and all $a, b, c, ...$. Once these coefficients (called amplitudes) are found, the wave function c in Equation (4.25) is known. The efficiency of the Coupled Cluster theory relies on the Taylor expansion of the exponential function, giving us the coefficients of quadruple excitations (the second ones more important ones after the double ones) as combinations of coefficients of the double excitations:

$$e^{\hat{T}} = \sum_{N=0}^{\infty} \frac{\hat{T}^N}{N!} = 1 + T + \frac{1}{2}T^2 + \frac{1}{3!}T^3 + ... \tag{4.27}$$

4.1.3 Density Functional Theory

The wave function methods, such as MP2 or CC, give very accurate results and allow to obtain structural and energetic properties of molecules and small aggregates. However, the big disadvantage of these methods is their high computational cost. Thus, the size of the molecular systems that can be processed is limited (up to 10-20 atoms for CC for example). Hence the need of developing more efficient methods which are still accurate.

In 1920, Thomas and Fermi proposed a new model for calculating the energy of the atom [221, 222]. This model allowed to develop a new vision of the calculation of the structure electronic chemical systems. In their early works, Thomas and Fermi proposed to express the energy of the atom as the sum of the kinetic energy of its electrons, this last in the form of a functional of the electronic density, and of the potential energy for the interaction of electrons with the nucleus and electrons among them.

However, this first model didn't include the exchange interaction and its results on molecules was not satisfactory. In 1930, Dirac attempted to refine this model by adding a term describing the exchange interaction expressed as a functional of the electronic density [223]. Despite these efforts, the Thomas-Fermi-Dirac model did not lead to satisfactory results for two main reasons: the electronic correlation was not taken into account and the form of the kinetic energy functional was a lot too simple.

4.1.3.1 Hohenberg and Kohn Theorems

The true revolution inside the open door by Thomas and Fermi came by the hand of Hohenberg and Kohn who brought a solid theoretical basis to the methodological developments based on the electronic density [224]. It was thanks to this solid basis, that Density Functional Theory (DFT) got the actual success in describing the electronic structure. The formulation of Hohenberg and Kohn is general and applicable to any system of interacting particles under the effect of an external field. Since the aim is the description of atom based systems both the time independent Hamiltonian and the Born-Oppenheimer approximation are going to be considered to solve the electronic Schrödinger Equation.

Before entering in the discussion of the formalism, some basic notation must be introduced:

- $n(\mathbf{r})$ will be the function describing the density which depends on the system's coordinates

- $n_f(\mathbf{r})$ will be the density function of the ground state.
- $E[n(\mathbf{r})]$ will be a functional representing the total energy of the system at the given density function.
- E_0 will be the value of the energy of the ground state arising from the minimization of $E[n(\mathbf{r})]$ to the $n_f(\mathbf{r})$.

First Hohenberg and Kohn theorem For any electronic system under the potential of an external field $V_{ext}(r)$ there is a biunivocal correspondence between the external field $V_{ext}(r)$ and the total density in its ground state $n_f(\mathbf{r})$. For any external potential $V_{ext}(r)$ it exists a functional $E[n(\mathbf{r})]$ which relates each density with its energy value.

Second Hohenberg and Kohn theorem For each external potential, the ground state energy E_0 is the one which minimises the functional on density variations.

From the 1st and 2nd Hohenber and Kohn theorems a total energy of the system functional can be written as sum of functionals of kinetic energy, potential energy of electron-electron interaction.:

$$E[n(\mathbf{r})] = T[n(\mathbf{r})] + V_{ee}[n(\mathbf{r})] + \int V_{ext}(\mathbf{r})n(\mathbf{r})d\mathbf{r} \tag{4.28}$$

4.1.3.2 Kohn-Sham Formalism

The problem of the Hohenberg and Kohn theory lies on the impossibility to express the terms $T[n(\mathbf{r})]$ and $V_{ee}[n(\mathbf{r})]$ for a system of interacting particles. So to solve this problem, Kohn and Sham proposed, similarly to the Hartree-Fock method, to start by accounting for non interacting electrons[225], being thus the density the sum of the monolectronic wavefunction densities:

$$n(\mathbf{r}) = \sum_{i=1}^{N} |\phi_i(\mathbf{r}, \sigma)|^2 \tag{4.29}$$

where $\phi_i(\mathbf{r})$ are the monoelectronic wavefunctions. The total energy of the system accordin to Kohn and Sham can be expressed as:

$$E[n(\mathbf{r})] = T_s[n(\mathbf{r})] + \frac{1}{2}\int\int \frac{n(\mathbf{r})n(\mathbf{r}')}{|\mathbf{r}-\mathbf{r}'|} + \int V_{ext}(\mathbf{r})n(\mathbf{r})d\mathbf{r} + E_{xc}[n(\mathbf{r})] \tag{4.30}$$

where $T_s[n(\mathbf{r})]$ is the kinetic energy of the non-interacting electrons and $E_{xc}[n(\mathbf{r})]$ is the so called exchange-correlation functional which allows to link the imaginary non-interacting system with the real one with electron-electron correlation. This functional is defined as:

$$E_{xc}[n(\mathbf{r})] = T[n(\mathbf{r})] - T_s[n(\mathbf{r})] + V_{ee}[n(\mathbf{r})] - \frac{1}{2}\int\int \frac{n(\mathbf{r})n(\mathbf{r}')}{|\mathbf{r}-\mathbf{r}'|} \tag{4.31}$$

the minimisation of the energy of the system with respect to the Kohn-Sham orbitals at constant number of particles gives the following equations:

$$\hat{H}^{KS}\phi_i(\mathbf{r}) = \varepsilon_i\phi(\mathbf{r}) \tag{4.32}$$

where the Kohn-Sham Hamiltonian is written:

$$\hat{H}^{KS} = \frac{\delta E[n(\mathbf{r})]}{\delta n(\mathbf{r})} = -\frac{1}{2}\nabla_i^2 + \int \frac{n(\mathbf{r}')}{|\mathbf{r}-\mathbf{r}'|}d\mathbf{r}' + V_{ext} + \frac{\delta E_{xc}[n(\mathbf{r})]}{\delta n(\mathbf{r})} \tag{4.33}$$

where the first term is the kinetic energy of the electrons, the second one the Hartree potential ($\hat{J}_j$ in Equation (4.12), the third term is the external potential generated by the nuclei and the fourth one the exchange-correlation potential.

4.1.3.3 Exchange-Correlation functional

Until this point the Exchange-Correlation energy, nor its functional, have been defined so far. The main problem of the DFT theory is indeed the expression for this term, since the HK theorems do not give any recipe in order to obtain it. It is needed to give the term a mathematical form based on the assumption of certain approximations. According to which approximations are used on their formulation the different Exchange-Correlation functionals can be classified in the following families:

- LDA for *local density approximation*,
- GGA for *generalized gradient approximation*,
- meta-GGA,
- hybrids.

LDA. It was the first approximation used for the $E_{xc}[n(\mathbf{r})]$. It is based on the description of the homogeneous electron gas, for which the exchange energy ϵ_x^{hom} is known and the correlation energy ϵ_c^{hom} can be calculated numerically at different electron densities. A parametrized expression for the correlation energy was formulated by Perdew based on quantum Monte-Carlo simulations from Ceperley and Alder [226, 227]. The following expression is then obtained:

$$E_{xc}^{LDA}[n(\mathbf{r})] = \int [\varepsilon_x^{hom}(n(\mathbf{r})) + \varepsilon_c^{hom}(n(\mathbf{r}))]n(\mathbf{r})d\mathbf{r} \tag{4.34}$$

This approximation is called local because it treats the system by splitting it into local domains and there calculate the exchange and correlation terms by assuming the whole system as an electron gas with the density of that domain. This approximation is quite extreme, when it is known that the correlation energy depends greatly on the environment, ie. its value depends on the value of the density on all other points of the space. On top of that, due to the fact that the exchange has been treated in an approximate way a non negligible part of self interaction is accounted. In spite of the extreme approximations assumed, the method leads to reasonable results, specially for metallic systems, where assuming an homogeneous electronic density is a more reasonable scenario.

An extension to LDA, aiming to better account for the exchange potential on spin polarized systems, was developed by splitting the density in up- and down-spin densities. The so called local spin density approximation is formulated as follows[228]:

$$E_{xc}^{LSDA}[n(\mathbf{r})] = \int [\varepsilon_x^{hom}(n^{\uparrow}(\mathbf{r}), n^{\downarrow}(\mathbf{r})) + \varepsilon_c^{hom}(n^{\uparrow}(\mathbf{r}), n^{\downarrow}(\mathbf{r}))]n(\mathbf{r})d\mathbf{r} \tag{4.35}$$

where $n^{\uparrow}(\mathbf{r})$ and $n^{\downarrow}(\mathbf{r})$ represent respectively the density of "up" and "down" spins. Note has to be taken that the treatment is only used for the exchange energy.

GGA For atomic or molecular systems, or in general for systems whose density changes rapidly with distance, the assumption of uniform distribution of electrons becomes a poor choice and the LDA approximation is not appliable. In order to solve that problem the GGA was developed by, in both the exchange and correlation functionals, taking into account not only the local density but also its gradient $\nabla n(\mathbf{r})$ [229, 230]. The functional takes then the form:

$$E_{xc}^{GGA}[n(\mathbf{r})] = \int [\varepsilon_x(n(\mathbf{r}), \nabla n(\mathbf{r})) + \varepsilon_c(n(\mathbf{r}), \nabla n(\mathbf{r}))]n(\mathbf{r})d\mathbf{r} \tag{4.36}$$

The building of the GGA functionals is less evident than LDA ones. Indeed the corrections based on the gradient depends on the conditions on the boundaries to reproduce the needed physical properties. A certain degree of empirism is then needed. Due to the diversity of constraints that can be applied, many implementations of the GGA exist- Among them there is the one developped by Perdew, Burke and Erzenhoff (PBE) [231] which had very good performances in many chemistry fields specially in the field of solids [232–234].

Hybrid functionals This generation of functionals was proposed by Becke in 1993 [235, 236]. The main idea arose from the fact that for complete uncorrelated systems, the Hartree-Fock energy is the exact solution, while for correlated ones, the LDA or GGA theories were giving better results. These two extremes are connected by a a continum of systems for which correlation lies in between i.e. with partially correlated systems. This concept is written in its mathematical form by using the following adiabatic connection.

$$E_{xc}[n(\mathbf{r})] = \int_0^1 E_{xc}[n(\mathbf{r})]\lambda d\lambda \tag{4.37}$$

where $\lambda = 0$ is the uncorrelated electrons system and $\lambda = 1$ the completely correlated one. The LDA and GGA functionals used as to make the amount of HF exchange to be used can be expressed by adjusting the parameters.

Many implementations of the hybrid functional idea have been developed along the years, which use different parameters on the different contributions. Rather successful has been the B3LYP[237] functional which uses three parameters [238] in order to do the adiabatic mixture:

$$E_{xc}[n(\mathbf{r})] = E_{xc}^{LDA}[n(\mathbf{r})] + a_0(E_{HF}^x - E_{LDA}^x) + a_x E_{GGA}^x + a_c E_{GGA}^c \tag{4.38}$$

These kind of functionals have had their greatest success in the description of molecular systems.

4.1.4 The Density-Functional based Tight Binding

The density functional theory (DFT) is a method that generally gives accurate results and which allows to obtain structural and energy characteristics of molecules and aggregates up to a few hundreds or $\sim$ 10,000 atoms for single point calculations. The main advantage of this method compared to the ones based on the wavefunction is its computational efficiency. However, when one wishes to study configurational changes, thermodynamical properties or the dynamic aspects of reactivity, the DFT efficiency is just not enough. Indeed, to carry out simulations of molecular dynamics with sufficient statistical sampling of the initial conditions or propagating sufficiently long trajectories, it is necessary to further simplify the method of calculation of the electronic structure, in order to reduce the calculation time for each configuration. Hückel (in chemistry) or Tight-Binding (TB) methods (in physics of the condensed matter) have been qualitative phenomenological tools, but mostly qualitatively [239, 240]. The goal of these approaches is a simplified calculation of the electronic structure by using a superposition of free atom wavefunctions. Foulkes and Haydock have shown that these approaches can be derived from the DFT method [241]. Later, Seifert, Porezag and Frauenheim used similar ideas to propose a systematic way of constructing tight binding parameters from DFT [242].

4.1.4.1 Linearization

In order to derive the equations for the DFTB formalism we shall start from the Kohn-Sham equations. Expressing the total density as sum of orbital densities, as in Equation (4.29) and introducing it into Equation (4.30) we get the expression:

$$E[n(\mathbf{r})] = \sum_{i}^{occ} \langle \phi_i | -\frac{1}{2}\nabla^2 + V_{ext}(\mathbf{r}) \int \frac{n(\mathbf{r}')}{|\mathbf{r}-\mathbf{r}'|} d\mathbf{r}' | \phi_i \rangle - E_{xc}[n(\mathbf{r})] \tag{4.39}$$

The derivation of the Density-Functional based Tight-Binding (DFTB) consists in expressing the density of the ground state $n_0(\mathbf{r})$ as a sum of a reference density and a perturbation $\delta n(\mathbf{r})$ [242]. In order to apply this concept to a system of particles, we rewrite as to transform the main elements of the matrix. For simplification purposes of the ensuing equations we adopt the following notation: $E[n(\mathbf{r})] = E$, $V_{ext}(\mathbf{r}) = V_{ext}$, $\int d\mathbf{r} \longrightarrow \int$, $\int d\mathbf{r}' \longrightarrow \int'$, $n(\mathbf{r}) \longrightarrow n$, $n(\mathbf{r}') \longrightarrow n'$. The energy expressed as sum of reference and perturbation is then written:

$$\begin{aligned} E = \sum_{i}^{occ} \langle \phi_i | -\frac{1}{2}\nabla^2 + V_{ext} + \int' \frac{n_0'}{|\mathbf{r}-\mathbf{r}'|} + V_{xc}[n_0] | \phi_i \rangle \\ -\frac{1}{2}\int\int' \frac{n_0'(n_0+\delta n)}{|\mathbf{r}-\mathbf{r}'|} - \int V_{xc}[n_0](n_0+\delta n) \\ +\frac{1}{2}\int\int' \frac{\delta n'(n_0+\delta n)}{|\mathbf{r}-\mathbf{r}'|} + E_{xc}[n_0+\delta n] \end{aligned} \tag{4.40}$$

After having expressed the exchange-correlation energy as a function of the reference density (by a Taylor expansion over E_{xc}), we obtain the total energy at the second order perturbation of the density. It's important to point out that lineal terms of δn got canceled and by grouping similar terms the following expression is obtained:

$$E = \overbrace{\sum_{i}^{occ} \langle \phi_i | \hat{H}^{DFTB} | \phi_i \rangle}^{\mathrm{E_{band}}} + \overbrace{\frac{1}{2} \int \int' \Big(\frac{1}{|\mathbf{r} - \mathbf{r}'|} + \frac{\delta^2 E_{xc}}{\delta n \delta n'} \Big|_{n_0} \Big) \delta n \delta n'}^{\mathrm{E_{2nd}}} \underbrace{- \frac{1}{2} \int \int' \frac{n_0' n_0}{|\mathbf{r} - \mathbf{r}'|} - \int V_{xc}[n_0] n_0 + E_{xc}[n_0]}_{\mathrm{E_{rep}}} \tag{4.41}$$

This regrouping of terms leads to the most known notation for the DFTB energy contributions: The Tight binding energy (E_{band}), the second order term (E_{2nd}), which mainly describes the Coulomb interaction at long range and finally the repulsive energy (E_{rep}). This decomposition of the energy with respect to the density sets the basis of the DFTB method which gets split into the two following versions:

- NCC-DFTB (Non-self-Consistent Charge DFTB): where the 2nd order term is neglected (i.e. $E = E_{band} + E_{rep}$)
- SCC-DFTB (Self-Consistent Charge DFTB): the three terms are considered for the obtention of total energy. (i.e. $E = E_{band} + E_{2nd} + E_{rep}$)

In both versions, as in all TB approaches, only valence electrons are considered this way improving the computational efficiency an thus significantly reducing the amount of computational effort. This treatment is qualitatively analogue to the spread usage of pseudopotentials in DFT and WF methods for heavy atoms. The approximations taken until now, may in some cases, pay the price of a loss of accuracy by simplifying important terms.

4.1.4.2 Tight Binding Energy

To find the total energy of the system all the terms in Section 4.1.4.1 are needed. Hereinafter a detailed explanation of the TB energy inside the DFTB frame is given starting from the expression for the band energy:

$$E_{\mathrm{band}} = \sum_{i}^{occ} \langle \phi_i | \hat{H}^{DFTB} | \phi_i \rangle \tag{4.42}$$

where neither Kohn-Sham orbitals ϕ_i nor the Hamiltonian $\hat{H}^{DFTB}$ are yet defined.

In this approach the Kohn-Sham molecular orbitals ϕ_i are expressed as linear combination of atomic orbitals ϕ_ν each with its coefficient $c_{\nu i}$ (LCAO):

$$\phi_i(\mathbf{r}) = \sum_{\nu} c_{\nu i} \phi_\nu(\mathbf{r}) \tag{4.43}$$

The DFTB Hamiltonian takes a similar form to the DFT one in Equation (4.33) except that we substituted the density n by the reference density n_0:

$$\hat{H}^{DFTB} = -\frac{1}{2}\nabla_i^2 + \int' \frac{n_0'}{|\mathbf{r}-\mathbf{r}'|} + V_{ext} + V_{xc}[n_0] = -\frac{1}{2}\nabla_i^2 + \hat{V}^{DFTB}[n_0] \qquad (4.44)$$

where we combined the last three terms into $\hat{V}^{DFTB}[n_0]$. Knowing the form of the Hamiltonian for two atoms α and β for which we know their atomic orbitals (ϕ_μ and ϕ_ν) we can obtain the elements of Hamilton matrix corresponding to $H_{\mu\nu}^{DFTB}$:

$$H_{\mu\nu}^{DFTB} = \langle\phi_\mu| -\frac{1}{2}\nabla_i^2 + \hat{V}^{DFTB}[n_0]|\phi_\nu\rangle, \qquad \forall\mu\in\alpha, \quad \nu\in\beta \qquad (4.45)$$

At this point, the problem, is that the density n_0, from which the operator $\hat{V}^{DFTB}$ depends on, is the sum of the atom-centered densities, $n_0 = \sum_{\lambda=1}^{N_{\text{at}}} n_0^\lambda$ where N_{at} is total number of of atoms in the system. This form is not easy to deal with for real-life systems and, as to simplify the treatment, the off-diagonal terms of the $H_{\mu\nu}^{DFTB}$ matrix are treated as two-center terms. This means that the three- and higher body interactions are neglected. In this case, $\hat{V}^{DFTB} = \hat{V}_\alpha^{DFTB} + \hat{V}_\beta^{DFTB}$. To sum up, the following cases are considered:

$$H_{\mu\nu}^{DFTB} = \begin{cases} \varepsilon_\mu^{free\ atom} & \text{, if} \quad \mu = \nu \\ \langle\phi_\mu|\hat{T} + \hat{V}_\alpha^{DFTB} + \hat{V}_\beta^{DFTB}|\phi_\nu\rangle & \text{, if} \quad \alpha \neq \beta \\ 0 & \text{, other cases} \end{cases} \qquad (4.46)$$

It can be seen that the eigenvalues of the free atoms are the diagonal terms and this grants the correct limit on the isolated atoms. For each pair of atoms, these elements are precalculated using DFT (typically using PBE or LDA) and their values saved in a parameters file to be read and used during DFTB calculations. For example, to describe the water molecule using DFTB the used elements of the matrix are H-H, O-O and O-H.

It is worth to point out that, by using this parametrization, at this point the reference density n_0 is equivalent to the density n in DFT.

4.1.4.3 2nd order energy

The 2nd term of Section 4.1.4.1 takes special importance in systems where chemical bonds are controlled by an equilibrium of charges among the atoms. This can be the case of charged species, ionic materials, semiconductors, or any system with an asymmetrical distribution of charges.

To include the associated effects in a TB concept, we develop δn in atom-centered contributions that decrease rapidly as inter-atomic distances increase. Thus, the second order term of Section 4.1.4.1 is written as follows:

$$E_{2\text{nd}} = \frac{1}{2}\sum_{\alpha\beta}\int\int'\Big[\frac{1}{\mathbf{r}-\mathbf{r}'} + \frac{\delta^2 E_{xc}[n]}{\delta n\delta n'}\Big]\delta n_\alpha \delta n'_\beta \qquad (4.47)$$

where δn is the analogue to the expansion of $n_0 = \sum_{\lambda=1}^{N_{at}} n_0$ in atomic centered contributions. For a given atom α, δn_α is developed in series of radial functions only $F_{00}^\alpha(\mathbf{r}-\mathbf{R}_\alpha)$:

$$\delta n_\alpha = \Delta q_\alpha F_{00}^\alpha(|\mathbf{r} - \mathbf{R}_\alpha|) \tag{4.48}$$

In this expression the total charge of the system is conserved (i.e. $\sum_\alpha \Delta q_\alpha F_{00}^\alpha = \int' \delta n$). By substituting Equation (4.48) into Equation (4.47) we obtain the final expression for the 2nd order energy:

$$E_{\text{2nd}} = \frac{1}{2}\sum_{\alpha\beta} \Delta q_\alpha \Delta q_\beta \gamma_{\alpha\beta} \tag{4.49}$$

After the considered simplifications, the 2nd term energy is actually calculated by analyzing the fluctuations of charge for each atom Δq_α and the parameter $\gamma_{\alpha\beta}$ for each pair, obtaining the value for the last one by the following expression:

$$\gamma_{\alpha\beta} = \int\int' \Gamma[\mathbf{r}, \mathbf{r}', n_0] \frac{F_{00}^\alpha(|\mathbf{r} - \mathbf{R}_\alpha|) F_{00}^\beta(|\mathbf{r} - \mathbf{R}_\beta|)}{4\pi} \tag{4.50}$$

where $\Gamma[\mathbf{r}, \mathbf{r}', n_0]$ takes a similar form than the integrand in Equation (4.47). Although conceptually simple, this expression is generally not used on implemented algorithms. Instead an approximation based on the observations from Pariser [243] that this parameter can be calculated as the difference between the Ionization Potential (IP), and the Electron Affinity (EA). For each atom α the parameter $\gamma_{\alpha\alpha}$ is linked to the chemical hardness η_α [244] and to the Hubbard parameter U_α: $\gamma_{\alpha\alpha} = IP - EA = 2\eta_\alpha = U_\alpha$, while $\gamma_{\alpha\beta} = 1/R_{\alpha\beta}$.

As for the parametrized integrals described in Section 4.1.4.2, the $\gamma_{\alpha\alpha}$ values are also precalculated (if not already known) and stored in a file from which they are read in SCC-DFTB calculations.

Once known the γ parameter, it is possible to obtain the charge fluctuations in Equation (4.49). In the DFTB approach the charge fluctuation is considered as the difference in charge when the atom is taking part in some kind off chemical bond q_α and when it is free q_α^0: $\Delta q_\alpha = q_\alpha - q_\alpha^0$. In the original formalism the Mulliken method [245] calculate charges is taken as the way to assign the formal charge in each atom of the system:

$$q_\alpha = \frac{1}{2}\sum_i^{occ} n_i \sum_{\mu\in\alpha}\sum_\nu (c_{\mu i}^* c_{\nu i} S_{\mu\nu} + c_{\nu i}^* c_{\mu i} S_{\nu\mu}). \tag{4.51}$$

where $S_{\mu\nu}$ are the elements of the overlap matrix.

$$S_{\mu\nu} = \langle \phi_\mu | \phi_\nu \rangle \qquad \forall \mu \in \alpha, \qquad \forall \nu \in \beta \tag{4.52}$$

As proposed for Rapacioli et al. [246] a better method to calculate atomic charges on molecular systems leads to better description of coulombic interaction and thus better global results for SCC-DFTB method. (e.g. CM3 [247, 248])

4.1.4.4 Repulsive Energy

The last term in Section 4.1.4.1 incorporates many complex contributions into its energy, from which the most important one is the repulsive energy of core electrons, not considered in a minimal basis set. Like in the other terms of the DFTB method, this contribution is not calculated during the execution of the program, but stored

its value in a file, and read when the term is needed. In order to account for both the repulsive interaction of core electrons and the other more complicated terms, the repulsive energy is obtained by the following expression:

$$E_{rep}(\mathbf{R}_\alpha - \mathbf{R}_\beta) = E_{ref} - E_{band} - E_{2nd} \tag{4.53}$$

where E ref is total energy obtained from a DFT calculation on typically the dimer. In some cases other environments are needed to be considered other than the dimer, to account for better description of the complex terms.

4.1.4.5 Spin Polarization Energy

Standard SCC-DFTB is based on the formalism herein presented, however, when dealing with transition type elements, where the electronic structure is determined by a balance between electronic delocalization and electronic spin coupling it has to be included an explicit atom centered spin term which allows the description of the mentioned equilibrium. In this case, the SCC-DFTB total energy is written as:

$$\begin{aligned} E^{\text{SCC-DFTB}} &= \frac{1}{2}\sum_{a,b}^{\text{atoms}} E_{ab}^{\text{rep}} + \sum_{i}^{\text{orbitals}} n_i \langle\varphi_i|\hat{H}^0|\varphi_i\rangle \\ &+ \frac{1}{2}\sum_{a,b}^{\text{atoms}} \Gamma_{ab} q_a q_b \\ &+ \frac{1}{2}\sum_{a}^{\text{atoms}} \zeta_a (q_a^\alpha - q_a^\beta)^2 \end{aligned} \tag{4.54}$$

where the first three terms, are the already discussed, repulsive energy, Tight Binding energy and 2nd order energy while the last term is the one in charge to describe the spin coupling. In this term, q_a^β are the charges of α and β spin electrons on atom a (with $q_a = q_a^\alpha + q_a^\beta$) and ζ_a is an atomic spin constant.

4.1.4.6 Variational Principle

Once we have all the terms in Section 4.1.4.1 we can formulate the secular equations for the DFTB method, as analogues to the DFT ones from Equation (4.33). By applying the variational principle, (i.e. by minimizing the total energy of the system with respect to the coefficients) we have:

$$\sum_\nu c_{\nu i}(H_{\mu\nu}^{SCC-DFTB} - \varepsilon_i S_{\mu\nu}) = 0 \qquad \forall \mu, i \tag{4.55}$$

Due to the fact that we have used the complete expression of the energy by including the second order term it is to point out that the Hamiltonian have been modified:

$$H_{\mu\nu}^{SCC-DFTB} = \underbrace{\langle\phi_\mu|\hat{H}^{DFTB}|\phi_\nu\rangle}_{H_{\mu\nu}^{DFTB}} + \underbrace{\frac{1}{2}S_{\mu\nu}\sum_\xi(\gamma_{\alpha\xi} + \gamma_{\beta\xi}\Delta q_\xi)}_{H_{\mu\nu}^{1}} \tag{4.56}$$

The H^{DFTB} and $S_{\mu\nu}$ terms are identical to the NCC-DFTB formalism matrix elements. The correction that describes charge fluctuations is represented by an off-diagonal contribution dependent on Mulliken charges ($H^1_{\mu\nu}$).

4.1.4.7 Forces

The DFTB method is born as a method to deal with very large systems for running both molecular dynamics, global optimization methods, or energy calculations on large amount of different systems. For many of these the calculation of not only the energy but also its derivatives, mainly the force. This can be obtained by deriving the final expression of the total SCC-DFTB energy with respct to the system coordinates :

$$\begin{aligned}\mathbf{F}_\alpha = &-\sum_i^{occ} n_i \sum_{\mu\nu} c_{\mu i} c_{\nu i} \left[\frac{\partial H^0_{\mu\nu}}{\partial \mathbf{R}_\alpha} - \left(\varepsilon_i - \frac{H^1_{\mu\nu}}{S_{\mu\nu}}\right)\frac{\partial S_{\mu\nu}}{\partial \mathbf{R}_\alpha}\right] \\ &- \Delta q_\alpha \sum_\xi^N \frac{\partial \gamma_{\alpha\xi}}{\partial \mathbf{R}_\alpha}\Delta q_\xi - \frac{\partial E_{\text{rep}}}{\partial \mathbf{R}_\alpha} - \frac{\partial E_{spin}}{\partial R_\alpha}\end{aligned} \tag{4.57}$$

It is trivial though important to note that in the NCC-DFTB version, terms depending on the second order energy disappear with its subsequent simplifications and save in computational time.

4.1.5 Global Optimization: Parallel-Tempering Molecular Dynamics (PTMD)

As mentioned in the Section 3.1, for atom-based systems, the PES gives the potential energy as a function of the system's given coordinates, (PES $\equiv V(\mathbf{r})$). The dimension of the PES grows as the system's size increases, by $3N-6$ where N is the number of atoms in the system. The number of minima in that PES grows as well as the PES grows in dimension, being the growth relation in this case higher than polynomial with respect to N, it is indeed thought to possibly be exponential [249]. Studies on the evolution of local minima with respect to, both the system's size and the type of potential have been performed during many years. These studies take the two body potentials like Lennard-Jones or Morse potentials to ease the computational effort. Regarding the size dependence, it was found that around 1000 different minima for 13 atoms [250, 251] while for 55 atoms, the number of different minima was found to be around 10^{12} [252]. Regarding the potential dependence, one can expect that systems with short-range (sticky) potentials will present a larger number of minima and a rougher PES than systems with soft potentials [253]. An important concept in PES landscape is the basin, the domain of all points whose local optimization leads to the same local minimum.

Although the tests were done using two-body potentials, it's not difficult to see that the same principle states for all types of interactions leading to different atomic arrangements (atoms, molecules, clusters, nanoparticles, condensed phases, both crystalline and amorphous). A complete sampling of the whole PES in search for all the minima is then clearly impossible, hence the need of finding algorithms which are able to find a fast convergence to low-lying minima. These algorithms are called Global optimization methods. However, depending on the interaction potential,

size, and composition of the cluster, there are PESs where most algorithms converge fast, and others (typically highly symmetric ones) where the absolute minimum is difficult to find. It is to be pointed out that no global optimization method is able to guarantee with absolute certainty that a minimum is really the lowest one.

4.1.5.1 Global optimization method families

Global Optimization has had an incredible proliferation of methods due to its applicability in fields that cover not only atomic systems, but economics, work scheduling, safety verification, or non-linear curve fitting. In the field of Potential/Gibbs Energy optimization as a function of atomic coordinates most methods are based, or combine the following families:

Genetic algorithms [254, 255] are based on the analogy of evolution through natural selection of, in this case, the Potential Energy. Simulation is started with a set of candidate structures. Each structure has a chromosome, its coordinates, and they can be exchanged between candidates or mutated (add a random perurbation) to generate a second generation which is compared to the older one in terms of potential energy to decide it's survival. The process is repeated with candidates presenting a better stability (including parents).

Basin Hopping [256, 257] is based on the canonical Monte-Carlo simulation at constant temperature on a new surface where,

$$\tilde{E}(\mathbf{R}) = \min_l(E(\mathbf{R})) \tag{4.58}$$

i.e. all the configurations have the energy of their basin minimum. The algorithms works by taking an initial configuration c_i, performing a random move to generate a new one c_{i+1}. A local optimization is performed to obtain the energy of its basin minimum and assign it to the configuration c_{i+1} however the geometrical configuration stays the one before the local optimization. Then, the Metropolis algorithm is applied to check whether the change is accepted or not. If it is accepted a new random move is taken from the c_{i+1} (not the one obtained after local optimization). Multiple runs can be run in parallel to optimize its efficiency.

Umbrella sampling [258, 259] is part of the so called biased molecular dynamics simulation on which the PES is modified to increase the probability to reach some kinetically forbidden zones. In the case of Umbrella sampling an attractive term in selected degrees of freedom, typically the ones considered to possibly be ways to a transistion state, is applied to favour the evolution of the system towards that degree f freedom. A prior knowledge of the system is needed for this kind of simulations.

Metadynamics [260] makes part of the biased methods, in this case a time dependent bias to the total potential energy, which drives the system to escape local free energy minimaby placing repulsive markers in the space spanned by a small number of chemically relevant collective variables.

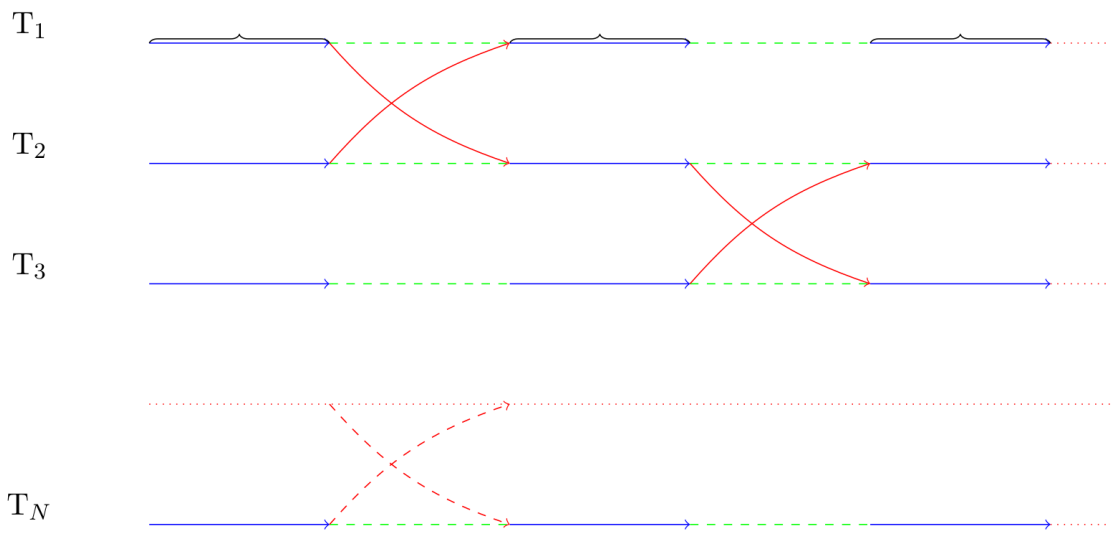

Figure 4.1: Scheme representing the working principle of the PTMD

Simulated anealing [261] makes part of the unbiased methods, which preserve the real shape of the system. This one is evolved at constant high T on the untransformed PES by either Monte Carlo or molecular dynamics, then slowly cooled down until a stable configuration is reached. The system can at that point be heated again and repeat the process.

4.1.5.2 Parallel-Tempering Molecular Dynamics

The Parallel Tempering Molecular Dynamics (PTMD) is the method that we have chosen to use as global optimization method to obtain the Ru clusters and nanoparticles. It consists in generating a number of replicas of the same system $C_i(i = 1, ..., N)$. An ordered discrete set of N temperatures among a given range $T_i(i = 1, ..., N)$, is generated and each temperature T_i is assigned to each replica C_i.For each replica/temperature a molecular dynamics trajectory is run independently, and in parallel to the others. At given number of MD steps exchanges in atomic configurations between neighbouring temperatures are tried, C_i can only exchange configurations with C_{i+1} and C_{i-1} corresponding to temperatures T_{i+1} and T_{i-1} respectively. The principle of the method is represented by Figure 4.1

The probability of carrying out a configurational exchange between two replicas is given by the Metropolis algorithm [262]:

$$W(C_i \longleftrightarrow C_j) = \min(1, e^{\Delta}), \tag{4.59}$$

where $W(C_i \longrightarrow C_j)$ is the exchange probability between two neighbouring replicas C_i and C_j, $\Delta = \Delta\beta\Delta E$. $\Delta\beta = \beta_i - \beta_j$ corresponds to the difference in the inverse of T_i and T_j and $\Delta E = E(C_i) - E(C_j)$ is the difference in potential energy between C_i and C_j. If the replica with higher temperature C_j (let's suppose $T_j > T_i$) has a lower potential energy than C_i, both $\Delta\beta$ and ΔE are positive, 1 is smaller than e^{Δ} and the exchange is always accepted. Else the probability of acceptance is e^{Δ} which is agorithmically done by generating a pseudo-random number χ and accepting only if χ is lower than e^{Δ}. In order to accelerate the equilibration of the system after the exchange, velocities of atoms are rescaled the following way:

$$v_\alpha^{\text{new}} = \sqrt{\frac{T^{\text{new}}}{T^{\text{old}}}} v_\alpha^{\text{old}} \tag{4.60}$$

The choice for extreme temperatures T_1 and T_N is of paramount importance to be able to explore the whole PES. T_1 must be a temperature sufficiently low to trap trajectories in any local minimum. T_N must be chosen to allow to overpass all barriers, typically one that is higher than melting point for solids, or dissociation temperature for molecular species. Finally intermediate temperatures must be chosen so as to provide sufficient overlap between the density of states of the adjacent replicas. Indeed, if this overlap is too small, exchange probability becomes also too small leading to an inefficient algorithm and thus a lack of exploration of the PES. If the overlap is too big, the algorithm is redundantly simulating trajectories and becomes inefficient in terms of computational cost.

4.2 Parametrization and computational details

The electronic parametrization used for evaluating the integrals in Equation (4.42) is that of Wahiduzzaman and collaborators [98] which have used the flexibility of the atomic orbital confinement to provide a new parametrization optimizing the band structure of the homogeneous bulk systems throughout the periodic table. We used the Slater Koster file kindly provided to us for ruthenium-ruthenium interactions. This parametrization only contains the electronic part and a Ru-Ru repulsive potential, as described in Section 4.1.4.4, had to be adjusted. The difficulty of course reside on the fact that many spin states may contribute in small clusters, often being closely degenerate and making the repulsive potential obtained from the dimer not extendable to bigger clusters.

4.2.1 Spin Treatment

The account of spin is compulsory on the atom to account for the Hundt's rule type coupling of ruthenium and ensure that the quintet term with d^7s^1 configuration is actually the atomic ground state, with respect to a d^8 singlet term. The DFTB framework used have been the restricted one, namely constraining doubly occupied orbitals to have the same α and β spatial orbitals. Convergence problems frequently occur in case of open shells. We solve this problem by incorporating a Fermi smoothing of the occupations, considering separate Fermi levels and hence separate Fermi occupations for the α and β spinorbitals, which is compatible with the treatment of open shells. This was able to smooth the switches of the orbital occupation numbers between values 2, 1 and 0 and solve the SCC convergency problems.

Finally the spin constant was taken as $\zeta_{Ru} = 0.0126178$ Hartree. With this constant, the splitting between the quintet d^7s^1 and the singlet d^8 configurations is $\delta E = 1.779$ eV. It is quite difficult to really fit an actual atomic spectrum, since DFTB does not actually include the necessary couplings to be associated with actual multiplet configurations. Nevertheless, this presents a more reasonable description of the atomic states and of course of the molecular or cluster correlations associated with these states than without accounting for it at all. Single DFTB determinants cannot generally be considered as spin configurations, except in the case of closed

shells or maximum spin in the case of open shells. Therefore the present scheme can be considered as a Restricted Open shell DFTB scheme only ensuring the value of the spin projection difference $\Sigma = (n_i^\alpha - n_i^\beta)/2$

4.2.2 Repulsive potential Fitting

In principle, the fitting of the repulsive potential can be done from total energy calculations on dimers[80–83]. This is somewhat tedious for systems such as ruthenium clusters which present many spin-states, and for which neither the DFT nor the DFTB calculation along a full evaporation pathway do dissociate correctly towards the sum of the independent atom energies, except for the highest multiplet, sometimes quite high above the true ground state in the compact region. Actually the ambiguity remains between the nature of the true ground state in Ru_2. While CASPT2 type and some DFT functionals provide the $^5\Sigma_g^+$ state as the lowest, the frequency of $^5\Delta_u$, in principle higher in energy, seems to be in better agreement with the spectroscopic data. Thus the repulsive potential was supposed to fit only the short distance range of the potentials taking as the asymptotic limit the dissociated atom energies calculated independently. The final fit was done considering the dimer Ru_2 and octamer Ru_8 as reference situations. The Ru_8 was shown to have a simple cubic structure very convenient for parametrization of two-body integrals with the distance, while Ru_2 ensured the absence of undesired intruder states leading to dimerization. The Ru-Ru repulsive potential was taken as $E_{RuRu}^{rep} = Aexp(-Br) + \frac{C}{r^{12}} +$ and adjusted through a least square fit in order to reproduce at best DFT/PBE calculations of Ru_2 and cubic Ru_8 as a function of the interatomic distance. Actual values for A, B and C are 640 E_h, 3.82785 Åand 19.2984 $E_h/Å^{12}$ Figure 4.2 shows the comparison between DFT and present DFTB calculations for Ru_8.

4.2.3 PTMD details

Parallel-Tempering Molecular Dynamics [263] (PTMD), which is sometimes also known as the "replica-exchange" algorithm, was used in combination with periodic quenching to achieve global optimization of neutral, cationic and anionic clusters in the range $n = 3 - 20$. The PTMD scheme involved simultaneous MD runs at 60 temperatures equally di stributed in the range 500-8000 K, the energy being computed at the $DFTB^0$ level. Fragmentation was hindered by using a spherical box. The MD timestep was set at 2 fs and exchanges were attempted using the Metropolis energy criterion every 100 timesteps. A chain of 5 Nose-Hoover thermostats [264, 265] with a unique frequency of 80 cm^{-1} was used to maintain the temperature.

Both the PTMD process and its subsequent relaxation was carried out for neutrals cationic and anionic clusters, starting from essentially random structures. The lengths of the trajectories were 0.2 ns, (100,000 PTMD steps). Over 1000 configurations, equally spaced in time, were selected from the trajectories at medium temperature (2000 K). They were subsequently locally optimized at the SCC-DFTB level with conjugated gradient scheme, providing a wealth of stable structures. This procedure generated a bunch of low energy isomers. All DFTB calculations were performed using the deMonNano code [266], in which the PTMD scheme was implemented [267]

For nanoparticles (e.g. cluster sizes larger than n=55), PTMD was not used and

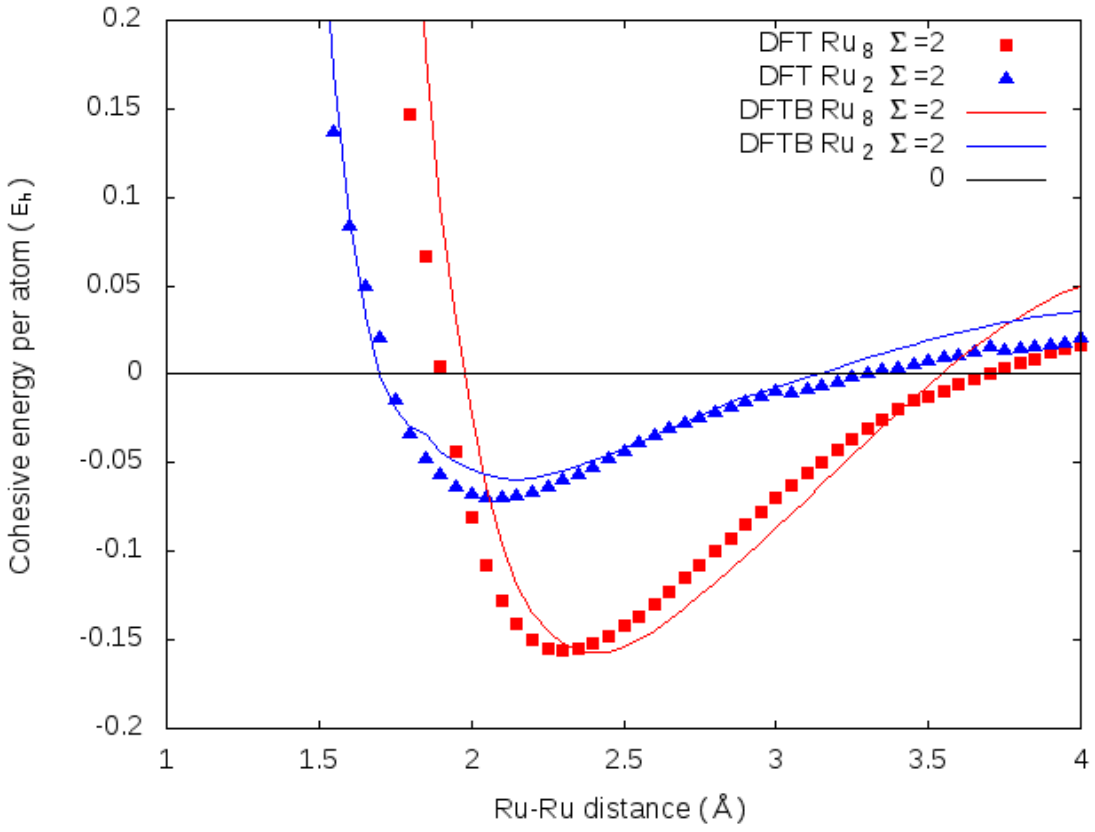

Figure 4.2: Cohesive energy per atom for Ru_8 and Ru_2 as a function of the internuclear distance : DFT/PBE (reference) and present DFTB

relaxation was made starting from different cuts of hcp, fcc crystalline structures adopting, cuboctahedral, icosahedral, and other truncated octahedral shapes.

4.3 Results and discussion

In this section the results obtained using the DFTB method are presented and compared to the existing literature data. The comparison is done with clusters in the size range n=3-20 atoms, both neutral, cationic and anionic, and nanoparticles both neutral and cationic ones. Structural, energetic and spin properties are analyzed and compared.

4.3.1 Structure of small clusters in the range n=3-20

For clusters up to n=20, all total spin projection configurations between $\Sigma = 0$ and the maximum spin projection $\Sigma_{max} = 2n$ have been considered.

4.3.1.1 Neutral Clusters

The characteristics (spin projection and spatial symmetry) of the three lowest-energy states and, in the case that the 2nd lowest significantly geometrically different isomer does not fall inside the mentioned three, the 2nd lowest significantly geometrically different isomer is listed as well on Table 4.1. For all of them their structural excitation energies above the lowest one are also listed in Table 4.1 are plotted . The various geometries in various spin states are often indistinguishable, while the corresponding isomers are listed in the tables, they have not been systematically plotted. Thus, isomer (a) is systematically plotted in Figure 4.3 and a second geometry is also given, namely that of the lowest energy isomer exhibiting a geometry different from that of isomer (a). The lowest structure for Ru_3 is an isosceles triangle (3a) with a high spin state ($\Sigma = 6$), while the second one is also a C_{2v} triangle, however with low spin projection ($\Sigma = 0$). Ru_4 is a square (4a) and a second isomer with a bent rhombus shape (4c) can be found. Ru_5 is a triangular basis bipyramid (5a) with high spin projection (Σ=9), a higher isomer (5e) is a capped square. Ru_6 is a deformed square bi-pyramid with quite high spin (Σ=7). The medium size structure (n=7-13) are mostly built around cubic motifs (7a, 8a, 9a, 9b, 10c, 12a, 12f, 13a, 13b) with cubic seeds consisting of the very regular clusters cubic Ru_8 (8a) and parallepipedic Ru_{12} and either defects (7a) or extra atoms organized in various capping patterns. Exceptions are provided by Ru_{10} (a) which occurs to be a double layered pentagon with D_{5h} symmetry, and Ru_{11} (11e) consisting of 10a plus one capping atom. In the range $n = 14 - 20$, several motifs, namely cubes, prisms and pentagonal or hexagonal structures appear and contribute to the various isomer geometries. Another point that deserves to be mentionned is that there is a quite significant degeneracy, even between the lowest-energy isomers and even for the smaller sizes n=3-6 where isomers (a) and (b) are separated by less than 0.06 eV. In many cases the structural excitation of the 3-4 lowest isomers is less than $\sim$ 0.5 eV.

The present DFTB results can be compared with previous calculations. As concerns DFTB, the only available result in this range is that of Shi et al. [92] who optimized the structure of Ru_{13} which was found to be the same as our present

isomer Ru_{13}(a). Most other calculations are DFT calculations. Demiroglu et al. [90] published DFT/PBE structures in the range n=3-12. The present DFTB is consistent with the former data except for Ru_5 and Ru_7 in which case the DFT structures are only found at higher energy with DFTB (Ru_5(e) and $Ru_7(g)$). One of the most thorough investigation on neutral Ru_n clusters in the range n=3-12 and larger ones (n=27,48,55 and 64) is the work of Zhang *et al.*[86] using PBC calculations with the PW91 functional and relaxing a number of guesses and crystal truncated blocks. They obtain a deformed (C_s) tetrahedron structure for Ru_4, a square pyramid for Ru_5 while the triangular bipyramid is found as the second isomer, a triangular prism for Ru_6, a compact C_{4v} structure for Ru_7, a cube for Ru_8, capped cubic structures for n=9, 10, 11 up to the double cube for Ru_{12} capped by a single atom in Ru_{13}. Li et al. [89] carried out a later DFT/PBC investigation in the range n=2-14 with a GGA functional, also relaxing specific guess structures. The present results are quite consistent with their for the lowest isomer (a). There are few exceptions, namely for n=5 (the lowest DFT structure being a capped square and our Ru_5 (a) bipyramidal structure being their second isomer, n=13 where again our DFTB lowest minimum is their second structure, and n=14 which they find a double hexagon structure and again our DFTB structure is similar to their second one. Aguilera-Granja et al. [88] also investigated ruthenium clusters by means of DFT in the range n=2-19 using the PBC code SIESTA within the GGA approximation for the exchange-correlation functional. They obtained the same results consistent with the other authors, Ru_4 square, Ru_5 square pyramid, Ru_6 prism, Ru_7 defected cube, Ru_8 cube, face-capped cube, Ru_{10} double pentagon, Ru_{11} capped cube, Ru_{12} double cube, Ru_{13} as our second isomer (8+5), Ru_{14} double hexagon, side-capped for Ru_{15}, deformation from $3 \times 3 \times 2$ or hexagonal and hexagonal for Ru_{18}, same capped for Ru_{19}. Let us notice that in the case n=14, we have checked that the DFTB double hexagon is a true minimum but it lies more than one eV above the global DFTB global minimum (a).

n	isomer	ΔE (eV)	Sym	Σ	n	isomer	ΔE (eV)	Sym	Σ
3	a	0.0000	C_{2v}	6	12	a	0.0000	D_{4h}	0
	b	0.1391	D_{3h}	5		b	0.4028	D_{4h}	1
	c	0.2058	D_{3h}	4		c	0.6975	D_{4h}	2
	d	0.4112	C_{2v}	0		f	1.5246	C_{2v}	0
4	a	0.0000	D_{4h}	2	13	a	0.0000	C_s	0
	b	0.0422	D_{2d}	7		b	0.1049	C_1	0
	c	0.0457	D_{2h}	0		c	0.1313	C_1	1
5	a	0.0000	D_{3h}	9	14	a	0.0000	C_{2v}	0
	b	0.2440	C_{2v}	8		b	0.0285	C_{2v}	1
	c	0.6034	C_s	7		c	0.1064	C_{2v}	2
	e	0.9851	C_s	6		d	0.3017	C_s	0
6	a	0.0000	D_3	10	15	a	0.0000	C_{2v}	0
	b	0.0321	D_{3h}	0		b	0.1048	C_{2v}	1
	c	0.0408	D_3	9		c	0.3441	C_1	0
7	a	0.0000	C_{3v}	0	16	a	0.0000	C_{2v}	1
	b	0.0564	C_{3v}	1		b	0.0627	C_{2v}	0
	c	0.1838	C_{3v}	4		c	0.2438	C_{2v}	2
	g	0.5270	C_{2v}	4		d	0.3555	C_s	0
8	a	0.0000	O_h	2	17	a	0.0000	C_1	1
	b	0.1370	O_h	1		b	0.0571	C_1	0
	c	0.2073	O_h	0		c	0.1703	C_1	2
	h	1.5311	C_{2v}	2		d	0.2439	C_1	0
9	a	0.0000	C_{2v}	2	18	a	0.0000	C_{2v}	0
	b	0.0242	C_s	1		b	0.0264	C_{2v}	1
	c	0.0899	C_{2v}	0		c	0.1813	C_{2v}	2
	e	0.3532	C_s	2		d	0.1859	C_{2v}	0
10	a	0.0000	D_{5h}	5	19	a	0.0000	C_s	0
	b	0.2105	D_{5h}	4		b	0.0115	C_1	1
	c	0.4013	C_{2v}	0		c	0.0176	C_1	0
11	a	0.0000	C_s	0	20	a	0.0000	D_{2h}	0
	b	0.0852	C_s	1		b	0.0908	D_{2h}	1
	c	0.1199	C_s	2		c	0.1038	C_2	0
	e	0.3977	C_{2v}	4					

Table 4.1: Excitation energies, spatial symmetry and spin projection of isomers of neutral Ru_n clusters for sizes 3-20. The three lowest-energy isomers and the next one with significantly different geometry are given

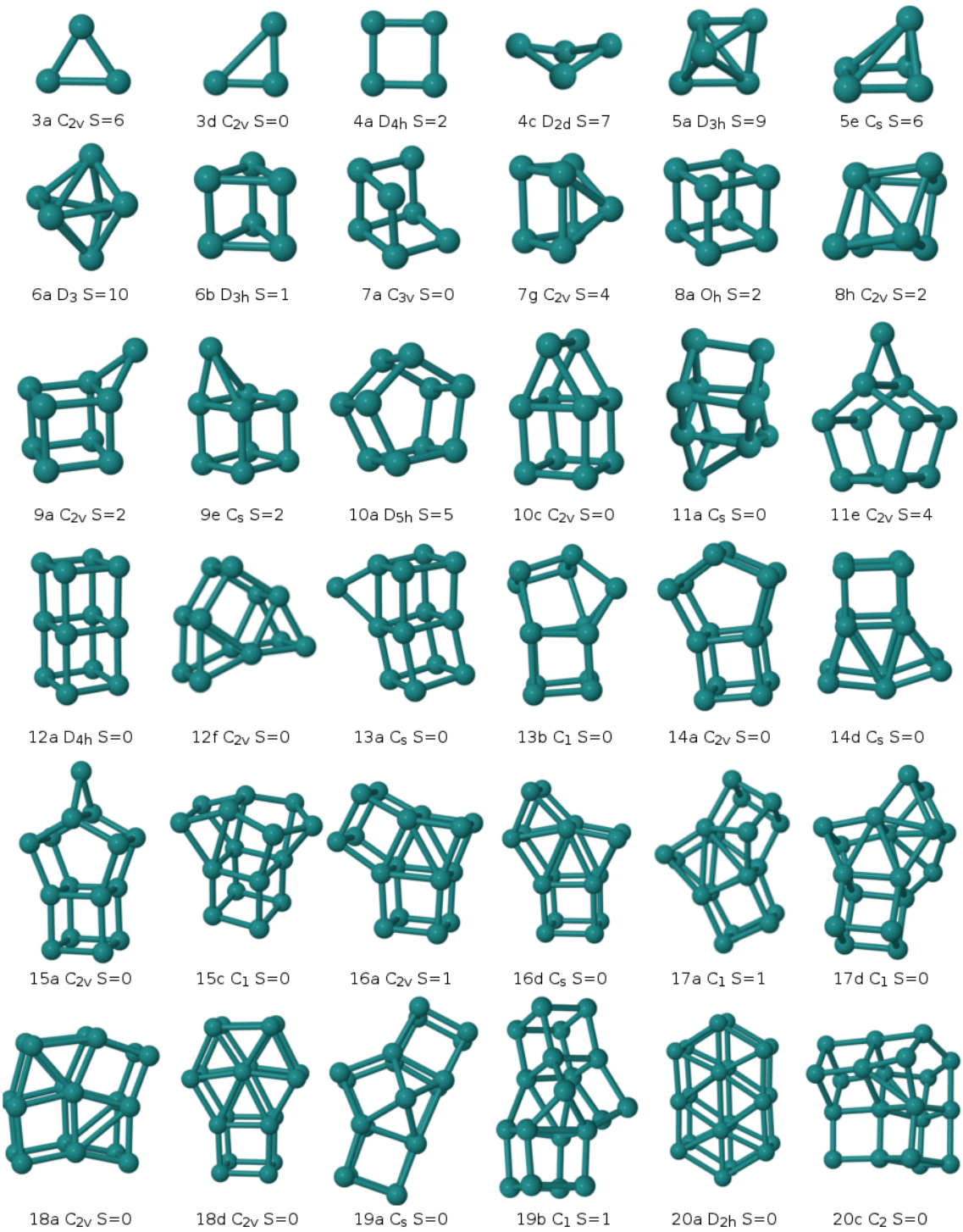

Figure 4.3: Structures of low-energy neutral Ru_n clusters, n=1,20. Spatial symmetry and spin are indicated

4.3.1.2 Cation clusters

The cationic cluster structures are displayed in Figure 4.4. The first result is that the positive charge does not induce extremely strong reorganization in the cluster geometries even for small clusters with $n < 14$. The first exception occurs at $n = 6$ where the ordering of the two lowest energy isomers is switched with respect to the neutral, the lowest one now being the prism with D_{3h} symmetry (6a in Figure 4.4). Isomer 10c is slightly different from neutral 10c, the two side atoms now capping an edge instead of a face. Isomer 11e is less ordered than its neutral correspondent. A significant change is observed for isomer 15a, the geometry of which results from the capping of one atom onto the structure of Ru_{14}. For larger sizes, some changes do appear, possibly linked to the increased possibilities of mixing cubic , pentagonal and rhombic/hexagonal motifs. Nevertheless, the structures of lowest isomers of Ru_{18} and Ru_{20} (18a and 20a) are the same as their neutral analogs, respectively.

There are much fewer theoretical reports about the structure of cations. The present results can be compared to the recent work of Kerpal et al.[268] who discussed the IR vibrational spectra and structures of Ru_7^+, Ru_8^+ and Ru_9^+ comparing DFT calculations and experiments. They found that the lowest energy structures of those three clusters was essentially built around a cubic motif with a defecting atom for n=7 and an extra one for n=9. The present DFTB results are essentially consistent with the DFT/PBE calculations of Kerpal et al. If the situation is explored in more details, slightly different competing cubic-like structures were found by Kerpal et al. for several sizes, presenting more or less symmetry. In the case of he heptamer the two DFT/PBE structure both have C_s symmetries. In the case of the octamer, the lowest energy structure was a perfect O_h cube, while a close-lying D_{2d} isomer was found the spectra of which corresponded better to the experimental one. The explanation given by the authors is that due to its high symmetry, the IR spectrum of the O_h cube consists in a single line, whereas significantly more active modes are observed for the isomer with lower symmetry, consistently with the experimental spectrum. Again in the case n=9, the previous authors found that the spectra of their second isomer (actually the lowest isomer 9a found wit DFTB) , presenting an edge capping rather than a face capping, did actually match better the experimental data. The previous authors have also shown that the spectra of clusters optimized with the DFT/PBE0 framework, namely a hybrid functional are strongly different and in much worse agreement with the IR experiment. Concerning the details of the IR spectra for the structures mentioned above, one may point out that the harmonic frequencies may not be accurate enough for a final assignment and that non harmonic dynamical spectra might be needed for cases where closely related topological structures yield very different IR spectra. For instance, the Ru_8 case would deserve inclusion of dynamical Jahn-Teller deformations which would enhance the forbidden transitions at equilibrium. Such investigation is possible with DFTB, but overpasses the scope of the present paper.

n	isomer	ΔE (eV)	Sym	Σ	n	isomer	ΔE (eV)	Sym	Σ
3	a	0.0000	C_{2v}	5.5	12	a	0.0000	D_{4h}	0.5
	b	0.0504	D_{3h}	4.5		b	0.3721	D_{4h}	1.5
	c	0.0896	D_{3h}	3.5		c	0.7779	D_{4h}	2.5
	d	0.2943	C_{2v}	0.5		e	1.3394	C_{2v}	3.5
4	a	0.0000	D_{4h}	1.5	13	a	0.0000	C_1	0.5
	b	0.0558	D_{2h}	2.5		b	0.2897	C_1	1.5
	c	0.0769	D_{2h}	0.5		c	0.3030	C_1	0.5
	d	0.1861	D_{2h}	7.5					
5	a	0.0000	C_{2v}	9.5	14	a	0.0000	C_{2v}	1.5
	b	0.0054	D_{3h}	8.5		b	0.0652	C_{2v}	0.5
	c	0.1100	C_{2v}	9.5		c	0.2373	C_{2v}	2.5
						d	0.5719	C_s	1.5
6	a	0.0000	D_{3h}	0.5	15	a	0.0000	C_{2v}	0.5
	b	0.0617	D_{3h}	1.5		b	0.1088	C_1	0.5
	c	0.1488	C_{2v}	3.5		c	0.1853	C_{2v}	1.5
	f	0.3896	D_{2d}	10.5					
7	a	0.0000	C_{3v}	0.5	16	a	0.0000	C_{2v}	0.5
	b	0.2617	C_{3v}	1.5		b	0.2493	C_{2v}	1.5
	c	0.3003	C_{3v}	3.5		c	0.4865	C_s	0.5
	e	0.5852	C_{2v}	1.5					
8	a	0.0000	O_h	1.5	17	a	0.0000	C_1	0.5
	b	0.0499	O_h	0.5		b	0.1191	C_1	1.5
	c	0.3116	O_h	2.5		c	0.4031	C_1	2.5
	g	1.7428	C_{2v}	2.5		e	0.5884	C_1	0.5
9	a	0.0000	C_{2v}	1.5	18	a	0.0000	C_{2v}	0.5
	b	0.0193	C_{2v}	0.5		b	0.1727	C_{2v}	1.5
	c	0.1637	C_{2v}	2.5		c	0.1857	C_{2v}	0.5
	d	0.2480	C_{3v}	0.5					
10	a	0.0000	D_{5h}	4.5	19	a	0.0000	C_1	0.5
	b	0.1318	D_{5h}	3.5		b	0.0331	C_s	0.5
	c	0.1584	C_{2v}	0.5		c	0.1925	C_1	1.5
11	a	0.0000	C_s	0.5	20	a	0.0000	D_{2h}	0.5
	b	0.0531	C_s	1.5		b	0.2591	D_{2h}	1.5
	c	0.3306	C_s	2.5		c	0.2885	C_2	0.5
	e	0.5034	C_1	1.5					

Table 4.2: Excitation energies, spatial symmetries and spin projections of the lowest-energy isomers of Ru_n^+ clusters for sizes 3-20. The three lowest energy isomers and the next one with significantly different geometry are given

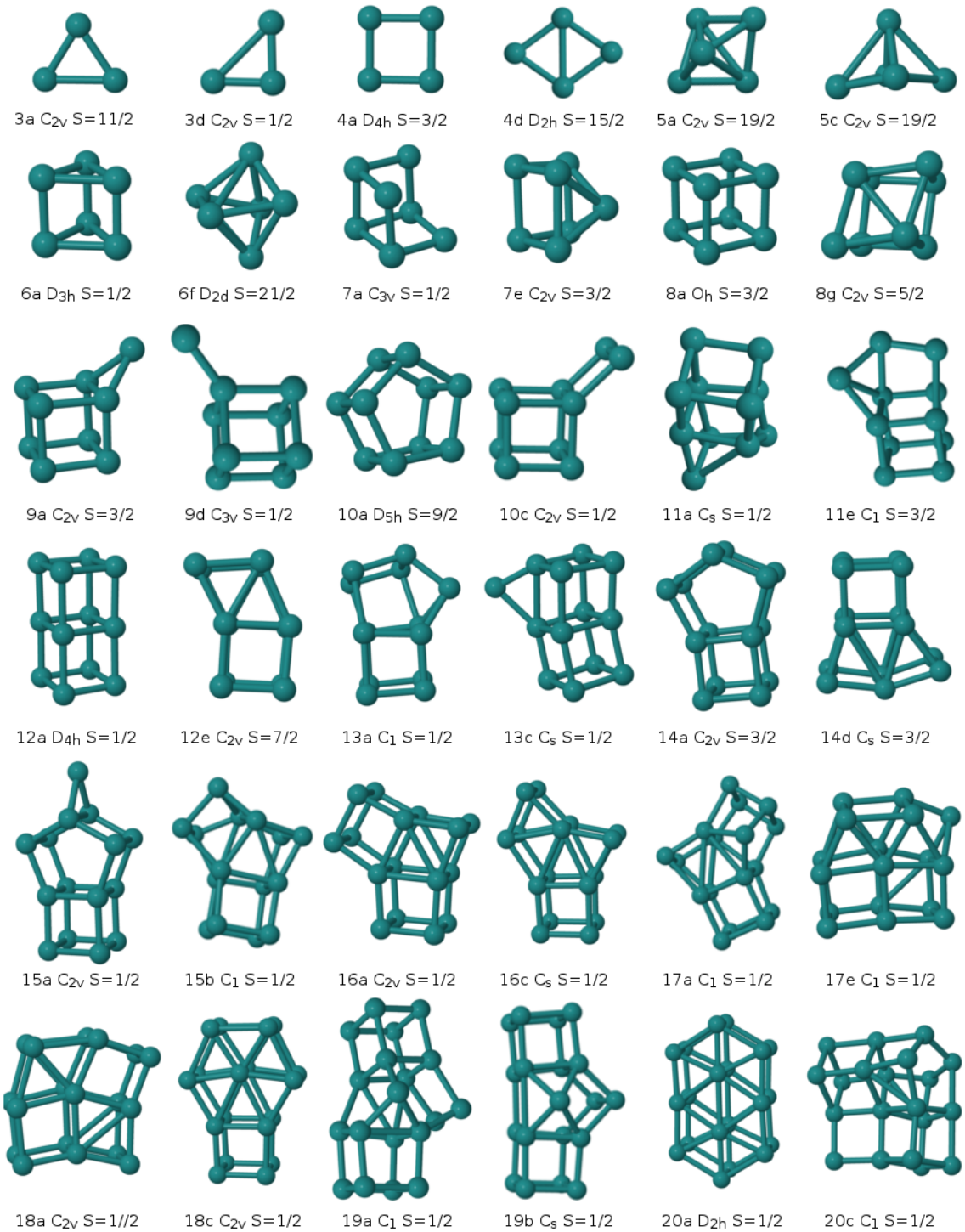

Figure 4.4: Structures of the lowest-energy Ru_n^+ cationic clusters, n=1,20. Spatial symmetry and spin are indicated

4.3.1.3 Anion clusters

The structure of small negative clusters anions in the range n=8-20 was investigated by Waldt et al.[269, 270] in a work combining Trapped Ion Electron diffraction and DFT calculations within a TPSS/Def2-SVP scheme. In the range 3-11, the present isomers (a) generally agree with the lowest DFT isomers found by Waldt et al. Two exceptions are Ru_5^- and Ru_7^- which are found as a bipyramid and an incomplete cube with DFTB, instead of a pyramid and a more compact C_s structure respectively in DFT. A small difference is also observed in the capping of the 9th atom in Ru_9^-(a), which locates on the cube edge in the case of DFTB, rather than on a face in DFT. Note that it is not always the lowest DFT isomer which provides the better concordance between the simulated diffraction pattern with the TIED data. In the range n=13-20, the present DFTB results differ from those of Waldt et al. The DFT data indicate a strong stability of structures based on a double hexagonal ring (Ru_{12}^- . The DFTB results are only in agreement with the former for Ru_{20}^- (energy isomer 7a), eventhough isomer (c) of Ru_{18}^- corresponds to the lowest DFT structure and that incomplete double hexagonal rings can be observed in Ru_{16}^-(c), and Ru_{17}^-(e). Let us mention that we have systematically checked the lowest-energy isomers of Waldt et al. in this range and they were not found as the lowest energy ones with DFTB (except for n=20).

n	isomer	ΔE (eV)	sym	S	n	isomer	ΔE (eV)	sym	S
3	a	0,0000	D_{3h}	5,5	12	a	0,0000	D_{4h}	0,5
	b	0,2744	D_{3h}	4,5		b	0,3708	D_{4h}	1,5
	c	0,6501	C_{2v}	3,5		c	0,6166	D_{4h}	2,5
	d	0,6837	C_{2v}	0,5		h	1,4309	C_{2v}	0,5
4	a	0,0000	D_{2d}	6,5	13	a	0,0000	C_s	0,5
	b	0,0957	T_d	6,5		b	0,2537	C_1	1,5
	c	0,1051	T_d	7,5		c	0,3484	C_1	0,5
5	a	0,0000	C_{2v}	8,5	14	a	0,0000	C_{2v}	0,5
	b	0,4180	C_{2v}	8,5		b	0,1047	C_{2v}	1,5
	c	0,7394	C_{2v}	6,5		c	0,1102	C_{2v}	2,5
	d	0,9614	C_s	6,5		d	0,2320	C_s	0,5
6	a	0,0000	D_3	9,5	15	a	0,0000	C_{2v}	0,5
	b	0,3289	D_{3h}	6,5		b	0,0483	C_{2v}	1,5
	c	0,3899	D_3	8,5		c	0,3117	C_{2v}	2,5
						d	0,3993	C_1	0,5
7	a	0,0000	C_{3v}	1,5	16	a	0,0000	C_{2v}	1,5
	b	0,0128	C_{3v}	4,5		b	0,0983	C_{2v}	0,5
	c	0,0331	C_{3v}	0,5		c	0,2394	C_{2v}	2,5
	f	0,2134	C_s	10,5		d	0,2693	C_{2v}	0,5
8	a	0,0000	O_h	2,5	17	a	0,0000	C_1	1,5
	b	0,1745	O_h	1,5		b	0,0369	C_1	0,5
	c	0,2314	O_h	3,5		c	0,1302	C_1	2,5
	h	1,4748	C_{2v}	2,5		e	0,3139	C_1	0,5
9	a	0,0000	C_s	2,5	18	a	0,0000	C_{2v}	1,5
	b	0,0099	C_s	1,5		b	0,0250	C_{2v}	0,5
	c	0,0871	C_s	0,5		c	0,1811	C_{2v}	0,5
	e	0,2830	C_{3v}	0,5					
10	a	0,0000	D_{5h}	4,5	19	a	0,0000	C_1	0,5
	b	0,0506	D_{5h}	5,5		b	0,0152	C_1	1,5
	c	0,0586	C_{2v}	0,5		c	0,0526	C_s	0,5
11	a	0,0000	C_s	0,5	20	a	0,0000	C_1	0,5
	b	0,0741	C_s	2,5		b	0,1863	D_{2h}	0,5
	c	0,0811	C_s	1,5		c	0,1927	C_1	1,5
	e	0,3909	C_1	0,5					

Table 4.3: Excitation energies, spin and spatial symmetries of Ru_n^- clusters for sizes 3-20. The three lowest energy isomers and the next one with signicantly different geometry are listed.

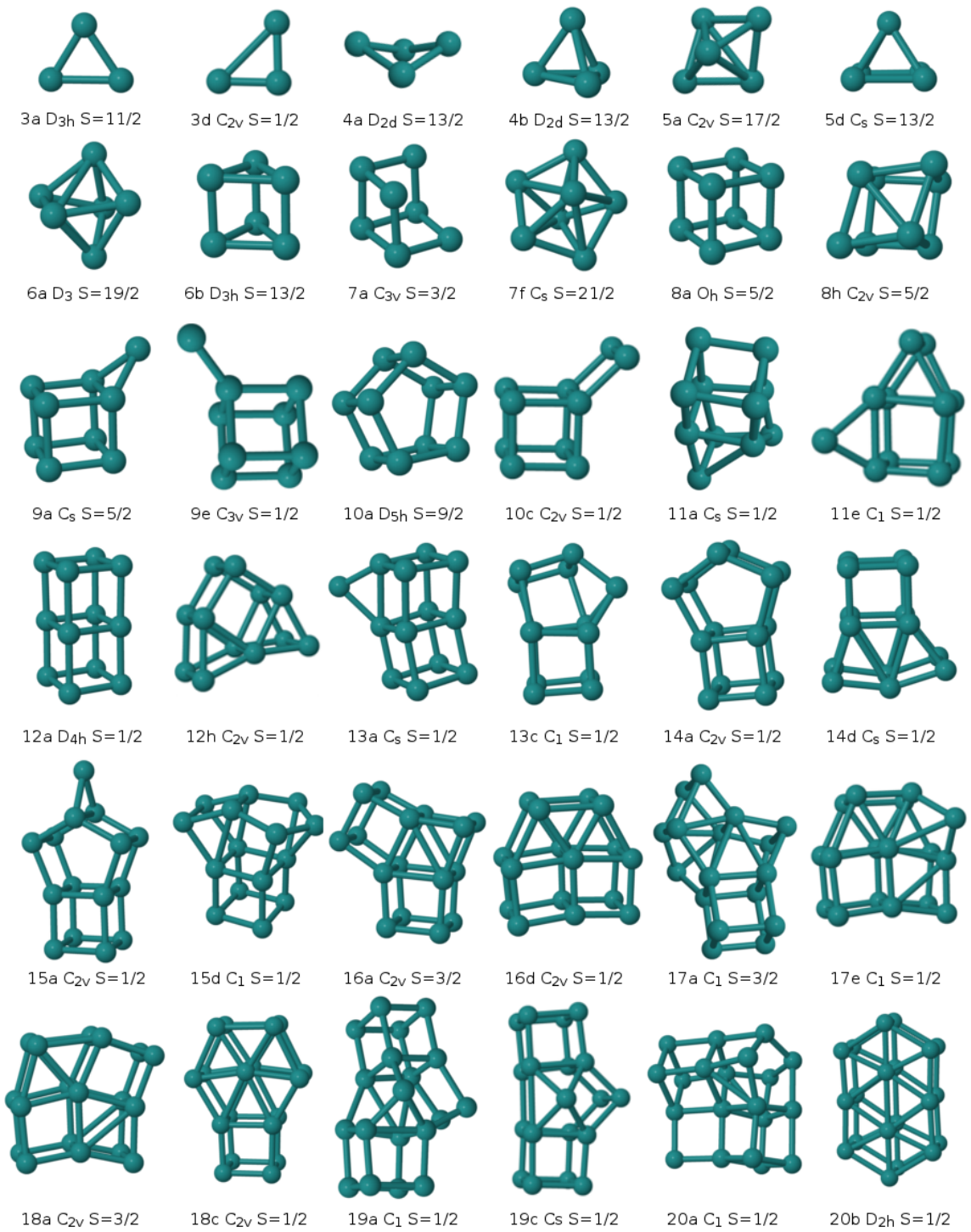

Figure 4.5: Structure of the lowest energy Ru_n^- anionic clusters, n=1,20. Spatial symmetry and spin are indicated

4.3.2 Nanoparticles

Several groups have been recently involved in the computational studies of the structure, stability and behaviour of larger clusters or nanoparticles. Soini et al.[95] published a detailed comparison of the stability of nanoparticles, relaxed either from fcc-based structures (icosahedrons and cuboctahedrons, truncated octahedrons) or hcp-based (truncated hcp blocks). They obtained consistent results using either scalar relativistic all-electron Gaussian type DFT/PBC calculations with ultra-soft relativistic potentials, except for a systematic difference in the cohesive energies. They inferred that hcp-type nanoparticles become energetically quite stable above n=55, behaving similarly to bulk material. From these calculations they provided extrapolation to the bulk for fcc and hcp nanoparticles. Very recently, Nanba et al. [94] extended the former study still using a DFT/PBC/PBE scheme adapted to large systems and provided an estimation of the cross-over between fcc-based structures and hcp-based nanoparticles over a larger size range n=55-1557, also calculated relaxing model geometries (however the truncated octahedrons and TO model candidates being different from those of Soini et al. They concluded that at large sizes, the hcp-type structures were the most stables and that among the fcc-type structures, the icosahedral was the most stable and even the most stable below N=103 atoms even with respect to the hcp ones. Posterior to this paper, it was shown experimentally that whereas the fcc phase for bulk ruthenium is not stable, fcc nanoparticles in diameter range 2-5.3 nm could be prepared using chemical reduction on an Al_2O_3 substrate.

We have tested with the present DFTB approach the nanoparticles samples of Soini et al., namely cuboctahedrons (n=55, 147 and 309), icosahedrons (n=55, 147 and 309), truncated octahedrons (n=79, 116, 140, 225, 260), truncated hcp structures (n=57, 87, 89, 114, 153, 210, 323). Soini et al. proposed two types of TO structures, one where the truncation perpendicular to the C_4 axis occurs close to the apex (b), and another one eliminating a larger part of the apex (c). In their publication, the former mentionned members of the fcc family, namely the cuboctahedron and the icosahedron (a) and (d) respectively. Similarly, the specific hcp structures were obtained from various truncations schemes, including a central atom or not, or involving different truncation planes. In the present work, DFTB structural gradient-driven relaxation of the previous structures was achieved for various spin possibilities.

We first specifically discuss size n=55. For this particular size, we have actually used the PTMD algorithm to search the low energy structures, as we did for the small clusters. The lowest-energy structure was obtained as a rather amorphous nanoparticle (see Figure 4.6, left), with spin projection $\Sigma = 5$. This seems to be in line with the DFTB work of Shi et al. [92] who report low-symmetry structures for n=55 and 81 from DFTB incorporated within a genetic algorithm. No such result was however mentionned in the DFT/PBE study of Soini et al. The lowest-energy icosahedral and cuboctahedral clusters were also obtained with non-zero spin projection Σ=3 and Σ=6 respectively, while stable nanoparticles with Σ=0 were also occasionally found, however at higher energies.

Table 4.4 reports the total energies and structural excitation energies of the nanoparticles investigated in the present DFTB study. Results for spin zero are systematically listed for all structures, while results for non-zero spin projection are only included whenever they happen to be the most stable, which occurs to be the

case for n=55 (amorphous), 57 (hcp) and 114 (hcp).

NP		Σ	ΔE (eV)	E_b/n (eV)	VIP (eV)
55	amor	5	0.00	5.302	5.878
	ico	3	8.50	5.147	5.992
	ico	0	8.55	5.146	5.848
	cubo	6	12.79	5.069	6.357
	cubo	0	12.88	5.068	5.745
57	hcp	1	0.00	5.213	5.711
	hcp	0	0.65	5.201	5.646
79	TO	12	0.00	5.382	6.890
	TO	0	0.75	5.372	5.569
87	hcp	0	0.00	5.456	5.364
89	hcp	0	0.00	5.433	5.537
114	hcp	2	0.00	5.534	5.510
	hcp	0	0.02	5.534	5.430
116	TO	2	0.00	5.553	5.451
	TO	0	0.00	5.523	5.485
140	TO	0	0.00	5.638	5.228
147	ico	0	0.00	5.636	5.487
	cubo	4	12.11	5.554	5.585
	cubo	0	12.16	5.553	5.437
153	hcp	0	0.00	5.658	5.425
210	hcp	0	0.00	5.767	5.363
214	hcp	0	0.00	5.801	5.291
225	TO	0	0.00	5.806	5.135
260	TO	0	0.00	5.825	5.240
309	ico	0	0.00	5.911	5.368
	cubo	0	24.49	5.832	5.208
323	hcp	0	0.00	5.934	5.224

Table 4.4: Structural excitation energies ΔE, cohesive energies E_b/n and vertical ionization potentials (VIP) of geometrically relaxed nanoparticles with various structural motifs and spin moment(see text)

NP	CN	NS	$\langle R_{NN} \rangle$	$\langle q \rangle$
114 hcp	6	24	2.81	-0.04
	7	18	2.83	0.01
	8	18	2.83	-0.01
	9	18	2.86	-0.06
	12	36	2.90	0.05
	surf	78	vol	36
153 hcp	5	10	2.79	0.01
	6	22	2.78	0.01
	7	30	2.84	-0.08
	8	10	2.85	0.00
	9	24	2.86	-0.03
	10	2	2.87	-0.04
	12	55	2.90	0.05
	surf	98	vol	57
210 hcp	5	6	2.75	0.05
	6	21	2.78	0.01
	7	36	2.83	-0.06
	8	24	2.87	-0.03
	9	36	2.86	-0.04
	12	87	2.91	0.05
	surf	123	vol	87
214 hcp	5	11	2.76	0.03
	6	16	2.80	-0.01
	7	33	2.84	-0.04
	8	43	2.88	-0.03
	9	22	2.89	-0.06
	10	1	2.78	0.22
	11	14	2.89	-0.02
	12	74	2.91	0.05
	surf	140	vol	89
323 hcp	5	12	2.75	0.06
	6	19	2.84	-0.02
	7	46	2.84	-0.03
	8	51	2.88	-0.05
	9	42	2.87	-0.04
	11	18	2.89	0.03
	12	135	2.92	0.03
	surf	188	vol	153

NP	CN	NS	$\langle R_{NN} \rangle$	$\langle q \rangle$
116 TO	6	24	2.83	-0.04
	7	24	2.78	-0.01
	8	6	2.84	-0.18
	9	24	2.83	-0.01
	12	38	2.91	0.06
	surf	78	vol	38
140 TO	6	24	2.80	0.02
	7	24	2.82	-0.01
	9	48	2.87	-0.05
	12	44	2.91	0.05
	surf	96	vol	44
147 cubo	5	12	2.78	-0.00
	7	48	2.80	-0.04
	8	24	2.83	-0.06
	9	8	2.82	0.01
	12	55	2.91	0.06
	surf	92	vol	55
147 ico	6	12	2.80	0.12
	8	60	2.87	-0.11
	9	20	2.90	0.07
	12	55	2.91	0.06
	surf	92	vol	55
225 TO	6	24	2.79	0.03
	7	36	2.85	-0.04
	9	80	2.87	-0.02
	12	85	2.92	0.03
	surf	140	vol	85
260 TO	6	24	2.77	0.01
	7	48	2.81	-0.05
	8	24	2.84	-0.07
	9	48	2.85	-0.02
	12	116	2.94	0.04
	surf	144	vol	116
309 cubo	5	12	2.74	-0.03
	7	72	2.85	-0.02
	8	54	2.84	-0.04
	9	24	2.87	-0.03
	12	147	2.92	0.03
	surf	162	vol	147
309 ico	6	12	2.80	0.08
	8	90	2.90	-0.08
	9	60	2.90	0.01
	12	147	2.92	0.04
	surf	162	vol	147

Table 4.5: Averaged nearest neigbour distances $\langle R_{NN} \rangle$ and atomic Mulliken charges $\langle q \rangle$ as a function of the coordination number (CN) in ruthenium nanoparticles with spin projection zero. NS is the corresponding number of sites. The total number of surface and volume atoms is also indicated.

A feature that has been little discussed in the previous studies is the effect of relaxation on the final shape of the cluster. With our DFTB approach, we often find a deformation from the very symmetric structure. Even whenever a global minimum exists close to the very symmetric starting structure, a deformation generally exists, sometimes somewhat distorting the global shape of the cluster via collective displacements and also local reconstruction of the cluster surface. Such deformations were discussed neither in the DFT work of Soini et al.[95] nor in that of Nanba et al [94]. They lower the cluster symmetry with respect to that of the initial regular model geometry and can be associated with Jahn-Teller instabilities. Besides of Ru_{55} which lowest structure is completely amorphous as mentionned above, this can be observed in particular for cluster structures of the hcp family as shown in Figure 4.8, namely for instance Ru_{57}, Ru_{87} and Ru_{89} and even to a less extent on the larger ones up to Ru_{323}. This generates coordinations which may be slightly different from those of very symmetric structures. Thus, some subsurface atoms present coordination numbers (CN) of 11 instead of 12, while similar exceptions can also affect surfaces atoms (Note that there is a degree of arbitrariness in the definition of the coordination numbers, depending on the chosen size of the coordination radius, here taken as twice the van der Waals radius of ruthenium, namely 1.65 Å). The deformation is not an artifact of DFTB since we can compare the present structures with the DFT ones provided by Soini et al. Figure 4.9 reports the DFT structures of Soini et al.[95] (DFT geometries provided in the Supplementary Information of the reference) and the present DFTB ones for hcp structures n=57, 153 and 323. It can be seen that the global and surface deformations provided by the two respective calculations are very similar.

In addition to the comparison of the stabilities of the various structures, it is also interesting to analyse more closely the distribution of atomic distance patterns characterizing the various nanoparticles. Table 4.5 provides the average nearest-neighbour distances $\langle R_{NN} \rangle$ of atomic sites with various coordinations numbers. For each nanoparticle size, the average is carried on all distances between a given site and its coordinated neighbours and over all sites with similar coordination. One can see that the NN distances between core atoms (coordination generally equal to 12, accidentally to 11) are larger (close to 2.90 Å) than the NN distances at the surface with coordination numbers ≤ 10 (in the range 2.75-2.85 AA). Thus the interatomic distances tend to increase when increasing the coordination. This is consistent with the trends already pointed out by Nanba et al. in their recent work[94]. Finally, we have also listed the averages of the Mulliken charges of sites characterized by a given coordination. Even in neutral nanoparticles, the DFTB data show a trend for a small electronic transfer (0.03-0.06) from the volume to the surface, again in line with the DFT results of Nanba et al[94] (using Bader's definition of the charges) who attributed the transfer as involving essentially the subsurface atoms.

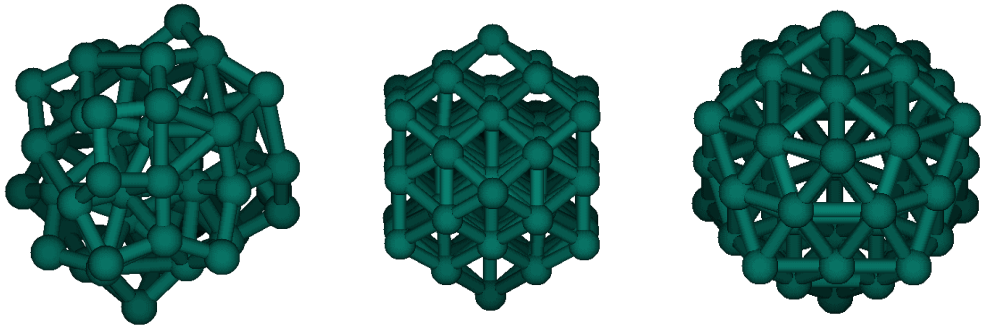

Figure 4.6: Relaxed isomer geometries of Ru_{55} with amorphous (Σ=5), cuboctahedral (Σ=0, 6), icosahedral (Σ=0, 3) geometries

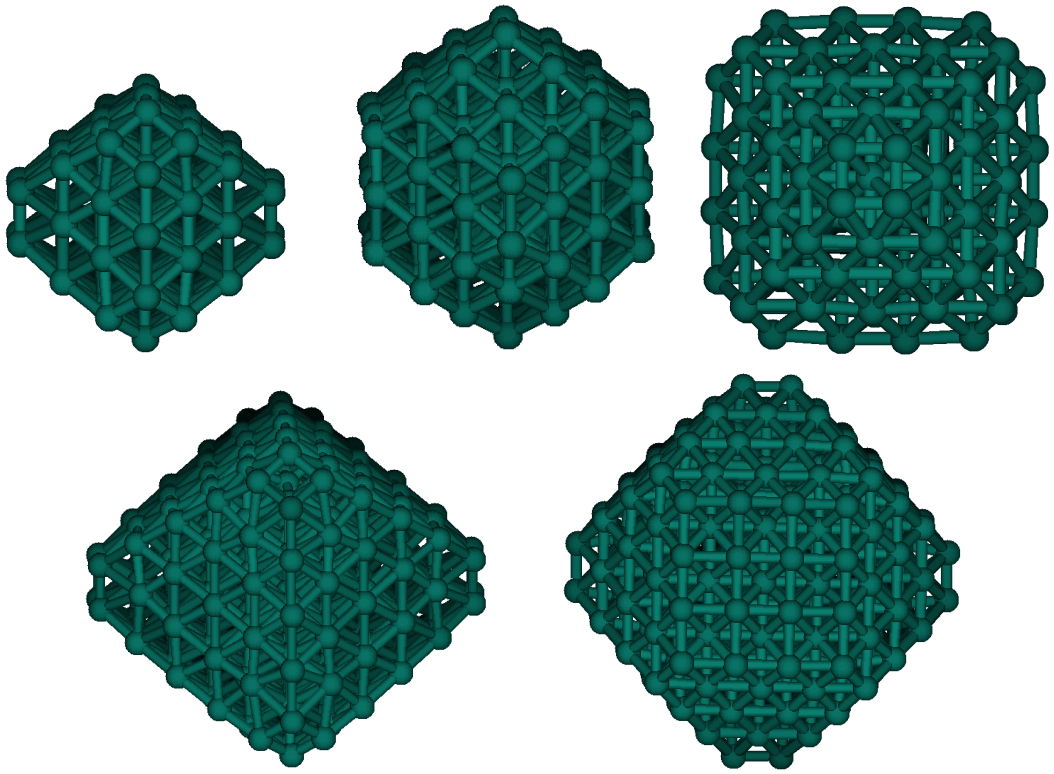

Figure 4.7: Relaxed geometries of nanoparticles starting from guesses based on truncated octahedron fcc motifs : from left to right and from top to bottom, Ru_{79}(Σ=0,12), Ru_{116}(Σ=0), Ru_{140}(Σ=0), Ru_{225}(Σ=0) and Ru_{260}(Σ=0.
. n=116 and 260 correspond to truncation case (c), whereas n=79,140 and 225 correspond to truncation case (b).

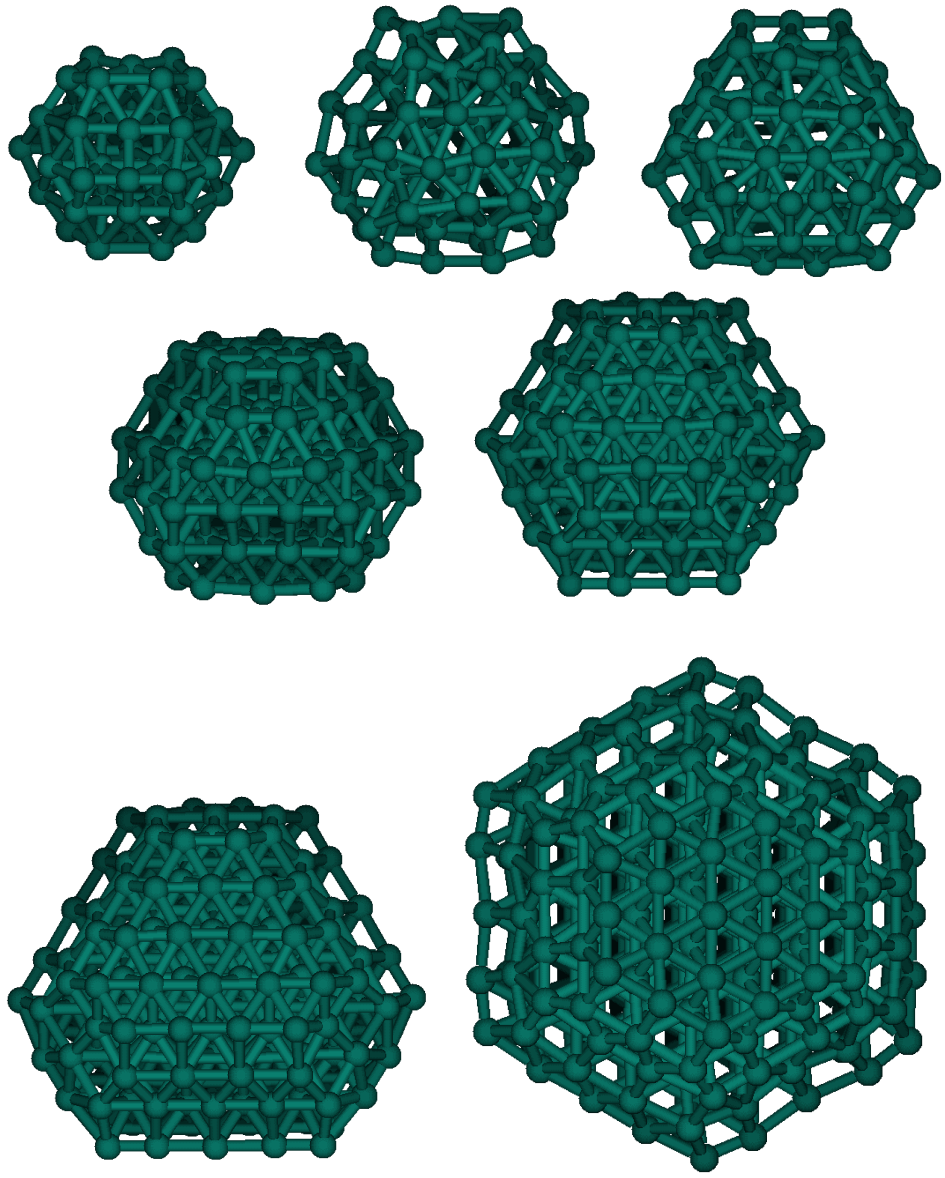

Figure 4.8: Relaxed geometries of nanoparticles based on various truncated hcp guesses : from left to right and from top to bottom, Ru_{57}(S=0), Ru_{87}(Σ=0), Ru_{89} (Σ=0), Ru_{114} (Σ=0), Ru_{153}(Σ=0), Ru_{214} (Σ=0) and Ru_{323} (Σ=0).

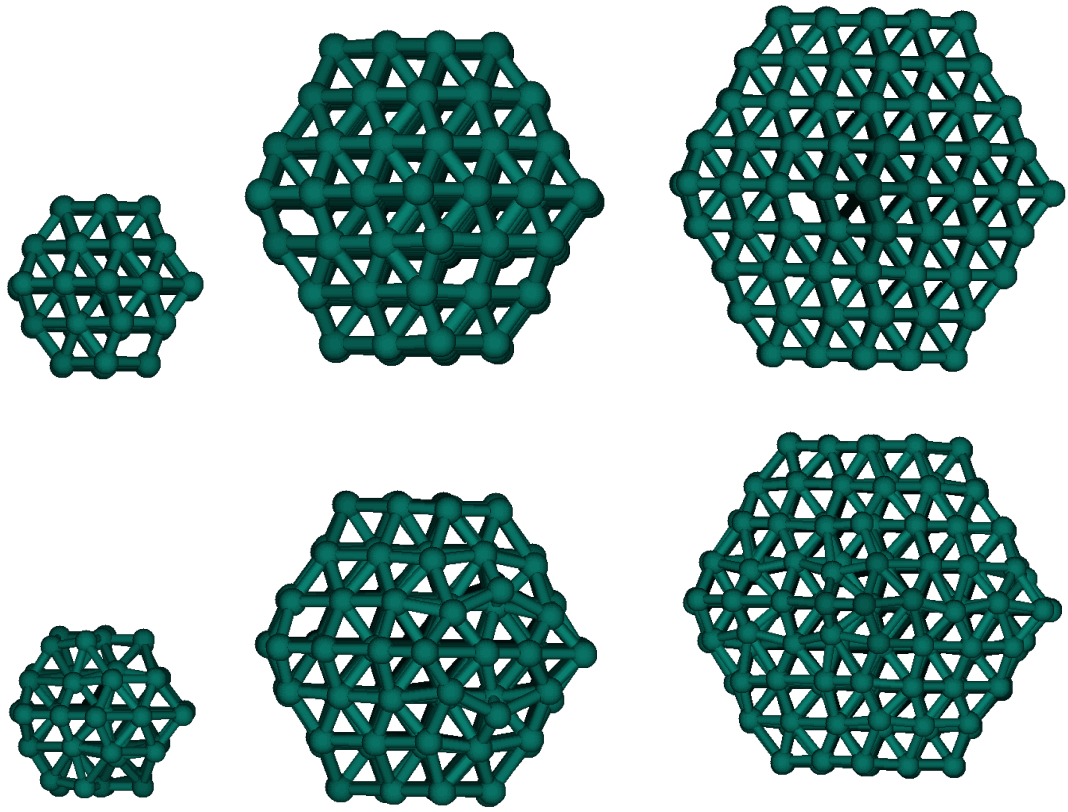

Figure 4.9: Comparison between relaxed DFT (top) and DFTB (bottom) hcp geometries of Ru_{57} Ru_{153} Ru_{323} respectively from left to right

4.3.3 Energetics

Taking the atomic energy of Ru as that of the ground state DFTB quintet state, the cohesive energy (same as binding energy) of neutral clusters an nanoparticles can be easily calculated as:

$$E_{b/n} = -\frac{E(Ru_n) - nE(Ru)}{n} \tag{4.61}$$

The evolution of the binding energies of small neutral clusters is shown in Figure 4.10 (left). It is found to be generally increasing with size except for n=9 and 13. Indeed, well-marked size effects are observed at n=8 and n=12. These two clusters, the structures of which are a simple cube and a double cube respectively, have clearly larger cohesive energies than their immediate neighbours and can be considered as having enhanced (magic) stabilities. The evolution of the cohesive energies of neutrals is remarkably similar to that of the DFT determinations of several authors, as shown in Figure 4.10, despite the occasional discrepancies on some of the geometries (and also among DFT calculations).

Figure 4.10 also shows the differential evolution of the cohesive energy for charged systems calculated as:

$$E_{b/n} = -\frac{E(Ru_n^{+/-}) - (n-1)E(Ru) - E(Ru^{+/-})}{n} \tag{4.62}$$

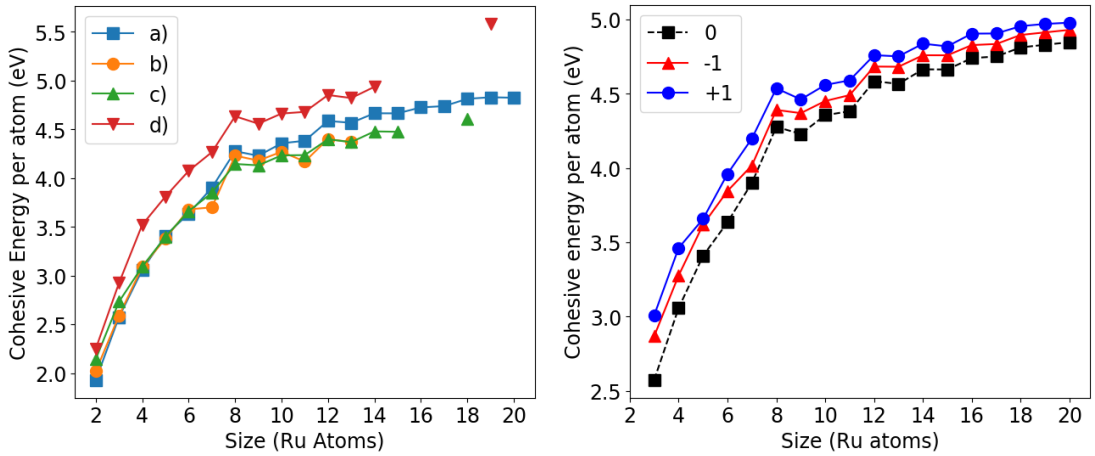

Figure 4.10: Left: Size evolution of the cohesive/binding energy per atom (eV) of Ru_n clusters: a) Present DFTB. b) DFT-VASP-PW91[86], c) DFT-SIESTA-PBE [88], d) DFT-VASP-PW91[89]. Right: Size evolution of the cohesive energy per atom (eV) for the neutral (black squares with dashed line) anionic (red triangles) and cationic (blue circles) clusters.

The effect of charge is expected to be more crucial for small clusters and indeed the size by size differences between the three curves is essentially observed for $n < 9$. It is to be noted that the special stabilities at $n = 8$ and 12 are conserved for the cations and even for the anion, in consistency with the persistence of the cube and double cube patterns for these two sizes. Obviously, the three energies should converge to the same value for large n, which is the observed trend but far to be

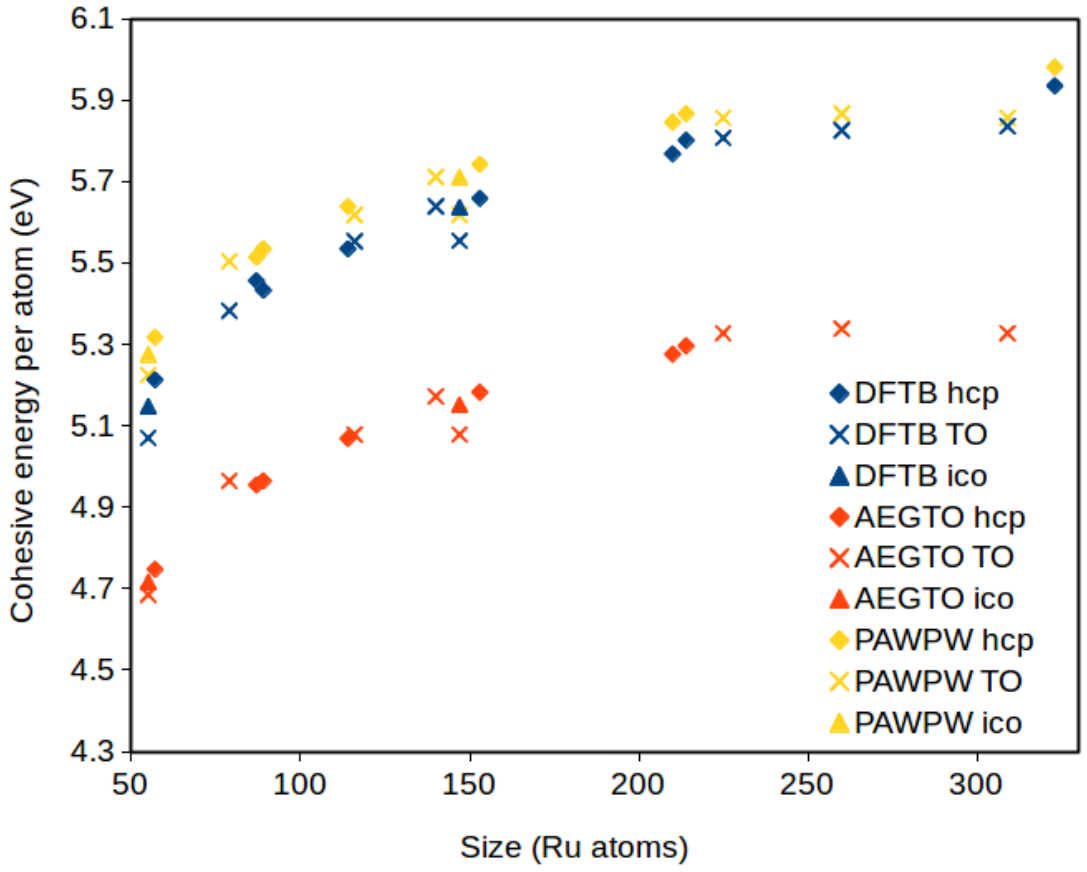

Figure 4.11: Comparison between DFTB results (blue), and the DFT/PBE results of Soini et al.[95] using all-electron Gaussian-type orbitals (AEGTO) (orange) and projector augmented wave plane-waves periodic type calculations (PAWPW) (yellow).

reached at size $n = 20$ where the differences in $E_{b/n}$ are still in the order of 0.3 eV between the value for cations (the largest) and that for neutrals (the smallest).

Before analysing the energetics of nanoparticles and independently of the finite size results, it is interesting to consider DFTB calculations for bulk ruthenium performed using periodic boundary conditions (PBC) using the unit cell (1x1x2 atoms). An optimization of the number of k points led to a value of 11 while the optimization of the cell parameters led to the values of a=3.028 Å and c=4.795 Å, somewhat higher than the experimental values reported in the bibliography [271], 2.706 and 4.282 Å, respectively. The cohesive energy was found to be 6.62 eV/atom. When using a larger cell (namely 4x4x4 atoms), the cell parameters were only slightly improved (a=2.949 Å, c=4.623 Å) while the cohesive energy was increased to 7.0945 eV/atom, to be compared with the experimental value 6.74 eV.[271]

We can now discuss the energetics of finite size nanoparticles. Figure 4.11 compares the DFTB results with those of Soini et al. One can observe that the evolution with size of the cohesive energies is quite close to the DFT/PBC plane wave (PAWPW) data of Soini et al. and so is the ordering of the different structures. While the fcc cuboctahedral structures (not shown in Figure 4.11) seem to be relatively less stable than the other fcc structures. Both DFT and DFTB results show a close competition between fcc/TO, fcc/ico and hcp type structures with a trend for a relative gradually increased stabilization with size of hcp structures. Note that in the work of Soini et al., the DFT results obtained with all-electron Gaussian Type Orbitals (AEGTO) and the equivalent PBE functional have a strictly parallel behaviour than the DFT/PBC (PAWPAW) results with, however, a shift of 0.5-0.6 eV in the cohesive energies.

In order to analyze the correlation between structure, coordination and energetics, we have fitted the present results considering an analytical expression of the nanoparticles cohesive energies, as introduced in a previous publication dealing with gold and silver nanoparticles[272]

$$\epsilon_{coh}(n) = \epsilon_v(n_v + \sum_i n_i(c_i/c_v)^\gamma)/n \tag{4.63}$$

This formula introduces the account of the reduction of the cohesive energies for surface, edge and apex sites according to their coordination number c_i, smaller than the volume coordination, namely $c_v = 12$ associated with a volume cohesive energy ϵ_v. We have fitted such a formula in the size range 55-323. In this range, the number of surface atoms is still very large. It also has the interest that it can be used to include in the fit various sizes and various structural arrangements with different surface coordinations, using only the two adjustable parameters ϵ_v and γ. From the above expression, it is straightforward to derive the volume and various site energies per atom $\epsilon_i = (c_i/c_v)^\gamma \epsilon_v$ which are listed in Table 4.6. We were not able to achieve a satisfactory and unique fit for the whole sample of nanoparticles. We have thus performed separate fits for hcp (n = 57, 87, 89, 114, 153, 210, 214, and 323), fcc/ico (n= 55, 147 and 309) and fcc/TO (n= 79, 116, 140, 225 and 260) structures. As already stated above, due to the global and surface deformations mentioned above, the actual coordinations of a few of the atoms differ from the expected ones of the original perfectly regular model structures. The result for the volume energy extrapolated from the hcp family is 7.03, while the values deduced from the two fcc samples are very close, namely 6.89 and 6.87 eV for fcc/ico and fcc/TO respectively.

c_i	ϵ_i (from hcp)	ϵ_i(from fcc/ico)	ϵ_i (from fcc/TO)
6	4.217	3.862	4.254
7	4.725	4.392	4.732
8	5.214	4.911	5.191
9	5.687	5.419	5.632
10	6.146	5.919	6.058
12 (ϵ_v)	7.031	6.892	6.872

Table 4.6: Site energies of ruthenium nanoparticles withh zeo spin moment

The hcp value is quite close to the DFTB/PBC value for the bulk using the largest $4 \times 4 \times 4$ cell (7.09 eV/atom). The γ values are 0.737, 0.836 and 0.692 respectively for hcp, fcc/ico and fcc/TO samples. The site energies according to coordination are also provided in Table 4.6. It can be observed that even though the γ values are different, the site energies obtained from the different samples are still reasonably similar and cohesive energies among ico and TO converge to the same value. This fact is in agreement with the interpretation of the ϵ_i and γ parameters which are cohesive energy of the bulk, and a factor shape respectively. The present DFTB data still show fluctuations with shape among the various fcc structure types and among the two fcc structure models. Thus it is delicate to infer from those results a clear switch between fcc and hcp stabilities. Tentative extrapolation to the bulk for sizes larger than 323 was nevertheless attempted using the simple scaling law.

$$\epsilon_{coh}(n) = \epsilon_v - a_s n^{-1/3} - a_c n^{-2/3} \tag{4.64}$$

for hcp, fcc/ico and fcc/TO clusters (for truncation type (b), the most stable), fixing the first term to the respective cohesive energies determined with the coordination formula above. a_s determines the surface term and a_c the curvature terms. Those extrapolations are shown in Figure 4.12. While the fcc/ico extrapolation (green) always lies below the hcp extrapolation (blue), the fcc/TO fit (black) intersects the hcp one only above n=350. Those conclusions are thus different from those of Nanba et al. who extrapolate the cohesive energy for the bulk to 6.23 eV. Note that the fcc/TO structures of Soini et al. investigated also here with DFTB are different from those probed by Nanba et al.[94]. The difference can also be explained by the somewhat different extrapolation scheme since in the present work a negative contribution for the surface energy is obtained ($a_s < 0$ which seems more physical since the surface atoms are less bound and should therefore contribute through a deficit in the cluster energy if the first term is associated with the bulk cohesive energy). The $n^{-2/3}$ dependance, although not vanishing, represents only a minor contribution. Note that the extrapolations of fcc/ico (green) and fcc/TO (black) samples merge for $n > 500$, which is consistent with the similarity of the above determined volumic cohesive energies.

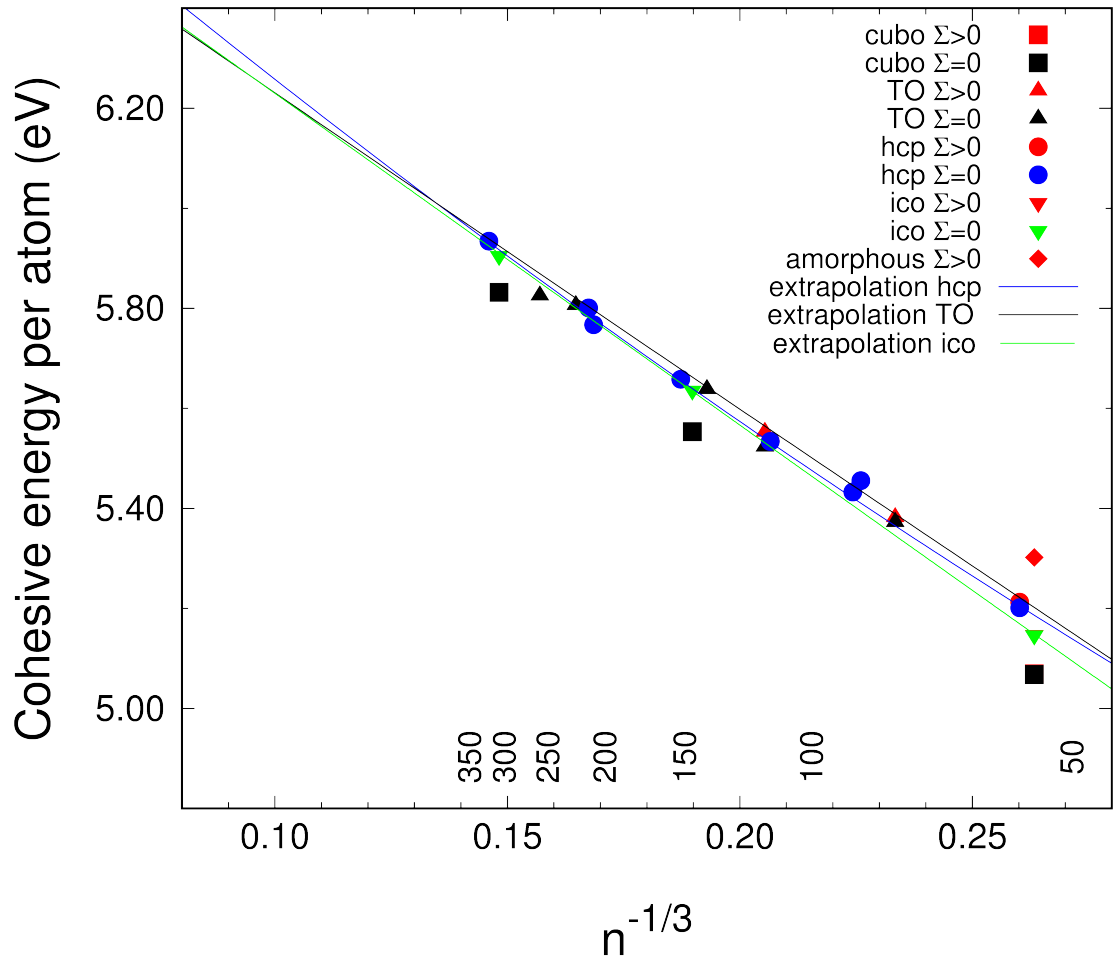

Figure 4.12: : Extrapolation of the cohesive energies as a function of $n^{-1/3}$. The hcp extrapolated limit for $n = \infty$ is 7.031 eV. All red symbols indicate nanoparticles with non-zero spin projection

4.3.4 Electronic properties

The Ionization Potential (IP) of atomic ruthenium is 7.360 eV [273] while the bulk work function of the metal (accepted value for polycrystalline ruthenium) is 4.71 eV [274–276]. In molecular or small polyatomic systems, one defines adiabatic and vertical Ionization Potential (IP). The adiabatic IP corresponds to a relaxation of the system both in the initial and the final state, whatever the spin moment, whereas the vertical IP is calculated as a difference at the initial (neutral) system geometry. For initial neutral systems with spin moment zero, transitions are generally defined between $\Sigma = 0$ (initial state) and $\Sigma = 1/2$ (final state). However there is an ambiguity in defining vertical IPs in the case where the neutral cluster is characterized by open shell and a high total spin, since selection rules allow two possibilities, namely $\Sigma_+ = \Sigma_0 \pm 1/2$. In a simple MO picture, removing an electron from the highest Singly Occupied Molecular Orbital (SOMO) leads to a smaller IP value than removing an electron from the highest doubly occupied molecular orbital, lower in energy, however electron correlation can change the ordering of electron energies. In the following, we will report the VIP at the neutral's geometry towards the $\Sigma_0 \pm 1/2$ state of the ion with lowest energy. The situation is similar for electron affinities (EA).

We will first discuss the case of small clusters. One can see in Figure 4.13 that the ionization potentials of ruthenium clusters in the range $n = 1 - 20$ show an overall decrease between the atomic value and ~ 5.7 eV. There is generally no significant difference between the vertical and the adiabatic IPs. The largest discrepancy occurs for n=6, which is a case where the lowest DFTB structures are reversed between the neutral and the cationic cluster (trigonal pyramid versus prism). This difference is also shown in minor extent for Ru_{13} and Ru_{17}, where some geometrical differences occur between neutral and charged clusters, being the difference between vertical and adiabatic energies due to the structure relaxation. The situation is quite similar for the evolution of the cluster electron affinities, which increase from 2 to 2.9 eV. Here the effect of relaxation is less than 0.1 eV and the adiabatic EAs are almost equal to the vertical attachment energies or electron affinities (taken at the geometry of the neutrals). One can observe that for size $n = 20$, the difference between the VIP and VEA values, which can to some extent be compared with the electronic gap, is still equal to 3.5 eV. In contrast, the average value (VIP+VEA)/2 is roughly 4.7 eV, rather close to the work function (WF) value of bulk ruthenium [274–276].

The convergence of the ionization potential towards the bulk WF can be actually discussed when considering nanoparticles in the range n=55-309. We have reported in Figure 4.14 the vertical IPs of the various nanoparticles investigated in Section 4.3.2. If we examine the clusters with Σ=0 only, one can see that the IP dispersion for a given size is of the order of 0.1-0.3 eV, reflecting the role of structure on the IPs. The difference between the fcc icosahedrons and cuboctahedrons tends to vanish (less than 0.05 eV for n=309). Note that the full lines in the figure are only present to easy the following of the IP evolution within a same structural family. The IPs are also essentially slowly decreasing from values close to 5.70 for Ru_{55} to 5.30 eV for Ru_{323}. The TO structures tend to have smaller IPs. In order to estimate the convergence of the present DFTB values of the IPs towards the bulk WF, we have added in the Figure 4.14 the Work Function of a sphere in the quantum Jellium Model (SJM), namely

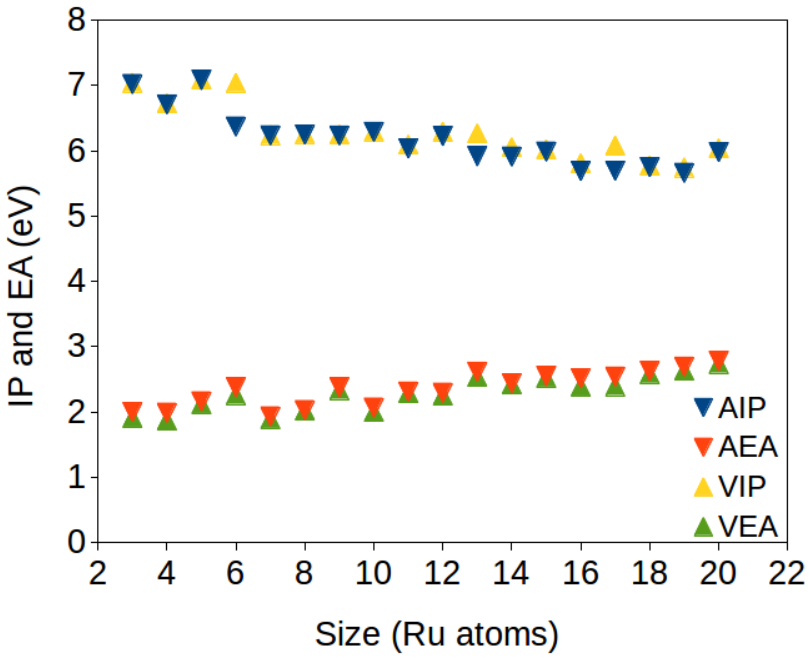

Figure 4.13: Ionization Potentials (IP) and Electron Affinities of of Ru_n clusters. Both (V)ertical and (A)diabatic

$$W_n = W_\infty + (\frac{1}{2} + a_q)\frac{1}{r_0}n^{-1/3} \tag{4.65}$$

W_∞ is the bulk work function (or that of an infinitely large sphere) and r_0 the Wigner Seitz radius of bulk ruthenium[277] (2.79 a_0). The coefficient of the Coulomb term is classically 1/2 but a quantum correction ($a_q \approx$ -0.08) must be added to take into account the electronic spill out, namely the quantum extension of the negative electronic density beyond the positive jellium sphere[278]. One can observe in Figure 4.14 that the DFTB IP values for low spin clusters ($\Sigma = 0$) fall close to the SJM estimation, which means that the DFTB IP values obtained for the nanoparticles in the present size range n=55-309 are consistent with the further decrease according to a Coulomb behaviour towards the bulk work function value 4.71 eV.

4.3.5 Spin considerations

Some of the DFT publications mentionned earlier have discussed the spin properties of clusters and nanoparticles, obtained within the Unrestricted Spin polarized DFT scheme. The present work traces such properties from small clusters to the bulk in a restricted ROKS/DFTB scheme as driven by the atomic spin part of the hamiltonian. The dependence of the cohesive energy on spin is illustrated for two example cases in Figure 4.15 for two different situations of Ru_8 and Ru_{55}. In the case of Ru_8, the most stable isomer is characterized by Σ=2 (see also Table 4.1). In the case 55, although the stability generally decreases with increasing spin one can clearly observe relatively strong variations of the stability associated with various geometrical isomers, the amorphous lowest structure having non-zero spin moment.

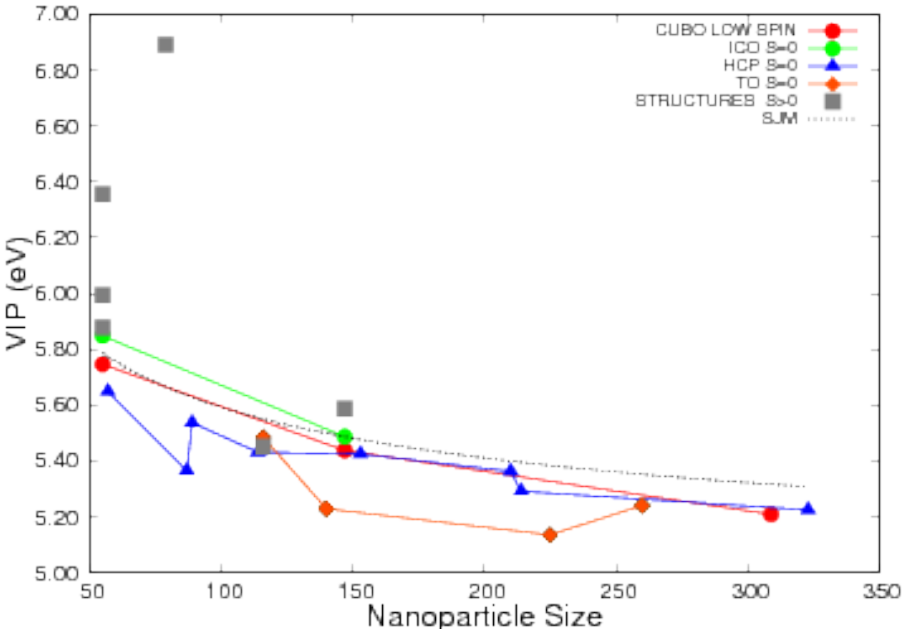

Figure 4.14: : Ionization potentials (vertical) of Ru_n nanoparticles, labeled according to structure (fcc/cubo, fcc/ico, fcc/TO and hcp) and spin (low spin projection Σ=0 or higher) as indicated in Table 4.4. The joining lines are drawn only for visualization.

As can bee seen from the Tables 4.1 to 4.3 of Section 4.3.1, high spin isomers tend to be the most stable in the very small cluster range up to n=10 with total spin projection between 6 and 10 for the small neutral clusters, and up to 11/2 and 19/2 for the cations and the anions, with strong size variations, but a 0.2-0.5 eV spacing between energies of states with various spin projections. Beyond $n = 10$, the occurence of clusters characterized by large spin projection values tend to vanish, the lowest energy isomers generally corresponding to a low spin value, generally Σ=0 for neutrals and Σ=1/2 for ions.

In the case of nanoparticles, a few structures with low however non-zero Σ values can still be obtained in the range n=55-147. This is particularly the case for the amorphous lowest energy isomer of Ru_{55} and also for a TO structure of Ru_{79}. However, when expressed in terms of Bohr magnetons per atom, this yields to very small values. Finally beyond $n = 100$, all the nanoparticles seem to have a preference for very low spin electronic structure (almost always Σ=0, with one exception).

Although the results corresponding to the present DFTB/RKS calculations instead of DFT/UKS calculations, and also because several states with different multiplicity may lie in a narrow energy range (see for instance the small clusters and even some nanoparticles like n=79, n=114), it is certainly quite hazardous to provide a detailed comparison of the present results with DFT results. Nevertheless, the trend for a rather quick decrease of the cluster magnetization (here roughly for $n > 10$) is in line with DFT results published for the clusters [86, 88, 90, 269] and nanoparticles [95]. From the spin point of view, ruthenium clusters achieve an early transition with size towards bulk ruthenium which is known to be non-magnetic.

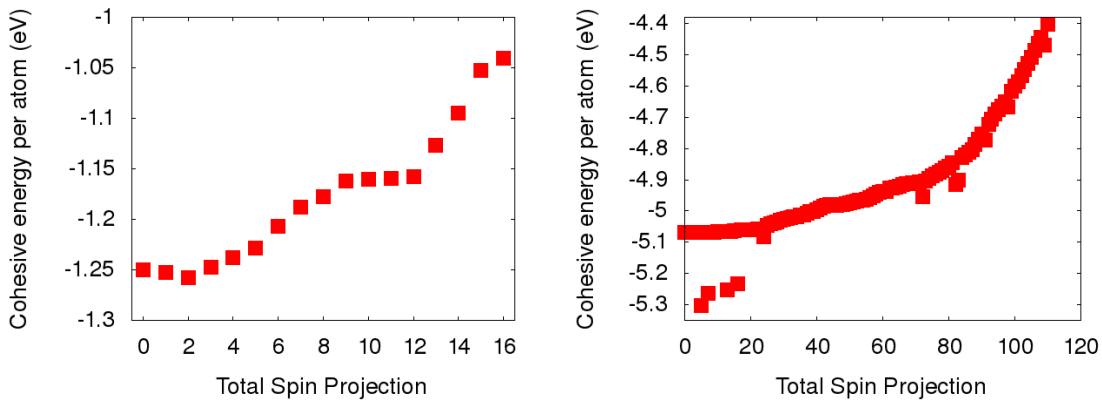

Figure 4.15: Cohesive energy per atom of the isomers of Ru_8 (lhs panel) and Ru_{55} (rhs panel) with all various possible spin projections Σ. For Ru_{55}, several spatial isomers can occur for a same value of Σ

.

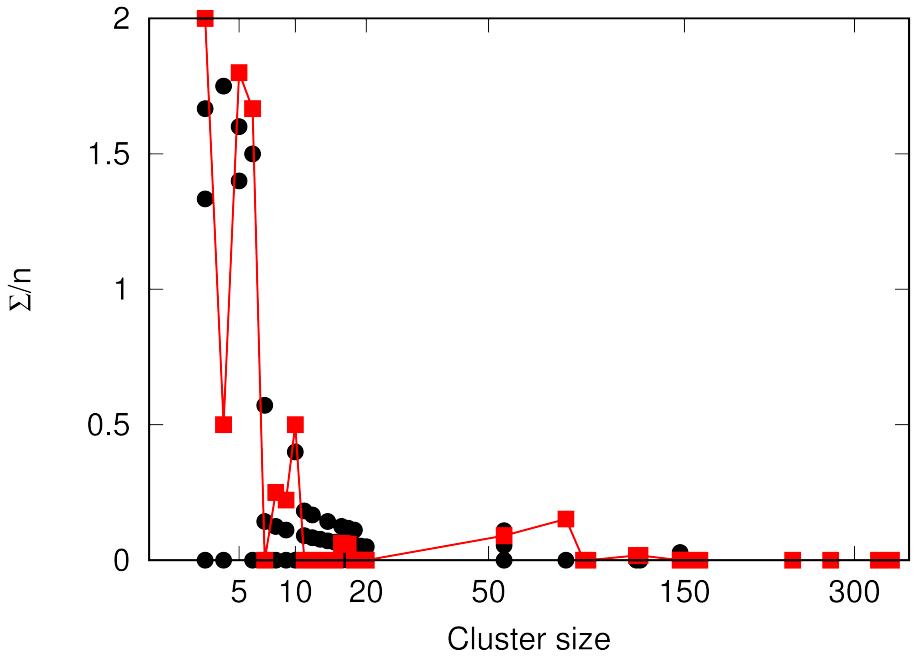

Figure 4.16: Total spin moment per atom Σ/n for neutral ruthenium clusters and nanoparticles. Lowest energy isomer: red squares with line; Other isomers : black dots.

4.4 Conclusion and outlook

The present investigation has tested the capacity of DFTB to cover, with a single efficient methodology and parametrization, the field from small clusters to nanoparticles and to the bulk for ruthenium materials, namely in a case of transition metals showing a more complex electronic structure than noble metal for instance, and where spin plays a significant role. In the case of small clusters and up to Ru_{55}, the present investigation was concerned with states with various charge and spin projection. The essential structural properties of small clusters seem to be correctly described by DFTB, in particular the predominance of cubic motifs for sizes with $n < 15$. Also, the cohesive energies are quite consistent with the existing DFT results, showing in the range $n = 3 - 20$ enhanced stabilities for n=8 and 12, corresponding to the cubic and doubly cubic shapes. The structures and stabilities of larger particles show the competition for fcc-based or hcp-based stuctures, the largest stability being observed for hcp and fcc/TO -based nanoparticles with increasing size. The cross-over size remains still difficult to precise. DFTB relaxation of symmetric model nanoparticles is characterized by significant global and surface relaxation and this seems to be also consistent with the work of Soini et al[95]. The occurence of stable high spin moment clusters for small sizes less than 10 while the most stable clusters beyond size 15 and nanoparticles above $n = 55$ essentially have stable low spin moment characterization is also consistent with a transition from Hundt's type high spin type coupling in atoms and non-magnetic bulk material. The extrapolated cohesive energies of the nanoparticles have been shown to be consistent with the DFTB/PBC values of the bulk. Finally we were able to determine some electronic properties such as the ionization potentials of clusters and nanoparticles or the electron affinities of small clusters. The ionization potentials seem to converge gradually towards the work function of bulk ruthenium, eventhough shape, spin and and size effects are still meaningful in the investigated range. From comparison with DFT and experiment, a few deficiencies can be listed: (i) it seems that, in the case of anions, structures with hexagonal motifs exist with DFTB but lie somewhat too high in energy if compared with the DFT/PBE results of Waldt et al.[269]; (ii) the second lattice parameter of bulk ruthenium is significantly overestimated. This could perhaps be improved if one would include the hcp bulk data in the fit of the DFTB repulsive potential.

Despite the questions just mentioned, the present parametrization seems to essentially validate DFTB as reasonable methodology to describe the electronic structure and geometrical properties of ruthenium materials. It opens a way to further works requiring extensive configurational sampling such as dynamical or thermodynamical studies of ruthenium clusters and small nanoparticles in their ground state, namely isomerization or determination the of caloric curves and phase changes at finite size. Spectroscopic investigations, possibly at finite temperature could also now be carried out for sizes in the range $n = 3 - 55$. Beyond harmonic vibrational analysis, this could bring some additional understanding about the relationship between IR spectra and geometries observed in experiments at finite temperatures. Finally, visible spectroscopy could be theoretically determined either using linearized TDDFTB or direct electronic dynamics. A last attracting perspective is of course the investigation of the chemistry of ruthenium clusters and NPs with organic or inorganic compounds and the dynamical aspects of nanocatalysis with special inter-

est in the Sabatier reaction, although it was originally the goal for its research, the complex electronic structure of ruthenium lead to an arduous parametrization procedure, extending the building of the repulsive potential on time together with its benchmark thus inhibiting the possibility to carry out dynamics calculations along the present thesis time. A next step would be to perform such calculations with a previous determination of DFTB parametrizaters for other pairs such as RuN, RuH, RuO and RuC, which should pave the next steps in this direction. Finally, similar tests for other transition metal materials obviously offer complementary interesting perspectives.

Chapter 5

General Conclusion

Throughout the three years of the PhD thesis, the investigation of different aspects concerning the Sabatier reaction have been studied using different approaches, from the commercial purely heterogeneous catalyzed process with its experimental implementation in a prototype apparatus and the modelling of its kinetics over the Ni (111) surface to the simulation of the reactions occurring in the plasma by means of reactive scattering methods, concretely the quantum-classical one, passing through the theoretical investigation of the high catalytically active ruthenium clusters and nanoparticles using the semiclassical SCC-DFTB method.

This thesis is a clear example of synergistic collaborations among entities, both from the private sector and from the academia, to work together in a project investigating different aspects of a problem by each putting over the table the own expertise in benefit of a global result.

The secondment at PLC System granted the possibility to work together with experimental chemists and physicists as as well as engineers from different fields, providing a different point of view respect to the one a theoretical chemist usually has highlighting problems of not only reaction related like balances of heat, matter, side reactions or measurement but also logistics, setting up and validation support.

The stage, also allowed the possibility to make a contrast among results of the simulated kinetics obtained by means of the kinetic Monte-Carlo method (KMC), with the experimental ones, taken from direct measurements done at the apparatus by the own collaborating researchers. The research was conducted by:

1. Selecting the involved processes, which in our case included the four candidates to be the key step through which the reaction evolved, according to experimental evidences published in literature, as well as diffusion

2. Calculating the rate coefficients using transition state theory. For the preexponential factor the $k_B T/h$ approximation was used, and activation energies were taken from literature [56–58]

3. Running calculations at different temperatures

4. Analysing the obtained results

In spite of the discrepancy in the predicted threshold temperature, when comparing the results of the kinetics and measurements at different temperatures, due to the higher complexity of the commercial catalyst, the KMC simulation shed light

on the possible mechanism occurring in the most active Ni surface, and also highlights the role of the different species appearing on the surface of the catalyst thus addressing the further investigations to improve the different aspects of the catalyst.

Furthermore, a small script has been implemented to be able to reproduce a finite-volume-reactor model. This was achieved by a split of the simulation into smaller subsimulations, on which a KMC results of one simulation were used to generate the input of the following simulation thus varying the partial pressures on which the simulation was starting.

One of the most important elementary reactions composing the mechanism of the plasma-assisted carbon dioxide methanation is the gas-phase collisional process of OH activated species (a radical) with one of the reagent, the H_2.

The study was carried out by means of the quantum-classical method, its hallmark is the separate treatment of the different degrees of freedom of the system, in our case, the vibration of each diatom was treated using quantum mechanics with its associated wavepacket to be propagated on time, the other degrees of freedom, the translational one (i.e. the relative movement between the two centers of mass of the two diatoms) and the rotational ones, both the internal rotation of the diatoms in their own axis and the orbital rotation, were treated classically.

Because of the method is a semiclassical one, and therefore it is based on the simulation of various trajectories, it stimulated us to parallelize the program and thus increase its computational efficiency. With the available computational resources the choice was to do a Shared memory parallelization, using the OpenMP implementation. The speedup test showed excellent results, as expected from a embarrassingly parallel algorithm with up to > 93 % efficiency at 48 cores.

The method proved to correctly describe the collisional process by reproducing the results obtained with a full-quantum study by Chen et al. with their new CXZ potential energy surface (PES) and also reproducing the well-known feature of reaction enhancement on vibrational excitation of hydrogen while not happening the same for OH vibrational excitation.

For inelastic scattering processes the required starting distance of 15 Åwas not suitable for the potential energy surface (PES) used, this was due to the fact that the fitting method used by that PES was based on neural networks and a training set limited to configurations not further than 15 bohr (7 Å*ca.*), leading to unphysical growth of the PES for distances larger than the fitted potential.

To correct that unphysical behaviour a new PES was developed based on the CXZ PES for the short-range interactions and a long-range tail based on the electrostatic interaction among the OH dipole and the quadrupole generated by the non uniform distribution of charge in the H_2 bond and the van der Waals interaction, modeled as an Improved Lennard Jones potential.

Results with the Improved PES showed its effects on inelastic scattering processes, namely vibrational energy exchange, reaction probabilities for OH excitation, reaction probabilities for low translational energy collisions, and quasiresonant transitions. Computed reaction rate coefficients with the new PES showed a better agreement with experimental findings published in literature.

Bond order variables were also implemented for both the OH + H_2 CXZ PES and the MF1 and MF2 PES for the system O_2 + N_2 scattering reaction. The variables were of foremost importance in order to have a correct representation and also sampling of the long range interaction by giving new insights on PES differences.

Lastly, the ruthenium clusters and nanoparticles, having a very important role in both the purely heterogeneously catalyzed carbon dioxide methanation and the plasma assisted one, have been studied by means of the DFTB method, a semiclassical method with a strict physical foundation, which takes certain simplifications on the DFT to highly increase the computational efficiency. The method has its major field of applicability in the run of dynamics of large systems (i.e. thousands to tenths of thousands of atoms) and on global optimization of big clusters and nanoparticles.

Parametrization of the repulsive potential has proven to be fundamental for the correct prediction of both structure, energetics, and spin properties of the considered systems. In our case, the choice of fitting the repulsive potential for both, the dimer and the cubic octamer led to a good description of ruthenium at all scales, crystalline structures and patterns.

Accounting for spin is of special importance for transition metals, and specially for ruthenium, were the equilibrium among the electronic delocalization of spatial orbitals and the spin coupling energy due to electronic correlation determines the correct electronic structure. For that an explicit atom centered spin term fitted with the energy of the quintet and the triplet obtained by means of CASPT2 calculations allowed the correct behaviour of that equilibrium.

Parallel tempering molecular dynamics (PTMD), a global optimization algorithm implemented in deMon (the used DFTB program), was used to obtain the lowest energy structures of ruthenium clusters for sizes 3-20. The method is based on the parallel run of multiple trajectories at different temperatures with configurational exchanges at fixed number of steps, this way a complete exploration of the PES is ideally achieved and thus obtain a pool of structures from which to carry out local optimization. Ideally the lowest energy structure is achieved with the method.

Geometries obtained with PTMD and DFTB showed excellent agreement with other studies reported on the literature by obtaining the cubic, pentagon and hexagon structures for both neutral, cationic and anionic clusters in the range n=3-20.

Nanoparticles investigation in the size range n=55-323 were found to be in agreement also with the results published in former studies. The energetics of clusters and nanoparticles showed an outstanding agreement with both experimental findings, being the accuracy of the method in the same range than higher level of theory like unapproximated DFT.

Extrapolating the results obtained from nanoparticles with a scaling method based on the coordination number of atoms in the nanoparticle, led to results in outstanding agreement with experimental findings.

Electronic properties like ionization potential and electron affinities were also obtained. The comparison of these quantities is however more difficult, in the lack of experimental evidences, but showing a qualitatively good agreement by being in between the extreme cases of the isolated atom and the bulk. Furthermore, the trend followed the expected tendency of the Jellium model

Finally, spin has proven to be an important factor in the systems by promoting certain geometries, like the amorphous behaviour of $Ru_5$5. However, systems rapidly decrease their total spin projection being the highest states found on the cluster scale.

The ability of DFTB to give correct prediction for pure ruthenium compounds, has thus been proven to be demonstrated.

To give a rundown, in this PhD thesis diverse approaches were used to study different problems related to the methanation of carbon dioxide reaction. The thesis not only included the interest for the possible application of the studied systems and reactions but was also driven by the methodological interest of investigating the ability of the used methods in correctly modelling the desired systems.

Appendices

Appendix A

Potential energy plots for OH + H_2 at different configurations

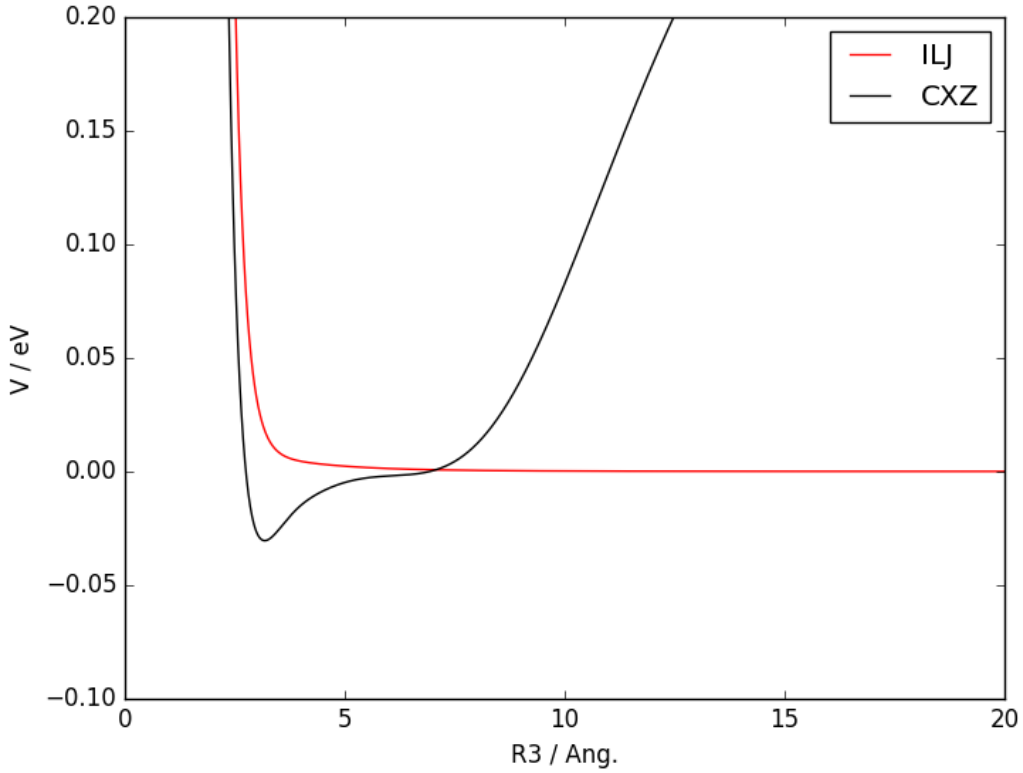

Figure A.1: Plot of the CXZ potential (black line) and the non-reactive ILJ potential (red line) for collinear configuration 1

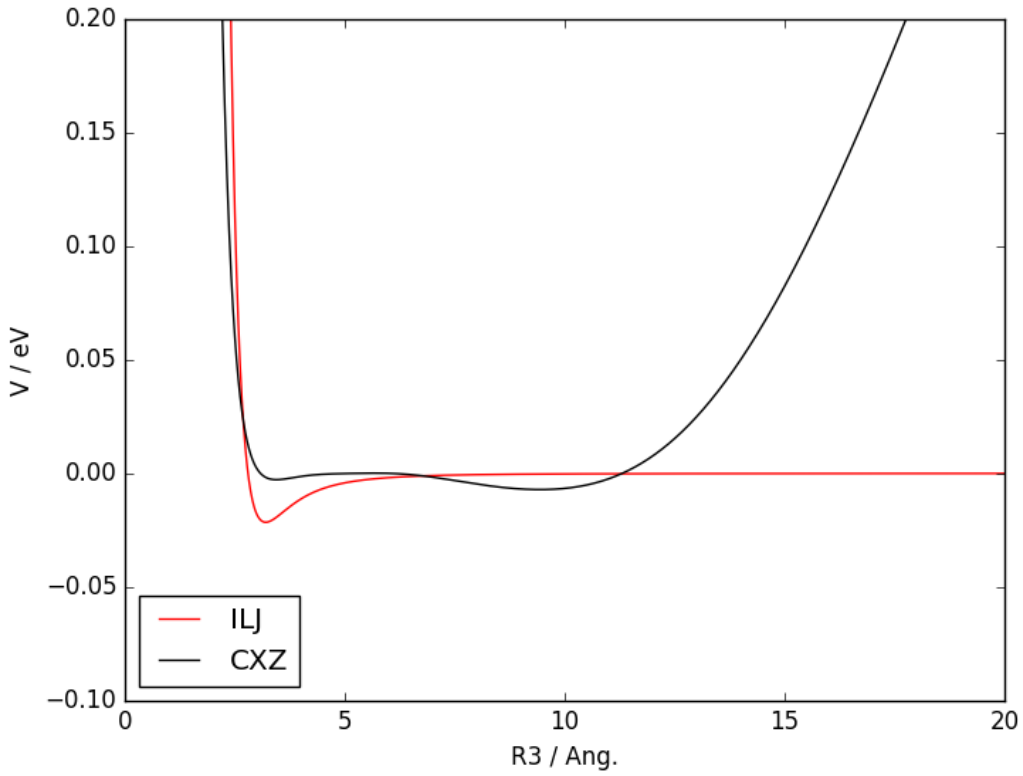

Figure A.2: Plot of the CXZ potential (black line) and the non-reactive ILJ potential (red line) for collinear configuration 2

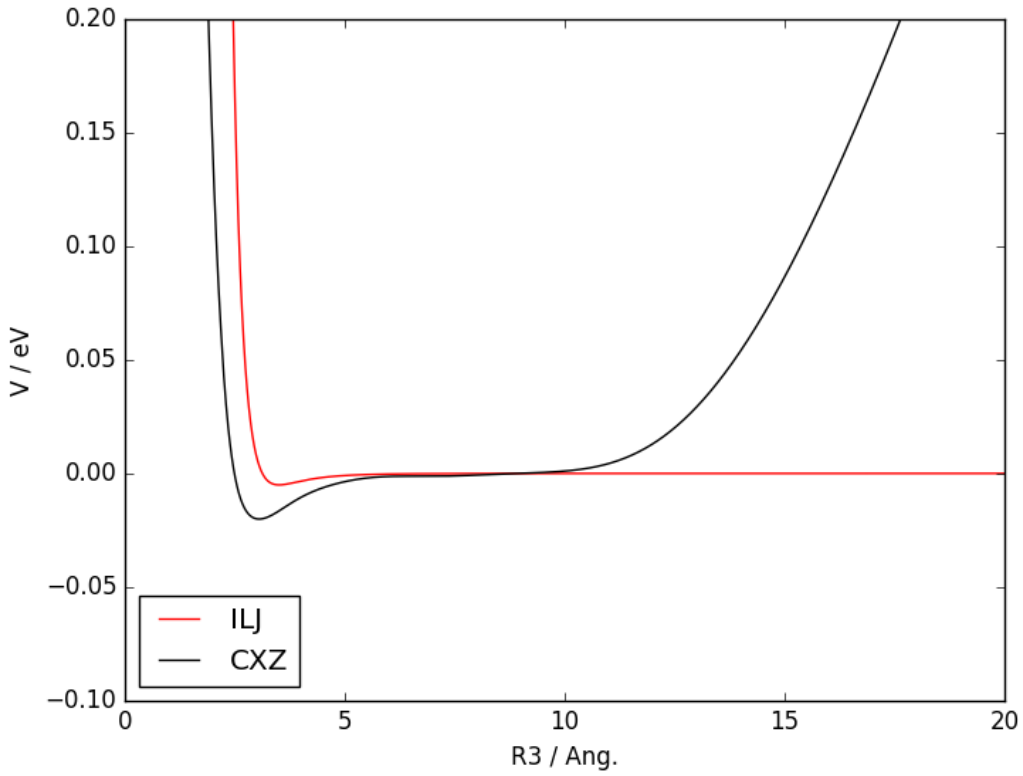

Figure A.3: Plot of the CXZ potential (black line) and the non-reactive ILJ potential (red line) for H configuration

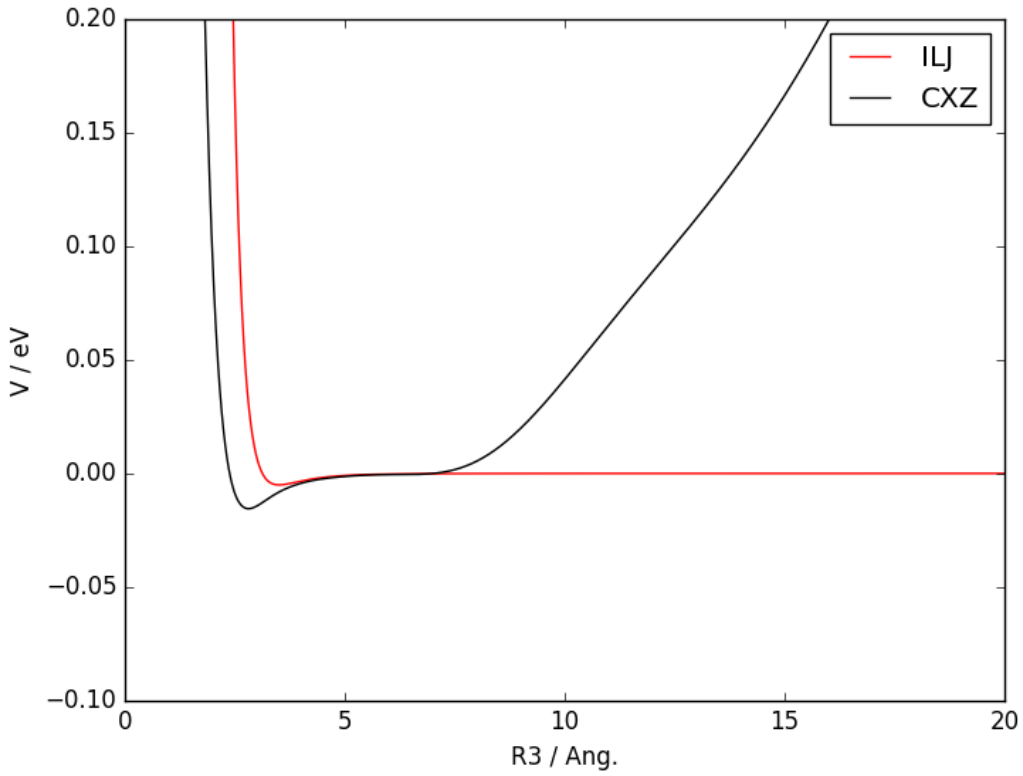

Figure A.4: Plot of the CXZ potential (black line) and the non-reactive ILJ potential (red line) for X configuration

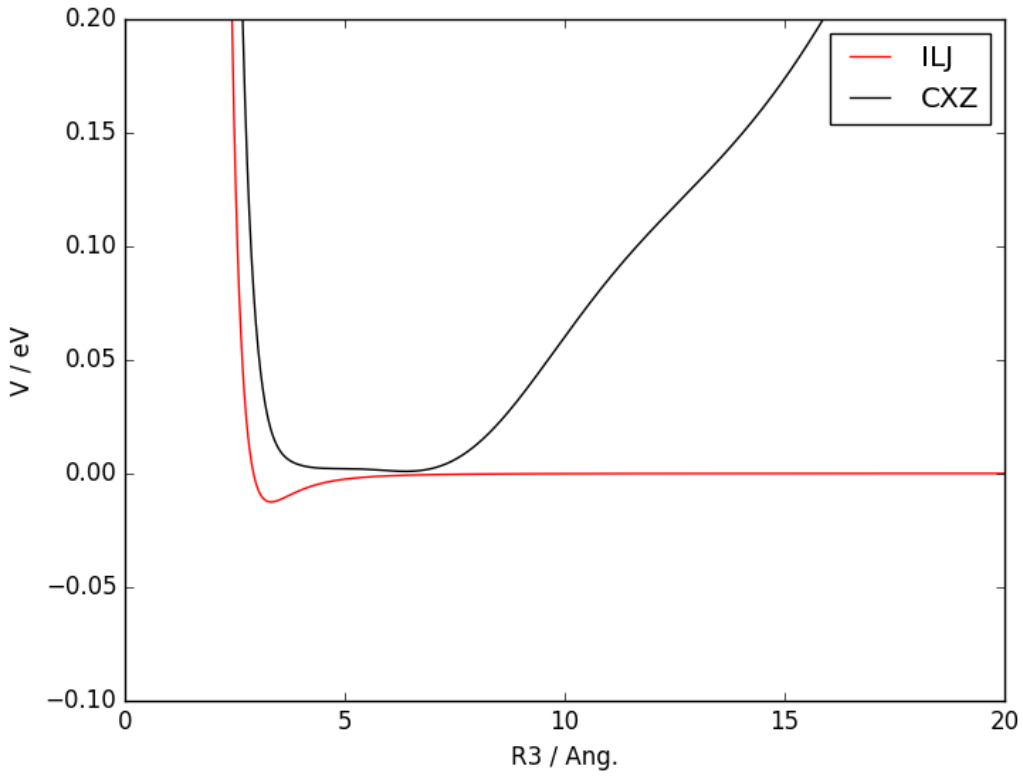

Figure A.5: Plot of the CXZ potential (black line) and the non-reactive ILJ potential (red line) for T1 configuration

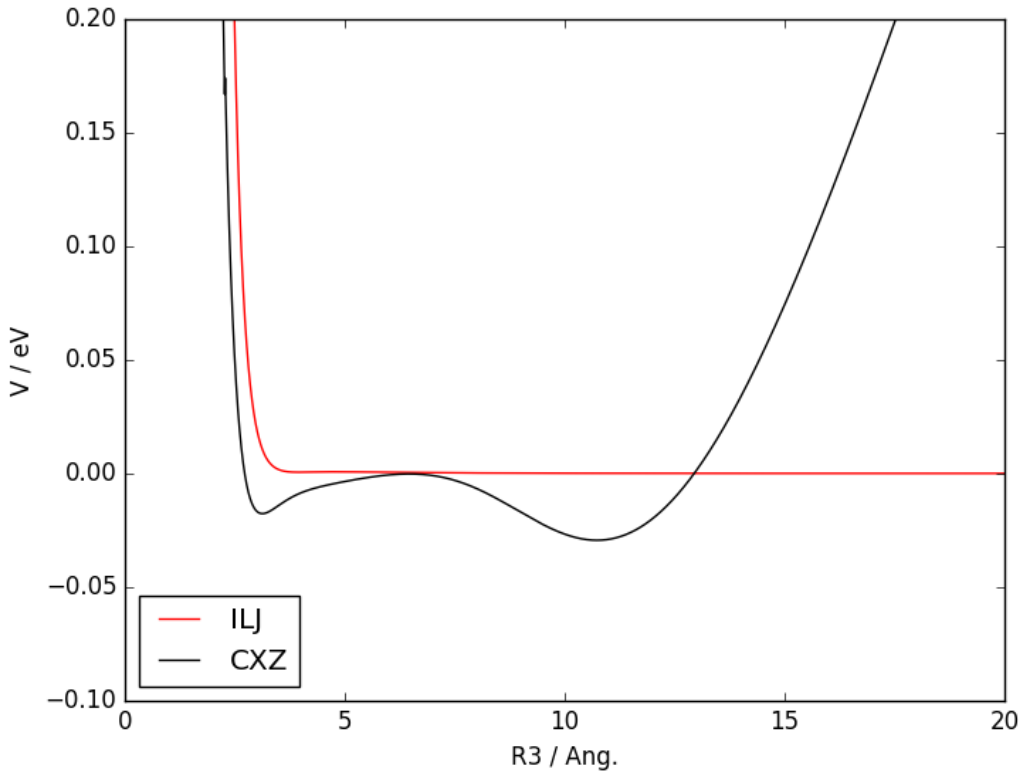

Figure A.6: Plot of the CXZ potential (black line) and the non-reactive ILJ potential (red line) for T2 configuration

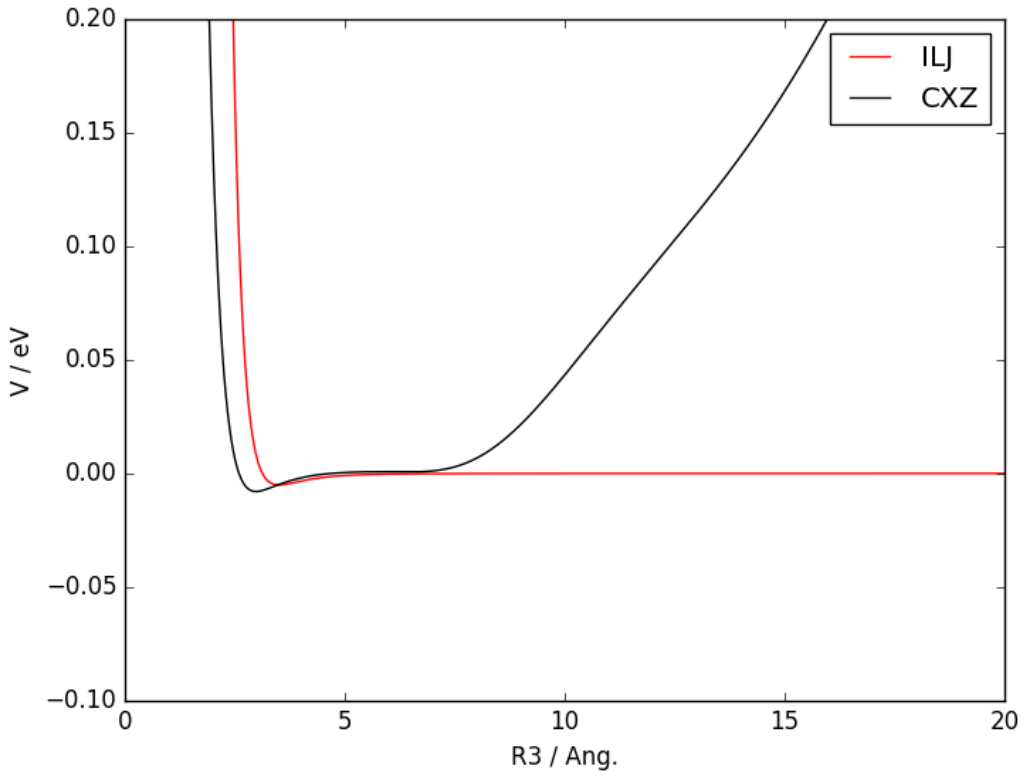

Figure A.7: Plot of the CXZ potential (black line) and the non-reactive ILJ potential (red line) for T3 configuration

Bibliography

[1] John Cook et al. "Quantifying the consensus on anthropogenic global warming in the scientific literature". In: *Environmental Research Letters* 8.2 (June 2013), p. 024024. ISSN: 1748-9326. DOI: 10.1088/1748-9326/8/2/024024. URL: http://stacks.iop.org/1748-9326/8/i=2/a=024024?key=crossref.ce047ab82872ab7fd19f230497d86fcb.

[2] Naomi Oreskes. "Beyond the ivory tower. The scientific consensus on climate change." In: *Science (New York, N.Y.)* 306.5702 (Dec. 2004), p. 1686. ISSN: 1095-9203. DOI: 10.1126/science.1103618. URL: http://www.ncbi.nlm.nih.gov/pubmed/15576594.

[3] William R L Anderegg et al. "Expert credibility in climate change." In: *Proceedings of the National Academy of Sciences of the United States of America* 107.27 (July 2010), pp. 12107–9. ISSN: 1091-6490. DOI: 10.1073/pnas.1003187107. URL: http://www.ncbi.nlm.nih.gov/pubmed/20566872%20http://www.pubmedcentral.nih.gov/articlerender.fcgi?artid=PMC2901439.

[4] John Cook et al. "Consensus on consensus: a synthesis of consensus estimates on human-caused global warming". In: *Environmental Research Letters* 11.4 (Apr. 2016), p. 048002. ISSN: 1748-9326. DOI: 10.1088/1748-9326/11/4/048002. URL: http://stacks.iop.org/1748-9326/11/i=4/a=048002?key=crossref.80d294a6c5d3b7882bc7dc12487e9f39.

[5] Intergovernmental Panel on Climate Change. "Summary for Policymakers". In: *Climate Change 2013 - The Physical Science Basis*. Ed. by Intergovernmental Panel on Climate Change. Cambridge: Cambridge University Press, 2014, pp. 1–30. DOI: 10.1017/CBO9781107415324.004. URL: https://www.cambridge.org/core/product/identifier/CBO9781107415324A009/type/book_part.

[6] Maarten Van Aalst et al. "Climate Change 2014: Impacts, Adaptation, and Vulnerability". In: *Assessment Report 5* October 2013 (2014). Ed. by Christopher B. Field et al., pp. 1–76. DOI: 10.1017/CBO9781107415379. URL: http://ebooks.cambridge.org/ref/id/CBO9781107415379.

[7] M. King Hubbert. "Nuclear Energy and the Fossil Fuel". In: (Jan. 1956). URL: https://www.onepetro.org/conference-paper/API-56-007.

[8] Ugo Bardi. "Peak oil: The four stages of a new idea". In: *Energy* 34.3 (Mar. 2009), pp. 323–326. ISSN: 0360-5442. DOI: 10.1016/J.ENERGY.2008.08.015. URL: https://www.sciencedirect.com/science/article/pii/S0360544208002132.

[9] R L Hirsch, Roger Bezdek, and Robert Wendling. *Peaking of world oil production: Impacts, mitigation, & risk management*. Tech. rep. Pittsburgh, PA, and Morgantown, WV (United States): National Energy Technology Laboratory, Feb. 2005. DOI: 10.2172/939271. URL: http://www.osti.gov/servlets/purl/939271/.

[10] Pedro de Almeida and Pedro D. Silva. "The peak of oil production—Timings and market recognition". In: *Energy Policy* 37.4 (Apr. 2009), pp. 1267–1276. ISSN: 0301-4215. DOI: 10.1016/J.ENPOL.2008.11.016. URL: https://www.sciencedirect.com/science/article/pii/S0301421508006630.

[11] K.-H. Robèrt et al. "Strategic sustainable development — selection, design and synergies of applied tools". In: *Journal of Cleaner Production* 10.3 (June 2002), pp. 197–214. ISSN: 0959-6526. DOI: 10.1016/S0959-6526(01)00061-0. URL: https://www.sciencedirect.com/science/article/pii/S0959652601000610.

[12] A.V Bridgwater. "Renewable fuels and chemicals by thermal processing of biomass". In: *Chemical Engineering Journal* 91.2-3 (Mar. 2003), pp. 87–102. ISSN: 1385-8947. DOI: 10.1016/S1385-8947(02)00142-0. URL: https://www.sciencedirect.com/science/article/pii/S1385894702001420.

[13] X Lang et al. "Preparation and characterization of bio-diesels from various bio-oils". In: *Bioresource Technology* 80.1 (Oct. 2001), pp. 53–62. ISSN: 0960-8524. DOI: 10.1016/S0960-8524(01)00051-7. URL: https://www.sciencedirect.com/science/article/pii/S0960852401000517.

[14] Ana María Aragonés. *How the U.S. caused the tortilla crisis*. 2007. URL: http://theweek.com/articles/522414/how-caused-tortilla-crisis.

[15] James Hider. *Tortilla crisis hits the poor as clean fuel drives up corn price — The Times*. 2007. URL: https://www.thetimes.co.uk/article/tortilla-crisis-hits-the-poor-as-clean-fuel-drives-up-corn-price-qlkc6063pwv.

[16] Catherine Elsworth. *Mexico's poor suffer as tortilla price rises - Telegraph*. 2007. URL: https://www.telegraph.co.uk/news/worldnews/1540947/Mexicos-poor-suffer-as-tortilla-price-rises.html.

[17] Michele Aresta and Angela Dibenedetto. "Utilisation of CO2 as a chemical feedstock: opportunities and challenges". In: *Dalton Transactions* 28 (July 2007), p. 2975. ISSN: 1477-9226. DOI: 10.1039/b700658f. URL: http://xlink.rsc.org/?DOI=b700658f.

[18] Toshiyasu Sakakura, Jun-Chul Choi, and Hiroyuki Yasuda. "Transformation of Carbon Dioxide". In: *Chemical Reviews* 107.6 (June 2007), pp. 2365–2387. ISSN: 0009-2665. DOI: 10.1021/cr068357u. URL: https://pubs.acs.org/doi/10.1021/cr068357u%20http://pubs.acs.org/doi/abs/10.1021/cr068357u.

[19] Toshiyasu Sakakura and Kazufumi Kohno. "The synthesis of organic carbonates from carbon dioxide". In: *Chemical Communications* 11 (Mar. 2009), p. 1312. ISSN: 1359-7345. DOI: 10.1039/b819997c. URL: http://xlink.rsc.org/?DOI=b819997c.

[20] Gabriele Centi and Siglinda Perathoner. “Opportunities and prospects in the chemical recycling of carbon dioxide to fuels”. In: *Catalysis Today* 148.3-4 (Nov. 2009), pp. 191–205. ISSN: 0920-5861. DOI: 10.1016/J.CATTOD.2009.07.075. URL: https://www.sciencedirect.com/science/article/pii/S0920586109004416?via%3Dihub.

[21] Yohan Richardson, Joël Blin, and Anne Julbe. “A short overview on purification and conditioning of syngas produced by biomass gasification: Catalytic strategies, process intensification and new concepts”. In: *Progress in Energy and Combustion Science* 38.6 (Dec. 2012), pp. 765–781. ISSN: 0360-1285. DOI: 10.1016/J.PECS.2011.12.001. URL: https://www.sciencedirect.com/science/article/pii/S0360128512000251.

[22] Karen Murdoch et al. “Sabatier Methanation Reactor for Space Exploration”. In: *1st Space Exploration Conference: Continuing the Voyage of Discovery*. Reston, Virigina: American Institute of Aeronautics and Astronautics, Jan. 2005. ISBN: 978-1-62410-022-2. DOI: 10.2514/6.2005-2706. URL: http://arc.aiaa.org/doi/10.2514/6.2005-2706.

[23] Christian Junaedi et al. “Compact and Lightweight Sabatier Reactor for Carbon Dioxide Reduction”. In: *41st International Conference on Environmental Systems*. Reston, Virigina: American Institute of Aeronautics and Astronautics, July 2011. ISBN: 978-1-60086-948-8. DOI: 10.2514/6.2011-5033. URL: http://arc.aiaa.org/doi/10.2514/6.2011-5033.

[24] Elspeth M. EM Petersen, AJ Anne J. Meier, and JP Jean-Philippe Tessonnier. “Carbon Dioxide Methanation for Human Exploration of Mars: A Look at Catalyst Longevity and Activity Using Supported Ruthenium”. In: (Apr. 2018). URL: https://ntrs.nasa.gov/search.jsp?R=20180002995.

[25] EC - European Commission. “Accelerating Clean Energy Innovation; COM(2016) 763 final”. In: (2016).

[26] Feg-Wen Chang et al. “Hydrogenation of CO2 over nickel catalysts on rice husk ash-alumina prepared by incipient wetness impregnation”. In: *Applied Catalysis A: General* 247.2 (July 2003), pp. 309–320. ISSN: 0926-860X. DOI: 10.1016/S0926-860X(03)00181-9. URL: https://www.sciencedirect.com/science/article/pii/S0926860X03001819?via%3Dihub.

[27] Marcin Kuśmierz. “Kinetic study on carbon dioxide hydrogenation over Ru/γ-Al2O3 catalysts”. In: *Catalysis Today* 137.2-4 (Sept. 2008), pp. 429–432. ISSN: 0920-5861. DOI: 10.1016/J.CATTOD.2008.03.003. URL: https://www.sciencedirect.com/science/article/pii/S0920586108001090?via%3Dihub.

[28] Kuo-Pin Yu et al. “Pt/titania-nanotube: A potential catalyst for CO2 adsorption and hydrogenation”. In: *Applied Catalysis B: Environmental* 84.1-2 (Oct. 2008), pp. 112–118. ISSN: 0926-3373. DOI: 10.1016/J.APCATB.2008.03.009. URL: https://www.sciencedirect.com/science/article/pii/S0926337308001100?via%3Dihub.

[29] Jung-Nam Park and Eric W. McFarland. "A highly dispersed Pd–Mg/SiO2 catalyst active for methanation of CO2". In: *Journal of Catalysis* 266.1 (Aug. 2009), pp. 92–97. ISSN: 0021-9517. DOI: 10.1016/J.JCAT.2009.05.018. URL: https://www.sciencedirect.com/science/article/pii/S0021951709001754.

[30] Tamás Szailer et al. "Effect of H2S on the hydrogenation of carbon dioxide over supported Rh catalysts". In: *Topics in Catalysis* 46.1-2 (Sept. 2007), pp. 79–86. ISSN: 1022-5528. DOI: 10.1007/s11244-007-0317-5. URL: http://link.springer.com/10.1007/s11244-007-0317-5.

[31] Wang Wei and Gong Jinlong. "Methanation of carbon dioxide: an overview". In: *Frontiers of Chemical Science and Engineering* 5.1 (Mar. 2011), pp. 2–10. ISSN: 2095-0179. DOI: 10.1007/s11705-010-0528-3. URL: http://link.springer.com/10.1007/s11705-010-0528-3.

[32] Guoan Du et al. "Methanation of carbon dioxide on Ni-incorporated MCM-41 catalysts: The influence of catalyst pretreatment and study of steady-state reaction". In: *Journal of Catalysis* 249.2 (July 2007), pp. 370–379. ISSN: 0021-9517. DOI: 10.1016/J.JCAT.2007.03.029. URL: https://www.sciencedirect.com/science/article/pii/S0021951707001388.

[33] Feg-Wen Chang, Ming-Tseh Tsay, and Shih-Ping Liang. "Hydrogenation of CO2 over nickel catalysts supported on rice husk ash prepared by ion exchange". In: *Applied Catalysis A: General* 209.1-2 (Feb. 2001), pp. 217–227. ISSN: 0926-860X. DOI: 10.1016/S0926-860X(00)00772-9. URL: https://www.sciencedirect.com/science/article/pii/S0926860X00007729?via%3Dihub.

[34] Costas G. Vayenas and Costas G. Koutsodontis. "Non-Faradaic electrochemical activation of catalysis". In: *The Journal of Chemical Physics* 128.18 (May 2008), p. 182506. ISSN: 0021-9606. DOI: 10.1063/1.2824944. URL: http://www.ncbi.nlm.nih.gov/pubmed/18532791%20http://aip.scitation.org/doi/10.1063/1.2824944.

[35] S. Bebelis, H. Karasali, and C. G. Vayenas. "Electrochemical promotion of CO2 hydrogenation on Rh/YSZ electrodes". In: *Journal of Applied Electrochemistry* 38.8 (Aug. 2008), pp. 1127–1133. ISSN: 0021-891X. DOI: 10.1007/s10800-008-9574-7. URL: http://link.springer.com/10.1007/s10800-008-9574-7.

[36] E.I. Papaioannou et al. "Electrochemical promotion of the CO2 hydrogenation reaction using thin Rh, Pt and Cu films in a monolithic reactor at atmospheric pressure". In: *Catalysis Today* 146.3-4 (Aug. 2009), pp. 336–344. ISSN: 0920-5861. DOI: 10.1016/J.CATTOD.2009.06.008. URL: https://www.sciencedirect.com/science/article/pii/S0920586109003356.

[37] Manuel Bailera et al. "Power to Gas projects review: Lab, pilot and demo plants for storing renewable energy and CO2". In: *Renewable and Sustainable Energy Reviews* 69 (Mar. 2017), pp. 292–312. ISSN: 1364-0321. DOI: 10.1016/J.RSER.2016.11.130. URL: https://www.sciencedirect.com/science/article/pii/S1364032116307833.

[38] *ZSW: PtG 250 (P2G®)*. URL: https://www.zsw-bw.de/en/projects/regenerative-kraftstoffe/ptg-250-p2gr.html#c3913.

[39] *Audi e-gas - Audi Technology Portal*. URL: https://www.audi-technology-portal.de/en/mobility-for-the-future/audi-future-lab-mobility_en/audi-future-energies_en/audi-e-gas_en.

[40] *Project*. URL: http://www.helmeth.eu/index.php/project#.

[41] Karim Ghaib and Fatima-Zahrae Ben-Fares. "Power-to-Methane: A state-of-the-art review". In: *Renewable and Sustainable Energy Reviews* 81 (Jan. 2018), pp. 433–446. ISSN: 1364-0321. DOI: 10.1016/J.RSER.2017.08.004. URL: https://www.sciencedirect.com/science/article/pii/S1364032117311346?via%3Dihub#bib223.

[42] M. A. A. Aziz et al. "CO ¡sub¿2¡/sub¿ methanation over heterogeneous catalysts: recent progress and future prospects". In: *Green Chemistry* 17.5 (May 2015), pp. 2647–2663. ISSN: 1463-9262. DOI: 10.1039/C5GC00119F. URL: http://xlink.rsc.org/?DOI=C5GC00119F.

[43] Gordon D. Weatherbee and Calvin H. Bartholomew. "Hydrogenation of CO2 on group VIII metals: II. Kinetics and mechanism of CO2 hydrogenation on nickel". In: *Journal of Catalysis* 77.2 (Oct. 1982), pp. 460–472. ISSN: 0021-9517. DOI: 10.1016/0021-9517(82)90186-5. URL: https://www.sciencedirect.com/science/article/pii/0021951782901865.

[44] John L. Falconer and A.Ercüment Zağli. "Adsorption and methanation of carbon dioxide on a nickel/silica catalyst". In: *Journal of Catalysis* 62.2 (Apr. 1980), pp. 280–285. ISSN: 0021-9517. DOI: 10.1016/0021-9517(80)90456-X. URL: https://www.sciencedirect.com/science/article/pii/002195178090456X.

[45] S. Fujita et al. "Methanation of carbon monoxide and carbon dioxide over nickel catalyst under the transient state". In: *Reaction Kinetics and Catalysis Letters* 33.1 (Mar. 1987), pp. 179–184. ISSN: 01331736. DOI: 10.1007/BF02066720. URL: http://link.springer.com/10.1007/BF02066720.

[46] C. Schild, A. Wokaun, and A. Baiker. "On the mechanism of CO and CO2 hydrogenation reactions on zirconia-supported catalysts: a diffuse reflectance FTIR study. Part II. Surface species on copper/zirconia catalysts: implications for methanoi synthesis selectivity". In: *Journal of Molecular Catalysis* 63.2 (Dec. 1990), pp. 243–254. ISSN: 03045102. DOI: 10.1016/0304-5102(90)85147-A. URL: https://www.sciencedirect.com/science/article/pii/030451029085147A.

[47] A. L. Lapidus et al. "The mechanism of carbon dioxide hydrogenation on copper and nickel catalysts". In: *Petroleum Chemistry* 47.2 (Mar. 2007), pp. 75–82. ISSN: 0965-5441. DOI: 10.1134/S0965544107020028. URL: http://link.springer.com/10.1134/S0965544107020028.

[48] R.E. Hayes, W.J. Thomas, and K.E. Hayes. "A study of the nickel-catalyzed methanation reaction". In: *Journal of Catalysis* 92.2 (Apr. 1985), pp. 312–326. ISSN: 0021-9517. DOI: 10.1016/0021-9517(85)90266-0. URL: https://www.sciencedirect.com/science/article/pii/0021951785902660.

[49] R.Z.C. van Meerten et al. "The kinetics and mechanism of the methanation of carbon monoxide on a nickel-silica catalyst". In: *Applied Catalysis* 3.1 (June 1982), pp. 29–56. ISSN: 0166-9834. DOI: 10.1016/0166-9834(82)80221-2. URL: https://www.sciencedirect.com/science/article/pii/0166983482802212.

[50] M. A. Vannice. "The Catalytic Synthesis of Hydrocarbons from Carbon Monoxide and Hydrogen". In: *Catalysis Reviews* 14.1 (Jan. 1976), pp. 153–191. ISSN: 0161-4940. DOI: 10.1080/03602457608073410. URL: http://www.tandfonline.com/doi/abs/10.1080/03602457608073410.

[51] G. A. Martin, M. Primet, and J. A. Dalmon. "Reactions of CO and CO2on Ni SiO2above 373 K as studied by infrared spectroscopic and magnetic methods". In: *Journal of Catalysis* 53.3 (July 1978), pp. 321–330. ISSN: 10902694. DOI: 10.1016/0021-9517(78)90104-5. URL: https://www.sciencedirect.com/science/article/pii/0021951778901045.

[52] Michel Marwood, Ralf Doepper, and Albert Renken. "In-situ surface and gas phase analysis for kinetic studies under transient conditions The catalytic hydrogenation of CO2". In: *Applied Catalysis A: General* 151.1 (Mar. 1997), pp. 223–246. ISSN: 0926-860X. DOI: 10.1016/S0926-860X(96)00267-0. URL: https://www.sciencedirect.com/science/article/pii/S0926860X96002670.

[53] D. E. Peebles, D. W. Goodman, and J. M. White. "Methanation of carbon dioxide on nickel(100) and the effects of surface modifiers". In: *The Journal of Physical Chemistry* 87.22 (Oct. 1983), pp. 4378–4387. ISSN: 0022-3654. DOI: 10.1021/j100245a014. URL: http://pubs.acs.org/doi/abs/10.1021/j100245a014.

[54] R.M. Watwe et al. "Theoretical Studies of Stability and Reactivity of CHx Species on Ni(111)". In: *Journal of Catalysis* 189.1 (Jan. 2000), pp. 16–30. ISSN: 0021-9517. DOI: 10.1006/JCAT.1999.2699. URL: https://www.sciencedirect.com/science/article/pii/S0021951799926994.

[55] M. Ackermann et al. "Hydrogenation of carbon monoxide on Ni(1 1 1) investigated with surface X-ray diffraction at atmospheric pressure". In: *Surface Science* 557.1-3 (May 2004), pp. 21–30. ISSN: 0039-6028. DOI: 10.1016/J.SUSC.2004.03.061. URL: https://www.sciencedirect.com/science/article/pii/S0039602804003449?via%3Dihub.

[56] D. Wayne Blaylock et al. "Computational Investigation of Thermochemistry and Kinetics of Steam Methane Reforming on Ni(111) under Realistic Conditions". In: *The Journal of Physical Chemistry C* 113.12 (Mar. 2009), pp. 4898–4908. ISSN: 1932-7447. DOI: 10.1021/jp806527q. URL: http://pubs.acs.org/doi/10.1021/jp806527q.

[57] Jun Ren et al. "Insights into the mechanisms of CO2 methanation on Ni(111) surfaces by density functional theory". In: *Applied Surface Science* 351 (Oct. 2015), pp. 504–516. ISSN: 0169-4332. DOI: 10.1016/J.APSUSC.2015.05.173. URL: https://www.sciencedirect.com/science/article/pii/S0169433215013148.

[58] Rafael C. Catapan et al. “DFT Study of the Water–Gas Shift Reaction and Coke Formation on Ni(111) and Ni(211) Surfaces”. In: *The Journal of Physical Chemistry C* 116.38 (Sept. 2012), pp. 20281–20291. ISSN: 1932-7447. DOI: 10.1021/jp302488f. URL: http://pubs.acs.org/doi/10.1021/jp302488f.

[59] Sang-Joon Choe et al. “Adsorbed Carbon Formation and Carbon Hydrogenation for CO ¡sub¿2¡/sub¿ Methanation on the Ni(111) Surface: ASED-MO Study”. In: *Bulletin of the Korean Chemical Society* 26.11 (Nov. 2005), pp. 1682–1688. ISSN: 0253-2964. DOI: 10.5012/bkcs.2005.26.11.1682. URL: http://koreascience.or.kr/journal/view.jsp?kj=JCGMCS&py=2005&vnc=v26n11&sp=1682.

[60] Franz Fischer, H Tropsch, and P Dilthey. “Reduction of carbon monoxide to methane in the presence of various metals”. In: *Brennst. Chem* 6 (1925), pp. 265–271.

[61] Paraskevi Panagiotopoulou, Dimitris I. Kondarides, and Xenophon. E. Verykios. “Selective methanation of CO over supported Ru catalysts”. In: *Applied Catalysis B: Environmental* 88.3-4 (May 2009), pp. 470–478. ISSN: 0926-3373. DOI: 10.1016/J.APCATB.2008.10.012. URL: https://www.sciencedirect.com/science/article/pii/S0926337308003986.

[62] Vicente Jiménez et al. “Methanation of CO, CO2 and selective methanation of CO, in mixtures of CO and CO2, over ruthenium carbon nanofibers catalysts”. In: *Applied Catalysis A: General* 390.1-2 (Dec. 2010), pp. 35–44. ISSN: 0926-860X. DOI: 10.1016/J.APCATA.2010.09.026. URL: https://www.sciencedirect.com/science/article/pii/S0926860X10006800.

[63] Leonardo Falbo et al. “Kinetics of CO2 methanation on a Ru-based catalyst at process conditions relevant for Power-to-Gas applications”. In: *Applied Catalysis B: Environmental* 225 (June 2018), pp. 354–363. ISSN: 0926-3373. DOI: 10.1016/J.APCATB.2017.11.066. URL: https://www.sciencedirect.com/science/article/pii/S0926337317311323.

[64] Jaroslaw Polanski et al. “Oxide passivated Ni-supported Ru nanoparticles in silica: A new catalyst for low-temperature carbon dioxide methanation”. In: *Applied Catalysis B: Environmental* 206 (June 2017), pp. 16–23. ISSN: 0926-3373. DOI: 10.1016/J.APCATB.2017.01.017. URL: https://www.sciencedirect.com/science/article/pii/S0926337317300103.

[65] E A Seddon and K R Seddon. *The Chemistry of Ruthenium*. Ed. by R J H Clark. Elsevier Science, 1984. ISBN: 9781483289908.

[66] David L King. “A Fischer-Tropsch study of supported ruthenium catalysts”. In: *Journal of Catalysis* 51.3 (1978), pp. 386–397. ISSN: 0021-9517. DOI: https://doi.org/10.1016/0021-9517(78)90277-4. URL: http://www.sciencedirect.com/science/article/pii/0021951778902774.

[67] Glenn Jones et al. “First principles calculations and experimental insight into methane steam reforming over transition metal catalysts”. In: *Journal of Catalysis* 259.1 (2008), pp. 147–160. ISSN: 0021-9517. DOI: https://doi.org/10.1016/j.jcat.2008.08.003. URL: http://www.sciencedirect.com/science/article/pii/S0021951708003096.

[68] Bielawa Hubert et al. “The Ammonia-Synthesis Catalyst of the Next Generation: Barium-Promoted Oxide-Supported Ruthenium”. In: *Angewandte Chemie International Edition* 40.6 (), pp. 1061–1063. DOI: 10.1002/1521-3773(20010316)40:6<1061::AID-ANIE10610>3.0.CO;2-B.

[69] T V Choudhary, C Sivadinarayana, and D W Goodman. “Catalytic ammonia decomposition: COx-free hydrogen production for fuel cell applications”. In: *Catalysis Letters* 72.3 (2001), pp. 197–201. ISSN: 1572-879X. DOI: 10.1023/A:1009023825549. URL: https://doi.org/10.1023/A:1009023825549.

[70] Sylwia Michlewska et al. “Ruthenium dendrimers as carriers for anticancer siRNA”. In: *Journal of Inorganic Biochemistry* 181 (2018), pp. 18–27. ISSN: 0162-0134. DOI: https://doi.org/10.1016/j.jinorgbio.2018.01.001. URL: http://www.sciencedirect.com/science/article/pii/S0162013417306396.

[71] Guan-Hao Chen et al. “Synthesis, characterization and cancer cell growth inhibition activity of ruthenium(II) complexes bearing bidentate pyrrole-imine ligands”. In: *Journal of Organometallic Chemistry* 868 (2018), pp. 122–130. ISSN: 0022-328X. DOI: https://doi.org/10.1016/j.jorganchem.2018.05.012. URL: http://www.sciencedirect.com/science/article/pii/S0022328X1830370X.

[72] Júlia Scaff Moreira Dias et al. “Pro-apoptotic activity of ruthenium 1-methylimidazole complex on non-small cell lung cancer”. In: *Journal of Inorganic Biochemistry* (2018). ISSN: 0162-0134. DOI: https://doi.org/10.1016/j.jinorgbio.2018.06.008. URL: http://www.sciencedirect.com/science/article/pii/S0162013418301892.

[73] Brian O’Regan and Michael Gratzel. “A Low-Cost, High-Efficiency Solar-Cell Based on Dye-Sensitized Colloidal TiO2 Films”. In: *Nature* 353.6346 (Oct. 1991), pp. 737–740. ISSN: 0028-0836. DOI: 10.1038/353737a0. URL: http://www.nature.com/doifinder/10.1038/353737a0.

[74] Feifei Gao et al. “A new heteroleptic ruthenium sensitizer enhances the absorptivity of mesoporous titania film for a high efficiency dye-sensitized solar cell”. In: *Chem. Commun.* 23 (2008), pp. 2635–2637. DOI: 10.1039/B802909A. URL: http://dx.doi.org/10.1039/B802909A.

[75] Nobuko Onozawa-Komatsuzaki et al. “Near-IR dye-sensitized solar cells using a new type of ruthenium complexes having 2,6-bis(quinolin-2-yl)pyridine derivatives”. In: *Solar Energy Materials and Solar Cells* 95.1 (2011), pp. 310–314. ISSN: 0927-0248. DOI: https://doi.org/10.1016/j.solmat.2010.05.003. URL: http://www.sciencedirect.com/science/article/pii/S0927024810002850.

[76] R K Vishnu Prataap et al. “Effect of electrodeposition modes on ruthenium oxide electrodes for supercapacitors”. In: *Current Applied Physics* 18.10 (2018), pp. 1143–1148. ISSN: 1567-1739. DOI: https://doi.org/10.1016/j.cap.2018.06.015. URL: http://www.sciencedirect.com/science/article/pii/S1567173918301834.

[77] Esra Sarıca, Serdar Akbayrak, and Saim Özkar. "Ruthenium(0) nanoparticles supported on silica coated Fe3O4 as magnetically separable catalysts for hydrolytic dehydrogenation of ammonia borane". In: *International Journal of Hydrogen Energy* (2018). ISSN: 0360-3199. DOI: https://doi.org/10.1016/j.ijhydene.2018.06.058. URL: http://www.sciencedirect.com/science/article/pii/S0360319918318706.

[78] Serdar Akbayrak et al. "Ruthenium(0) nanoparticles supported on magnetic silica coated cobalt ferrite: Reusable catalyst in hydrogen generation from the hydrolysis of ammonia-borane". In: *Journal of Molecular Catalysis A: Chemical* 394 (2014), pp. 253–261. ISSN: 1381-1169. DOI: https://doi.org/10.1016/j.molcata.2014.07.010. URL: http://www.sciencedirect.com/science/article/pii/S1381116914003021.

[79] Amendra Fernando et al. "Quantum Mechanical Studies of Large Metal, Metal Oxide, and Metal Chalcogenide Nanoparticles and Clusters". In: *Chemical Reviews* 115.12 (June 2015), pp. 6112–6216. ISSN: 0009-2665. DOI: 10.1021/cr500506r. URL: http://pubs.acs.org/doi/abs/10.1021/cr500506r.

[80] F Albert Cotton and Irene Shim. "Bonding in the diruthenium molecule by ab initio calculations". In: *Journal of the American Chemical Society* 104.25 (1982), pp. 7025–7029. DOI: 10.1021/ja00389a023. URL: https://doi.org/10.1021/ja00389a023.

[81] Kalyan K Das and K Balasubramanian. "Electronic states of Ru2". In: *The Journal of Chemical Physics* 95.4 (1991), pp. 2568–2571. DOI: 10.1063/1.460961. URL: https://doi.org/10.1063/1.460961.

[82] Joonghan Kim and Jeongho Kim. "Density functional and multireference ab initio study of the ground and excited states of Ru2". In: *Chemical Physics Letters* 592 (2014), pp. 24–29. ISSN: 0009-2614. DOI: https://doi.org/10.1016/j.cplett.2013.12.002. URL: http://www.sciencedirect.com/science/article/pii/S0009261413014826.

[83] Selvarengan Paranthaman et al. "Performance of Density Functional Theory and Relativistic Effective Core Potential for Ru-Based Organometallic Complexes". In: *The Journal of Physical Chemistry A* 120.13 (2016), pp. 2128–2134. DOI: 10.1021/acs.jpca.6b00654. URL: https://doi.org/10.1021/acs.jpca.6b00654.

[84] L.-L. Wang and D D Johnson. "Removing Critical Errors for DFT Applications to Transition-Metal Nanoclusters: Correct Ground-State Structures of Ru Clusters". In: *The Journal of Physical Chemistry B* 109.49 (2005), pp. 23113–23117. DOI: 10.1021/jp0555347. URL: https://doi.org/10.1021/jp0555347.

[85] David J Dooling, Robert J Nielsen, and Linda J Broadbelt. "A density-functional study of the interaction of nitrogen with ruthenium clusters". In: *Chemical Engineering Science* 54.15 (1999), pp. 3399–3409. ISSN: 0009-2509. DOI: https://doi.org/10.1016/S0009-2509(98)00387-X. URL: http://www.sciencedirect.com/science/article/pii/S000925099800387X.

[86] Wenqin Zhang, Haitao Zhao, and Lichang Wang. "The Simple Cubic Structure of Ruthenium Clusters". In: *The Journal of Physical Chemistry B* 108.7 (Feb. 2004), pp. 2140–2147. ISSN: 1520-6106. DOI: 10.1021/jp035995x. URL: https://pubs.acs.org/doi/abs/10.1021/jp035995x%20http://pubs.acs.org/doi/abs/10.1021/jp035995x.

[87] Young-Cho Bae et al. "Atomic Structures and Magnetic Behavior of Small Ruthenium Clusters". In: *Materials transactions* 46.2 (2005), pp. 159–162. DOI: 10.2320/matertrans.46.159.

[88] F. Aguilera-Granja et al. "Study of the Structural and Electronic Properties of Rh N and Ru N Clusters (N ¡ 20) within the Density Functional Theory". In: *Journal of Physical Chemistry A* 113.48 (Dec. 2009), pp. 13483–13491. ISSN: 10895639. DOI: 10.1021/jp905188t. URL: http://pubs.acs.org/doi/abs/10.1021/jp905188t.

[89] Shunfang Li et al. "Structural and electronic properties of Run clusters (n=2-14) studied by first-principles calculations". In: *Physical Review B - Condensed Matter and Materials Physics* 76.4 (2007), p. 45410. ISSN: 10980121. DOI: 10.1103/PhysRevB.76.045410. URL: https://link.aps.org/doi/10.1103/PhysRevB.76.045410.

[90] Ilker Demiroglu et al. "DFT Global Optimization of Gas-Phase Subnanometer Ru-Pt Clusters". In: *The Journal of Physical Chemistry C* 121.20 (2017), pp. 10773–10780. DOI: 10.1021/acs.jpcc.6b11329. URL: https://doi.org/10.1021/acs.jpcc.6b11329.

[91] Jeppe Gavnholt and Jakob Schiotz. "Structure and reactivity of ruthenium nanoparticles". In: *Phys. Rev. B* 77.3 (2008), p. 35404. DOI: 10.1103/PhysRevB.77.035404. URL: https://link.aps.org/doi/10.1103/PhysRevB.77.035404.

[92] Hongbo Shi, Pekka Koskinen, and Ashwin Ramasubramaniam. "Self-Consistent Charge Density-Functional Tight-Binding Parametrization for PtRu Alloys". In: *The Journal of Physical Chemistry A* 121.12 (2017), pp. 2497–2502. DOI: 10.1021/acs.jpca.7b00701. URL: https://doi.org/10.1021/acs.jpca.7b00701.

[93] Rana. O Abdaljalil and Nibras. M Umran. "Effect of encapsulation (Ru & Pd) small clusters in fullerene (C60) on electronic and magnetic properties: DFT". In: *AIP Conference Proceedings* 1888.1 (2017), p. 20001. DOI: 10.1063/1.5004278. URL: https://aip.scitation.org/doi/abs/10.1063/1.5004278.

[94] Yusuke Nanba, Takayoshi Ishimoto, and Michihisa Koyama. "Structural Stability of Ruthenium Nanoparticles: A Density Functional Theory Study". In: *The Journal of Physical Chemistry C* 121.49 (2017), pp. 27445–27452. DOI: 10.1021/acs.jpcc.7b08672. URL: https://doi.org/10.1021/acs.jpcc.7b08672.

[95] Thomas M.Soini et al. "Extending the cluster scaling technique to ruthenium clusters with hcp structures". In: *Surface Science* 643 (2016), pp. 156–163. DOI: doi.org/10.1016/j.susc.2015.06.020.

[96] Th. Frauenheim et al. “A Self-Consistent Charge Density-Functional Based Tight-Binding Method for Predictive Materials Simulations in Physics, Chemistry and Biology”. In: *Phys. Status Solidi B* 217 (2000), pp. 41–62.

[97] Thomas Frauenheim et al. “Atomistic Simulations of Complex Materials: Ground-State and Excited-State Properties”. In: *J. Phys.: Condens. Matter* 14 (2002), pp. 3015–3047.

[98] Mohammad Wahiduzzaman et al. “DFTB Parameters for the Periodic Table: Part 1, Electronic Structure”. In: *Journal of Chemical Theory and Computation* 9.9 (2013), pp. 4006–4017. DOI: 10.1021/ct4004959. URL: https://doi.org/10.1021/ct4004959.

[99] E. Jwa et al. “Plasma-assisted catalytic methanation of CO and CO2 over Ni–zeolite catalysts”. In: *Fuel Processing Technology* 108 (Apr. 2013), pp. 89–93. ISSN: 0378-3820. DOI: 10.1016/J.FUPROC.2012.03.008. URL: https://www.sciencedirect.com/science/article/pii/S0378382012001014?via%3Dihub.

[100] Magadalena Nizio et al. “Hybrid plasma-catalytic methanation of CO2 at low temperature over ceria zirconia supported Ni catalysts”. In: *International Journal of Hydrogen Energy* 41.27 (July 2016), pp. 11584–11592. ISSN: 0360-3199. DOI: 10.1016/J.IJHYDENE.2016.02.020. URL: https://www.sciencedirect.com/science/article/pii/S0360319915307400.

[101] Guoxing Chen et al. “Plasma assisted catalytic decomposition of CO2”. In: *Applied Catalysis B: Environmental* 190 (Aug. 2016), pp. 115–124. ISSN: 0926-3373. DOI: 10.1016/J.APCATB.2016.03.009. URL: https://www.sciencedirect.com/science/article/pii/S092633731630176X.

[102] Magdalena Nizio et al. “Low temperature hybrid plasma-catalytic methanation over Ni-Ce-Zr hydrotalcite-derived catalysts”. In: *Catalysis Communications* 83 (Aug. 2016), pp. 14–17. ISSN: 1566-7367. DOI: 10.1016/J.CATCOM.2016.04.023. URL: https://www.sciencedirect.com/science/article/pii/S1566736716301492.

[103] Jim Van Durme et al. “Combining non-thermal plasma with heterogeneous catalysis in waste gas treatment: A review”. In: *Applied Catalysis B: Environmental* 78.3-4 (Feb. 2008), pp. 324–333. ISSN: 0926-3373. DOI: 10.1016/J.APCATB.2007.09.035. URL: https://www.sciencedirect.com/science/article/pii/S0926337307003037.

[104] M.A. Malik, Y. Minamitani, and K.H. Schoenbach. “Comparison of catalytic activity of aluminum oxide and silica gel for decomposition of volatile organic compounds (VOCs) in a plasmacatalytic Reactor”. In: *IEEE Transactions on Plasma Science* 33.1 (Feb. 2005), pp. 50–56. ISSN: 0093-3813. DOI: 10.1109/TPS.2004.842323. URL: http://ieeexplore.ieee.org/document/1396121/.

[105] Ester Marotta et al. “DC corona electric discharges for air pollution control. Part 1. Efficiency and products of hydrocarbon processing”. In: *Environmental Science and Technology* 41.16 (2007), pp. 5862–5868. ISSN: 0013936X. DOI: 10.1021/es0707411. URL: https://pubs.acs.org/doi/abs/10.1021/es0707411.

[106] Roger Atkinson and Janet Arey. "Gas-phase tropospheric chemistry of biogenic volatile organic compounds: a review". In: *Atmospheric Environment* 37 (Jan. 2003), pp. 197–219. ISSN: 1352-2310. DOI: 10.1016/S1352-2310(03)00391-1. URL: https://www.sciencedirect.com/science/article/pii/S1352231003003911.

[107] Tomohiro Nozaki et al. "Dissociation of vibrationally excited methane on Ni catalyst: Part 1. Application to methane steam reforming". In: *Catalysis Today* 89.1-2 (Feb. 2004), pp. 57–65. ISSN: 0920-5861. DOI: 10.1016/J.CATTOD.2003.11.040. URL: https://www.sciencedirect.com/science/article/pii/S0920586103006059?via%3Dihub.

[108] J. Christopher Whitehead. "Plasma catalysis: A solution for environmental problems". In: *Pure and Applied Chemistry* 82.6 (Apr. 2010), pp. 1329–1336. ISSN: 1365-3075. DOI: 10.1351/PAC-CON-10-02-39. URL: http://www.degruyter.com/view/j/pac.2010.82.issue-6/pac-con-10-02-39/pac-con-10-02-39.xml.

[109] Helen J. Gallon et al. "Plasma-assisted methane reduction of a NiO catalyst—Low temperature activation of methane and formation of carbon nanofibres". In: *Applied Catalysis B: Environmental* 106.3-4 (Aug. 2011), pp. 616–620. ISSN: 0926-3373. DOI: 10.1016/J.APCATB.2011.06.023. URL: https://www.sciencedirect.com/science/article/pii/S0926337311002992?via%3Dihub.

[110] Christophe De Bie et al. "Dielectric barrier discharges used for the conversion of greenhouse gases: modeling the plasma chemistry by fluid simulations". In: *Plasma Sources Science and Technology* 20.2 (Apr. 2011), p. 024008. ISSN: 0963-0252. DOI: 10.1088/0963-0252/20/2/024008. URL: http://stacks.iop.org/0963-0252/20/i=2/a=024008?key=crossref.b20074652040dacb5ba1ef1fd9b517fa.

[111] Vasilii I. Avdeev and Valentin N. Parmon. "Molecular Mechanism of the Formic Acid Decomposition on V ¡sub¿2¡/sub¿ O ¡sub¿5¡/sub¿ /TiO ¡sub¿2¡/sub¿ Catalysts: A Periodic DFT Analysis". In: *The Journal of Physical Chemistry C* 115.44 (Nov. 2011), pp. 21755–21762. ISSN: 1932-7447. DOI: 10.1021/jp204652n. URL: http://pubs.acs.org/doi/10.1021/jp204652n.

[112] E C Neyts and A Bogaerts. "Understanding plasma catalysis through modelling and simulation—a review". In: *Journal of Physics D: Applied Physics* 47.22 (June 2014), p. 224010. ISSN: 0022-3727. DOI: 10.1088/0022-3727/47/22/224010. URL: http://stacks.iop.org/0022-3727/47/i=22/a=224010?key=crossref.787b02256bb1265c91c0ab861f0be21b.

[113] J. Mazur and Robert J. Rubin. "Quantum Mechanical Calculation of the Probability of an Exchange Reaction for Constrained Linear Encounters". In: *The Journal of Chemical Physics* 31.5 (Nov. 1959), pp. 1395–1412. ISSN: 0021-9606. DOI: 10.1063/1.1730605. URL: http://aip.scitation.org/doi/10.1063/1.1730605.

[114] George C. Schatz and Aron Kuppermann. “Quantum mechanical reactive scattering for three-dimensional atom plus diatom systems. II. Accurate cross sections for H+H ¡sub¿2¡/sub¿”. In: *The Journal of Chemical Physics* 65.11 (Dec. 1976), pp. 4668–4692. ISSN: 0021-9606. DOI: 10.1063/1.432919. URL: http://aip.scitation.org/doi/10.1063/1.432919.

[115] Uwe Manthe, Tamar Seideman, and William H. Miller. “Full-dimensional quantum mechanical calculation of the rate constant for the H ¡sub¿2¡/sub¿ +OH-¿H ¡sub¿2¡/sub¿ O+H reaction”. In: *The Journal of Chemical Physics* 99.12 (Dec. 1993), pp. 10078–10081. ISSN: 0021-9606. DOI: 10.1063/1.465514. URL: http://aip.scitation.org/doi/10.1063/1.465514.

[116] George C. Schatz and Henry Elgersma. “A quasi-classical trajectory study of product vibrational distributions in the OH + H2 -¿ H2O + H reaction”. In: *Chemical Physics Letters* 73.1 (July 1980), pp. 21–25. ISSN: 00092614. DOI: 10.1016/0009-2614(80)85193-1. URL: http://linkinghub.elsevier.com/retrieve/pii/0009261480851931.

[117] Guillermo Ochoa de Aspuru and David C. Clary. “New Potential Energy Function for Four-Atom Reactions. Application to OH + H 2”. In: *The Journal of Physical Chemistry A* 102.47 (1998), pp. 9631–9637. ISSN: 1089-5639. DOI: 10.1021/jp982433i. URL: https://pubs.acs.org/doi/10.1021/jp982433i%20http://pubs.acs.org/doi/abs/10.1021/jp982433i.

[118] Guo-sheng Wu et al. “A new potential surface and quasiclassical trajectory study of H+H2O-¿OH+H2”. In: *The Journal of Chemical Physics* 113.8 (Aug. 2000), pp. 3150–3161. ISSN: 0021-9606. DOI: 10.1063/1.1287329. URL: https://aip.scitation.org/doi/10.1063/1.1287329%20http://aip.scitation.org/doi/10.1063/1.1287329.

[119] Minghui Yang et al. “Ab initio potential-energy surfaces for the reactions OH+H2¡-¿H2O+H”. In: *The Journal of Chemical Physics* 115.1 (July 2001), pp. 174–178. ISSN: 0021-9606. DOI: 10.1063/1.1372335. URL: http://aip.scitation.org/doi/10.1063/1.1372335.

[120] Jun Chen et al. “A global potential energy surface for the H 2 + OH ¡-¿ H 2 O + H reaction using neural networks”. In: *The Journal of Chemical Physics* 138.15 (Apr. 2013), p. 154301. ISSN: 0021-9606. DOI: 10.1063/1.4801658. URL: http://aip.scitation.org/doi/10.1063/1.4801658.

[121] N. Balakrishnan and G. D. Billing. “Integral cross sections and rate constants for the reaction OH+H ¡sub¿2¡/sub¿ -¿H ¡sub¿2¡/sub¿ O+H: A semiclassical wave packet approach”. In: *The Journal of Chemical Physics* 101.4 (Aug. 1994), pp. 2785–2792. ISSN: 0021-9606. DOI: 10.1063/1.468469. URL: http://aip.scitation.org/doi/10.1063/1.468469.

[122] N Balakrishnan and G.D. Billing. “A mixed quantal/classical study of the reaction OH + H2 -¿ H2O + H”. In: *Chemical Physics Letters* 233.1-2 (Feb. 1995), pp. 145–153. ISSN: 00092614. DOI: 10.1016/0009-2614(94)01388-C. URL: http://linkinghub.elsevier.com/retrieve/pii/000926149401388C.

[123] *ProGeo — Projects — H2020 — CORDIS — European Commission*. URL: https://cordis.europa.eu/project/rcn/203571_en.html.

[124] "Centro Ricerche Casaccia". In: (). URL: http://www.enea.it/it/centro-ricerche-frascati%20http://www.enea.it/it/Ricerca_sviluppo/documenti/efficienza-energetica/scheda-zecomix.

[125] Antonio. Laganà and A Riganelli. *Reaction and molecular dynamics : proceedings of the European School on Computational Chemistry, Perugia, Italy, July (1999)*. 75. Springer, 2000, xi, 312 p.

[126] Andrea Lombardi et al. "A bond-bond portable approach to intermolecular interactions: Simulations for N-methylacetamide and carbon dioxide dimers". In: *Lecture Notes in Computer Science (including subseries Lecture Notes in Artificial Intelligence and Lecture Notes in Bioinformatics)*. Vol. 7333 LNCS. PART 1. Springer, Berlin, Heidelberg, 2012, pp. 387–400. ISBN: 9783642311246. DOI: 10.1007/978-3-642-31125-3{_}30. URL: http://link.springer.com/10.1007/978-3-642-31125-3_30.

[127] Stefano Falcinelli et al. "Modeling the intermolecular interactions and characterization of the dynamics of collisional autoionization processes". In: *Lecture Notes in Computer Science (including subseries Lecture Notes in Artificial Intelligence and Lecture Notes in Bioinformatics)*. Vol. 7971 LNCS. PART 1. Springer, Berlin, Heidelberg, 2013, pp. 69–83. ISBN: 9783642396366. DOI: 10.1007/978-3-642-39637-3-6. URL: http://link.springer.com/10.1007/978-3-642-39637-3_6.

[128] David Cappelletti et al. "Experimental Evidence of Chemical Components in the Bonding of Helium and Neon with Neutral Molecules". In: *Chemistry - A European Journal* 21.16 (Apr. 2015), pp. 6234–6240. ISSN: 15213765. DOI: 10.1002/chem.201406103. URL: http://doi.wiley.com/10.1002/chem.201406103.

[129] B. Brunetti et al. "Energy dependence of the Penning ionization electron spectrum of Ne* (3P2,0)+Kr". In: *European Physical Journal D*. Vol. 38. 1. EDP Sciences, Apr. 2006, pp. 21–27. DOI: 10.1140/epjd/e2005-00312-5. URL: http://www.springerlink.com/index/10.1140/epjd/e2005-00312-5.

[130] M. Alagia et al. "The soft X-ray absorption spectrum of the allyl free radical". In: *Phys. Chem. Chem. Phys.* 15.4 (Dec. 2013), pp. 1310–1318. ISSN: 1463-9076. DOI: 10.1039/C2CP43466K. URL: http://xlink.rsc.org/?DOI=C2CP43466K.

[131] Stefano Falcinelli et al. "Measurements of Ionization Cross Sections by Molecular Beam Experiments: Information Content on the Imaginary Part of the Optical Potential". In: *Journal of Physical Chemistry A* 120.27 (July 2016), pp. 5169–5174. ISSN: 15205215. DOI: 10.1021/acs.jpca.6b00795. URL: http://pubs.acs.org/doi/10.1021/acs.jpca.6b00795.

[132] David Cappelletti, Stefano Falcinelli, and Fernando Pirani. "The intermolecular interaction in D¡inf¿2¡/inf¿ - CX¡inf¿4¡/inf¿ and O¡inf¿2¡/inf¿ - CX¡inf¿4¡/inf¿ (X = F, Cl) systems: Molecular beam scattering experiments as a sensitive probe of the selectivity of charge transfer component". In: *Journal of Chemical Physics* 145.13 (Oct. 2016), p. 134305. ISSN: 00219606. DOI: 10.1063/1.4964092. URL: http://aip.scitation.org/doi/10.1063/1.4964092.

[133] *PLC S.p.a. — /EN/ABOUT US — L'energia che crea il tuo futuro*. URL: https://www.plcgroupspa.com/en/about-us.php.

[134] Andrea Capriccioli. "Report on PROGEO progress". In: *Virt&l-comm* 8 (2015), pp. 1–2. URL: http://services.chm.unipg.it/ojs/index.php/virtlcomm/article/view/90.

[135] *Contatti*. URL: https://www.vitevino.it/contatti.html.

[136] *Johnson Matthey offers the series of KATALCO methanation catalysts for hydrogen production*. URL: http://www.jmprotech.com/methanation-catalysts-for-hydrogen-production-katalco.

[137] Stefano Falcinelli et al. "Methane production by CO2 hydrogenation reaction with and without solid phase catalysis". In: *Fuel* 209 (Dec. 2017), pp. 802–811. ISSN: 0016-2361. DOI: 10.1016/J.FUEL.2017.07.109. URL: https://www.sciencedirect.com/science/article/pii/S0016236117309717?via%3Dihub.

[138] A. B. Bortz, M. H. Kalos, and J. L. Lebowitz. "A new algorithm for Monte Carlo simulation of Ising spin systems". In: *Journal of Computational Physics* 17.1 (Jan. 1975), pp. 10–18. ISSN: 10902716. DOI: 10.1016/0021-9991(75)90060-1. URL: https://www.sciencedirect.com/science/article/pii/0021999175900601?via%3Dihub.

[139] H. Müller-Krumbhaar and K. Binder. "Dynamic properties of the Monte Carlo method in statistical mechanics". In: *Journal of Statistical Physics* 8.1 (May 1973), pp. 1–24. ISSN: 00224715. DOI: 10.1007/BF01008440. URL: http://link.springer.com/10.1007/BF01008440.

[140] Wei Cai et al. "Intrinsic Mobility of a Dissociated Dislocation in Silicon". In: *Phys. Rev. Lett.* 84 (15 Apr. 2000), pp. 3346–3349. DOI: 10.1103/PhysRevLett.84.3346. URL: https://link.aps.org/doi/10.1103/PhysRevLett.84.3346.

[141] B. Meng and W.H. Weinberg. "Dynamical Monte Carlo studies of molecular beam epitaxial growth models: interfacial scaling and morphology". In: *Surface Science* 364.2 (1996), pp. 151–163. ISSN: 0039-6028. DOI: https://doi.org/10.1016/0039-6028(96)00597-3. URL: http://www.sciencedirect.com/science/article/pii/0039602896005973.

[142] W M Young and E W Elcock. "Monte Carlo studies of vacancy migration in binary ordered alloys: I". In: *Proceedings of the Physical Society* 89.3 (1966), p. 735. URL: http://stacks.iop.org/0370-1328/89/i=3/a=329.

[143] Stephan A. Baeurle, Takao Usami, and Andrei A. Gusev. "A new multiscale modeling approach for the prediction of mechanical properties of polymer-based nanomaterials". In: *Polymer* 47.26 (2006), pp. 8604–8617. ISSN: 0032-3861. DOI: https://doi.org/10.1016/j.polymer.2006.10.017. URL: http://www.sciencedirect.com/science/article/pii/S0032386106011797.

[144] Michail Stamatakis and Dionisios G. Vlachos. "A graph-theoretical kinetic Monte Carlo framework for on-lattice chemical kinetics". In: *The Journal of Chemical Physics* 134.21 (June 2011), p. 214115. ISSN: 0021-9606. DOI: 10.1063/1.3596751. URL: http://aip.scitation.org/doi/10.1063/1.3596751.

[145] Reinhard Diestel. *Graph Theory*. 5th. Springer Publishing Company, Incorporated, 2018. ISBN: 3662575604, 9783662575604.

[146] Keith J. (Keith James) Laidler. *Chemical kinetics*. Harper & Row, 1987, p. 531. URL: https://books.google.fr/books/about/CHEMICAL_KINETICS_3rd_edition_Edition_en.html?id=GLcPAQAAMAAJ&source=kp_book_description&redir_esc=y.

[147] P J Birbara and F. Sribnik. *Development of an improved Sabatier reactor*. Vol. 79-ENAS-36. Jan. 1979, pp. 1–10. URL: https://www.osti.gov/biblio/5087687.

[148] Jens Nielsen et al. "Parallel kinetic Monte Carlo simulation framework incorporating accurate models of adsorbate lateral interactions". In: *The Journal of Chemical Physics* 139.22 (Dec. 2013), p. 224706. ISSN: 0021-9606. DOI: 10.1063/1.4840395. URL: http://aip.scitation.org/doi/10.1063/1.4840395.

[149] Cecilia Coletti and Gert D. Billing. "Quantum-Classical Methods: a Quantum-Classical Approach to Diatom-Diatom Reactive Scattering and VV Energy Transfer". In: *Reaction and Molecular Dynamics*. Ed. by A Laganà and A Riganelli. Springer, 2000, pp. 257–270. ISBN: 978-3-642-57051-3. DOI: 10.1007/978-3-642-57051-3{_}18. URL: http://link.springer.com/10.1007/978-3-642-57051-3_18.

[150] N Balakrishnan and G D Billing. "Integral cross sections and rate constants for the reaction OH+H 2 -¿H 2 O+H: A semiclassical wave packet approach". In: *The Journal of Chemical Physics* 101.4 (Aug. 1994), pp. 2785–2792. ISSN: 0021-9606. DOI: 10.1063/1.468469. URL: http://aip.scitation.org/doi/10.1063/1.468469.

[151] Trygve Helgaker, Einar Uggerud, and Hans Jørgen Aa. Jensen. "Integration of the classical equations of motion on ab initio molecular potential energy surfaces using gradients and Hessians: application to translational energy release upon fragmentation". In: *Chemical Physics Letters* 173.2-3 (Oct. 1990), pp. 145–150. ISSN: 0009-2614. DOI: 10.1016/0009-2614(90)80068-O. URL: https://www.sciencedirect.com/science/article/pii/000926149080068O?via%3Dihub.

[152] Wei Chen, William L. Hase, and H.Bernhard Schlegel. "Ab initio classical trajectory study of H2CO-¿H2+CO dissociation". In: *Chemical Physics Letters* 228.4-5 (Oct. 1994), pp. 436–442. ISSN: 0009-2614. DOI: 10.1016/0009-2614(94)00939-2. URL: https://www.sciencedirect.com/science/article/pii/0009261494009392?via%3Dihub.

[153] Rozeanne Steckler et al. "Ab initio direct dynamics study of OH+HCl-¿Cl+H 2 O". In: *The Journal of Chemical Physics* 106.10 (June 1997), pp. 3926–3933. ISSN: 0021-9606. DOI: 10.1063/1.473981. URL: http://aip.scitation.org/doi/10.1063/1.473981.

[154] Yuliya Paukku et al. “Erratum: “Global ¡i¿ab initio¡/i¿ ground-state potential energy surface of N ¡sub¿4¡/sub¿ ” [J. Chem. Phys. 139, 044309 (2013)]”. In: *The Journal of Chemical Physics* 140.1 (Jan. 2014), p. 019903. ISSN: 0021-9606. DOI: 10.1063/1.4861562. URL: http://aip.scitation.org/doi/10.1063/1.4861562.

[155] Sergio Rampino. “Configuration-Space Sampling in Potential Energy Surface Fitting: A Space-Reduced Bond-Order Grid Approach”. In: *The Journal of Physical Chemistry A* 120.27 (July 2016), pp. 4683–4692. ISSN: 1089-5639. DOI: 10.1021/acs.jpca.5b10018. URL: http://pubs.acs.org/doi/10.1021/acs.jpca.5b10018.

[156] Toshimasa Ishida and George C. Schatz. “Automatic potential energy surface generation directly from ab initio calculations using Shepard interpolation: A test calculation for the H2+H system”. In: *The Journal of Chemical Physics* 107.9 (June 1998), p. 3558. ISSN: 0021-9606. DOI: 10.1063/1.474695. URL: https://aip.scitation.org/doi/10.1063/1.474695.

[157] Moumita Majumder, Steve Alexandre Ndengue, and Richard Dawes. “Automated construction of potential energy surfaces”. In: *Molecular Physics* 114.1 (Jan. 2016), pp. 1–18. ISSN: 0026-8976. DOI: 10.1080/00268976.2015.1096974. URL: http://www.tandfonline.com/doi/full/10.1080/00268976.2015.1096974.

[158] J. N. (John Norman) Murrell. *Molecular potential energy functions*. J. Wiley, 1984, p. 197. URL: https://books.google.fr/books/about/Molecular_Potential_Energy_Functions.html?id=9GpIAQAAIAAJ&source=kp_book_description&redir_esc=y.

[159] E. Garcia and A. Lagana’. “Diatomic potential functions for triatomic scattering”. In: *Molecular Physics* 56.3 (Oct. 1985), pp. 621–627. ISSN: 0026-8976. DOI: 10.1080/00268978500102561. URL: http://www.tandfonline.com/doi/abs/10.1080/00268978500102561.

[160] Frank O. Ellison. “A Method of Diatomics in Molecules. I. General Theory and Application to H2O”. In: *Journal of the American Chemical Society* 85.22 (Nov. 1963), pp. 3540–3544. ISSN: 15205126. DOI: 10.1021/ja00905a002. URL: http://pubs.acs.org/doi/abs/10.1021/ja00905a002.

[161] Bina Fu, Eugene Kamarchik, and Joel M. Bowman. “Quasiclassical trajectory study of the postquenching dynamics of OH A2+ by H2/D2 on a global potential energy surface”. In: *The Journal of Chemical Physics* 133.16 (Oct. 2010), p. 164306. ISSN: 0021-9606. DOI: 10.1063/1.3488167. URL: http://aip.scitation.org/doi/10.1063/1.3488167.

[162] D. H. Zhang, M. A. Collins, and S. Y. Lee. “First-principles theory for the H + H2O, D2O reactions”. In: *Science* 290.5493 (Nov. 2000), pp. 961–963. ISSN: 00368075. DOI: 10.1126/science.290.5493.961.

[163] Chris M. Handley and Paul L. A. Popelier. “Potential Energy Surfaces Fitted by Artificial Neural Networks”. In: *The Journal of Physical Chemistry A* 114.10 (Mar. 2010), pp. 3371–3383. ISSN: 1089-5639. DOI: 10.1021/jp9105585. URL: http://pubs.acs.org/doi/abs/10.1021/jp9105585.

[164] Fernando Pirani et al. “Beyond the Lennard-Jones model: a simple and accurate potential function probed by high resolution scattering data useful for molecular dynamics simulations”. In: *Physical Chemistry Chemical Physics* 10.36 (Sept. 2008), p. 5489. ISSN: 1463-9076. DOI: 10.1039/b808524b. URL: http://xlink.rsc.org/?DOI=b808524b.

[165] Anthony Stone. *The Theory of Intermolecular Forces*. Oxford University Press, Jan. 2013. ISBN: 9780199672394. DOI: 10.1093/acprof:oso/9780199672394.001.0001. URL: http://www.oxfordscholarship.com/view/10.1093/acprof:oso/9780199672394.001.0001/acprof-9780199672394.

[166] Susana Gómez-Carrasco and Octavio Roncero. “Coordinate transformation methods to calculate state-to-state reaction probabilities with wave packet treatments”. In: *The Journal of Chemical Physics* 125.5 (Aug. 2006), p. 054102. ISSN: 0021-9606. DOI: 10.1063/1.2218337. URL: http://aip.scitation.org/doi/10.1063/1.2218337.

[167] *Lecture Notes — Physical Chemistry — Chemistry — MIT OpenCourseWare*. URL: https://ocw.mit.edu/courses/chemistry/5-61-physical-chemistry-fall-2013/lecture-notes/.

[168] Gabriel G. Balint-Kurti, Richard N. Dixon, and C. Clay Marston. “Grid methods for solving the Schrödinger equation and time dependent quantum dynamics of molecular photofragmentation and reactive scattering processes”. In: *International Reviews in Physical Chemistry* 11.2 (Sept. 1992), pp. 317–344. ISSN: 0144-235X. DOI: 10.1080/01442359209353274. URL: http://www.tandfonline.com/doi/abs/10.1080/01442359209353274.

[169] Edward A. McCullough and Robert E. Wyatt. “Quantum Dynamics of the Collinear (H, H ¡sub¿2¡/sub¿) Reaction”. In: *The Journal of Chemical Physics* 51.3 (Aug. 1969), pp. 1253–1254. ISSN: 0021-9606. DOI: 10.1063/1.1672133. URL: http://aip.scitation.org/doi/10.1063/1.1672133.

[170] Edward A. McCullough and Robert E. Wyatt. “Dynamics of the Collinear H+H ¡sub¿2¡/sub¿ Reaction. II. Energy Analysis”. In: *The Journal of Chemical Physics* 54.8 (Apr. 1971), pp. 3592–3600. ISSN: 0021-9606. DOI: 10.1063/1.1675385. URL: http://aip.scitation.org/doi/10.1063/1.1675385.

[171] M.D Feit, J.A Fleck, and A Steiger. “Solution of the Schrödinger equation by a spectral method”. In: *Journal of Computational Physics* 47.3 (Sept. 1982), pp. 412–433. ISSN: 0021-9991. DOI: 10.1016/0021-9991(82)90091-2. URL: https://www.sciencedirect.com/science/article/pii/0021999182900912?via%3Dihub.

[172] D Kosloff and R Kosloff. “A fourier method solution for the time dependent Schrödinger equation as a tool in molecular dynamics”. In: *Journal of Computational Physics* 52.1 (Oct. 1983), pp. 35–53. ISSN: 0021-9991. DOI: 10.1016/0021-9991(83)90015-3. URL: https://www.sciencedirect.com/science/article/pii/0021999183900153?via%3Dihub.

[173] J.V. Lill, G.A. Parker, and J.C. Light. “Discrete variable representations and sudden models in quantum scattering theory”. In: *Chemical Physics Letters* 89.6 (July 1982), pp. 483–489. ISSN: 0009-2614. DOI: 10.1016/0009-2614(82)83051-0. URL: https://www.sciencedirect.com/science/article/pii/0009261482830510?via%3Dihub.

[174] J. C. Light, I. P. Hamilton, and J. V. Lill. "Generalized discrete variable approximation in quantum mechanics". In: *The Journal of Chemical Physics* 82.3 (Feb. 1985), pp. 1400–1409. ISSN: 0021-9606. DOI: 10.1063/1.448462. URL: http://aip.scitation.org/doi/10.1063/1.448462.

[175] J. A. Fleck, J. R. Morris, and M. D. Feit. "Time-dependent propagation of high energy laser beams through the atmosphere". In: *Applied Physics* 10.2 (June 1976), pp. 129–160. ISSN: 0340-3793. DOI: 10.1007/BF00896333. URL: http://link.springer.com/10.1007/BF00896333.

[176] André D. Bandrauk and Hai Shen. "Improved exponential split operator method for solving the time-dependent Schrödinger equation". In: *Chemical Physics Letters* 176.5 (Jan. 1991), pp. 428–432. ISSN: 0009-2614. DOI: 10.1016/0009-2614(91)90232-X. URL: https://www.sciencedirect.com/science/article/abs/pii/000926149190232X.

[177] André D. Bandrauk and Hai Shen. "Higher order exponential split operator method for solving time-dependent Schrödinger equations". In: *Canadian Journal of Chemistry* 70.2 (Feb. 1992), pp. 555–559. ISSN: 0008-4042. DOI: 10.1139/v92-078. URL: http://www.nrcresearchpress.com/doi/10.1139/v92-078.

[178] André D. Bandrauk and Hai Shen. "Exponential split operator methods for solving coupled time-dependent Schrödinger equations". In: *The Journal of Chemical Physics* 99.2 (July 1993), pp. 1185–1193. ISSN: 0021-9606. DOI: 10.1063/1.465362. URL: http://aip.scitation.org/doi/10.1063/1.465362.

[179] H. Tal-Ezer and R. Kosloff. "An accurate and efficient scheme for propagating the time dependent Schrödinger equation". In: *The Journal of Chemical Physics* 81.9 (Nov. 1984), pp. 3967–3971. ISSN: 0021-9606. DOI: 10.1063/1.448136. URL: http://aip.scitation.org/doi/10.1063/1.448136.

[180] C. Lanczos. "An iteration method for the solution of the eigenvalue problem of linear differential and integral operators". In: *Journal of Research of the National Bureau of Standards* 45.4 (Oct. 1950), p. 255. ISSN: 0091-0635. DOI: 10.6028/jres.045.026. URL: https://nvlpubs.nist.gov/nistpubs/jres/045/jresv45n4p255_A1b.pdf.

[181] Tae Jun Park and J. C. Light. "Unitary quantum time evolution by iterative Lanczos reduction". In: *The Journal of Chemical Physics* 85.10 (Nov. 1986), pp. 5870–5876. ISSN: 0021-9606. DOI: 10.1063/1.451548. URL: http://aip.scitation.org/doi/10.1063/1.451548.

[182] Henry H. Suzukawa et al. "Empirical testing of the suitability of a nonrandom integration method for classical trajectory calculations: Comparisons with Monte Carlo techniques". In: *The Journal of Chemical Physics* 59.8 (Oct. 1973), pp. 4000–4008. ISSN: 0021-9606. DOI: 10.1063/1.1680591. URL: http://aip.scitation.org/doi/10.1063/1.1680591.

[183] N. P. (Nikolaĭ Panteleĭmonovich) Buslenko et al. *The Monte Carlo method : the method of statistical trials*, p. 396. ISBN: 9781483155579.

[184] Leon. Lapidus and John H. Seinfeld. *Numerical solution of ordinary differential equations*. Academic Press, 1971, p. 299. ISBN: 9780080955834.

[185] J C Butcher. *Numerical Methods for Ordinary Differential Equations*. J. Wiley, 2008, p. 425. ISBN: 9780471967583. URL: https://www.wiley.com/en-us/Numerical+Methods+for+Ordinary+Differential+Equations+-p-9780471967583.

[186] Donald G. Truhlar and James T. Muckerman. "Reactive Scattering Cross Sections III: Quasiclassical and Semiclassical Methods". In: *Atom - Molecule Collision Theory*. Boston, MA: Springer US, 1979, pp. 505–566. DOI: 10.1007/978-1-4613-2913-8{_}16. URL: http://link.springer.com/10.1007/978-1-4613-2913-8_16.

[187] M F Herman. "Dynamics by Semiclassical Methods". In: *Annual Review of Physical Chemistry* 45.1 (Oct. 1994), pp. 83–111. ISSN: 0066-426X. DOI: 10.1146/annurev.pc.45.100194.000503. URL: http://www.annualreviews.org/doi/10.1146/annurev.pc.45.100194.000503.

[188] Gert D. Billing. "Quantum corrections to the classical path equations: Multitrajectory and Hermite corrections". In: *The Journal of Chemical Physics* 107.11 (June 1998), p. 4286. ISSN: 0021-9606. DOI: 10.1063/1.474804. URL: https://aip.scitation.org/doi/10.1063/1.474804.

[189] Gert D. Billing. "Mixed Quantum-Classical Methods". In: *Encyclopedia of Computational Chemistry*. Chichester, UK: John Wiley & Sons, Ltd, Apr. 2002. DOI: 10.1002/0470845015.cma016. URL: http://doi.wiley.com/10.1002/0470845015.cma016.

[190] Gert D. Billing. "Time-dependent quantum dynamics in a Gauss–Hermite basis". In: *The Journal of Chemical Physics* 110.12 (Mar. 1999), p. 5526. ISSN: 0021-9606. DOI: 10.1063/1.478450. URL: https://aip.scitation.org/doi/10.1063/1.478450.

[191] Gert D. Billing. "Trajectory driven second quantization approach to quantum dynamics". In: *Chemical Physics* 242.3 (Apr. 1999), pp. 341–351. ISSN: 0301-0104. DOI: 10.1016/S0301-0104(99)00046-4. URL: https://www.sciencedirect.com/science/article/pii/S0301010499000464.

[192] Gert D. Billing. "Quantum-Classical Methods". In: Springer, Berlin, Heidelberg, 2000, pp. 115–129. DOI: 10.1007/978-3-642-57051-3{_}8. URL: http://link.springer.com/10.1007/978-3-642-57051-3_8.

[193] Gordon E. Moore. "Cramming more components onto integrated circuits". In: *Electronics* 38 (1965), p. 4.

[194] Gordon E. Moore. "Progress in digital integrated electronics [Technical literaiture, Copyright 1975 IEEE. Reprinted, with permission. Technical Digest. International Electron Devices Meeting, IEEE, 1975, pp. 11-13.]" In: *IEEE Solid-State Circuits Society Newsletter* 11.3 (Sept. 2006), pp. 36–37. ISSN: 1098-4232. DOI: 10.1109/N-SSC.2006.4804410. URL: http://ieeexplore.ieee.org/document/4804410/.

[195] L. Dagum and R. Menon. "OpenMP: an industry standard API for shared-memory programming". In: *IEEE Computational Science and Engineering* 5.1 (1998), pp. 46–55. ISSN: 10709924. DOI: 10.1109/99.660313. URL: http://ieeexplore.ieee.org/document/660313/.

[196] Miguel Hermanns. *Parallel Programming in Fortran 95 using OpenMP*. Tech. rep. 2002. URL: https://www.openmp.org/wp-content/uploads/F95_OpenMPv1_v2.pdf.

[197] Antonio Laganà. "A rotating bond order formulation of the atom diatom potential energy surface". In: *The Journal of Chemical Physics* 95.3 (Aug. 1991), pp. 2216–2217. ISSN: 0021-9606. DOI: 10.1063/1.460973. URL: http://aip.scitation.org/doi/10.1063/1.460973.

[198] Antonio Laganà et al. "Potential energy representations in the bond order space". In: *Chemical Physics* 168.2-3 (Dec. 1992), pp. 341–348. ISSN: 0301-0104. DOI: 10.1016/0301-0104(92)87167-8. URL: https://www.sciencedirect.com/science/article/pii/0301010492871678?via%3Dihub.

[199] A. Kurnosov et al. "Closer versus Long Range Interaction Effects on the Non-Arrhenius Behavior of Quasi-Resonant O ¡sub¿2¡/sub¿ + N ¡sub¿2¡/sub¿ Collisions". In: *The Journal of Physical Chemistry A* 121.27 (July 2017), pp. 5088–5099. ISSN: 1089-5639. DOI: 10.1021/acs.jpca.7b04204. URL: http://pubs.acs.org/doi/10.1021/acs.jpca.7b04204.

[200] Leonardo Pacifici et al. "A high-level ¡i¿ab initio¡/i¿ study of the N ¡sub¿2¡/sub¿ + N ¡sub¿2¡/sub¿ reaction channel". In: *Journal of Computational Chemistry* 34.31 (Dec. 2013), pp. 2668–2676. ISSN: 01928651. DOI: 10.1002/jcc.23415. URL: http://doi.wiley.com/10.1002/jcc.23415.

[201] E. Garcia and A. Lagana'. "A new bond-order functional form for triatomic molecules". In: *Molecular Physics* 56.3 (Oct. 1985), pp. 629–639. ISSN: 0026-8976. DOI: 10.1080/00268978500102571. URL: http://www.tandfonline.com/doi/abs/10.1080/00268978500102571.

[202] Paolo Palmieri, Ernesto Garcia, and Antonio Laganá. "A potential energy surface for the Li+HCl reaction". In: *The Journal of Chemical Physics* 88.1 (Jan. 1988), pp. 181–190. ISSN: 0021-9606. DOI: 10.1063/1.454634. URL: http://aip.scitation.org/doi/10.1063/1.454634.

[203] Antonio Lagana et al. "Scalar and vector properties of the magnesium + hydrogen fluoride reaction on a bond order surface". In: *The Journal of Physical Chemistry* 95.21 (Oct. 1991), pp. 8379–8384. ISSN: 0022-3654. DOI: 10.1021/j100174a062. URL: http://pubs.acs.org/doi/abs/10.1021/j100174a062.

[204] Antonio Laganà et al. "Ab initio calculations and dynamical tests of a potential energy surface for the Na+FH reaction". In: *The Journal of Chemical Physics* 106.24 (Aug. 1998), p. 10222. ISSN: 0021-9606. DOI: 10.1063/1.474049. URL: https://aip.scitation.org/doi/10.1063/1.474049.

[205] A. Laganà, G. Ochoa de Aspuru, and E. Garcia. "The largest angle generalization of the rotating bond order potential: Three different atom reactions". In: *The Journal of Chemical Physics* 108.10 (June 1998), p. 3886. ISSN: 0021-9606. DOI: 10.1063/1.475836. URL: https://aip.scitation.org/doi/10.1063/1.475836.

[206] Ernesto Garcia et al. “Modeling the global potential energy surface of the N + N2 reaction from ab initio data”. In: *Physical Chemistry Chemical Physics* 10.18 (Apr. 2008), p. 2552. ISSN: 1463-9076. DOI: 10.1039/b800593a. URL: http://xlink.rsc.org/?DOI=b800593a.

[207] Aurelio Rodriguez et al. “A LAGROBO strategy to fit potential energy surfaces: the OH + HCl reaction”. In: *Chemical Physics Letters* 360.3-4 (July 2002), pp. 304–312. ISSN: 0009-2614. DOI: 10.1016/S0009-2614(02)00835-7. URL: https://www.sciencedirect.com/science/article/pii/S0009261402008357?via%3Dihub.

[208] R Zellner and W Steinert. “Vibrational rate enhancement in the reaction OH + H2($\nu = 1$) -¿ H2O + H”. In: *Chemical Physics Letters* 81.3 (Aug. 1981), pp. 568–572. ISSN: 00092614. DOI: 10.1016/0009-2614(81)80465-4. URL: http://linkinghub.elsevier.com/retrieve/pii/0009261481804654%20https://www.sciencedirect.com/science/article/pii/0009261481804654.

[209] G.C. Light and J.H. Matsumoto. “The effect of vibrational excitation in the reactions of OH with H2”. In: *Chemical Physics Letters* 58.4 (Oct. 1978), pp. 578–581. ISSN: 00092614. DOI: 10.1016/0009-2614(78)80023-2. URL: http://scitation.aip.org/content/aip/journal/jcp/68/6/10.1063/1.436078%20http://linkinghub.elsevier.com/retrieve/pii/0009261478800232.

[210] Dong H. Zhang and John Z. H. Zhang. “Full-dimensional time-dependent treatment for diatom–diatom reactions: The H 2 +OH reaction”. In: *The Journal of Chemical Physics* 101.2 (July 1994), pp. 1146–1156. ISSN: 0021-9606. DOI: 10.1063/1.467808. URL: http://scitation.aip.org/content/aip/journal/jcp/101/2/10.1063/1.467808%20http://aip.scitation.org/doi/10.1063/1.467808.

[211] Bin Zhao, Zhigang Sun, and Hua Guo. “State-to-State Mode Specificity: Energy Sequestration and Flow Gated by Transition State”. In: *Journal of the American Chemical Society* 137.50 (Dec. 2015), pp. 15964–15970. ISSN: 0002-7863. DOI: 10.1021/jacs.5b11404. URL: http://pubs.acs.org/doi/10.1021/jacs.5b11404.

[212] A R Ravishankara et al. “Kinetic study of the reaction of hydroxyl with hydrogen and deuterium from 250 to 1050 K”. In: *The Journal of Physical Chemistry* 85.17 (Aug. 1981), pp. 2498–2503. ISSN: 0022-3654. DOI: 10.1021/j150617a018. URL: http://pubs.acs.org/doi/abs/10.1021/j150617a018%20http://dx.doi.org/10.1021/j150617a018.

[213] V. Schmidt et al. “Study of OH Reactions at High Pressures by Excimer Laser Photolysis - Dye Laser Fluorescence”. In: *Berichte der Bunsengesellschaft für physikalische Chemie* 89.3 (Mar. 1985), pp. 321–322. ISSN: 00059021. DOI: 10.1002/bbpc.19850890337. URL: http://doi.wiley.com/10.1002/bbpc.19850890337.

[214] W. Heisenberg. “Mehrkrperproblem und Resonanz in der Quantenmechanik”. In: *Zeitschrift fur Physik* 38.6-7 (June 1926), pp. 411–426. ISSN: 1434-6001. DOI: 10.1007/BF01397160. URL: http://link.springer.com/10.1007/BF01397160.

[215] P. A. M. Dirac. "On the Theory of Quantum Mechanics". In: *Proceedings of the Royal Society A: Mathematical, Physical and Engineering Sciences* 112.762 (Oct. 1926), pp. 661–677. ISSN: 1364-5021. DOI: 10.1098/rspa.1926.0133. URL: http://rspa.royalsocietypublishing.org/cgi/doi/10.1098/rspa.1926.0133.

[216] J. C. Slater. "The Theory of Complex Spectra". In: *Physical Review* 34.10 (Nov. 1929), pp. 1293–1322. ISSN: 0031-899X. DOI: 10.1103/PhysRev.34.1293. URL: https://link.aps.org/doi/10.1103/PhysRev.34.1293.

[217] Chr. Møller and M. S. Plesset. "Note on an Approximation Treatment for Many-Electron Systems". In: *Physical Review* 46.7 (Oct. 1934), pp. 618–622. ISSN: 0031-899X. DOI: 10.1103/PhysRev.46.618. URL: https://link.aps.org/doi/10.1103/PhysRev.46.618.

[218] E. Schrödinger. "Quantisierung als Eigenwertproblem". In: *Annalen der Physik* 385.13 (1926), pp. 437–490. ISSN: 00033804. DOI: 10.1002/andp.19263851302. URL: http://doi.wiley.com/10.1002/andp.19263851302.

[219] L. D. (Lev Davidovich) Landau et al. *Quantum mechanics : non-relativistic theory*. Butterworth Heinemann, 1977, p. 677. ISBN: 9780080503486.

[220] Christopher J. Cramer. *Essentials of Computational Chemistry Theories and Models*. Vol. 42. 2. Wiley, 2004, pp. 334–342. ISBN: 0470091819. DOI: 10.1021/ci010445m.

[221] L. H. Thomas. "The calculation of atomic fields". In: *Mathematical Proceedings of the Cambridge Philosophical Society* 23.05 (Jan. 1927), p. 542. ISSN: 0305-0041. DOI: 10.1017/S0305004100011683. URL: http://www.journals.cambridge.org/abstract_S0305004100011683.

[222] Enrico Fermi. "Un metodo statistico per la determinazione di alcune proprieta dell atomo". In: *Accademia Nazionale dei Lincei* 6 (1927), pp. 602–607.

[223] P. A. M. Dirac. "Note on Exchange Phenomena in the Thomas Atom". In: *Mathematical Proceedings of the Cambridge Philosophical Society* 26.03 (July 1930), p. 376. ISSN: 0305-0041. DOI: 10.1017/S0305004100016108. URL: http://www.journals.cambridge.org/abstract_S0305004100016108.

[224] P. Hohenberg and W. Kohn. "Inhomogeneous Electron Gas". In: *Physical Review* 136.3B (Nov. 1964), B864–B871. ISSN: 0031-899X. DOI: 10.1103/PhysRev.136.B864. URL: https://link.aps.org/doi/10.1103/PhysRev.136.B864.

[225] W. Kohn and L. J. Sham. "Self-Consistent Equations Including Exchange and Correlation Effects". In: *Physical Review* 140.4A (Nov. 1965), A1133–A1138. ISSN: 0031-899X. DOI: 10.1103/PhysRev.140.A1133. URL: https://link.aps.org/doi/10.1103/PhysRev.140.A1133.

[226] D. M. Ceperley and B. J. Alder. "Ground State of the Electron Gas by a Stochastic Method". In: *Physical Review Letters* 45.7 (Aug. 1980), pp. 566–569. ISSN: 0031-9007. DOI: 10.1103/PhysRevLett.45.566. URL: https://link.aps.org/doi/10.1103/PhysRevLett.45.566.

[227] J. P. Perdew and Alex Zunger. "Self-interaction correction to density-functional approximations for many-electron systems". In: *Physical Review B* 23.10 (May 1981), pp. 5048–5079. ISSN: 0163-1829. DOI: 10.1103/PhysRevB.23.5048. URL: https://link.aps.org/doi/10.1103/PhysRevB.23.5048.

[228] G. Ortiz and P. Ballone. "Correlation energy, structure factor, radial distribution function, and momentum distribution of the spin-polarized uniform electron gas". In: *Physical Review B* 50.3 (July 1994), pp. 1391–1405. ISSN: 0163-1829. DOI: 10.1103/PhysRevB.50.1391. URL: https://link.aps.org/doi/10.1103/PhysRevB.50.1391.

[229] Frank Herman, John P. Van Dyke, and Irene B. Ortenburger. "Improved Statistical Exchange Approximation for Inhomogeneous Many-Electron Systems". In: *Physical Review Letters* 22.16 (Apr. 1969), pp. 807–811. ISSN: 0031-9007. DOI: 10.1103/PhysRevLett.22.807. URL: https://link.aps.org/doi/10.1103/PhysRevLett.22.807.

[230] John P. Perdew and Kieron Burke. "Comparison shopping for a gradient-corrected density functional". In: *International Journal of Quantum Chemistry* 57.3 (Feb. 1996), pp. 309–319. ISSN: 0020-7608. DOI: 10.1002/(SICI)1097-461X(1996)57:3<309::AID-QUA4>3.0.CO;2-1. URL: http://doi.wiley.com/10.1002/%28SICI%291097-461X%281996%2957%3A3%3C309%3A%3AAID-QUA4%3E3.0.CO%3B2-1.

[231] John P. Perdew, Kieron Burke, and Matthias Ernzerhof. "Generalized Gradient Approximation Made Simple". In: *Physical Review Letters* 77.18 (Oct. 1996), pp. 3865–3868. ISSN: 0031-9007. DOI: 10.1103/PhysRevLett.77.3865. URL: https://link.aps.org/doi/10.1103/PhysRevLett.77.3865.

[232] Yingkai Zhang, Wei Pan, and Weitao Yang. "Describing van der Waals Interaction in diatomic molecules with generalized gradient approximations: The role of the exchange functional". In: *The Journal of Chemical Physics* 107.19 (Aug. 1998), p. 7921. ISSN: 0021-9606. DOI: 10.1063/1.475105. URL: https://aip.scitation.org/doi/abs/10.1063/1.475105.

[233] B. Montanari, P. Ballone, and R. O. Jones. "Density functional study of molecular crystals: Polyethylene and a crystalline analog of bisphenol-A polycarbonate". In: *The Journal of Chemical Physics* 108.16 (June 1998), p. 6947. ISSN: 0021-9606. DOI: 10.1063/1.476110. URL: https://aip.scitation.org/doi/10.1063/1.476110.

[234] David C. Patton, Dirk V. Porezag, and Mark R. Pederson. "Simplified generalized-gradient approximation and anharmonicity: Benchmark calculations on molecules". In: *Physical Review B* 55.12 (Mar. 1997), pp. 7454–7459. ISSN: 0163-1829. DOI: 10.1103/PhysRevB.55.7454. URL: https://link.aps.org/doi/10.1103/PhysRevB.55.7454.

[235] Axel D. Becke. "A new mixing of Hartree–Fock and local density-functional theories". In: *The Journal of Chemical Physics* 98.2 (Jan. 1993), pp. 1372–1377. ISSN: 0021-9606. DOI: 10.1063/1.464304. URL: http://aip.scitation.org/doi/10.1063/1.464304.

[236] Axel D. Becke. "Density-functional thermochemistry. III. The role of exact exchange". In: *The Journal of Chemical Physics* 98.7 (Apr. 1993), pp. 5648–5652. ISSN: 0021-9606. DOI: 10.1063/1.464913. URL: http://aip.scitation.org/doi/10.1063/1.464913.

[237] Chengteh Lee, Weitao Yang, and Robert G. Parr. "Development of the Colle-Salvetti correlation-energy formula into a functional of the electron density". In: *Physical Review B* 37.2 (Jan. 1988), pp. 785–789. ISSN: 0163-1829. DOI: 10.1103/PhysRevB.37.785. URL: https://link.aps.org/doi/10.1103/PhysRevB.37.785.

[238] Axel D. Becke. "Density-functional thermochemistry. IV. A new dynamical correlation functional and implications for exact-exchange mixing". In: *The Journal of Chemical Physics* 104.3 (Aug. 1998), p. 1040. ISSN: 0021-9606. DOI: 10.1063/1.470829. URL: https://aip.scitation.org/doi/abs/10.1063/1.470829.

[239] Jean-Louis. Calais. *Quantum chemistry workbook : basic concepts and procedures in the theory of the electronic structure of matter*. Wiley, 1994, p. 204. ISBN: 9780471594352. URL: https://www.wiley.com/en-us/Quantum+Chemistry+Workbook%3A+Basic+Concepts+and+Procedures+in+the+Theory+of+the+Electronic+Structure+of+Matter-p-9780471594352.

[240] C M Goringe, D R Bowler, and E Hernández. "Tight-binding modelling of materials". In: *Reports on Progress in Physics* 60.12 (Dec. 1997), pp. 1447–1512. ISSN: 0034-4885. DOI: 10.1088/0034-4885/60/12/001. URL: http://stacks.iop.org/0034-4885/60/i=12/a=001?key=crossref.a7092d85428fe010871220eed60ffb44.

[241] W. Matthew C. Foulkes and Roger Haydock. "Tight-binding models and density-functional theory". In: *Physical Review B* 39.17 (June 1989), pp. 12520–12536. ISSN: 0163-1829. DOI: 10.1103/PhysRevB.39.12520. URL: https://link.aps.org/doi/10.1103/PhysRevB.39.12520.

[242] D. Porezag et al. "Construction of tight-binding-like potentials on the basis of density-functional theory: Application to carbon". In: *Physical Review B* 51.19 (May 1995), pp. 12947–12957. ISSN: 0163-1829. DOI: 10.1103/PhysRevB.51.12947. URL: https://link.aps.org/doi/10.1103/PhysRevB.51.12947.

[243] Rudolph Pariser. "Theory of the Electronic Spectra and Structure of the Polyacenes and of Alternant Hydrocarbons". In: *The Journal of Chemical Physics* 24.2 (Feb. 1956), pp. 250–268. ISSN: 0021-9606. DOI: 10.1063/1.1742461. URL: http://aip.scitation.org/doi/10.1063/1.1742461.

[244] Robert G. Parr and Ralph G. Pearson. "Absolute hardness: companion parameter to absolute electronegativity". In: *Journal of the American Chemical Society* 105.26 (Dec. 1983), pp. 7512–7516. ISSN: 0002-7863. DOI: 10.1021/ja00364a005. URL: http://pubs.acs.org/doi/abs/10.1021/ja00364a005.

[245] R. S. Mulliken. "Electronic Population Analysis on LCAO–MO Molecular Wave Functions. I". In: *The Journal of Chemical Physics* 23.10 (Oct. 1955), pp. 1833–1840. ISSN: 0021-9606. DOI: 10.1063/1.1740588. URL: http://aip.scitation.org/doi/10.1063/1.1740588.

[246] Mathias Rapacioli et al. "Correction for dispersion and Coulombic interactions in molecular clusters with density functional derived methods: Application to polycyclic aromatic hydrocarbon clusters". In: *The Journal of Chemical Physics* 130.24 (June 2009), p. 244304. ISSN: 0021-9606. DOI: 10.1063/1.3152882. URL: http://www.ncbi.nlm.nih.gov/pubmed/19566150%20http://aip.scitation.org/doi/10.1063/1.3152882.

[247] Jason D. Thompson, Christopher J. Cramer, and Donald G. Truhlar. "Parameterization of charge model 3 for AM1, PM3, BLYP, and B3LYP". In: *Journal of Computational Chemistry* 24.11 (Aug. 2003), pp. 1291–1304. ISSN: 0192-8651. DOI: 10.1002/jcc.10244. URL: http://doi.wiley.com/10.1002/jcc.10244.

[248] Paul Winget et al. "Charge Model 3: A Class IV Charge Model Based on Hybrid Density Functional Theory with Variable Exchange". In: *The Journal of Physical Chemistry A* 106.44 (Nov. 2002), pp. 10707–10717. ISSN: 1089-5639. DOI: 10.1021/jp021917i. URL: https://pubs.acs.org/doi/abs/10.1021/jp021917i%20http://pubs.acs.org/doi/abs/10.1021/jp021917i.

[249] David J. Wales et al. "Energy Landscapes: From Clusters to Biomolecules". In: Wiley-Blackwell, Mar. 2007, pp. 1–111. DOI: 10.1002/9780470141748.ch1. URL: http://doi.wiley.com/10.1002/9780470141748.ch1.

[250] M. R. Hoare and J. McInnes. "Statistical mechanics and morphology of very small atomic clusters". In: *Faraday Discussions of the Chemical Society* 61 (Jan. 1976), p. 12. ISSN: 0301-7249. DOI: 10.1039/dc9766100012. URL: http://xlink.rsc.org/?DOI=dc9766100012.

[251] C. J. Tsai and K. D. Jordan. "Use of an eigenmode method to locate the stationary points on the potential energy surfaces of selected argon and water clusters". In: *The Journal of Physical Chemistry* 97.43 (Oct. 1993), pp. 11227–11237. ISSN: 0022-3654. DOI: 10.1021/j100145a019. URL: http://pubs.acs.org/doi/abs/10.1021/j100145a019.

[252] Jonathan P.K. Doye and David J. Wales. "Calculation of thermodynamic properties of small Lennard-Jones clusters incorporating anharmonicity". In: *The Journal of Chemical Physics* 102.24 (June 1995), pp. 9659–9672. ISSN: 00219606. DOI: 10.1063/1.468785. URL: http://aip.scitation.org/doi/10.1063/1.468785.

[253] Francesca Baletto and Riccardo Ferrando. "Structural properties of nanoclusters: Energetic, thermodynamic, and kinetic effects". In: *Reviews of Modern Physics* 77.1 (May 2005), pp. 371–423. ISSN: 0034-6861. DOI: 10.1103/RevModPhys.77.371. URL: https://link.aps.org/doi/10.1103/RevModPhys.77.371.

[254] Bernd Hartke. "Global geometry optimization of clusters using genetic algorithms". In: *The Journal of Physical Chemistry* 97.39 (Sept. 1993), pp. 9973–9976. ISSN: 0022-3654. DOI: 10.1021/j100141a013. URL: http://pubs.acs.org/doi/abs/10.1021/j100141a013.

[255] Yongliang Xiao and Donald E. Williams. "Genetic algorithm: a new approach to the prediction of the structure of molecular clusters". In: *Chemical Physics Letters* 215.1-3 (Nov. 1993), pp. 17–24. ISSN: 0009-2614. DOI: 10.1016/0009-2614(93)89256-H. URL: https://www.sciencedirect.com/science/article/pii/000926149389256H.

[256] Z Li and H A Scheraga. "Monte Carlo-minimization approach to the multiple-minima problem in protein folding." In: *Proceedings of the National Academy of Sciences of the United States of America* 84.19 (Oct. 1987), pp. 6611–5. ISSN: 0027-8424. URL: http://www.ncbi.nlm.nih.gov/pubmed/3477791%20http://www.pubmedcentral.nih.gov/articlerender.fcgi?artid=PMC299132.

[257] Jonathan P. K. Doye and David J. Wales. "Thermodynamics of Global Optimization". In: *Physical Review Letters* 80.7 (Feb. 1998), pp. 1357–1360. ISSN: 0031-9007. DOI: 10.1103/PhysRevLett.80.1357. URL: https://link.aps.org/doi/10.1103/PhysRevLett.80.1357.

[258] Glenn M. Torrie and John P. Valleau. "Monte Carlo free energy estimates using non-Boltzmann sampling: Application to the sub-critical Lennard-Jones fluid". In: *Chemical Physics Letters* 28.4 (Oct. 1974), pp. 578–581. ISSN: 0009-2614. DOI: 10.1016/0009-2614(74)80109-0. URL: https://www.sciencedirect.com/science/article/pii/0009261474801090?via%3Dihub.

[259] G.M. Torrie and J.P. Valleau. "Nonphysical sampling distributions in Monte Carlo free-energy estimation: Umbrella sampling". In: *Journal of Computational Physics* 23.2 (Feb. 1977), pp. 187–199. ISSN: 0021-9991. DOI: 10.1016/0021-9991(77)90121-8. URL: https://www.sciencedirect.com/science/article/pii/0021999177901218?via%3Dihub.

[260] Alessandro Laio and Michele Parrinello. "Escaping free-energy minima." In: *Proceedings of the National Academy of Sciences of the United States of America* 99.20 (Oct. 2002), pp. 12562–6. ISSN: 0027-8424. DOI: 10.1073/pnas.202427399. URL: http://www.ncbi.nlm.nih.gov/pubmed/12271136%20http://www.pubmedcentral.nih.gov/articlerender.fcgi?artid=PMC130499.

[261] S Kirkpatrick, C D Gelatt, and M P Vecchi. "Optimization by simulated annealing." In: *Science (New York, N.Y.)* 220.4598 (May 1983), pp. 671–80. ISSN: 0036-8075. DOI: 10.1126/science.220.4598.671. URL: http://www.ncbi.nlm.nih.gov/pubmed/17813860.

[262] Nicholas Metropolis et al. "Equation of State Calculations by Fast Computing Machines". In: *The Journal of Chemical Physics* 21.6 (June 1953), pp. 1087–1092. ISSN: 0021-9606. DOI: 10.1063/1.1699114. URL: http://aip.scitation.org/doi/10.1063/1.1699114.

[263] Yuji Sugita and Yuko Okamoto. "Replica-exchange molecular dynamics method for protein folding". In: *Chemical Physics Letters* 314.1-2 (Nov. 1999), pp. 141–151. ISSN: 0009-2614. DOI: 10.1016/S0009-2614(99)01123-9. URL: https://www.sciencedirect.com/science/article/pii/S0009261499011239.

[264] Shuichi Nosé. "A molecular dynamics method for simulations in the canonical ensemble". In: *Molecular Physics* 52.2 (June 1984), pp. 255–268. ISSN: 0026-8976. DOI: 10.1080/00268978400101201. URL: http://www.tandfonline.com/doi/abs/10.1080/00268978400101201.

[265] William G. Hoover. "Canonical dynamics: Equilibrium phase-space distributions". In: *Physical Review A* 31.3 (Mar. 1985), pp. 1695–1697. ISSN: 0556-2791. DOI: 10.1103/PhysRevA.31.1695. URL: https://link.aps.org/doi/10.1103/PhysRevA.31.1695.

[266] T Heine et al. "DeMonNano software package". 2015.

[267] Augusto F Oliveira, Pier Philipsen, and Thomas Heine. "DFTB Parameters for the Periodic Table, Part 2: Energies and Energy Gradients from Hydrogen to Calcium". In: *J. Chem. Theory Comput.* 11.11 (2015), pp. 5209–5218.

[268] Christian Kerpal et al. "Far-IR Spectra and Structures of Small Cationic Ruthenium Clusters: Evidence for Cubic Motifs". In: *The Journal of Physical Chemistry C* 119.20 (2015), pp. 10869–10875. DOI: 10.1021/jp510471k.

[269] Eugen Waldt et al. "Structural evolution of small ruthenium cluster anions". In: *The Journal of Chemical Physics* 142.2 (2015), p. 24319. DOI: 10.1063/1.4905267. URL: https://doi.org/10.1063/1.4905267.

[270] Waldt Eugen et al. "Structures of Medium-Sized Ruthenium Clusters: The Octahedral Motif". In: *ChemPhysChem* 15.5 (), pp. 862–865. DOI: 10.1002/cphc.201400011. URL: https://onlinelibrary.wiley.com/doi/abs/10.1002/cphc.201400011.

[271] Charles. Kittel. *Introduction to solid state physics*. Wiley, 2005, p. 680. ISBN: 9780471415268. URL: https://www.wiley.com/en-us/Introduction+to+Solid+State+Physics%2C+8th+Edition-p-9780471415268.

[272] Luiz F L Oliveira et al. "Benchmarking Density Functional Based Tight-Binding for Silver and Gold Materials: From Small Clusters to Bulk". In: *The Journal of Physical Chemistry A* 120.42 (2016), pp. 8469–8483. DOI: 10.1021/acs.jpca.6b09292. URL: http://dx.doi.org/10.1021/acs.jpca.6b09292.

[273] C E Moore. *No Title*. Ed. by National Bureau of Standards. Vol. Circular 4. 1949.

[274] J Hölzl and F K Schulte. *Work Function of Metals*. Springer Verlag, Berlin, 1979.

[275] J C Rivière. "Work function : measurements and results". In: *Solid State Surface Science* 1 (1969). Ed. by Mino Green and Marcel Dekker.

[276] Herbert B Michaelson. "The work function of the elements and its periodicity". In: *Journal of Applied Physics* 48.11 (1977), pp. 4729–4733. DOI: 10.1063/1.323539. URL: https://doi.org/10.1063/1.323539.

[277] M.O. Selme and P. Pecheur. "Electronic structure of hexagonal iron layers". In: *Journal of Magnetism and Magnetic Materials* 93 (Feb. 1991), pp. 285–289. ISSN: 0304-8853. DOI: 10.1016/0304-8853(91)90347-D. URL: https://www.sciencedirect.com/science/article/abs/pii/030488539190347D.

[278] M. Seidl and M. Brack. “Liquid Drop Model for Charged Spherical Metal Clusters”. In: *Annals of Physics* 245.2 (Feb. 1996), pp. 275–310. ISSN: 0003-4916. DOI: 10.1006/APHY.1996.0010. URL: https://www.sciencedirect.com/science/article/pii/S000349169690010X.

Titre : Simulation de processus de stockage chimique pour l'énergie renouvelable.

Résumé : L'objectif de la présente thèse englobe différents processus liés au stockage d'énergie provenant de sources renouvelables. Concrètement, cette thèse vise à étudier, d'un point de vue théorique, les processus liés à la réaction de Sabatier assistée par plasma (CO 2 + 4 H2 → CH4 + 2 H2O), où le catalyseur hétérogène est composé d'éléments Ni / Ru. La recherche est par conséquent divisée en thèmes développés dans les spécialités de chaque partenaire. À l'université de Pérouse, les processus plasma / phase gazeuse sont pris en compte, concrètement l'étude de l'OH + H 2 selon la méthode quantique classique. La principale procédure innovante a été d'ajouter une surface potentielle à longue portée à la surface d'énergie potentielle (PES) déjà disponible, en la convertissant en une surface appropriée pour les processus non réactifs, tout en maintenant la précision de la mesure initiale, nécessaire aux processus réactifs. Dans ce sens, nous avons mené une étude sur la diffusion OH + H2 en utilisant une méthode quantique classique, traitant les vibrations quantiques et classiquement les translations et les rotations. Le bon accord entre les probabilités réactives classiques quantiques spécifiques à l'état et les probabilités quantiques complètes correspondantes a conduit à l'extension de l'étude aux probabilités d'état à état pour les échanges d'énergie vibratoire non réactifs. L'étude a montré que la dynamique de la réaction H 2 dépend de l'excitation vibratoire, alors que celle non réactive est principalement adiabatique sur le plan vibratoire. Au contraire, la dynamique réactionnelle de l'OH n'est pas affectée par son excitation vibratoire, alors que la non-réactive pourrait en produire un pompage jusqu'à des états vibratoires plus élevés. Dans l'université Paul Sabatier de Toulouse, les grappes et nanoparticules de Ru, faisant partie du catalyseur industriel, sont étudiées selon l'approche DFTB. L'intention était d'étudier la capacité de la DFTB à fournir des résultats fiables sur la structure électronique, les propriétés structurelles et la stabilité des systèmes monométalliques à base de ruthénium, allant de petites grappes à des nanoparticules plus grosses et globalement. Étant donné que le collage électronique et l'organisation structurelle du groupe de ruthénium sont quelque peu spécifiques par rapport aux autres groupes de métaux, il est difficile de déterminer si la DFTB est capable de prendre en compte de telles particularités. La dynamique moléculaire à revenu parallèle (PTMD) a été utilisée en association avec une extinction périodique pour obtenir une optimisation globale des grappes neutres, cationiques et anioniques dans la plage n = 3-20. Les résultats ont montré un très bon accord avec les calculs expérimentaux et théoriques de niveau plus élevé en considérant l'énergétique des clusters, pour sa structure, ses potentiels d'ionisation et ses affinités électroniques. De plus, toutes les propriétés se sont révélées cohérentes avec les limites définies par l'atome isolé et l'ensemble. Il a été prouvé que Spin joue un rôle majeur dans la description des clusters, permettant à certaines configurations spatiales d'avoir leur stabilité particulière. L'étude des nanoparticules a conduit à un excellent accord avec les résultats de la DFT et les valeurs expérimentales à la fois pour son énergie et sa structure, conservant non seulement les tendances entre la forme standard des nanoparticules, mais prédisant également la même valeur que celle obtenue pour d'autres études sur la structure cristalline transition entre simple cubique à, d'abord, fcc à, enfin, hcp. Enfin, nous étudions la cinétique du processus catalytique hétérogène à la surface de Ni (111) afin de contribuer au développement de l'appareil Progeo. Nous avons utilisé ZACROS, un système cinétique de Monte Carlo (KMC), pour simuler des phénomènes moléculaires sur des surfaces catalytiques. Sur la méthodologie KMC de graphes théoriques. Un résultat important de nos calculs est illustré dans lequel, contrairement à la suggestion d'une analyse statique ne prenant en compte que l'énergétique des états de transition, montre que le processus dominant menant à la production de CH4 est l'hydrogénation du CO. autres procédés possibles en phase gazeuse produisant du CO.

Mots clés : Énergie renouvelable - Catalyse - Nanoparticules - Dynamique moléculaire.

Title: Network computing for ab initio modeling the chemical storage of alternative energy.

Abstract : The aim of the present thesis encompasses different processes related to the storage of energy coming from renewable sources. Concretely, this thesis aims to study, from a theoretical point of view, the processes related to the plasma-assisted Sabatier reaction (CO 2 + 4 H2 → CH4 + 2 H2O), where the heterogeneous catalyst is composed by Ni/Ru elements. The research is consequently split in the topics developed at each partner specialties. In the university of Perugia, the plasma/gas phase processes are considered, concretely the study of the OH + H 2 using the quantum-classical method. The main innovative procedure has been to add a long-range potential tail to the already available. Potential Energy Surface (PES), converting it into a suitable one for non reactive processes, while maintaining the accuracy of the ab initio, necessary for the reactive processes. In this sense we carried out a study of OH + H2 scattering using a quantum-classical method, treating quantally vibrations and classically both translations and rotations. The good agreement between the state specific quantum-classical reactive probabilities and the corresponding full quantum ones prompted the extension of the study to state to state probabilities for non reactive vibrational energy exchange. The study showed that H 2 reactive dynamics depends on the vibrational excitation, while the non reactive one is mainly vibrationally adiabatic. On the contrary, OH reactive dynamics is not affected by its vibrational excitation, whereas the non reactive one might produce some pumping up to higher vibrational states. In the university Paul Sabatier of Toulouse, the Ru clusters and nanoparticles, part of the industrial catalyst are studied using the DFTB approach. The intend was to investigate the ability of DFTB to provide reliable results about electronic structure, structural properties and stability of monometallic ruthenium systems covering the size range from small clusters to larger nanoparticles and the bulk. Due to the fact that the electronic bonding and structural organization of ruthenium cluster are somewhat specific in regard of other metal clusters, it is challenging to examine whether DFTB is able to account for such peculiarities. Parallel-Tempering Molecular Dynamics (PTMD), was used in combination with periodic quenching to achieve global optimization of neutral, cationic and anionic clusters in the range n=3-20. Results showed a very good agreement with both experimental and higher level of theory calculations from considering the energetics of the clusters, for its structure, ionization potentials and electron affinities. Moreover, all properties showed to be consistent with the limits set by the isolated atom and the bulk. Spin was proven to play a major role in the description of the clusters, enabling certain spatial configurations to have their special stability. Study of the Nanoparticles led to an excellent agreement with the DFT results and experimental values for both its energetics and its structure, conserving not only the trends between the standard nanoparticle shape, but also predicting the same value as obtained for other studies in the crystalline structure transition between simple cubic to, first, fcc to, finally, hcp. Finally study of the kinetics of the heterogeneous catalytic process on the Ni(111) surface are done to assist the development of the Progeo apparatus.use has been made of ZACROS a Kinetic Monte Carlo (KMC), for simulating molecular phenomena on catalytic surfaces leveraging on the Graph-Theoretical KMC methodology. An important outcome of our calculations is illustrated in which, in contrast with the suggestion of static analysis considering only the energetics of transition states, show that the dominant process leading to the production of CH4 is the hydrogenation of CO. This has suggested us to investigate possible alternative gas phase processes producing CO.

Keywords: Renewable energy, Catalysis, Nanoparticles, Molecular dynamics.